PhD thesis

UNIVERSITE DE LILLE

Ecole doctorale Sciences de la Matière, du Rayonnement et de l'Environnement

UFR de Chimie

To obtain the grade of

DOCTOR

in Materials Sciences

by

Julie GODON

Graduate Engineer of

Ecole Nationale Supérieure de Chimie de Lille

INFLUENCE OF STEEL CLEANLINESS ON THE WIRE DRAWING OF HYPEREUTECTOID STEEL FINE FILAMENTS

The thesis was presented and defended in Lille on January 21, 2020

Alexandre LEGRIS	Professor, Université de Lille, France	president and examiner
Zoia DURIAGINA	Professor, LPNU, Ukraine	reviewer
Alain HAZOTTE	Professor, Université de Lorraine, France	reviewer
Cristelle PAREIGE	Professeur, Université de Rouen, France	examiner
Pascal ANTOINE	Dr and Senior R&D manager, Bekaert, Belgium	industrial supervisor
Jérémie BOUQUEREL	Assistant professor, ENSCL, Lille France	PhD supervisor
Jean-Bernard VOGT	Professor, ENSCL, Lille France	PhD director

Thèse de doctorat
UNIVERSITE DE LILLE
Ecole doctorale Sciences de la Matière, du Rayonnement et de l'Environnement
UFR de Chimie

Pour l'obtention du grade de
DOCTEUR
en sciences des matériaux

par
Julie GODON
Ingénieur diplômée de
l'Ecole Nationale Supérieure de Chimie de Lille

INFLUENCE DE LA PROPRETÉ INCLUSIONNAIRE SUR LA TRÉFILABILITÉ DES FINS FILAMENTS D'ACIERS HYPEREUTECTOÏDES

La thèse a été présentée et défendue à Lille le 21 janvier 2020

Alexandre LEGRIS	Professeur, Université de Lille, France	président et examinateur
Zoia DURIAGINA	Professeur, LPNU, Ukraine	rapporteur
Alain HAZOTTE	Professeur, Université de Lorraine, France	rapporteur
Cristelle PAREIGE	Professeur, Université de Rouen, France	examinatrice
Pascal ANTOINE	Dr and Senior R&D manager, Bekaert, Belgique	encadrant industriel
Jérémie BOUQUEREL	Maître de conférences, ENSCL, Lille France	co-encadrant de thèse
Jean-Bernard VOGT	Professeur, ENSCL, Lille France	directeur de thèse

Table of contents

List of figures

Introduction

- Background and context of the study

This PhD work results from a collaboration between “Université de Lille” and Bekaert NV.
Bekaert NV is a wire company dedicated to the transformation and coatings of steel wires for multiple applications as automotive. This report gives enough elements to understand the context and the content of the report even though for confidential reasons some technical details are not mentioned on this report.
To stay competitive, steel industries have to develop more and more high specialty steel products with greater mechanical properties. For special applications, steel wires have to be everyday thinner while keeping their incredible mechanical properties. For that, wire companies have to develop the best process to succeed this challenge. Fine drawing has to be developed and controlled to obtain fine filaments with ultra-high strength. Wire properties and drawing parameters have to be optimum to design the perfect microstructure and to obtain the required mechanical properties. The ductility, mechanical strength and fatigue properties have to be also straightly controlled in order to fit with the specifications of customers.
Today, the challenge of the Bekaert NV is to draw fine filaments up to 0.06mm in diameter. A spool of 240 000m is required by the customer. The major issue for the filaments drawing is the occurrence of fractures. The occurrence of fractures during wet wire drawing (WWD) causes for the company a financial and a time loss and impact the image of the company. Therefore, it becomes important for Bekaert NV to understand the causes of these fractures in order to have a chance to reduce the fractures of the wire.

- Preliminary study

To understand the origin and the causes of the fractures of 0.06mm filament during wet wire drawing, a preliminary study has been performed on fractures obtained during WWD. For all testing conditions and different wires, more than 200 fractures were analysed. This preliminary study pointed out that 90% of the fractures were induced by the presence of a non-metallic inclusion in the fracture. Those inclusions were always on the top of a cup and cone fracture. After this statement, it was decided to bring the focus on the impact of inclusion on fracture occurrence during the wet wire drawing of 60µm filaments.

- Objectives of the present study

The principal objective of the present study is to understand what are the different factors that promote the fracture of a 60µm diameter filament during wire drawing when an inclusion is present. So the three specific aspects of the study are the following: the wire drawing, the fine filaments and the presence of an inclusion. The wire drawing presents a complex mode of loading compared to basic mechanical testing as tensile test, fatigue. The loading is not uniaxial and monotonic which makes the study of the deformation complex. The diameter of the final filaments is also a challenge. Working with fine diameter filaments is challenging for sample preparation, observation, and mechanical tests.

To understand the occurrence of fractures during the wire drawing, the first part consisted in the study of the fracture causes, taking into account the statistical aspect. As mentioned on the preliminary study, since inclusions are responsible of 90% of the fractures, it is therefore necessary to identify the critical inclusions responsible of fracture in term of size, composition and shape

The purpose of the second part is to understand the impact of steel cleanliness and the role of inclusions in hypereutectoid steel wires during fine drawing. In other words, the study consisted in establishing the correlation between the drawability, meaning the occurrence of fracture due to inclusions during fine drawing, and inclusions characteristics present into the wire rod like the number, the size, the morphology, and the composition of non-metallic inclusions. Again, since the study was performed taking into account the statistical aspect, it was necessary to develop an experimental strategy that allows the analysis of a very large number of data. The selection of the technics and their combination held a large part of the project. Those methods will be applied on wire rod and on fine filament to study the impact of wire drawing on inclusions. Different grades of steel from different suppliers will be analysed for a comparison between inclusions properties and drawability for fine drawing.

Then, a study of the impact of drawing parameters on inclusions behaviour and on fracture occurrence has been performed in view to characterize the best drawing conditions to reduce the fracture ratio due to inclusions.

Once the inclusions were identified in details, the research was focused on the local investigation of the matrix around the inclusions in terms of strain partition. A deeper analysis of the fracture mechanisms due to an inclusion by using different techniques to image the strain repartition around the inclusion during the deformation has been undertaken.

Finally, the study ended by suggesting a fracture mechanism of steel fine filaments during WWD that contain an inclusion.

The manuscript will be organized on the following plan. First a literature study explains the context and the studies related to the subject. A second part will describe the materials and the experimental methods applied during this study. The results part will be organized according to the four previous parts. First the fracture analysis and the identification of critical inclusions, the second part links the drawability and the cleanliness, the third part will present the impact of the drawing parameters and wire properties on the fracture behaviour. In the fourth part, the understanding of the impact of the inclusion into the matrix during drawing will be analysed.

Chapter I: Literature review

Literature review

The bibliographic study is divided in five major parts. The first part will deal with the description of hyper eutectoid steel wires. The second part will explain the drawing process, the influence of the drawing parameters and their effects on the microstructure. The third part will focus on the principal inclusions features and briefly their formation. Finally, the last part will detail the influence of these inclusions on the mechanical properties and the deformation process in general. A more detailed part will interpret the previous study on the role of an inclusion during the wire drawing.

1 Hypereutectoid Steel wires

A hypereutectoid steel is an iron matrix where the carbon content is superior to the eutectoid point, which corresponds to 0.80%wt carbon. This addition of carbon to the steel matrix leads to a change of mechanical properties. The hypereutectoid steels are known to be ultra-high resistant to tension but with a low ductility. Hypereutectoid steels with high strength find applications in tire cord and in other high strength wire applications. For this study, the selected wires are above the eutectoid with a carbon content of about 1.0%wt. Referring to the Fe-C diagram (Figure 1), the microstructure is expected to be pearlitic with a proeutectoid cementite, the latter being formed at grain boundaries and brittle. It is needed to find some ways to avoid it in the microstructure. The basis for this possible breakthrough in the elimination of this brittle proeutectoid network is an appropriate processing procedure and the choice of alloying elements. Alloying elements known to reduce the formation of this inter granular pro eutectoid cementite are Si and Mn. With the combination of an appropriate heat treatment and the alloying elements, the microstructure of the hypereutectoid steel wires is fully pearlitic as presented in Figure 2.

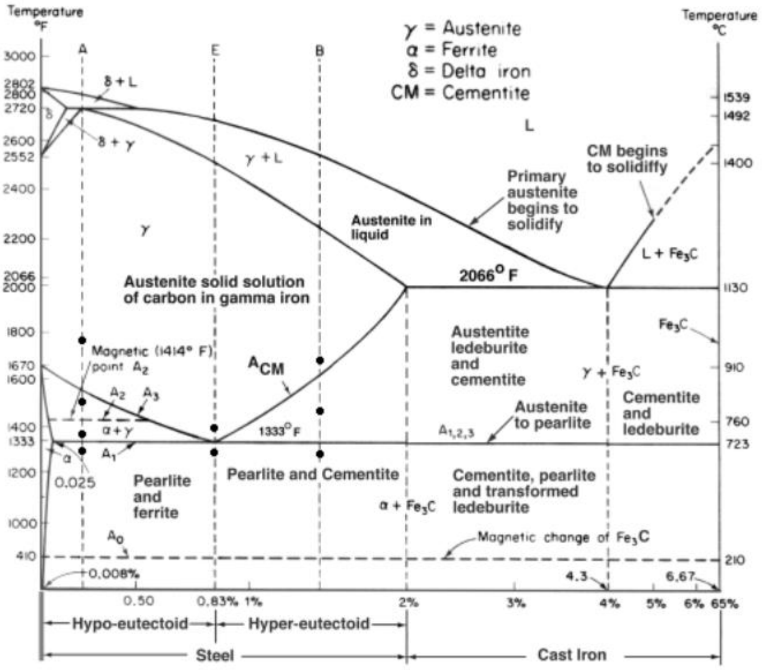

Figure 1 : Iron-Carbon phase diagram**[1]**

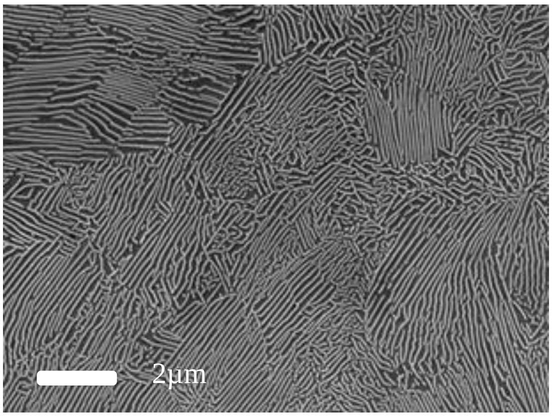

Figure 2 : SEM images of a fully pearlitic structure in a hypereutectoid steel

- <u>Pearlitic structure</u>

Pearlite is a two-phased structure composed of alternating layers of ferrite (87.5 wt%) and cementite (12.5 wt%). If the lamellar pearlite undergoes a severe thermal treatment, the lamellar structure can degenerate to the globular structure. In the following, only lamellar pearlite is considered. Two types of lamellar pearlitic structure exist: the coarse and the fine pearlite. The coarse pearlite is more ductile and tougher but less resistant to tension that the fine pearlite. Lamellar pearlite is a product of eutectoid decomposition that usually takes place during high temperature (550°C to 720°C) transformation of steel under isothermal cooling [2]. Microstructure of pearlitic steels generally consists of pearlite nodules in which multiple colonies formed with lamellar ferrite and cementite. Pearlite nodule is generally defined as the region of fully transformed microstructure that grows up from a single pearlite nucleus whereas pearlite colony refers to the region in which ferrite lamellae and cementite align alternately and are parallel to each other as the result of a common growth direction during pearlite transformation [3–5]. Figure 3 describes a schematic representation of grains, nodules and colonies that reveals a hierarchical structure of pearlite. Such a structure creates three types of boundaries, nodular boundary, colony boundary and phase boundary between ferrite lamellae and cementite lamellae. As a result, it is difficult to determine the nodule size or colony size using metallography images.

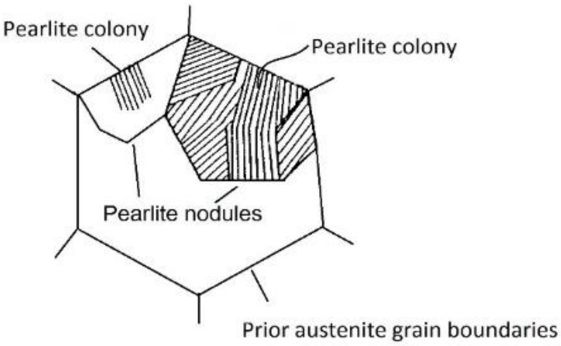

Figure 3 : Schematic of pearlitic structure[6]

2 Basic theory of drawing

2.1 Introduction on drawing

Wire drawing is one of the most used processes for fabrication of electrical cable and metallic wires. In the wire drawing process the cross-sectional area of a wire is reduced by pulling it through a die creating a long product with a constant cross section that has an excellent surface finish and closely controlled dimensions. Drawing is usually conducted at room temperature using a number of passes or reductions through consecutively located dies, reducing thus progressively the section of the wire.

The drawing process is considered as an indirect compression process, in which the major forming stress results from the compressive stresses because of the direct tensile stresses exerted in drawing.

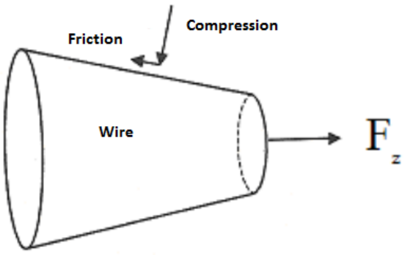

Figure 4: Schematic illustration of forces in drawing [7]

The elongation of the metal results from the strain field that causes a plastic flow in view to obtain the required geometry. The process leads to big modifications of mechanical properties. The properties changes are used in view to obtain the required geometry, mechanical properties, and a specific surface state to have the perfect wire quality.

Although it may be believed that the forces and power in wiredrawing compared to simple tension, deformation conditions in wire are, in fact, far more complex due to compressive and drag forces generated by the die surface. In the drawing process, a pulling force and a pressure force, from the die, are combined to extend and reduce in cross-sectional area, while passing through the die. Because of this combined effect, the pulling force or drawing force can be less than the force that would cause the wire to stretch, neck, and break downstream from the die. On the other hand, if a reduction too large in cross-sectional area is attempted at the die, the drawing force may break the wire

2.2 Description of the effort applied on the wire during the drawing process

During the drawing process, the wire is pulled through the die by a pulling force. The plastic flow of the metal is possible thanks to the combined action of the axial tension force and radial compression imposed by the die. At the die-wire interface, a lateral pressure is imposed by the die due to friction. The necessary force to draw the wire is the sum of the necessary force to plastically deform the wire and the force to overcome the friction force.

The total work consumed at a draw stand can be partitioned into three components. These are: (a) useful (homogeneous) work required to reduce the cross section, (b) work required to overcome frictional resistance, and (c) redundant (inhomogeneous) work required to change the flow direction (Figure 5)

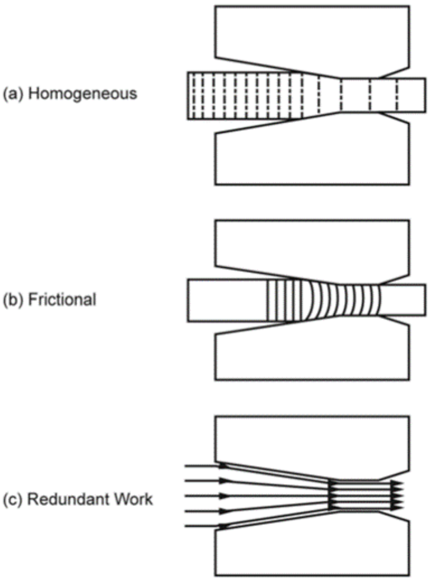

Figure 5: Illustration of (a) homogeneous, (b) frictional, and (c) redundant work in wiredrawing [8]

Redundant work and frictional work have adverse effects on wire properties in addition to the energy needed for drawing. One consequence is that mechanical properties will not be homogeneous across the wire cross section.

Layers at the wire surface will not only undergo a change in cross section, but they will also deform by shear because of drag presented by the die surface (see Figure 5). Even for highly polished die surfaces and hydrodynamic lubrication, a certain amount of frictional work will be present. Frictional work dominates at low die angles where surface drag is increased as a result of higher contact length in the approach zone for a given reduction.

The total drawing force is described as an important parameter of the drawing process. Persson described this as the sum of distinct terms: [9]

$$Ft = F_1 + F_2 + F_3 + F_4 \tag{1}$$

Where

Ft – The total drawing force [N]

F_1 - The homogeneous force [N]

F_2 - The friction force [N]

F_3– The heterogeneous force [N]

F_4 – The friction force produced in cylindrical area from the die [N]

The four components defined as follow:

$$F_1 = A_1 . \sigma_C . \ln(\frac{A_0}{A_1}) \tag{2}$$

$$F_2 = A_1 . \sigma_c . \left(\frac{\mu}{\alpha}\right) . \ln(\frac{A_0}{A_1}) \tag{3}$$

$$F_3 = A_1 . \sigma_c . 2\alpha/3 \tag{4}$$

$$F_4 = \pi d_1 . l_1 . R_e . \mu \tag{5}$$

With:

A_0- The cross section of the wire before drawing process [mm²]

A_1- The cross section of the after the drawing process [mm²]

σ_C- The mean of the Yield tensions before and after drawing process [N.mm^{-2}]

2α - The die angle [radians]

μ - The friction coefficient

d_1- The wire diameter after the drawing process [mm]

l_1- The length of the cylindrical area for the die [mm]

R_e- The yield strength of the filament after the drawing process [N.mm^{-2}]

The total drawing force is expressed by the equation 6 [10]:

$$F_t = A_1.\sigma_c.\left(ln\frac{A_0}{A_1}+\frac{\mu}{\alpha}.ln\frac{A_0}{A_1}+\frac{2\alpha}{3}\right)+\pi.d_1.l_1.R_e.\mu \tag{6}$$

To summarize, it can be concluded that the force applied to the wire during the wire drawing depends mainly on the **die geometry**, **the reduction of the wire**, **the mechanical properties** of the wire and the **friction coefficient.**

Moreover, the wire drawing process gives rise to the development of strain inhomogeneity, which leads to inhomogeneity of the mechanical properties and of microstructure along the radial direction of the drawn wire. Therefore, wire drawing imparts the stress states different from those experienced during other deformation modes since wire drawing process involves the reduction of the cross-sectional area of wire by forcing the wire through series of conical dies. This complexity of the stress states imparted during wire drawing is illustrated into where the stress inhomogeneity into the wire cross section was modelled (Figure 76). The centre area has a tensile stress during the whole drawing process, while the surface area has a combination of tensile, compressive and shear stresses. The stress profiles for the centre and the surface of the wire are presented in Figure 7.

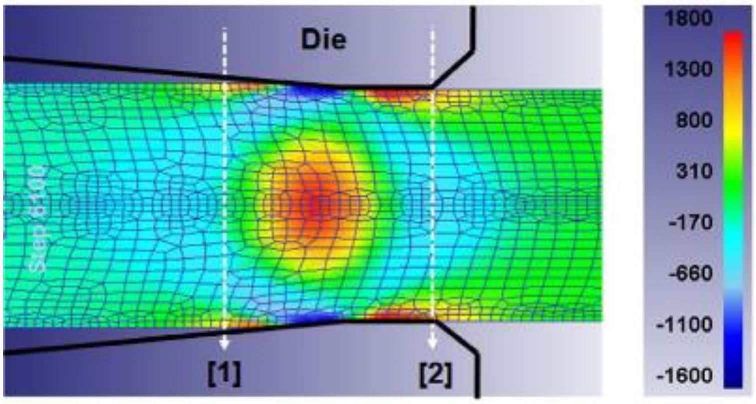

Figure 6: Axial stress (MPa) distribution of the wire [11]

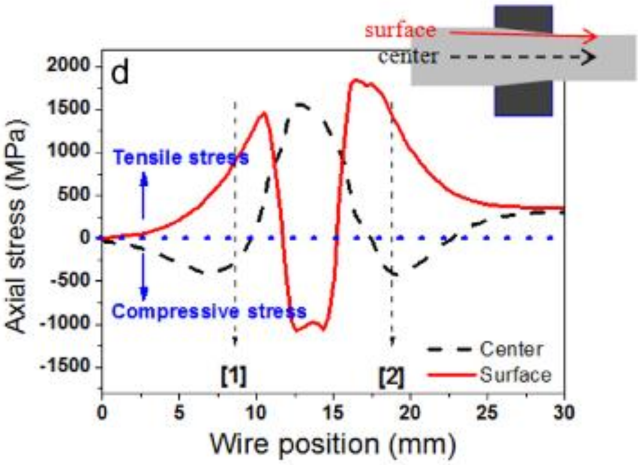

Figure 7: Stress profiles along the axial direction [11]

This diagram underlines the inhomogeneity of the stress repartition at the edge and the surface. This modelling was performed on a Ø30mm rod. For thinner wires, it is more complex to represent those strains as there is an overlap of the compressive and tensile stress.

2.3 From wire to filament

As Bekaert is not a metal producer, the wire rod is directly provided from different suppliers. The typical wire rod has a diameter of a 5.5mm. Different grades and chemical compositions of wire rod are used depending on the final application. Several reductions and treatments have to be applied to the wire rod in view to obtain the 60µm filament. Typically, the process of wire rod includes six steps: (Figure 8)

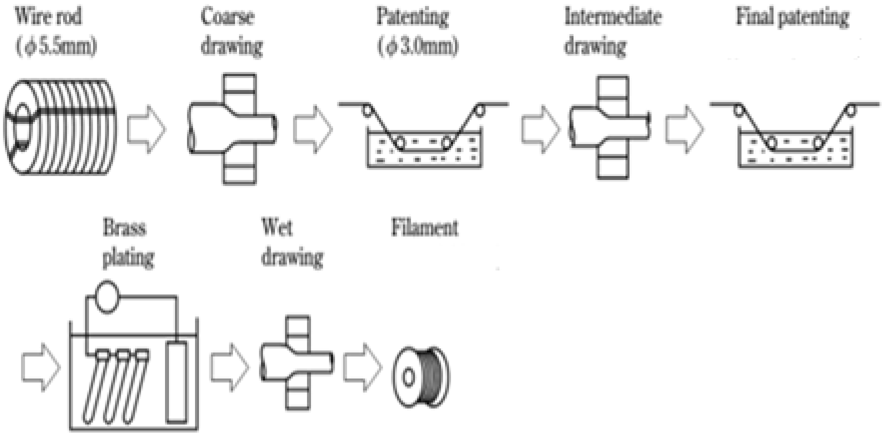

Figure 8: Schematic of the process from wire rod to filament [12]

- Coarse drawing to reduce the diameter from 5.5mm to ~3mm
- First patenting corresponding to a thermal treatment in view to release the stress induced into the wire after the first drawing and to control the microstructure
- An intermediate drawing to reduce the wire section until the necessary diameter for the following wet wire drawing step. The intermediate diameter depends exclusively on the final use of the product and the final diameter required
- The final patenting to release the stress accumulated on the grain during the drawing step and to recover the microstructure
- Brass plating for a lower friction during the wet wire drawing; since the brass coating is much softer than the steel wire, it acts as some kind of lubricant during the wet wire drawing process, ensuring a smooth deformation
- Finally, the Wet Wire Drawing (WWD) to obtain the final filament (60µm)

Dry drawing

The dry drawing is a multi passes process where the wire is reduced at each pass by use of a die. The wire is pulled into drawing dies to reduce the diameter thanks to a solid lubricant e.g. soap. The dry drawing is mostly used for bigger diameters (superior to Ø0.5mm).

Patenting

Patenting is a thermal treatment used to obtain the adequate microstructure for the following step. After drawing, the microstructure is totally deformed due to the internal strain to which the wire is subjected to. The patenting consists of an austenitisation followed by a controlled cooling in lead bath. This process permits to release the deformed microstructure due to drawing and to obtain a fully pearlitic microstructure. The temperature is also controlled in view to avoid residual carbides.

2.4 Wet wire drawing process

2.4.1 The wet wire drawing machine

The wet wire drawing machine is a multi-pass process machine, which allows the presence of more than 20 dies. The wet wire drawing is mostly used for fine filament drawing. As a difference with dry drawing, the wet drawing is done in presence of liquid lubricant. Almost all the dies and the wire are fully immerged in the lubricant during the drawing process (Figure 9), expect the last die called head die. This head die is partially in contact with lubricant and air. The wire, after the last die, is directly in contact with air to be spooled.

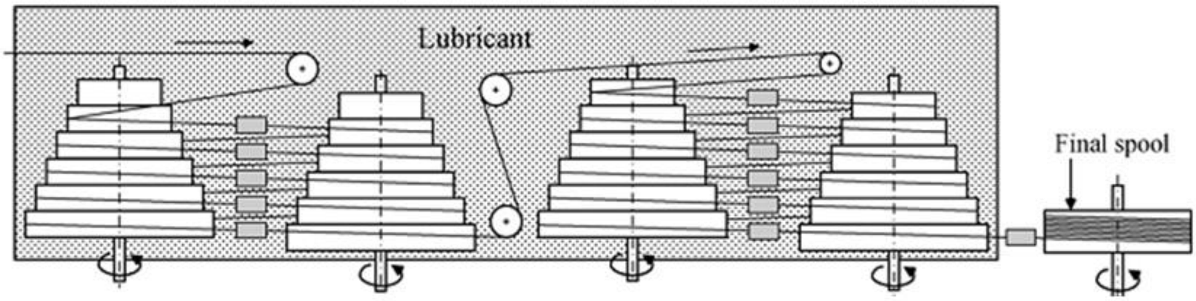

Figure 9: Schematic of a wet wire drawing machine [13]

In this process, the reduction ratio from the initial to the final wire is more than 90% and the final drawing speed is very fast. Specifically, the final drawing speed for fine high carbon steel wire is several hundred m/min.

2.4.2 Wet wire drawing parameters

The wet wire drawing process is controlled by different parameters which influence the quality of the final product and its mechanical properties.

- The drawing strain: as showed before, the drawing strain of the wire is defined as following:

  $$\varepsilon = \ln(\lambda) = 2\ln(\frac{D_i}{D_f}) \qquad (7)$$

  This parameter depends mainly on the initial diameter D_i used at the beginning of the process and the final diameterD_f.

  At high drawing strain, the reduction is higher meaning by consequence that the reduction per pass is higher. A high drawing strain tends to increase tensile resistance, but also to decrease the ductility of the final filament. The occurrence of fracture is also favoured at higher drawing strain.
- The drawing speed: Different drawing speeds can be used for the wire drawing. The drawing speed is adapted to the process and to the diameter of the final product. A higher speed permits a gain of time for the process and a reduction of friction. The drawback of a higher speed during the WWD is the dynamic ageing by an increase in temperature. The dynamic ageing is known to promote the tensile strength but will disfavour the ductility.

➢ Dies

The die is the conical part used for the reduction of wire during the drawing. It is composed of two parts, the nib, a hard part that enables the reduction of the wire and the casing, a metallic part that supports the nib (Figure 10). The casing must be resistant enough to deal with the high pressure and loading from drawing process. The nib composition depends on the drawing step. For dry drawing, TiC dies are used because of the high pressure on the dies. For the thinner drawing diamond die are used

As explained before the die geometry is an important factor on the wire drawing. The three important factors are the following: The semi die angle, the bearing length and the reduction of the die.

The effect of the approach angle on the material flow cannot be easily considered. Commercial dies generally exhibit a semi die angle (2α) in the range of 4 to 10° and a drawing reduction around 20%. The die geometry influences the shape of the deformation zone. This shape is characterized by the Δ factor as defined by the equation 8 where the Δ factor depends also on the reduction of the die.

$$\Delta = (average\ height\ of\ zone \perp to\ drawing\ axis)/(length\ of\ zone\ \backslash\backslash to\ drawing\ axis) \qquad (8)$$

Δ can be approximately written as:

$$\Delta \approx \left(\frac{\alpha}{r}\right)\left[1+(1-r)^{\frac{1}{2}}\right]^{2} \approx 4\tan(\alpha/\ln(1/(1-r)) \qquad (9)$$

Where:

- α is the semi die angle of the die (rad)
- r is the reduction of the wire defined by equation 10

$$r = 1 - A_1/A_0 \qquad (10)$$

Where A_0 and A_1 are respectively the entrance and the exit cross section of the wire.

The industrial Δ values typically range from 1.5 to 3. A higher value of Δ implies a lower reduction and a higher die angles which will accentuate the frictional work between the wire and the drawing die while a low Δ corresponds to a high reduction with lower angles. This will lead to a higher redundant work (work that is not used for the wire reduction).

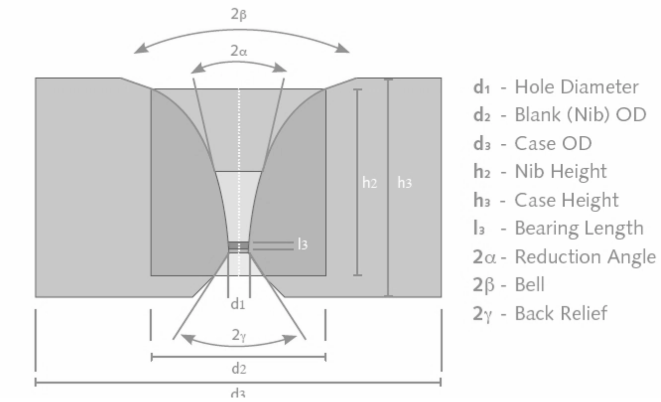

Figure 10 : Schematic of a wire passing through a die and die structure [14]

- Impact of drawing on microstructure deformation

Due to the severe plastic deformation applied during wire drawing, the microstructure is subjected to transformation. After patenting, the pearlite colonies are randomly oriented. After drawing, the pearlite nodules are oriented to lead to a nanoscale microstructure. This change in microstructure is responsible for the exceptional mechanical properties of steel wires. Lamellae alignment, cementite decomposition, localization of plastic flow, dynamic aging and residual stress development are relevant processes occurring in heavily drawn steel wires and are described below.

- Lamellae alignment

In a study of Zhang et al. [15], the deformation of pearlitic microstructure implied by wire drawing is studied. Microstructural investigations were performed at intermediate steps of the wire drawing process (referred as paternoster in the following chapter) from the as patented wire (1.26mm) to the final drawn wire (0.2mm) on both longitudinal and cross-sections. The as patent wire exhibits a fine pearlitic microstructure. This microstructure is taken as a reference state at a $\varepsilon=0$. In Figure 11, it is observed that the cementite plates within each pearlite colony are randomly distributed without preferential distribution.

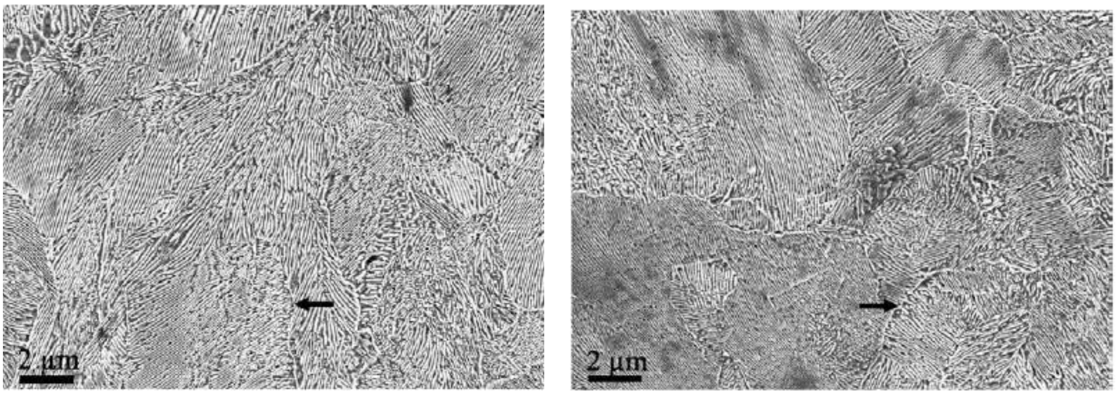

Figure 11 : SEM images of the as patented wire microstructure (left) longitudinal section (right) cross section [16]

Figure 12 shows the longitudinal and the transverse section of the wire at a strain of 0.7. It is observed that the cementite plates start to be oriented into the drawing direction. In the transverse section, twisting (curling) is heavy.

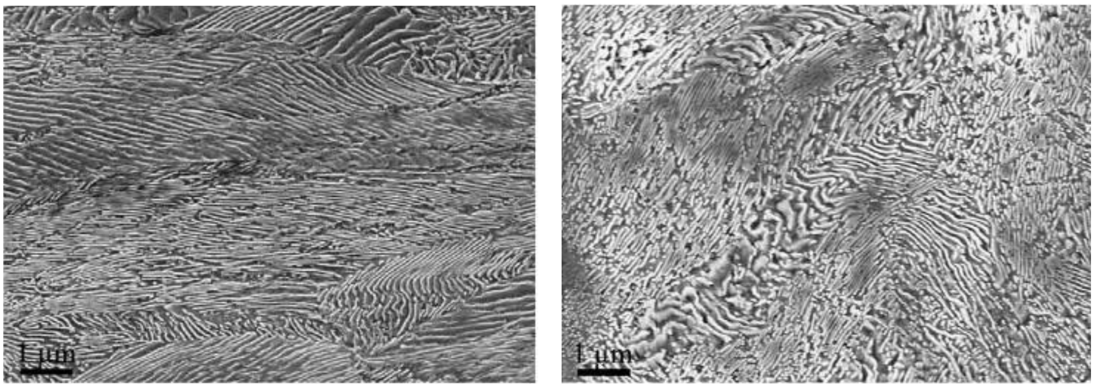

Figure 12 : SEM images of a wire at $\varepsilon=0.7$ microstructure (left) longitudinal section (right) cross section [16]

In the material strained up to $\varepsilon=2.7$ (Figure 13), the observation of the longitudinal section shows that all the cementite plates are oriented along the drawing direction and more stretched compared to the lower strains. In the cross section, the twisting of cementite is severe and the cementite lamellae are thinner compared with those seen in the material strained at $\varepsilon=0.7$. On the cross section, the morphology is completely curled. Randomly, some shear bands are observed across the cementite plates (black square on the right corner).

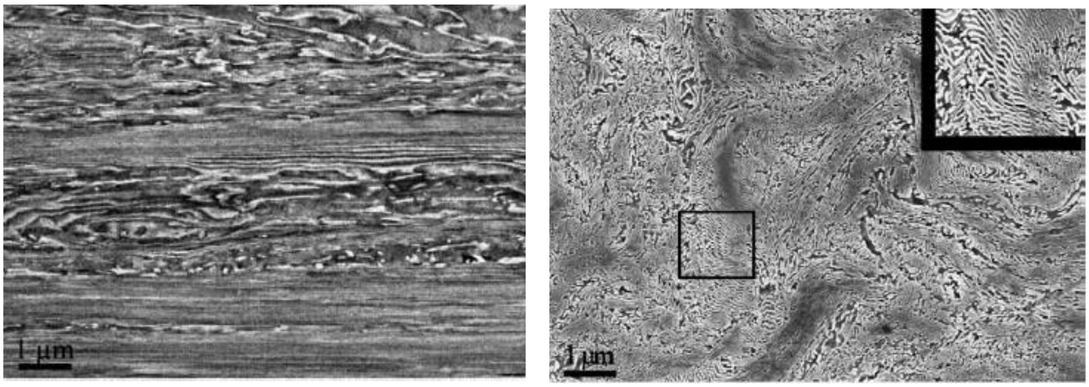

Figure 13 : SEM images of a wire at ε = 2.7 microstructure (left) longitudinal section (right) cross section [16]

More than the alignment of the lamellae, the WWD induces a reduction of cementite plate thickness (Figure 14). Drawing to higher strains than ε=1.5 results in a lengthening and thinning of cementite. Some fracture of the cementite plates takes place, related primarily to the curling deformation seen in the transverse cross section.

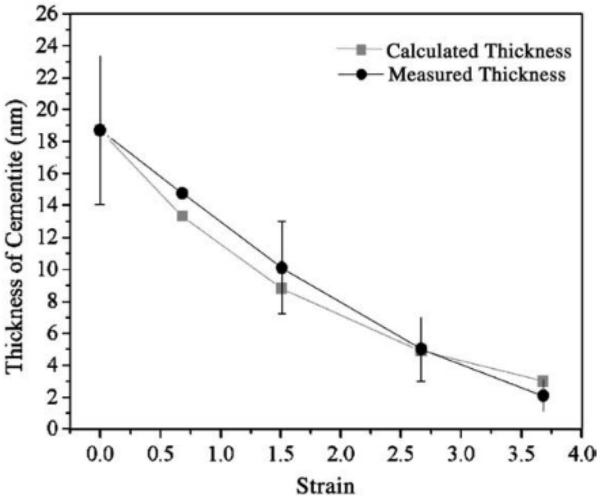

Figure 14 : Reduction of cementite thickness for higher drawing strain[15]

In the concerned PhD study, the material will be strained at a value of ε> 4. This deformed microstructure is an issue to be observed. The microstructure of the matrix at the surrounding of an inclusion and of the matrix far from inclusion is different. All those microstructure changes during WWD have to be taken into account which requires tough and non-easy investigation of the drawn wires. This will complicate the study of drawn wire.

3 Steel cleanliness

One way to provide steels with high performance, high reliability and durability is to control non-metallic inclusions particles embedded in the matrix of steel.

The ASM handbook defines non-metallic inclusion as particles of foreign material in a metallic matrix. Typically, inclusions contain a metallic part such as Mg, Mn, Al and a non-metallic one as Si, O, S, N, and C. The particles are usually compounds such as oxides, sulphides, and carbides but may be any substance insoluble in the matrix.

The presence of non-metallic inclusions in the finished steel can have a large effect on certain properties of the final product. For that reason, the steelmaking industry is motivated to produce cleaner steels, steel cleanliness being related to the presence of non-metallic inclusions and other impurities that influence the quality of the final product. Since specific applications involve specific steel properties, the requirements on steel cleanliness are largely dependent on the application.

Table 1 [17] shows different cleanliness requirements for different applications.

Table 1 : Typical steel cleanliness requirements for high performance steels [17]

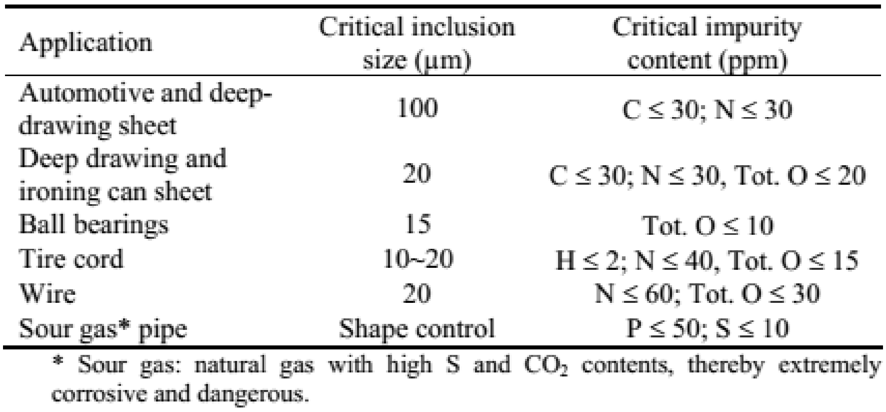

Application	Critical inclusion size (μm)	Critical impurity content (ppm)
Automotive and deep-drawing sheet	100	$C \leq 30$; $N \leq 30$
Deep drawing and ironing can sheet	20	$C \leq 30$; $N \leq 30$, Tot. $O \leq 20$
Ball bearings	15	Tot. $O \leq 10$
Tire cord	10~20	$H \leq 2$; $N \leq 40$, Tot. $O \leq 15$
Wire	20	$N \leq 60$; Tot. $O \leq 30$
Sour gas* pipe	Shape control	$P \leq 50$; $S \leq 10$

* Sour gas: natural gas with high S and CO_2 contents, thereby extremely corrosive and dangerous.

3.1 Origin of inclusions

3.1.1 Inclusion during steel making

Non-metallic inclusions are generally classified according to their source. They can be divided into two groups: indigenous or exogenous [18].

Exogenous inclusions arise primarily from the incidental chemical and mechanical interaction of liquid steel with its environment. Their causes are various. One of them is by slag entrapment. This occurs especially during transfers between steelmaking vessels. Exogenous inclusions can also be due to dust, refractory brickwork or ceramics lining particles. Some of the characteristic features of exogenous inclusions in steels noted by Kiessling [18] are larger size compared to indigenous inclusions, sporadic occurrence, irregular shapes, and complex structures due to their origins. Exogenous inclusions, in general, are harmful to material behaviour [19].

Indigenous inclusions are deoxidization products or precipitated inclusions during cooling and solidification of steel.

Ironmaking [20,21] involves the production of liquid iron, called hot metal, from iron ore. The steel making process is sintered iron ore, coke and other fluxes are fed into a blast furnace, where iron oxide is reduced by carbon and CO gas, producing molten pig iron. After the blast furnace, the hot metal contains 4 to 4.5wt% C and other impurities, such as Mn, Si, P and S, and as such is not suitable for most engineering applications.

To achieve the required properties of steel, the steel composition, temperature and cleanliness must be adjusted. Refining treatments are carried out during the secondary steelmaking process. Crude steel is transferred in the ladle, in which some elements are added or removed in order to adjust the composition, depending on the specification of the final steel grade.

After blast furnace stage, the melted iron contains a very high content of carbon (around 2-3%) [22]. To remove the carbon, oxygen is blown on molten cast iron to reduce the carbon, by oxidation to form CO_2. This stage happens in the Basic Oxygen Steelmaking (BOS). The steelmaking process is explained in Figure 15. After the BOS process, the steel has a very high dissolved oxygen content (400 to 1000ppm). In order to prevent oxidizing of steel components during solidification, the oxygen content of liquid steel need to be reduced. To remove dissolved oxygen, elements with high affinity towards oxygen are added to the liquid metal. This is done by deoxidation of steel. The most common deoxidizers are ferromanganese, ferrosilicon, silicomanganese and aluminium. The choice and the amount of deoxidant depend on the steel grade and on the residual dissolved oxygen required. The deoxidation products consist of oxide inclusions such as Al_2O_3, SiO_2, MgO …

In general, the indigenous inclusions are formed by reaction in the molten metal and their formation is dedicated either by addition to the molten metal or by changes in solubility during the solidification process. Oxides and sulphides are examples of indigenous non-metallic inclusions in steels.

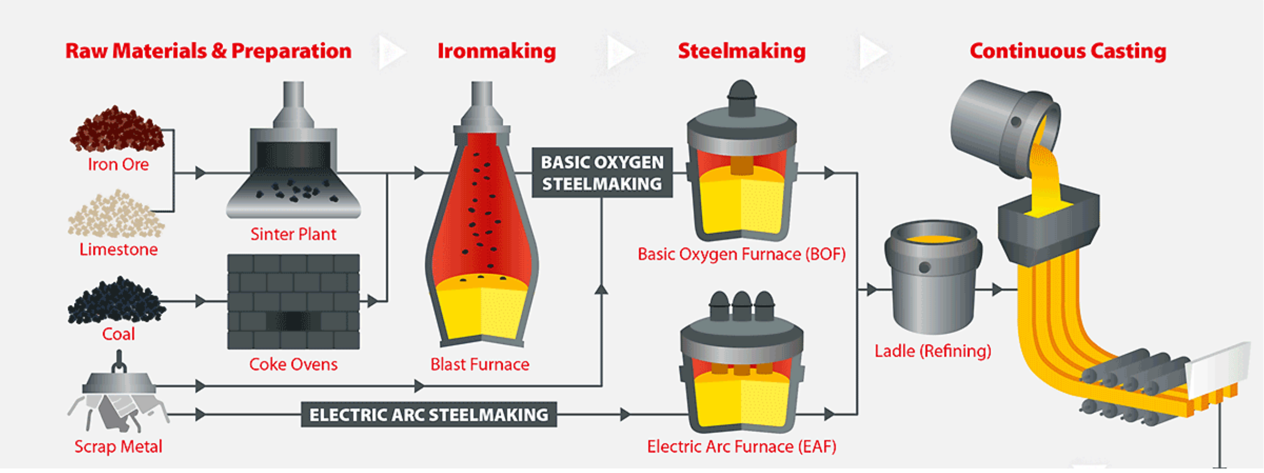

Figure 15 : Diagram of cast iron and steel making process [23]

3.2 Type of inclusions in high carbon steels

Choudhary [24] studied the inclusions present into high carbon steel wire. He reported that inclusions present initially on the wire rod are divided into two major types: the sulphides inclusions and the oxide inclusions. Oxides inclusions are divided in two parts depending on their deformability: the partially deformable and the non-deformable oxides.

3.2.1 Sulphide inclusions

Majority of sulphides inclusions in the wire rod samples are manganese sulphides. MnS essentially originates from segregation of Mn and S during the solidification of steel and for now, there is no way to eliminate them completely. As they are deformable, fine stringers of MnS were observed throughout the wire rod samples. An example of MnS stringers is presented in Figure 16. In general, MnS has a high deformation index. As MnS and steel have comparable deformability, it is normally considered harmless for the wire drawing. This is the reason why, even if the MnS are the major type of inclusions, we decided to not study them in detail.

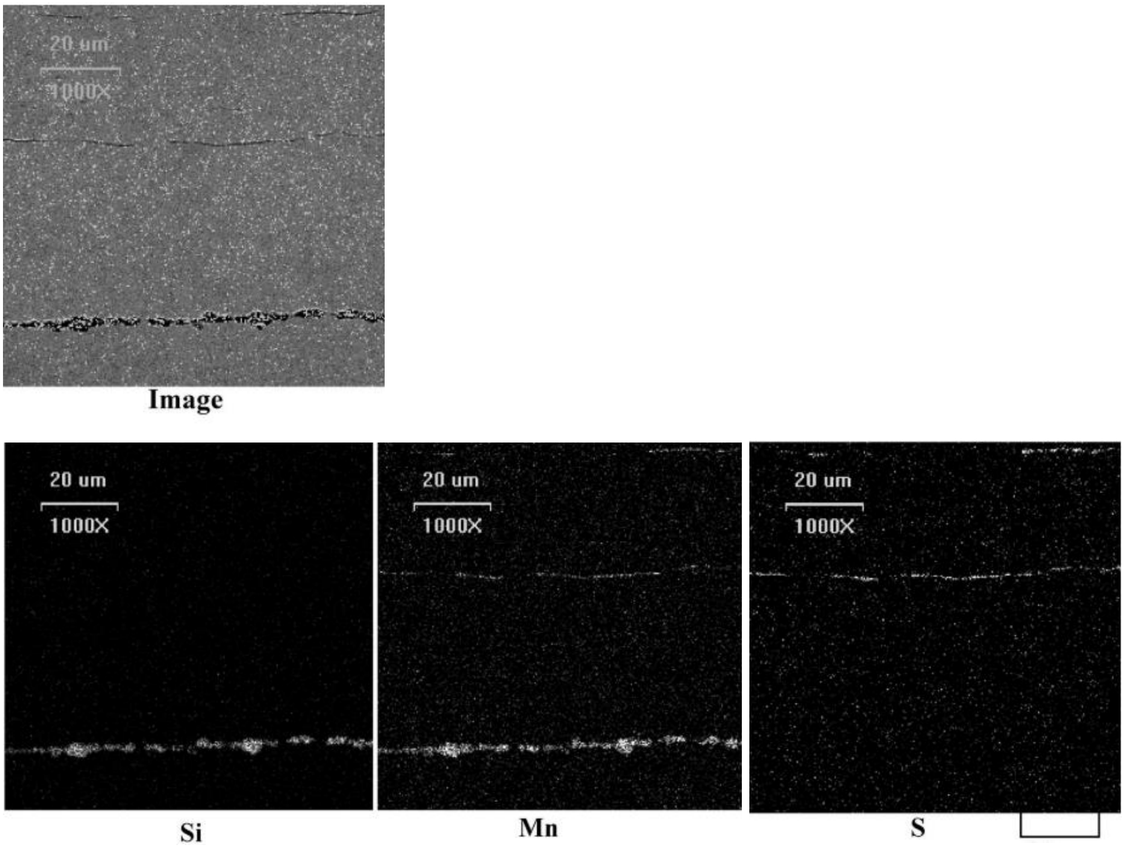

Figure 16 :SEM image of MnS stringer and oxides stringer and their EDS mapping [24]

3.2.2 Oxides inclusions

In comparison to MnS inclusions, oxide inclusions exhibit quite complex characteristics in the wire rod. As explained before, they are divided into two groups: large oxide stringers (partially deformable) and globular oxides (non-deformable).

- Oxide stringers

This type of inclusion looks like a MnS stringer with several pieces of hard inclusions separated by a deformable part. Those inclusions are aligned along the rolling direction of wire rod. SEM image of one of such oxide stringers is shown in Figure 16 along with the X-ray map of its constituent elements. In the literature, they are observed to exhibit variable deformability due to variations in their chemical composition. This type of inclusion has been found to be largely responsible for impairing the cleanliness of wire rod samples of the given steel samples. Fortunately, occurrence of such inclusions has been effectively controlled in the modified practice.

- Globular oxides

Large numbers of globular oxide inclusions were seen on all wire rod samples. Those globular inclusions were found to contain CaO, SiO_2, MgO, MnO, and Al_2O_3. Presence of such inclusions would become potential sites for cracks at the following fine wire drawing stage. The origin of those inclusions is established to come from deoxidation process itself. “Oxides inclusions” is the general term but are in fact complex compounds and are classified as a function of their chemical compositions. The oxide inclusions can have a simple composition such as SiO_2, Al_2O_3, CaO or a more complex composition as SiO_2-MgO, SiO_2-CaO… Choudhary [24] showed that the globular oxides are composed of not only one, but several components. In addition, a MnS ring is also present around the globular oxide part (Figure 167).

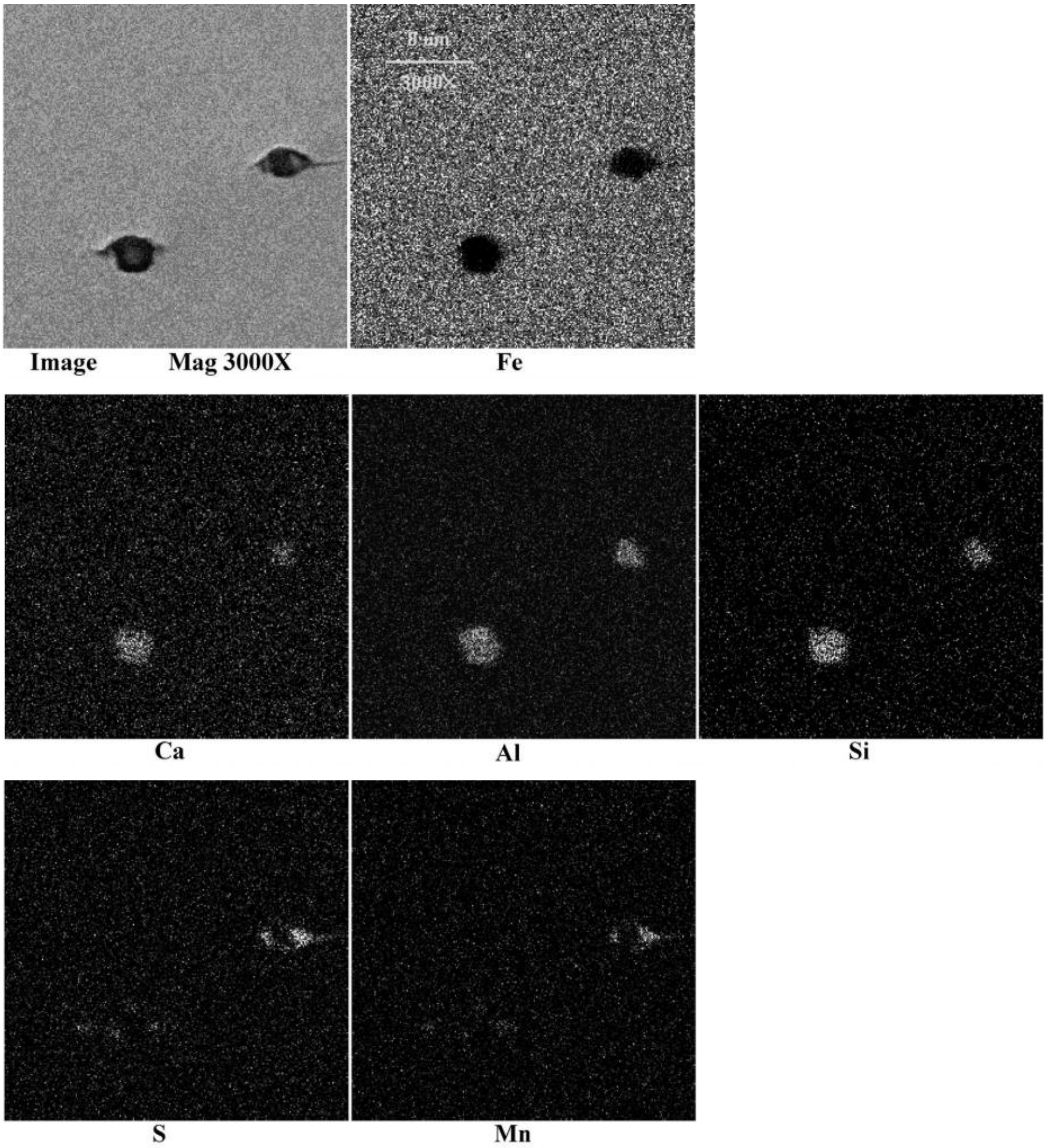

Figure 17 : SEM images of globular oxides surrounded by MnS ring [24]

The complex inclusions such as SiO_2-CaO-Al_2O_3 have already been studied as well as their mechanism of formation. Wang et al [25] studied the solidification mode of those inclusions. During the casting and the precipitation, inclusions are multi-phased. Some phases of pure SiO_2 solidified and an alloy forms constituted with a mix of SiO_2 and other alloying elements (in this study: Al, Mn). During the process step (rolling/drawing), the inclusion morphology changes. The hard part composed of pure SiO_2, non-deformable, keeps it initial shape, while the second phase, multicompounded, is deformed and elongated along the axis of deformation (Figure 168). Those observations underline the importance of chemical composition of the inclusion on their mechanical properties

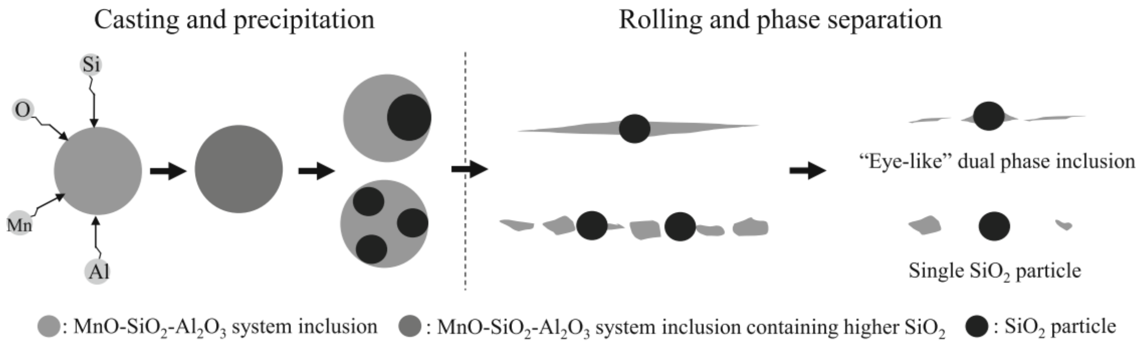

Figure 18 : Schematic diagram of formation mechanism of SiO_2-type inclusions in wire rods [25]

4 Deformability of inclusions

Inclusions can be also classified according to their deformation ability and fracture characteristics [26]:

- Plastic inclusion
- Non crystalline glassy inclusion, which are rigid at low temperature and become plastic after the non-plastic/plastic transition temperature
- Crystalline ionic solid. Those inclusions show no plasticity and often behave in a brittle manner

4.1 Deformability

Deformability of inclusions was also intensively studied by several authors [25,27–35].
Deformation behaviour of inclusions during forming processes is important regarding their properties. They act as a stress raiser by forming cavities and or micro voids in the steel matrix. Inclusion morphology, size distribution and composition can be modified during the deformation. The deformability of inclusions is an extremely important property required in steels for wire drawing. Kiessling [18] identified that the principal physical properties for inclusion deformation is the difference in plasticity of inclusions as compared as the plasticity of steel.

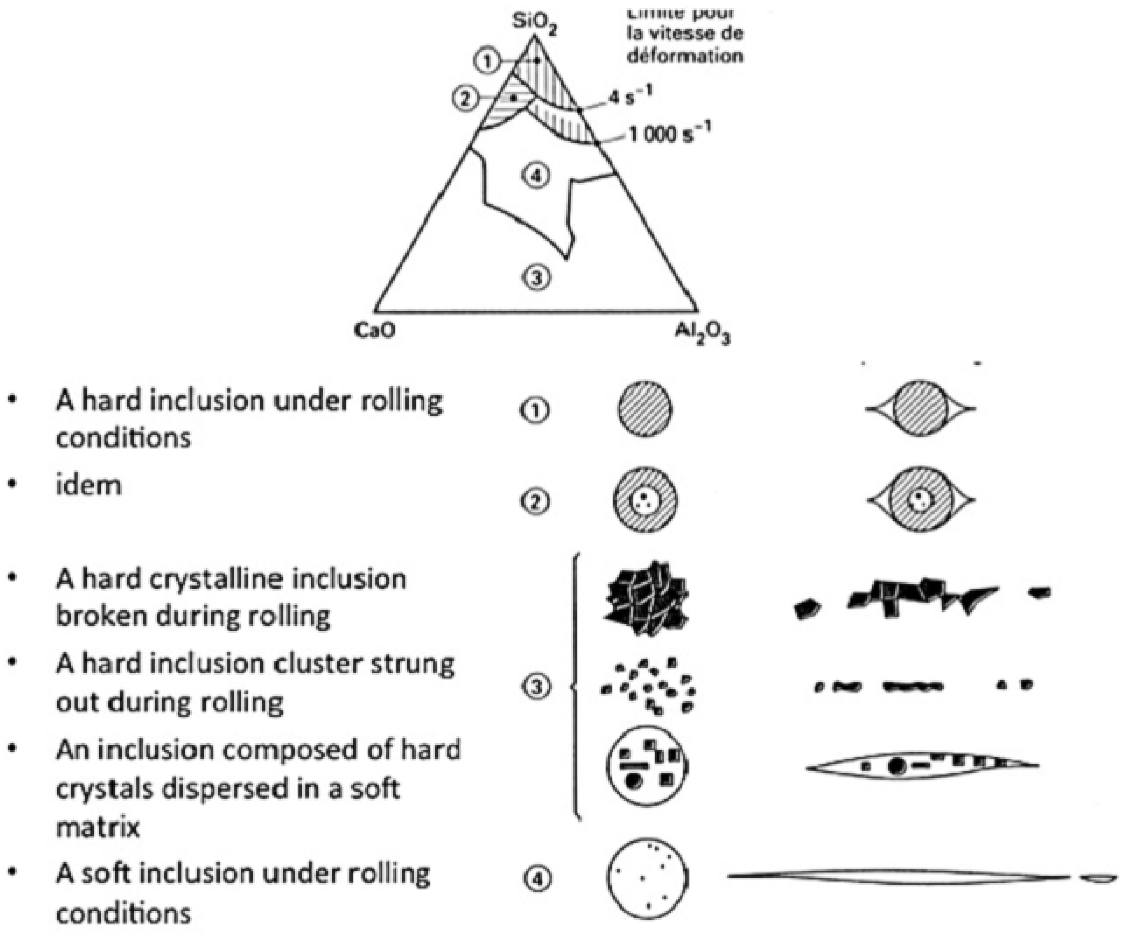

Figure 19 : Schematic representation of inclusions before and after deformation under rolling [36]

Figure 19 represents schematically the principal ways of deformation of inclusions. It compares the shape of inclusions under rolling conditions. 3c) and 4) type are “soft” inclusions. There are deformed at the same time as the matrix. Mainly, there are sulphides, such as MnS. The inclusions represented in 1), 2), 3b) 3a) are hard inclusions. type 1) is typically globular oxide such as silicates. type 2) represents high alumina crystalline calcium aluminate and type 3a) clusters of alumina for example.

The behaviour of inclusion during hot or cold working depends on the plasticity of the inclusion itself. The determination of the absolute plasticity of an inclusion embedded in steel matrix is impossible. But Malkiewick & Rudnik [32] defined a deformation index ν which aims at measuring the relative plasticity of the inclusion to the steel matrix

$$\nu = \frac{\varepsilon_i}{\varepsilon_m} = \frac{2ln\lambda}{3lnh} \qquad (11)$$

Where ε_i is the true strain of the inclusion and ε_m is the true strain of steel matrix, λ is the aspect ratio of inclusion and h is the reduction ratio of steel.

The deformability index can vary from ν =0 when the inclusion does not deform during the working of steel to ν = 1, when the inclusion is as impacted as the steel matrix and deform during working.

From the deformability index, the behaviour of different types of inclusions can be determined at different working temperatures of steel. The conclusions of several authors are summarized below : [18]

- Oxide inclusions in the size range below 1µm are little influenced by deformation of steel matrix
- Inclusion phases of the corundum type Me_2O_3 as well as calcium aluminates are non-deformable at all temperatures of importance and at all deformation levels
- Inclusion phases of the spinel type, $AO.B_2O_3$ do not deform plastically at the normal working temperatures and with a deformability $\nu \approx 0$
- Pure silica inclusions are non-deformable for temperature range under 1200°C
- Sulphides inclusions have a deformability index similar to the steel matrix. They are plastically deformed at the same time of the matrix. MnS has a value of ν close to 1 at all deformation temperatures.

Inclusions with an index of deformability ν=0.5-1 have been found to deform normally with a low frequency of micro-cracks at inclusion-steel interface. Those with ν=0.03-0.3 often give a fishtail and conical voids. Inclusions with a ν value lower than 0.03 remain non-deformable during working of steel. Rudnik [32] suggested that inclusions with a deformability index ν=0.5-1 are harmless or even advantageous for working.

With this equation 11, it was possible to compare the relative plasticity for different types of inclusions.

The deformation index of oxide inclusions present in high carbon steel wire rod has been studied by Choudhary [24]. In Figure 20 are represented the distributions of deformability index for oxide inclusions on high carbon steel wire rod.

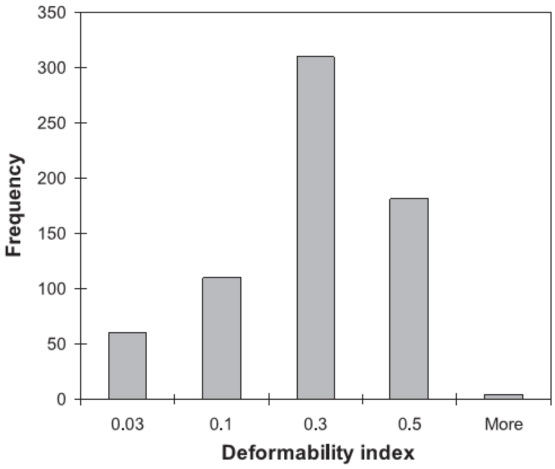

Figure 20 : Deformability index (ν) of oxide inclusions in high carbon steel wire rod sample [24]

Some authors claimed that the deformability of inclusion is linked to their melting point [29,30]. Therefore, to achieve a good plasticity, the composition of the inclusions should be controlled by the regions having a low melting point [31–33,35,37,38]. The analysis of the melting point temperature on the deformability is suitable for the processes including a high temperature as hot rolling, welding etc. Cold drawing of tire cord wires and wet wire drawing are usually carried out at room temperature, which is significantly lower than the solidus temperature of the inclusions. So the melting temperature of the inclusions is a good factor to determine the deformability of the oxides inclusions but is not always applicable. To contain the impact of the inclusions on cold process (as drawing for example), several authors have decided to look at the problem from another angle and to study other parameters besides the melting temperature of the inclusion.

Bernard et al [30] studied the relationship between the viscosity and the deformability of the system SiO_2-MnO-Al_2O_3 and SiO_2-CaO-Al_2O_3. Near the corner corresponding to the pure SiO_2 phase, inclusions were too viscous to be deformed, whereas the inclusions with low viscosity were more deformable. Kimura et al [28] studied the fracture behaviour of different oxides as alumina, zirconia, zircon, and silica during hot rolling and cold drawing at laboratory scale. It was reported that the compressive strength of the oxide inclusions plays a role and it could be predicted from the Young moduli of the inclusions and the mean atomic volume of the oxides. However, only few single inclusions were investigated. Zhang et al [39] studied the deformability of inclusions at high and low temperature. By computer simulation, the Young modulus of complex inclusions were determined for two complete systems SiO_2-CaO-Al_2O_3 and SiO_2-MnO-Al_2O_3. The results of their investigation are reported in Figure 21. The hypothesis is that the deformability of the inclusions of oxides during cold drawing is inversely proportional to the Young modulus. It is proposed to reduce the fracture of the wire during the drawing by control of the inclusions, favouring the dark blue regions where the content of SiO_2 is higher. Also, Figure 21 shows that Al_2O_3 is detrimental to the deformability of oxide due to its high Young modulus.

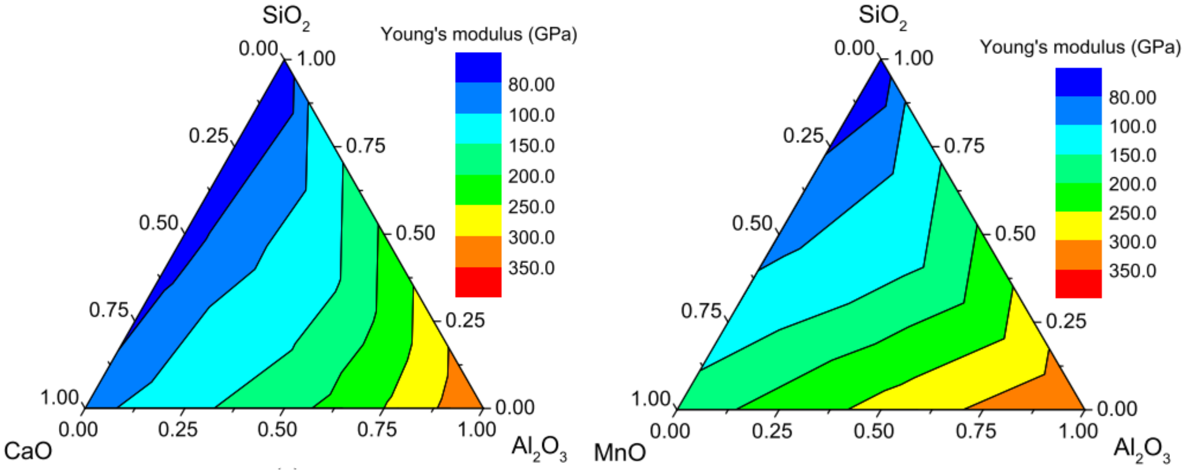

Figure 21 : Young's modulus distribution of a) Al_2O_3-SiO_2-CaO and b) Al_2O_3-SiO_2-MnO systems [39]

During plastic deformation, stresses are applied on the inclusion by the steel matrix. These tend to make them deform in a similar manner that the matrix around. But it exists many factors which can affect the inclusion deformation [40–43] :

- Strength of inclusion and matrix
- Composition
- Inclusion-matrix interface
- Temperature
- Strain and strain rate
- Particle size
- Stress state
- Second-phase particles

5 Impact on mechanical properties of steel

5.1 Generalities

Non-metallic inclusions are considered to be detrimental to mechanical properties of steels. Inclusions have different properties than the steel matrix, such as plasticity and thermal expansion coefficient, resulting in different behaviours upon mechanical and thermal stresses in comparison with the steel matrix [21]. Inclusions present in steel are in the micron size range. However, they can have a significant effect on the macro-scale properties during processing (see 2). Distribution of inclusions in the matrix, along with their composition, morphology, size and relative strength, plays an important role in determining their effects on the performance of the steel. Inclusions disturb the homogeneity of the structure and affect various mechanical properties (for example, strength, drawability, machinability, brittle fracture, fracture toughness, hardness, corrosion, polishability and fatigue strength) both during the processing as well as in the final finished product [21, 44]

Table 2 : Influence of typical impurities on mechanical properties [17]

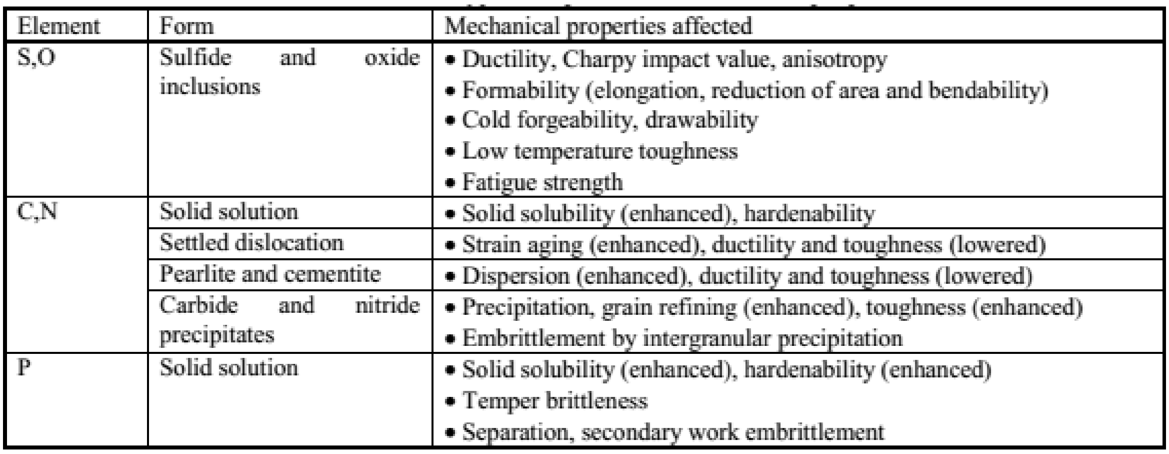

Element	Form	Mechanical properties affected
S,O	Sulfide and oxide inclusions	• Ductility, Charpy impact value, anisotropy • Formability (elongation, reduction of area and bendability) • Cold forgeability, drawability • Low temperature toughness • Fatigue strength
C,N	Solid solution	• Solid solubility (enhanced), hardenability
	Settled dislocation	• Strain aging (enhanced), ductility and toughness (lowered)
	Pearlite and cementite	• Dispersion (enhanced), ductility and toughness (lowered)
	Carbide and nitride precipitates	• Precipitation, grain refining (enhanced), toughness (enhanced) • Embrittlement by intergranular precipitation
P	Solid solution	• Solid solubility (enhanced), hardenability (enhanced) • Temper brittleness • Separation, secondary work embrittlement

.

5.2 Influence on fatigue

The study of the influence of inclusions on fatigue properties has extensively been studied during decades. High strength steels or high hardness steels are widely used in bearings, springs, cold forging tools and aircraft components. The fatigue properties of several materials [45–48] are topics already treated by several authors. For high strength steels, the short and long fatigue lives are affected by the presence of inclusions [49–51]. The short fatigue lives are controlled by surface crack initiations at surface defects and the long fatigue lives are controlled by internal crack initiations at inclusions.

For heavily deformed high carbon steel wires, inclusions are also considered as detrimental for fatigue life. A deformed area is observed around the inclusion after fatigue test of heavily drawn wire. Though the microstructure of heavily drawn wires is difficult to be observed, Lambrighs [52] underlined an altered microstructure around the inclusion after fatigue in Ø0.2mm wire as shown in Figure 22.

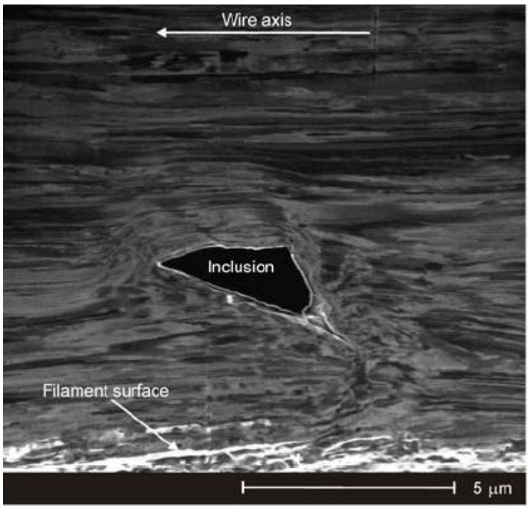

Figure 22 : SEM image of the altered microstructure around inclusion after fatigue test of a Ø0.2mm heavily drawn wire [52]

5.3 Effect on toughness

5.3.1 Generality

Inclusions can be responsible of different fracture behaviours. One of these is ductile fracture. Ductile fracture in steels is caused by the nucleation, growth, and coalescence of voids nucleated at hard particles (such as inclusions, pearlite nodules, and carbides) [53,54]. Inclusions being harder than the surrounding matrix at room temperature, void nucleation results from the stress and strain concentration in the matrix during deformation. It follows that, the strain to cause ductile fracture is dependent on the volume fraction and on the shape of the inclusions. Voids are first nucleated, either by decohesion of the particle–matrix interface or by particle fracture. Voids nucleate more easily especially as the inclusion particle is rigid, has a low cohesion with the matrix, or has low internal fracture strength. Fracture is frequently initiated by large inclusions, followed by void formation and growth around small inclusions [55]. Figure 23 illustrates the micro void nucleation around small inclusions.

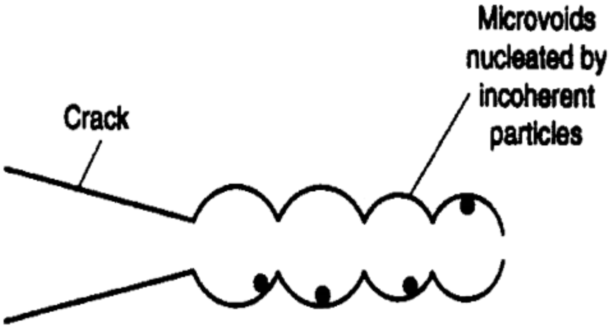

Figure 23 : Schematic diagram of micro void nucleation by incoherent inclusions [55]

For steel matrix, the three main important characteristics of inclusions on toughness are the inclusion volume fraction, the inclusion spacing and the resistance of the inclusions to void nucleation [56]. Fractographs of Figure 24 present the typical ductile fracture face with the presence of small inclusions.

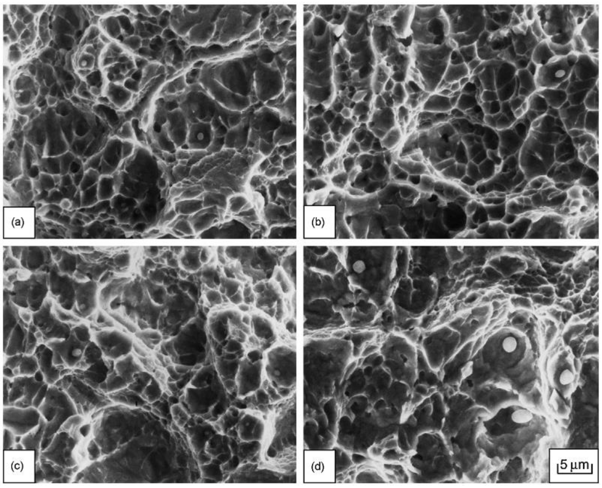

Figure 24 : Fractographs of the compact tension specimens used to measure fracture toughness of four different wires [56]

Reducing the content of inclusions increases the resistance to void nucleation and is effective in improving the mechanical properties of steels.

For the elongated sulphides, voids are nucleated by breaking up of the particles into segments. During the fracture process, voids are first formed at MnS inclusions, which are usually the largest, then at smaller oxide inclusions and finally at small carbides [57].

Uniform arrangement of inclusions in the steel matrix can be considered as harmless for the fracture toughness. At the high hardness level, the inclusions can be treated as natural obstacles to crack propagation.

5.4 Effect on processing – Hot and cold working

5.4.1 Generality

It is sometimes convenient to separate the influence of inclusions during processing from that during application, as the conditions in processing are normally not the ones envisaged for the steel application. This is true even considering that most of the problems associated with inclusions discussed in this section are related to their relative plasticity and their influence on steel ductile fracture. Inclusions that occupy a significant portion of the material may cause fracture during processing. Figure 25 illustrates the fracture of a tire cord wire during cold drawing, caused by the presence of a large inclusion [29]. Controlling the volume fraction, size and distribution of inclusions is thus important. Furthermore, inclusion engineering is important [43] on the wire operations of tire cord and springs.

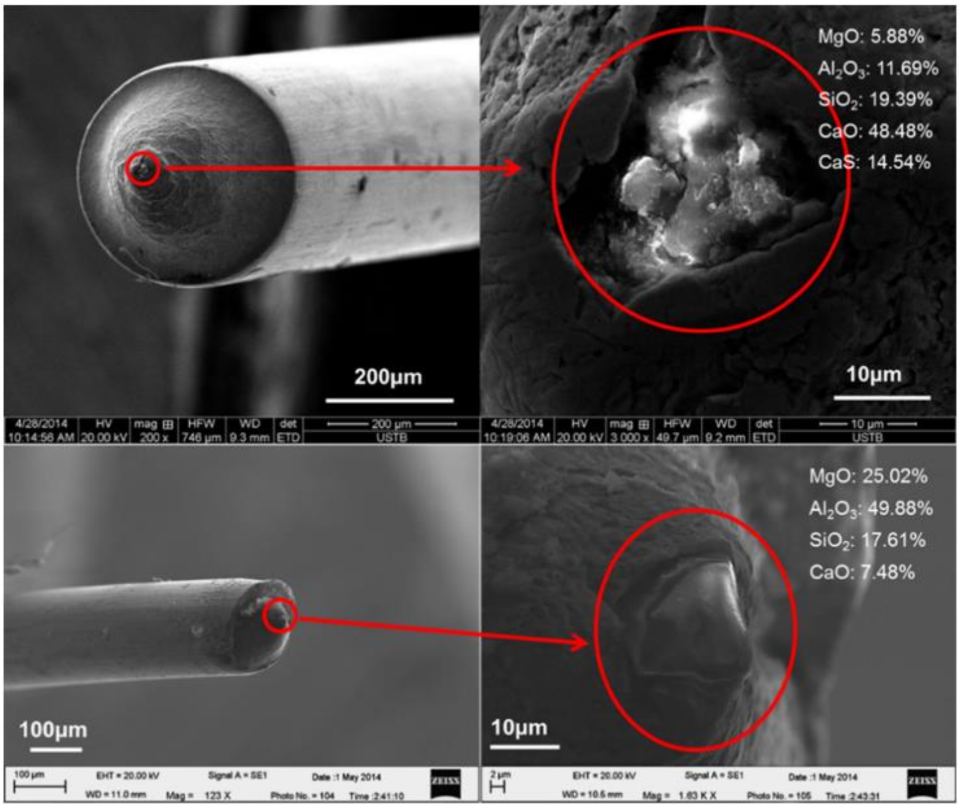

Figure 25 : Example of fracture due to inclusions on Ø0.20mm wires [27]

5.4.2 Drawability

Inclusions are known to reduce drawability of steels. Inclusions higher in hardness and melting point are harmful to high-strength steel rods like tire cords and saw wires because inclusions often act as fracture initiation sites when subjected to cold drawing. It would be much more desirable for the remained inclusions to be small in size and to demonstrate improved deformability.

The impact of inclusions types on the drawability of steel wire has been intensively studied by different authors. However, the majority of the studies considered the drawing of tire cord steel with a diameter around 0.20mm. The diameter of tire cord filament is much bigger compared to the thin filaments. If the influence of the inclusions type can be assimilated to a thinner drawing, the influence of size has also to be considered.

5.4.3 Drawability of steel wires

Yilmaz et al [58] have studied the failures during production and in service of steel wires. As can be seen in Table 3, The causes of failures during steel wire drawing are various. Most of those fractures are related to the presence of inclusions (81%) but originated also from other reasons. These inclusions limit the minimum diameter of wire, which can be drawn in the wire drawing process.

Table 3: Fracture causes during production and use of steels [58]

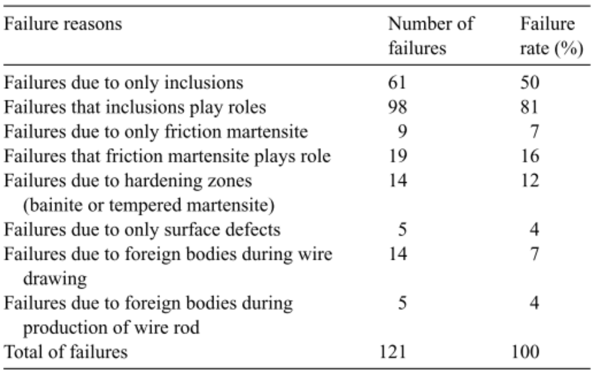

Failure reasons	Number of failures	Failure rate (%)
Failures due to only inclusions	61	50
Failures that inclusions play roles	98	81
Failures due to only friction martensite	9	7
Failures that friction martensite plays role	19	16
Failures due to hardening zones (bainite or tempered martensite)	14	12
Failures due to only surface defects	5	4
Failures due to foreign bodies during wire drawing	14	7
Failures due to foreign bodies during production of wire rod	5	4
Total of failures	121	100

Zhang et al.[27] studied the inclusions responsible of fracture during the tire cord drawing as their physical properties. By fracture analysis with SEM/EDS, they determined the size and the chemical composition of inclusions. Inclusions were present in the centre of the wire and a cone fracture is observed. The size and the chemical composition of the inclusions are reported in Table 4

Table 4 : Chemical composition and size of inclusions responsible of fractures[27]

No.	MgO (wt pct)	Al_2O_3 (wt pct)	SiO_2 (wt pct)	CaO (wt pct)	CaS (wt pct)	Size (μm)
1	19.37	17.37	42.20	21.05	0	9.7
2	17.61	9.75	17.36	55.27	0	20.9
3	5.88	11.69	19.39	48.48	14.54	21.4
4	10.97	25.07	39.16	24.79	0	25.3
5	49.66	1.31	49.02	0	0	15.4
6	25.02	49.88	17.61	7.48	0	17.7
7	25.94	67.08	3.04	3.94	0	22.3
8	28.60	64.45	4.56	2.39	0	17.3

Compared to fatigue, inclusions responsible of fracture were present in the centre of the fracture more than at the edge of the wire. The size of the inclusions responsible of fracture represents in average 10% of the final diameter with an average size closed to 20µm.This study also underlines that critical inclusions responsible of fracture are mainly oxides. However, this results stand for large diameter filaments (approximately Ø0.20mm).

A study of Ji et al [59] on the impact of a non-metallic inclusion on damage value and ductile fracture during dry drawing of high carbon steel wire emphases the effect of inclusion with a size ranging from 5µm up to 50µm.

The damage value expends the risk of fracture occurrence during wire drawing. The maximum damage value increases when the size of inclusion increases.

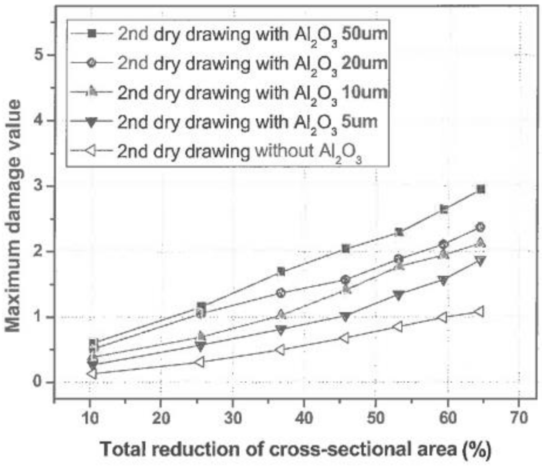

Figure 26 : Damage reduction around inclusions of different sizes during dry drawing [59]

5.4.4 Drawability of fine filaments

Few studies are available on the effect of inclusions for fine drawing in steel. However, these kinds of studies have already been performed on other materials, like copper.

Some FEM studies on impact of inclusions on the resistance to rupture in copper during fine drawing have been made by Cho et al [60]. They took into account the effect of inclusion size, the reduction ratio, and the distance between inclusions Table 5.

Table 5 : Parameters studied by FEM simulation [60]

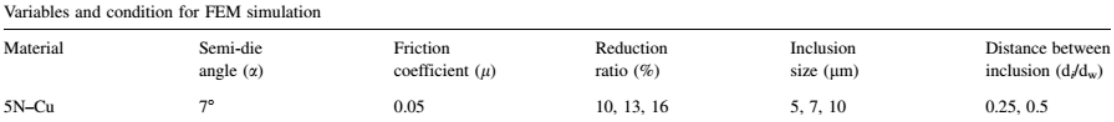

Variables and condition for FEM simulation

Material	Semi-die angle (α)	Friction coefficient (μ)	Reduction ratio (%)	Inclusion size (μm)	Distance between inclusion (d_i/d_w)
5N–Cu	7°	0.05	10, 13, 16	5, 7, 10	0.25, 0.5

- Effect of inclusion size on wire breaks

Three different sizes of inclusions were considered in the simulation: no inclusion, 5µm, 7µm and 10µm. Figure 27 shows the total reduction ratio plotted as a function the inclusion size present on the wire.

This study shows that the drawability of the wire depends mainly on the presence and on the size of inclusions embedded in the wire. It decreases rapidly when the inclusion size increases and remains for medium size inclusion (8-10µm)

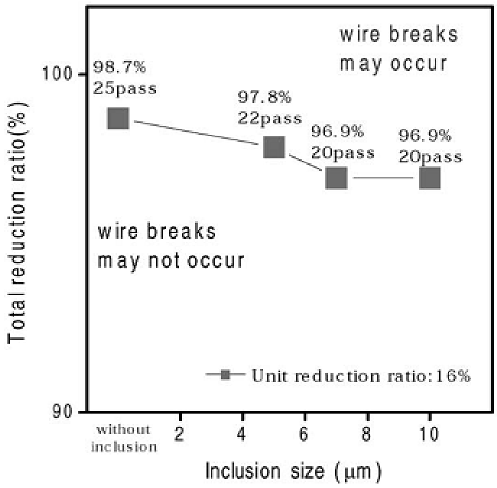

Figure 27 : Effect of inclusion size on wire breaks [60]

The comparison with the present process in Bekaert is difficult because first, copper does not deform as pearlitic steel. In addition, the reduction per pass is lower for Bekaert process and the reduction ratio is higher than 95% with more than 20 passes. Therefore, if these results obtained in copper wire should be adapted for steel wires, the differences between the behaviour of the two matrixes have to be taken into account.

- Effect of distance between inclusions on drawability

The effect of distance between inclusions on occurrence of central burst during drawing has been studied for copper filaments by Cho et al [60]. Two different spacing between inclusions (0.25 and 0.5mm before drawing) were considered. No remarkable effect of distance has been noticed on wire breaks and because the distance between inclusions expanded during multistage wiredrawing process, a reciprocal action between inclusions cannot be expected.

- Effect of shape of the inclusion

Norasethasopon [61] studied the impact of the shape of the inclusion on copper wires. The inclusion aspect ratio is defined as the ratio between the width and the length. Numerical simulations of the drawing stress included b the width of the inclusions, 2a the length of the inclusion and h the radius of the wire (Figure 28).

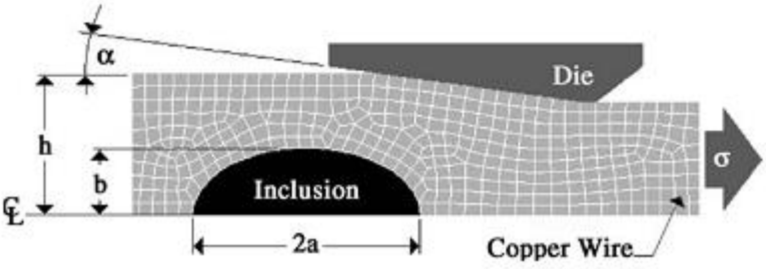

Figure 28 : Inclusions parameters for FEM of copper wire [61]

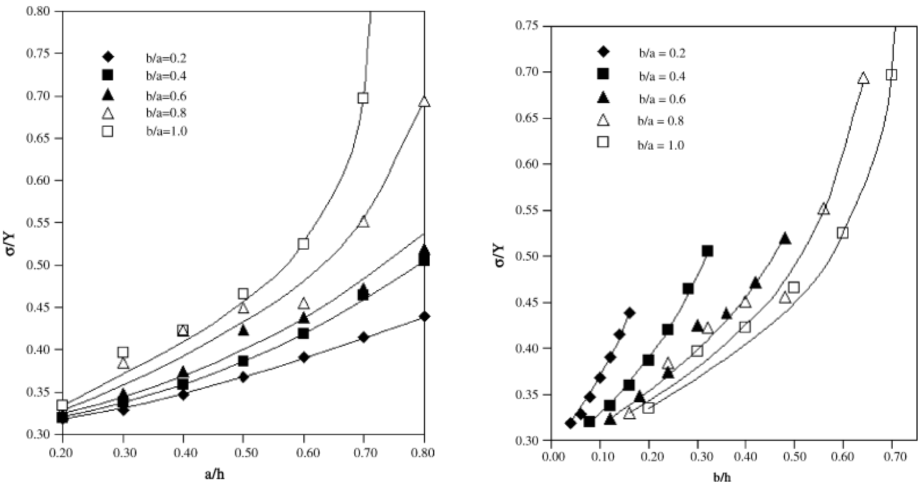

Figure 29 : Maximum of drawing stress ratio for at different aspect ratio 1) for different a/h ratios b) for different b/h ratios [61]

5.4.5 Impact of drawing on inclusion

Inclusions have an impact on drawing but drawing has also an impact on inclusions since the process generates high stress. Deformability of inclusion is already known in rolled wire (section 4) but no studies have been made on impact of fine drawing. Some studies have been performed on wire drawn at lowest drawing strain.

Yan et al [62] investigated the stability of inclusions in a wire rod and steel cord wire to point out the influence of drawing on inclusions.

Table 6 : Difference of inclusions between wire rod and a Ø0.22mm cord wire [62]

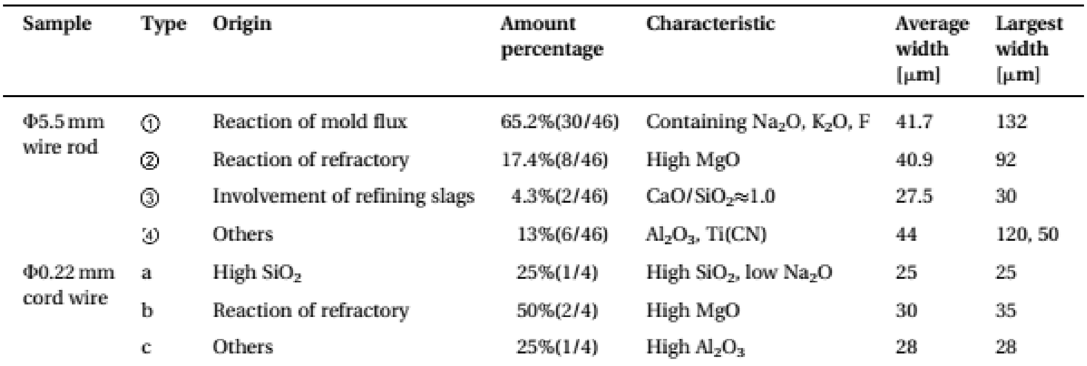

Sample	Type	Origin	Amount percentage	Characteristic	Average width [μm]	Largest width [μm]
Φ5.5 mm wire rod	①	Reaction of mold flux	65.2%(30/46)	Containing Na_2O, K_2O, F	41.7	132
	②	Reaction of refractory	17.4%(8/46)	High MgO	40.9	92
	③	Involvement of refining slags	4.3%(2/46)	$CaO/SiO_2 \approx 1.0$	27.5	30
	④	Others	13%(6/46)	Al_2O_3, Ti(CN)	44	120, 50
Φ0.22 mm cord wire	a	High SiO_2	25%(1/4)	High SiO_2, low Na_2O	25	25
	b	Reaction of refractory	50%(2/4)	High MgO	30	35
	c	Others	25%(1/4)	High Al_2O_3	28	28

This study showed that the average width and largest width of inclusions in the steel cord wire are less than the ones in the wire rod. It is also proved that most of inclusions in steel cord wires are still multiple phase inclusions from reaction of mold flux or refractory with initial inclusions, but the amount of oxides inclusions containing K or Na decreases. The amount of high MgO content and high Al_2O_3 increases. Those two inclusions are regarded as high hardness and non-brittle inclusions.

Since experiments were based on electrolysis, no information about the modification of localization of inclusions into the wire is available.

One of the results of the study is that inclusions size obtained by electrolysis is far larger than the inclusions detected by metallographic microscope. Most exogenous inclusions were found by electrolysis but must homogenous inclusions are found by metallographic microscope. Most inclusions by SEM evaluation are micro inclusions from deoxidation product or from reaction of slag and molten steel. Those macro inclusions have less possibility to cause breakage during the drawing process.

5.5 Cohesion between non-metallic inclusion and matrix

Debonding, sliding and separation may occur at the inclusion/matrix interface during the deformation processing [63,64]. Non-metallic inclusions are nucleation site of micro-damage in steels. Inclusions are randomly distributed in the matrix. The decohesion depends:[43]

- On the type of the inclusion – Chemical composition

- On the structure of the “inclusion – matrix” phase boundary (interphase),
- On the proportion of the ductility characteristics of the inclusion and the matrix,
- On the strength of the inclusion, of the matrix, and of the phase boundary.

The mechanisms of formation of tough interphase cracks (voids) are connected with the entrance of lattice dislocations into “inclusion – matrix” interphases and interaction between these dislocations and interphase dislocations at high and low temperatures.

5.5.1 Void nucleation

- Generalities

Inclusions are, at room temperature, harder than the surrounding matrix. This leads to a stress and strain concentration in the matrix which can produce voids by matrix-particles decohesion or by fracture of the particle. A necessary condition for nucleation is that a critical value of normal stress must be exceeded at the inclusion-matrix interface which is function of dislocation density (strain) and triaxiality (or mean stress) [65]. Void nucleation is amplified if : [18]

- The particles are rigid
- The particles have a low cohesion with to the matrix
- The particles have a low internal fracture strength

During rolling (Figure 30), the void coalescence is induced on the side of the inclusion. The internal forces imposed by the flow of metal and the frictional forces result in a conical void along the drawing direction.

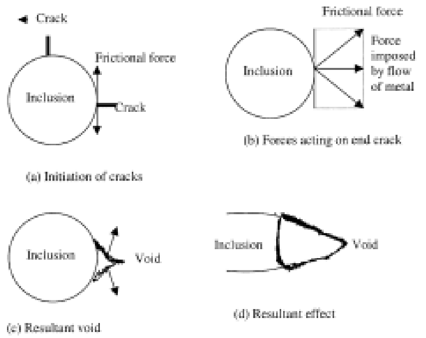

(a) Initiation of cracks
(b) Forces acting on end crack
(c) Resultant void
(d) Resultant effect

Figure 30 : Void nucleation process initiated by an inclusion during rolling [40]

- During Wire drawing

Melander [66] studied void growth around rigid particles during wire drawing and tensile testing of copper, based on the results from wire drawing and interrupted tensile tests. The experimental testing showed that the void acquires a conical shape. The void length increases during tensile testing as predicted by a homogenous growth model, but the voids did not grow only along the tensile testing direction as predicted by that model but also on the orthogonal direction at sufficiently low hydrostatic pressures in the neck of the wire during tensile testing.

.

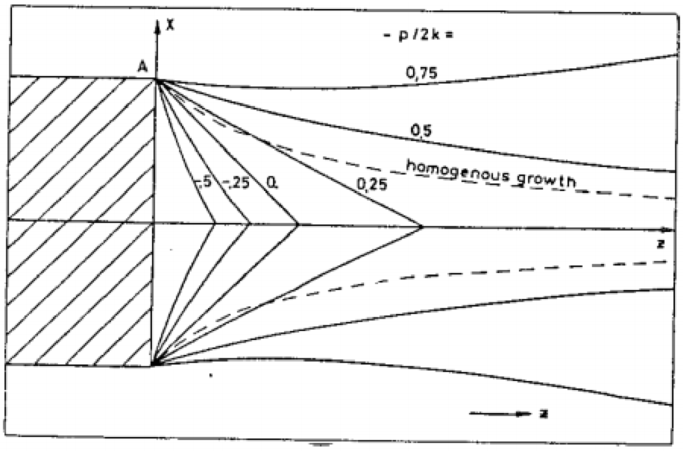

Figure 31: Melander model of homogeneous void growth around inclusions [66]

The example given in Figure 31 illustrates that the void grows in the tensile direction but also in the orthogonal direction at sufficiently low pressures.

5.5.2 Void coalescence during wet wire drawing

The peeling and cracks are easily generated at the boundary between the inclusion and the matrix due to the large tensile stress around the inclusion. Those voids and cracks are produced by hydrostatic pressure around the inclusion induced by wire drawing. Those phenomena can happen even with drawing condition under the safety limits. The voids grow until their softening effect on the matrix is so large that sudden strain localization occurs leading to failure. Figure 32 shows the simulation of coalescence of void around an inclusion.

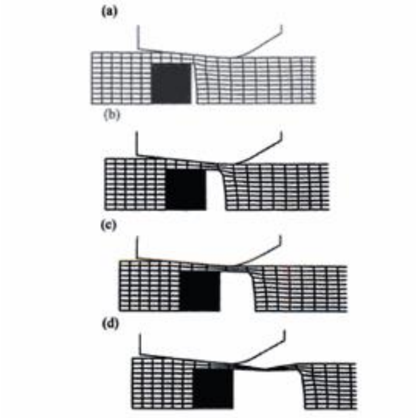

Figure 32 : coalescence and growth of defect during wire drawing as the draw length increases [67]

A FEM simulation has demonstrated the impact of several drawing passes on damage value around a 5µm inclusion (Figure 33). After 22 passes, the damages are expected in the wire. Void coalescence happens as well as the inclusion/matrix interface but also nearby the inclusion. The central burst happens in majority at the inclusion point but the drawn matrix ahead the inclusion is also clearly impacted. A defect of central burst type is observed along the centre line in drawn wire. Since tensile stress acts in the drawing direction at the centre of the wire, an internal crack is easy to occur in front of or at the back of the inclusion when wire passes through a die.

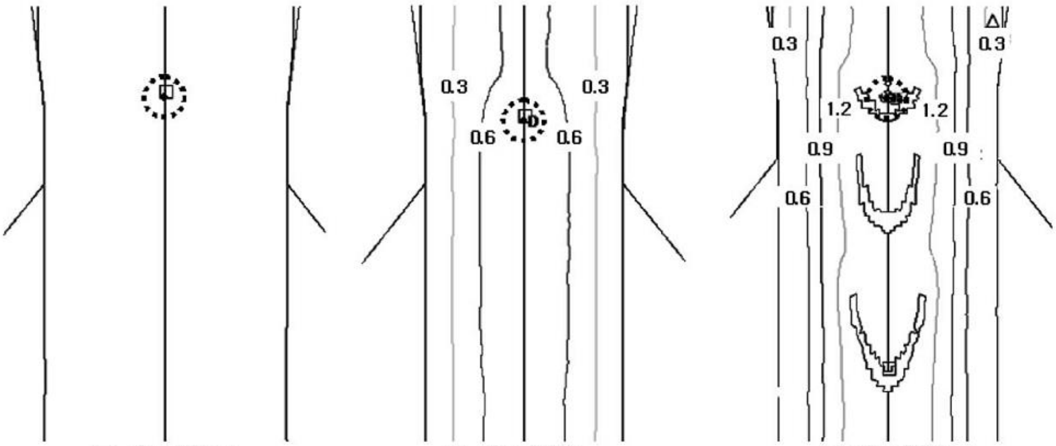

(a) after 1Pass
Total R/A:16%

(b) after 11Pass
Total R/A:85.3%

(c) after 22Pass
Total R/A:97.8%

Figure 33 : FEM simulation on damage value during drawing around an inclusion of 5µm on copper wire [60]

6 Conclusions

This literature part reviewed three major aspects of the subject connected with the present PhD work: the hypereutectoid steels, the drawing process and the inclusions in steel.

Hypereutectoid steel shows a pearlitic microstructure with alternate lamellae of ferrite and cementite. The microstructure is hierarchical and can be described with three major units: grain, nodule and colony. A pearlitic nodule is composed of several colonies, the latter being a set of aligned and parallel lamellae that grow together during transformation. A grain of pearlite gathers numerous nodules. While it is rather easy to differentiate them in a fully annealed pearlite, it is more problematic to distinguish them in heavily deformed material.

Concerning the second part, it appears obvious that the drawing process cannot be reduced to a mechanical test (traction, torsion, fatigue) and is far from a simple uniaxial loading condition. Three forces governs the wire drawing process: the drawing force, the die force (compression) and the friction force. The overlapping of these three forces creates a complex phenomenon. The adapted drawing parameters as drawing speed, die angle are primordial to optimize the drawing process and to avoid extra damages to the wire.

The presence of inclusions is inherent to steel process. Inclusions cannot be totally removed from steel. Their population can however be reduced and their composition adapted to be less critical. Three main types of inclusion exist in high carbon steel: oxides, sulphides and oxy-sulphides inclusions. Sulphide inclusions are deformable and less critical for wire drawing and only oxide inclusion are considered as detrimental for wire drawing. The deformability of oxides inclusions is known to be relative to their melting points. But this is mostly valid for hot process as hot rolling.

Inclusions are detrimental for many applications as well during processing of materials as during service. The consequence of the presence of inclusions has been already investigated during drawing of wires with diameter of a few hundreds of micrometres but not for fine filaments for steel matrix.

Learning points:

- **Hypereutectoid steel shows a pearlitic microstructure.**
- **Pearlite is a hierarchical microstructure divided into three major units: grain, the nodule and the colony**
- **Wire drawing is a complex process governed by three forces: the drawing force, the die force (compression) and the friction force**
- **Inclusions are detrimental for many applications, creating a weakening point into the steel matrix**
- **Inclusions cannot be removed from steel.**
- **Their population can be reduced and their composition adapted to be less critical.**
- **Inclusions in high carbon are divided into three categories: oxides, sulphides and oxy-sulphides inclusions**

Chapter II: Experimental methods

7 Experimental methods

The preliminary study underlined that the fracture occurrence is mainly associated with the presence of an inclusion. Therefore, it seems necessary to analyse the inclusion population and properties in a very precise way. The determination of steel cleanliness will enable the investigation of the role of the inclusions on the drawing process. To be able to analyse and identify the inclusions present into the wire rods, different techniques for inclusions characterization have to be investigated. Obviously, it was quickly observed that a single method cannot bring all the information necessary for a full investigation of the inclusions properties.

The different inclusion detection methods will be described and evaluated in view to obtain a full method for inclusions characterization.

7.1 Cleanliness assessment

As it has been proved since a long time, one unique method is not sufficient to have an accurate idea of the inclusion state in steel sample. Each method has advantages and limitations.

Zhang & Thomas listed extensively all the methods of inclusions detection and measurement for steels [68]. It exists some direct and indirect methods for inclusions characterization.

The principal direct methods to evaluate steel cleanliness are the following:

- The metallographic microscope observation with light optical microscope: This method consists in the observation of a polished surface of the steel to find and count by eyes with light optical microscope the inclusions. This method does not require special equipment, however, it is time consuming and the interpretation of the results depends mainly on the operator. Also, only the number and the size of inclusion can be evaluated.
- Image Analysis is the same principle than the metallographic microscope observation but automated by using a high-speed computer that automatically detects the inclusions. The detection is based on a difference in brightness/contrast between matrix and inclusions. It allows analysing a greater surface and a better statistics on inclusion size. However, the risk of misinterpreting by the computer is high. Scratches or dust can be detected and counted as inclusions.
- The sulphur print is a technique to detect macro-inclusions by etching the sulphur-rich areas. This method is subjected to all same problems as all the 2D methods and considered only macro inclusion (>20µm). Those inclusions are not present into our wires.
- The Scanning Electron Microscope (SEM) coupled with EDS (Energy dispersive X-ray Spectrometry) or EPMA (Electron Probe Microanalysis) is also a 2D technique based on the

contrast/brightness difference. This method brings additionally information on inclusions chemical composition thanks to EDS or EPMA measurements. The density, the size, the shape and the distribution of the inclusions can be determined with this technique. However, it stays a 2D technique and does not allow a perfect measurement of inclusion size and morphology. It is also time consuming. This method will be more detailed on section 7.4.

- The OES-PDA is a spectroscopy method consisting in dissolving the steel matrix and inclusions by spark generation and then analysing them by spectroscopy. Inclusions cause high-intensity spark peaks (relative to the background signal from the dissolved elements). It is a fast method to determine the density, the chemical composition and the approximate size of the inclusions. This method will be also more detailed on section 7.6.
- The Laser Microprobe Mass Spectrometry (LAMMS) is a method based on irradiation of individual particles by a pulse laser beam.
- The X-ray Photoelectron Spectroscopy (XPS) use X-rays to map the chemical state of individual inclusions larger than 10µm. Inclusions of smaller size are also interesting in our evaluation so this technique cannot be applied for this study.

In addition, several methods directly measure inclusions in the three- dimensional steel matrix listed below:

- The Conventional Ultrasonic Scanning (CUS) is a non- destructive method which detects and counts inclusions larger than 20µm in solidified steel samples. This non-destructive method could be an assess for this application. However, the size detection limit is too important to be applied to our study.
- Slime (Electrolysis), further referred as extraction method, it is an accurate but time consuming method. A piece of steel sample is completely dissolved in acids and the non-metallic inclusions are collected for further analysis which allows measuring the density, the chemical composition and a greater statistics. This method is further explained on section 7.5.
- Electron Beam melting (EB) concerns only Al-killed samples. The sample is melted by an electron beam under vacuum. Inclusions float to the upper surface and form a raft on top of the molten sample. This method is too restrictive to be useful for this project.
- Cold Crucible (CC) melting Inclusions are first concentrated at the surface of the melted sample as in EB melting. After cooling, the sample surface is then dissolved, and the inclusions are filtered out of the solute. This method improves the EB melting by melting a larger sample and being able to detect SiO_2. However, after deeper analysis, this can only be performed on massive samples and cannot be applied to wire.

7.2 Selection of methods

Before the start of the PhD study, Bekaert was using two methods to measure the inclusions state on wire rod. The first one, the Light Optical Microscopy (LOM), is a good technique for inclusion determination for basic steel grades. For wire rods used in this project, this technique is not enough sufficient to distinguish steel grades due to the low resolution and the lack of chemical composition measurement. Indeed, with LOM, the inclusions are observed manually and therefore the size and the shape of the inclusions can be analysed. However, it does not bring any information on the chemical composition of inclusions. Therefore, SEM/EDS automated analyses were used for specific grades. The SEM/EDS method is described later and showed problems of repeatability

To improve the cleanliness measurement at Bekaert, it was decided to invest new inclusion detection methods. The new detection methods considered by Bekaert took into account several parameters: the accuracy and the repeatability of the measurements, the ease to use, the time and cost of analysis, and the improvement of the statistics. In addition, the size of the inclusions must be considered. Indeed, several inclusions measurement methods have some limit of detection higher than the average size of the inclusion present into the wire.

Some technics had to be selected in view of new investment. The purpose of the selection of analysis technique is to compensate limitations of one method by another one. In Table 7, the three methods chosen are compared.

An indirect method was also selected: the “total oxygen” measurement. This method permits to measure oxygen contained in steel.

Table 7 : Differences between three direct methods of inclusion analysis

Technique	Dimensional view	Fast analysis	Morphology information	Matrix effect	Big size inclusion analysis	Measure of size	Localization on metal specimen
SEM / EDS	2D	Yes / no	Yes (partially)	Yes	Yes/no	Rough	Very good
OES / PDA	2D	Yes	No	Yes	No	Rough	Approximate
Extraction	3D	No	Yes	No	Yes	Very precise	Not possible

The principles of the different methods are briefly explained below.

7.3 Total oxygen measurement

The determination of the total oxygen content in steel, for short "total oxygen", is an indirect method which is widely used to evaluate steel cleanliness. Total oxygen is the sum of soluble oxygen in liquid steel and that present as oxide inclusion [17,68]. Because the oxygen content in steel is low (around 5ppm) and considered as constant, the total oxygen content is considered as a reasonable value of the total amount of oxide inclusions [68]. The relation between the oxide density and the total oxygen has already been proved as illustrated in Figure 34 [69].

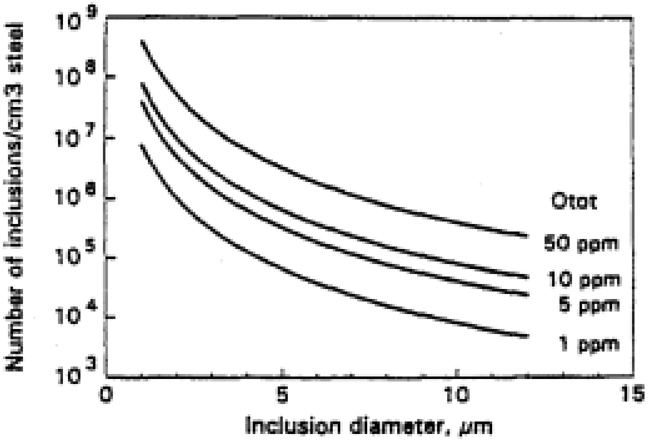

Figure 34 : The number of inclusions in 1 cm³ steel as a function of the total oxygen content and inclusion size, assuming all oxygen being bound in equal size Al_2O_3-inclusions [69]

However, the oxygen content does not give any information on the size, morphology and distribution of inclusions. Steels with the same oxygen content might have different size distributions. The specific chemical composition is not measurable with this technique. However, it allows a fast analysis of a relatively large amount of inclusions, and this improves the statistics of the measurement.

The total oxygen and nitrogen contents of the sample were determined with a LECO (TC500) combustion analyser using the inert gas fusion method. The principle is based on fusion of approximately 1 gram of sample in high purity graphite crucible in an inert gas (argon). The oxygen in the sample, present in all forms, reacts with the carbon of the crucible to form gaseous CO and CO_2. Oxygen is detected as CO and/or CO_2 using infrared absorption. The calibration of the instrument is performed with standard steel samples of known oxygen concentration, which are selected to be within the expected range of concentration of the unknown sample. The total oxygen measurement was repeated five times to obtain an average value. Abnormally high total oxygen results were disregarded due to possible surface oxidation.

7.4 SEM/EDS

Automated SEM/EDS provides the means to characterize inclusion populations. This method is quite complete, providing information about the amount, the size, the chemical composition and the distribution of inclusions into the steel matrix. This method is based on bi-dimensional view of inclusions distributed in space.

The samples are imaged in BSE contrast mode which enables the distinction of chemical contrast. The detection of inclusions is based on the difference in threshold between the matrix and the inclusions. Particles with a low average atomic weight like oxides or sulphides inclusions appear darker in a bright iron matrix which is composed of element with higher atomic weight as shown in Figure 35. To obtain the most reproducible and repeatable results for the different samples, the SEM parameters are fixed at specific constant values.

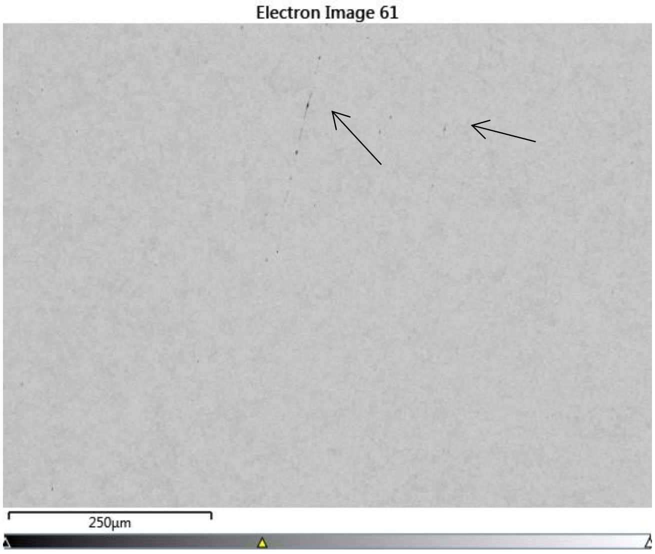

Figure 35 : Field of view obtained by BSE for inclusion detection

The SEM/EDS analyses were performed on a JEOL 7200F FEG/SEM equipped with an Oxford Energy Dispersive system (EDS). The Aztec software was used for the measurement, the data collection and processing.

The surface analysed is the longitudinal section taken in the drawing axis. This sample preparation permits to study the elongation of deformable inclusions such as sulphides. A surface of approximately 60mm² was analysed in order to have a representative measurement of inclusions. The acceleration voltage was set to 15kV and the current probe to 15nA at magnification 350. This setting permitted to detect features with a minimum equivalent diameter of 2µm.

7.5 Extraction method

Extraction method for inclusions investigation consists in dissolving the metallic matrix in view to collect non-metallic inclusions. This method permits to have a 3D view of inclusions and to have an accurate measure of the composition, avoiding the measurement of surrounding matrix. The extraction method enables also the analysis of a large number of inclusions. This improves the statistics of inclusions measurement.

The standard dissolution consists in putting the iron piece directly in a strong acid at a certain temperature to dissolve the metallic matrix. This method is also called Dekker method.

This method permits to dissolve an important quantity of steel (several grams) during a short time (~3h). The acid extraction method offers the advantages of a rapid and easy extraction of inclusions, which have high stability. The principal disadvantage is the attack and dissolution of certain types of inclusions by acid.

The methods used in the present PhD work for the extraction employed a chemical solution composed of HNO_3, H_2SO_4 and H_2O in the respective proportion 1:38:61. Several grams of wire were dissolved in this solution heated at 80-90°C. This operation lasted 2-3h depending on the quantity of steel introduced. At the end of the reaction, the solution was filtered through a Nucleopore membrane with Ø0.4µm pore diameter. The filtration was followed by several steps of rinsing with hot H_2O, and hot solution of diluted NaOH. Then the filter was dried and put on a specimen holder for SEM/EDS analysis.

7.6 OES/PDA

Optical emission spectroscopy is a technique known since decades to measure the chemical composition of a bulk piece of metal. Its principle is based on electrical sparks emision. A high-energetic discharge of electric sparks (2000-3000 sparks) at a frequency of 100-800Hz ablates the sample surface. A spark emited between the electrode and the metallic piece permits to dissolve and vaporize the atoms from the metallic piece. Those atoms are brought to high state energy to form a plasma discharge. Excited atoms and ions present in the plasma create an unique spectrum specific for each element. Ligth generating from the spark is split by diffraction gratting. The light intensity for each wavelenght is measured with photomultipliers (Figure 36). Based on a specific calibration function, the total mass fraction of each element in the ablated part is determined. A qualitative measurement is possible with the wavelength detected. A quantitative measurement is possible with the measurement of the intensity of peaks.

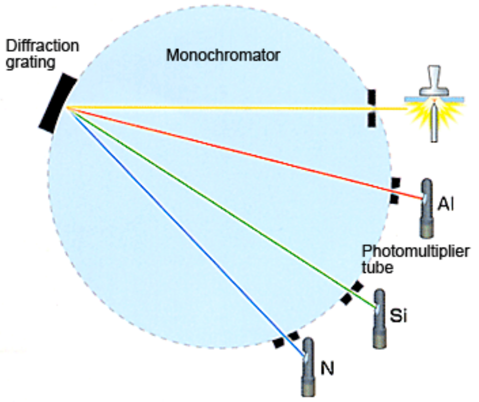

Figure 36 : Schematic illustration of OES/PDA [70]

The PDA option (pulse discrimination analysis) is an option on OES analysis that permits to measure inclusions present in the matrix. When a spark ablates the inclusion and a part of the matrix, the composition is analysed by spectroscopy as described before. The high light intensity (outliers) which are related to the given elements present in the inclusions can be evaluated by PDA (Figure 37).

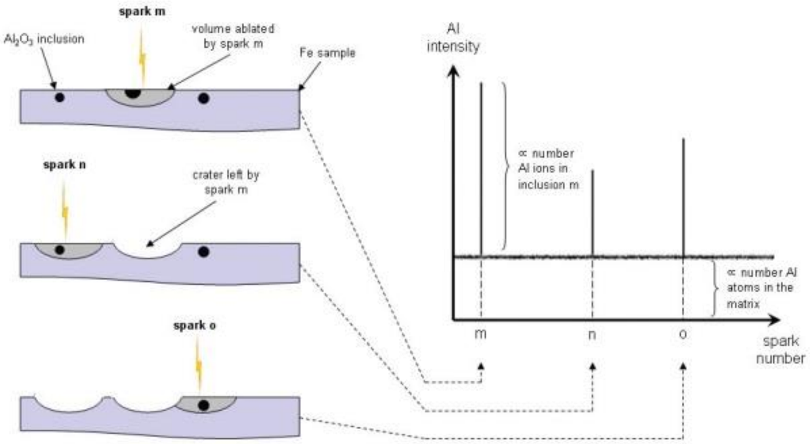

Figure 37 : Scheme of spark ablation of matrix with inclusion and transcription on element spectrum results [70]

For each element, a spark-by-spark chart is obtained (Figure 38). These outliers are identified as intensity exceeding the median intensity of the metallic background (matrix). The limit to distinguish matrix from outliers is defined as follow: Outliers > Average of peak intensity + K(Standard deviation). Peaks above this limit are considered as outliers (so inclusion). K is considered as the detection factor. A low K value will consider noise from the matrix as inclusions. With a high value of K, the smallest inclusions will not be detected. By default, the factor K is set at 3.

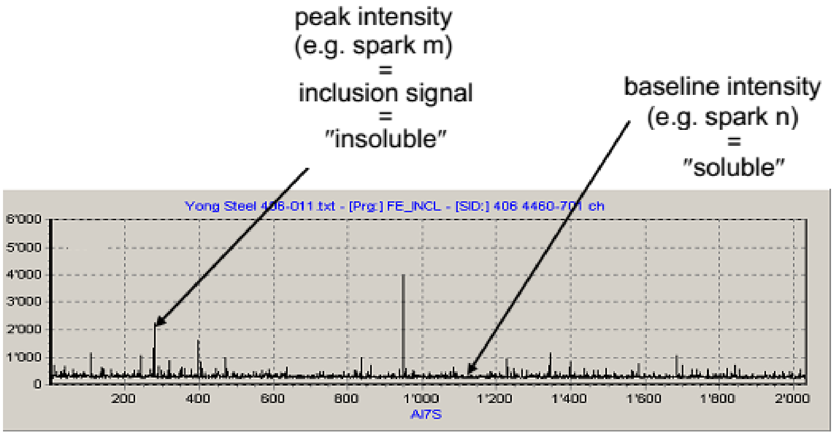

Figure 38 : Example of a spark-by-spark chart obtained for each element after the measurement [70]

The identification of the complex inclusions (which contain several chemical elements) is based on the outlier's coincidences detected in one spark. As presented in Figure 39, inclusion type (chemical composition) can be evaluated based on coincident peaks of two elements. There is a high probability that the two elements are present in the same inclusion if they are detected on the same spark.

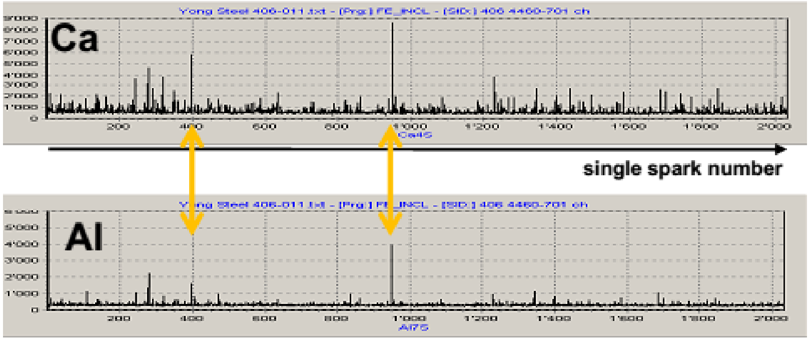

Figure 39 : Multi-compound inclusion detection with PDA option [70]

8 Evaluation of inclusion identification methods

Most of these techniques were not in use in the Bekaert lab and one of the objectives of the PhD was to organize a combination of these techniques to asses very accurately all the features of the inclusions.

8.1 OES/PDA vs. SEM/EDS

A preliminary work on the device had to be performed in view to improve the algorithms and the detection limits of the device. The OES/PDA is a complex method with many modifiable parameters, as the spark frequency, the source conditions, the detection limit, the measurement window …

The device was delivered by the supplier with an existing inclusion method that is common for steel. This method had to be adapted as a function of the inclusion of interest, the size and shape of the sample. OES measurements are optimal on bulk sample. In our case, the studied samples were wire rod of Ø5.5mm.

The analyses of fractures during wet wire drawing underline that inclusions present on the fractures are mostly Si-based inclusions. Si is always the major element present into the inclusion. Our focus with OES/PDA was mainly on Si inclusion detection. The number of outliers peaks for Si compound were measured ten times on ten different pieces of the same wire rod. These series were repeated three times. After the repetition of measurement (Table 8), it was observed that the repeatability was not satisfactory.

Table 8 : Number of outlier's peaks detected for Si on the same wire rod – three series of 10 measurements

	Series 1	**Series 2**	**Series 3**
Analysis 1	10	2	292
Analysis 2	6	7	363
Analysis 3	18	173	343
Analysis 4	16	167	342
Analysis 5	19	165	328
Analysis 6	19	155	285
Analysis 7	16	29	243
Analysis 8	7	25	223
Analysis 9	14	6	233
Analysis 10	28	16	230
Average	15	74	288

To understand the problem, the spark-by-spark chart used to Si outlier's detection is extracted. By studying this chart, it appeared that the detection of outliers' peak was not optimum. Compared to a "good" spark by spark chart (Figure 40) where the baseline is well defined and the outlier peaks are visible, the spark by spark chart of Si is more disorganized and noisy (Figure 41). The baseline noise peaks cannot be distinguished from the outliers peaks. The signal to noise ratio is very low. Consequently, as the number of detected particles depends on the quality of this chart, the number of particles detected is not accurate.

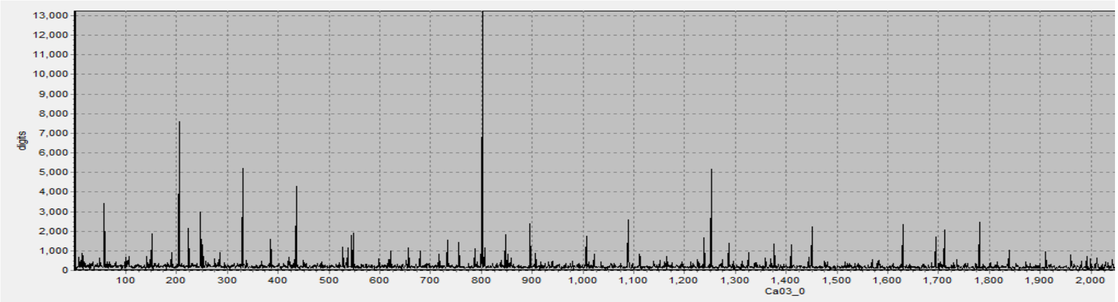

Figure 40: Example of Ca spark-by-spark chart

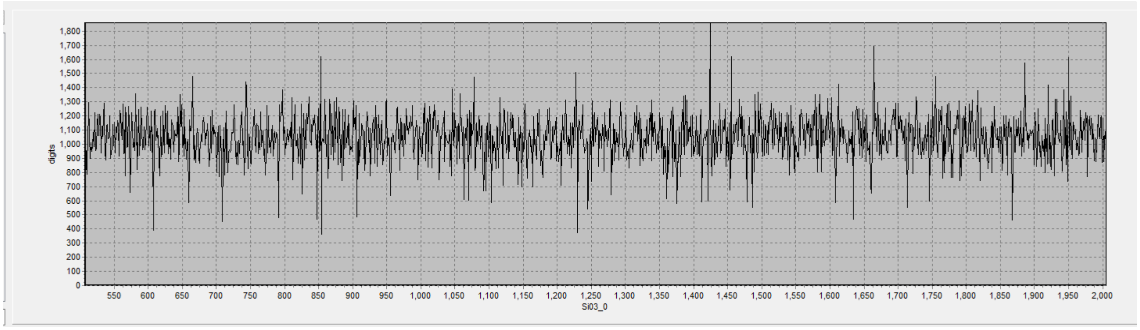

Figure 41 : Example of Si spark-by-spark chart

Despite the disparate results obtained on the measurements, the results obtained for different wire qualities with SEM EDS were compared to results obtained with OES/PDA. The number of Si peaks detected by OES is supposed to be comparable to a density. Indeed, the volume ablated during each OES analysis is the same. Five different qualities were analysed. The results are presented in Figure 42.

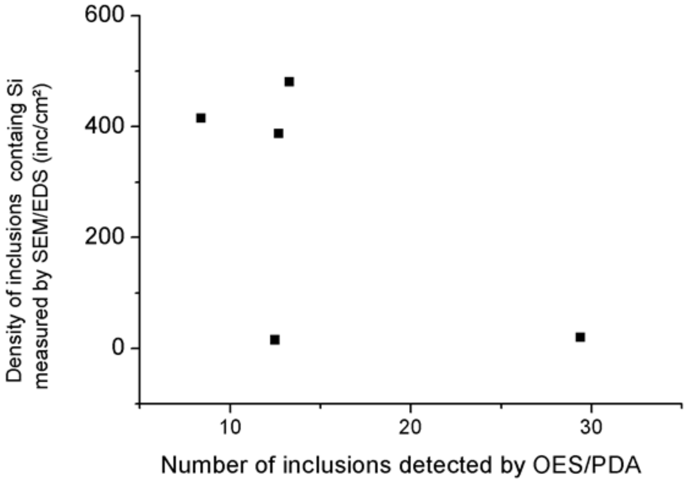

Figure 42 : SEM/EDS and OES/PDA correlation for Si particles

Figure 42 shows that no visible correlation between the Si peaks detected by OES and the Si particles density measured by automated SEM EDS method. In conclusions, with these analysis parameters, no distinction is possible between the different qualities of wire rods.

To solve the problem concerning Si detection with OES/PDA, some procedures mentioned in the European Research project RAMSCI [71] working on several aspects of OES/PDA were considered. It was concluded that companies using OES PDA to identify inclusions containing Al, Ca, Mg, Ti, and S found these elements as “easy” in the way that the background level of the steel matrix is very low. To be more precise, these elements are present in a low quantity in the matrix, so the detection of outlier’s peaks is easier.

For other elements as Si and Mn, the detection of inclusions with OES PDA is more difficult. These two elements are most of the time present in a great quantity in the steel matrix. Therefore, the noise from the background of the spectrum obtained after spectroscopy is important. Due to that, only relatively large inclusions (several µm in widths) can be detected for those two elements and the risk to include ‘false’ outliers from noise increases.

To attenuate the problem of detection between outliers and matrix signal, a modification of the analysis parameters was advised. As explained before, several parameters are modifiable as the source condition, the spark frequency and the measurement window aperture. Figure 43 shows the difference in spark-by-spark charts obtained after the modification of the window aperture. By applying a certain delay and width of aperture, the spark-by-spark chart seems more readable and the identification of outlier’s peaks seems easier.

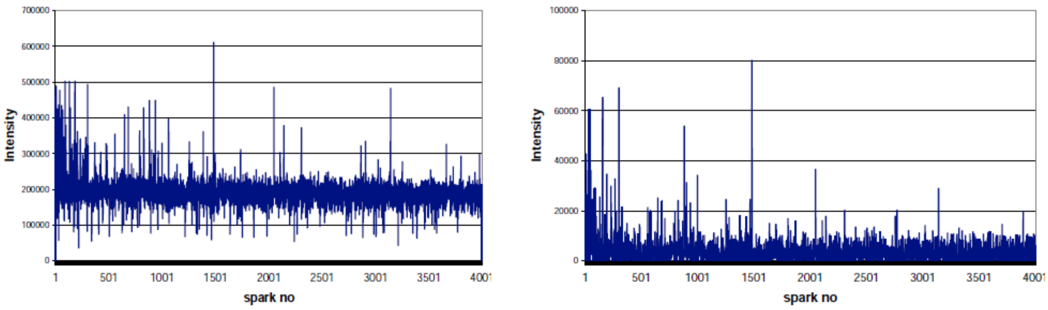

Figure 43 : Improvement of spark-by-spark chart by changing the window aperture [71]

The “by default” parameters summed up in Table 9 do not allow a correct detection of the inclusions and a good repeatability of the results. Several parameters were studied to improve the repeatability and to find the best combination of parameters. For that, several tests have been carried out and the frequency and the window of detection have been modified until it was repeatable and reproducible. The source condition which represents the profile of intensities of the spark overtime has been modified. It was found that by decreasing the spark frequency and intensity, the quality of the results was improved. The answer studied were the number of inclusions detected for several elements as Ca, Al, Mg... However, the concern was mostly focused on Si, the major element of the inclusions present into the wire. Some new measurements were performed with these updated analysis parameters.

Table 9 : By default analysis parameters for OES/PDA measurement

OES parameters	**Values**
Pre integration and integration argon flow (L/min)	4
Pre integration duration (ms)	500
Integration duration (ms)	10000
Spark frequency (Hz)	400
Window aperture	
Start (µs)	50
Duration (µs)	150

Seven wires from different suppliers and with different qualities have been measured with OES/PDA. The studied answer was the total number of inclusions. The oxide density measured by SEM/EDS was compared with the number of oxide inclusions detected by OES/PDA. We considered that the volume ablated for each OES/PDA measurement was constant. Therefore, a number of peaks measured by OES/PDA can be compared to an inclusion density measured by SEM/EDS. The results are reported in Figure 44.

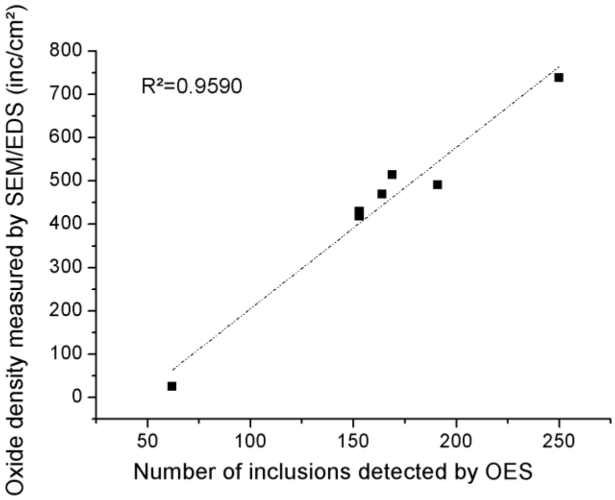

Figure 44: Relation between the oxide density measured by SEM/EDS and the number of oxides inclusions detected by OES/PDA

A linear relation linked the total number of peaks measured by OES/PDA and the total oxide density measured by SEM/EDS. The coefficient of determination $R^2=0.9560$ proved the linear relation between the two studied results. When the oxide density is low, the OES detects a low number of outliers peaks, and when the oxide density is high the number of detected peaks is also high. For the zone in between, the results are more difficult to interpret. The distinction between the different qualities is more difficult. For that, the study of each element distinctly is needed.

The following graphs represent the comparison between the density of inclusions measured by SEM/EDS and the number of peaks detected by OES/PDA for respectively Mg, Ca and Al.

By studying calcium and magnesium (Figure 45), a linear relation is observed between the results obtained by SEM/EDS and the number of peak detected by OES/PDA. For both elements, the qualities of the wire can be differentiated. Even if the R^2 values linking both parameters are lower than for the measurement of the density, a linear correlation is visible.

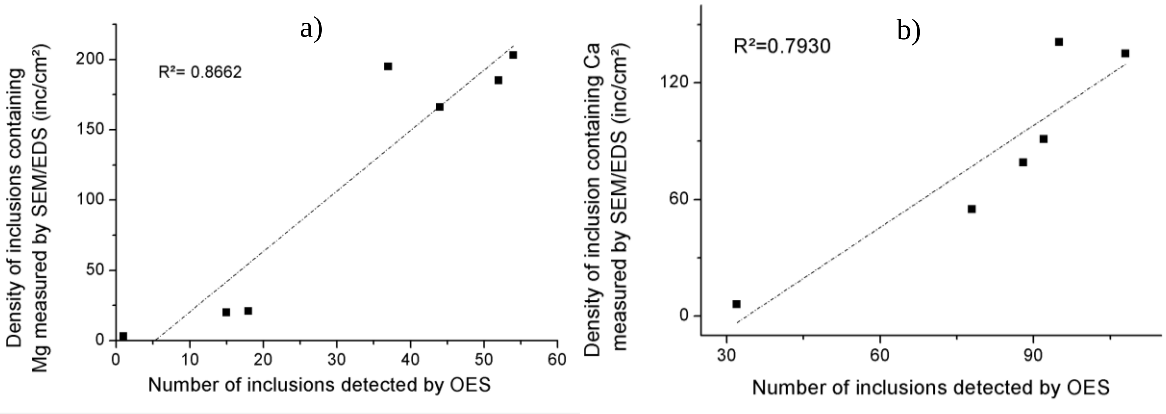

Figure 45 : Relation between the density of inclusions containing a) Mg b) Ca measured by SEM/EDS and the number of a) Mg b) Ca peaks detected by OES/PDA

For aluminium, the correlation is more difficult, even if the concentration of Al in the matrix is low. Especially for one outlier point the disparity of results may come from the sample preparation. The grinding paper used for sample preparation is mainly composed of Al_2O_3 particles; these grinding particles can stick on the steel surface and be considered as inclusions.

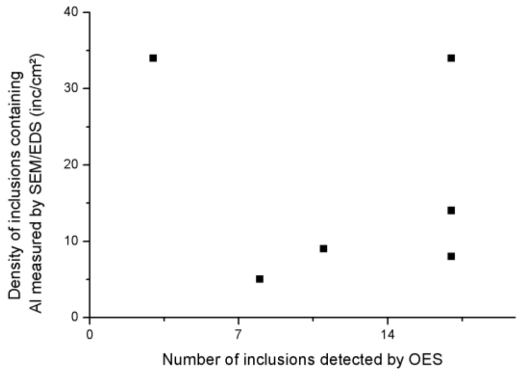

Figure 46 : Relation between the density of inclusions containing Al measured by SEM/EDS and the number of Al inclusions detected by OES/PDA

For the detection of Si inclusions, an intensive work was performed to try to detect it. By studying several parameters as the window aperture, the spark frequency, the source conditions and the limit of detection, it was possible to find a correlation between the density of inclusions containing silicon and the number of peak detected with OES/PDA, as presented in Figure 47.

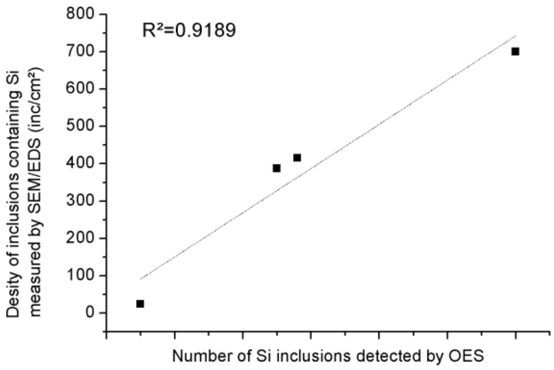

Figure 47 : relation between the density of inclusions containing Si measured by SEM/EDS and the number of Si inclusions detected by OES/PDA

After the development of the method and the optimization of several parameters, a linear correlation was obtained between the results obtained by SEM/EDS and the OES/PDA for the detection of Si particles.

The long development, now, allows a fast detection of the density and the chemical composition of the inclusions of each type: Si, Ca, Al, Mg. Anyhow, the detection of inclusion size is still not possible. However, the development of the calculation algorithms enables the fast measurement of the inclusions present into the wire. Unfortunately, the results of this technique were obtained on the last year of the PhD.

8.1.1 Inclusion extraction

After the dissolution of the steel matrix and the extraction of the inclusions, the filter was analysed with the automated SEM/EDS measurement. Nevertheless, the principle is different from that for the analysis of the steel section. For the automated inclusion detection on steel, the inclusion appears dark on a bright matrix. For the filter, the filter appears dark while the inclusions appear brighter on the filter. An example of the inclusion detection is presented in Figure 48.

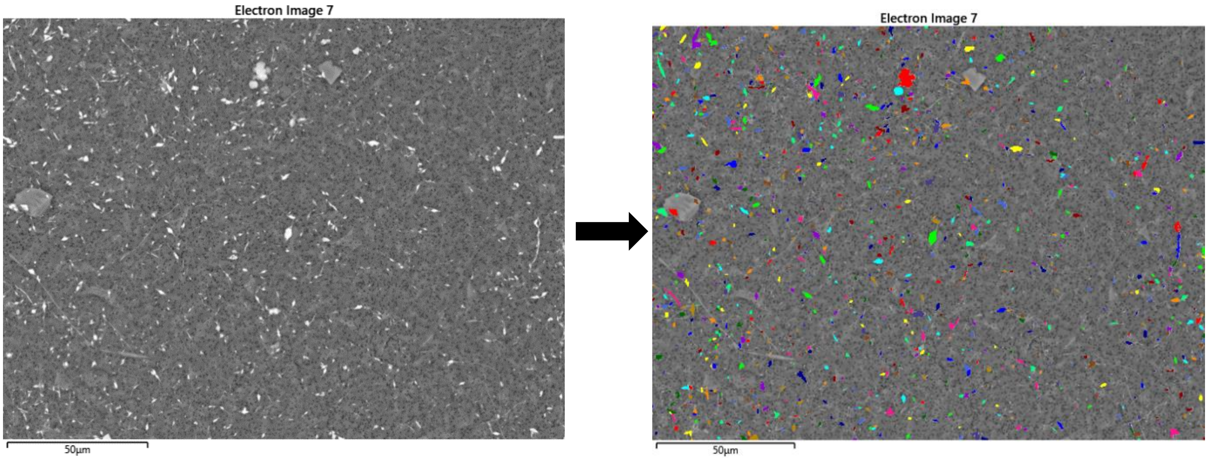

Figure 48 : SEM images of a) filter containing inclusions b) particles detected by Aztec software for automated SEM EDS measurement of inclusions

The principal interest of using the extraction method is to observe the morphology of inclusions, and also to improve the statistics about the counting of inclusions. Indeed, the dissolution method allowed analysing a greater number of inclusions.

The acid extraction was evaluated with the same approach than for OES PDA. The results of the dissolution methods were compared with the results obtained from the automated SEM/EDS on steel surfaces. The inclusions of the wire rod were measured with the dissolution method. 5 grams of wire rod were dissolved, inclusions were collected and then analysed by the automated SEM method. The two methods were compared by considering three factors: the inclusion density, the chemical composition of inclusion and the size.

- Density

For the density measurement ($N_{surface}$) with the 2D SEM/EDS technique, the number of particles n measured is divided by the analysed surface of the sample as described in equation 12:

$$N_{surface} = \frac{n}{Surface} \tag{12}$$

Referring to the Dehoff's equation, the volumetric density N_{vol} of inclusions can be assessed with equation 13:

$$N_{vol} = \frac{2}{\pi} \frac{N_{surface}}{\bar{d}} \tag{13}$$

Where $\bar{d}$ is defined by equation 14:

$$\frac{1}{\bar{d}} = \frac{1}{n} \sum \frac{1}{d_i} \tag{14}$$

Where d_i is the apparent particle size of i^{th} inclusion among n inclusions and $\bar{d}$ is the harmonic mean of inclusion particle size (m),

For the dissolution technique, the calculation of density is more complex. As the entire filter cannot be analysed, a calculation step has to be added. The total number of inclusions per unit volume is calculated with equation 15 [72].

$$Nv_{dissolution} = \sum Nvi \tag{15}$$

With:

$$Nvi = ni.\frac{A_f}{A_{obs}}.\frac{\rho_M}{W_{dis}} \tag{16}$$

Where ni is the number of inclusions on the field i, A_f and A_{obs} are respectively the total area of the film filter with inclusions and the total observed area . ρ_M is the density of the steel (0.00785g/mm^3) and W_{dis} is the dissolved weight of the metal sample.

The volumetric density of inclusions of a same wire rod is given Figure 49 according to the employed technique.

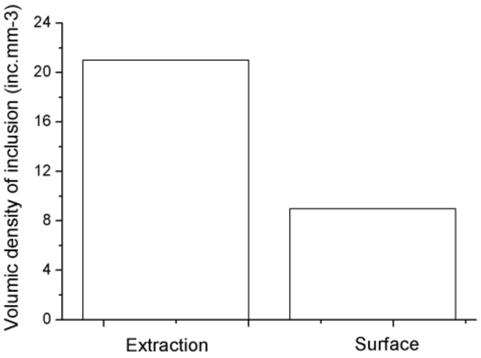

Figure 49 : Difference in volumetric density of inclusion measured after extraction and on steel surface

The volumetric densities measured with both techniques are different. The volumetric density measured after extraction is higher than the one measured on steel surface. This difference can be due to the difficulty to differentiate inclusions from dusts present on the filter. Though the extraction method involves a lighter amount of material especially inclusions, and seems therefore to be more reliable for density assessment, it is also involving unwanted particles such as dust which does not improve finally the measurement assessment.

- Chemical composition

Concerning the chemical composition of inclusions, the distribution of inclusions type measured on surface with SEM/EDS was compared with the inclusions types measured after dissolution. The ternary diagrams (SiO_2-Al_2O_3-(MgO-CaO)) (Figure 50) show that differences are observed between the composition distributions of the inclusions depending on the analysis technique. The composition is quite dispersed by using the extraction method while for inclusion analysis on steel surface, the inclusion composition is grouped. However, the dominating zone is the same for both techniques. The differences between the two methods can be explained by two reasons. First, the extraction method enables analysis of a higher quantity of inclusions than on the steel surface, which can explain that more different types of inclusions are analysed. The second reason is the difference of measurement between the two methods as the "background" differs. For the steel matrix, the background is the surrounding steel matrix. For the dissolution, the background is the filter composed of polycarbonate, meaning mainly carbon. So the dusts present on the filter cannot be excluded by measuring the carbon of the particle. The inclusion identification is easier on the steel matrix than on the filter after dissolution.

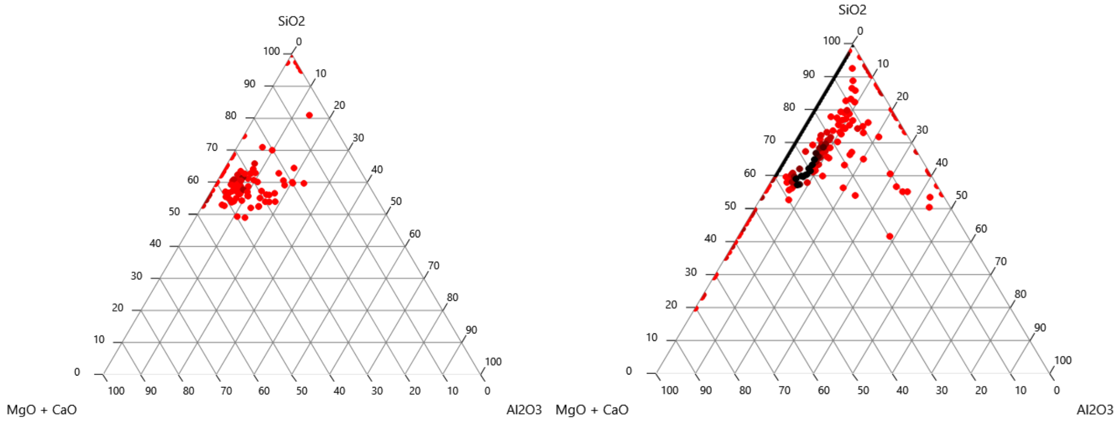

Figure 50 : Ternary diagrams obtained after SEM/EDS automated analysis a) on steel surface b) after dissolution

But if we compare the inclusion types measured by the classification established, no difference can be observed between the inclusion distributions measured on the steel surface and on the filter after extraction, as presented in Figure 51.

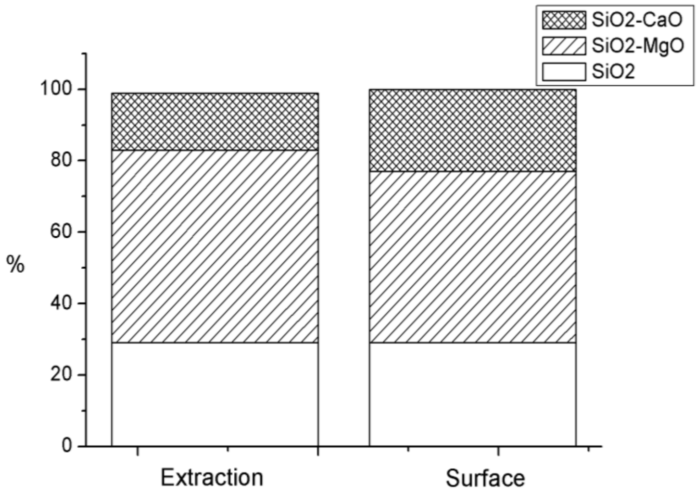

Figure 51 : Repartition of the inclusion type after extraction and after measurement on the steel surface

- Size of inclusions

Concerning the size of inclusions, the extraction method simplifies the detection of bigger inclusions. As the number of analysed inclusions is increased, the real size distribution is revealed. Figure 52 shows the size distribution for both techniques.

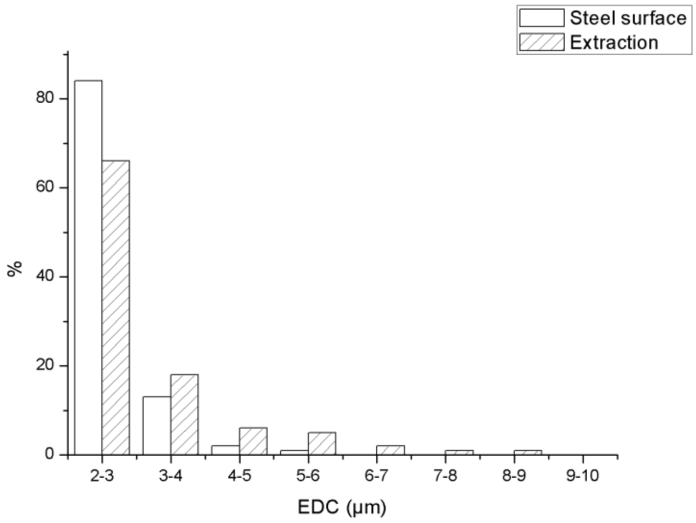

Figure 52 : Size distribution for inclusion analysis of steel surface and after dissolution

It is clear from Figure 52 that the size distribution differs for both measurement methods. The size distribution is more spread with the extraction technique. The average size of inclusions detected is also impacted. The average inclusions size is respectively 2.53µm and 3.11µm for measurement on steel surface and after dissolution. Eliminating the steel matrix permits a full observation of the inclusion size, explaining the difference of size distribution between the two methods.

The difference in the size distributions comes from the 2D images. The field of view does not allow having an accurate measure of the size of the particles. As represented on Figure 52, the size of the inclusion measured by SEM/EDS on steel surface is sometimes not representative of the maximum size of an inclusion. Only a section of the inclusion is observed and measured. The probability to cut through all the inclusion at their maximum diameter is poor. So the 3D analysis of inclusions is also required to have an accurate measurement of inclusions size. More than the size, the morphology of the inclusions is much more accurate with dissolution technique

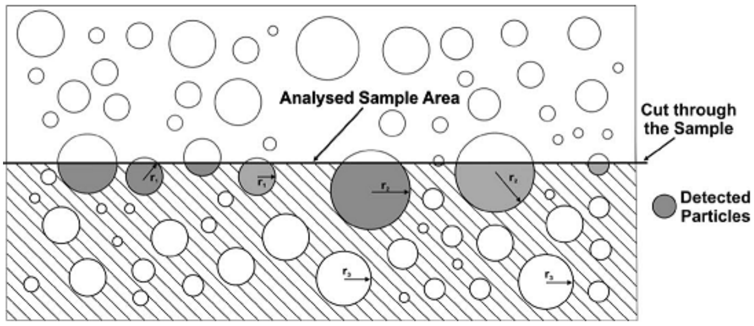

Figure 53 : Scheme of the apparent size distribution of non-metallic inclusions on surface of analysis [73]

The extraction method is so a complementary method to the SEM/EDS measurements performed at the steel surface. The results are similar than the surface measurement concerning the inclusion types. However, the volumetric density is not comparable between the two methods. The advantage of the extraction method versus the inclusion measurement on surface is a better statistics for the size and morphology measurement. Nonetheless, the extraction method is time consuming. Though it brings extra information, it cannot be used as a routine method.

8.2 Oxygen total measurement

As explained in the section 7.3, the oxygen content measurement is a reasonable indirect method for the determination of oxide inclusion density The density of oxide inclusion was measured by two techniques: automated SEM/EDS and LECO combustion measurement to determine the oxygen total present into the wire rod. The results are reported in Figure 54. A linear correlation rules the two parameters. The two parameters are directly and well correlated. So the oxygen total measurement by LECO can give very quickly good information of the oxide density present into the wire rod and the global cleanliness.

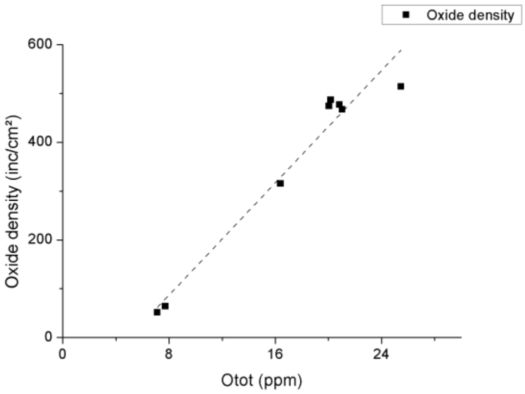

Figure 54: Comparison of total oxygen measured by LECO measurement and oxide density measured by SEM/EDS

9 Conclusions

The different methods for inclusions analysis have been reviewed in this chapter. Among them, four methods were selected: the automated SEM/EDS measurement, the OES/PDA, the extraction method and the oxygen total measurement. These methods were developed and adapted to measure with the highest precision the inclusion present into the wires. Among the four methods, the SEM/EDS method was found to be the most complete technique to measure the inclusion chemical composition, size and density. The other methods selected were compared with the automated SEM/EDS method to evaluate their reliability.

The OES/PDA allows obtaining good results for the inclusion density and the inclusion chemical composition. The long development, now, allows a fast detection of the density and the chemical composition of the inclusions. Anyhow, the detection of inclusion size is still not possible. However, the development of the calculation algorithms enables the fast measurement of the inclusions present into the wire. Unfortunately, the results of this technique were obtained on the last year of the PhD. The correlation between the OES results and the drawability cannot be established.

The principal advantage of the extraction method is to observe the morphology of the inclusions and enable the detection of bigger inclusions by increasing the statistics. In addition, the detection of the different chemical composition is comparable with the results obtained with SEM/EDS. However, the density measured with the extraction method is in average higher than the one measured by SEM/EDS due to the detection of undesired particles during the measurement of the inclusions. Nevertheless, the time consuming of this method is a real brake for it to become a routine analysis.

Concerning the oxygen total measurement, a correlation was found between the oxide density measured with SEM/EDS and the total oxygen measured by combustion analysis. This fast technique can be used to give a realistic idea of the oxide density present into the wire rod. However, no other information and be found with this technique

From the comparative analysis of the inclusions analysis method, it was decided to investigate the inclusions in the wires mainly with the automated SEM/EDS. The oxygen total and the extraction method will be used sporadically, for this specific purpose, to evaluate the shape of the inclusion or to improve the statistics. On the other hand, it will be employed when the diameter of the wire does not enable a measurement on the surface.

Learning points:

Four different inclusion measurement techniques were considered and optimized for this PhD study:

- **the automated SEM/EDS**
- **the OES/PDA**
- **the extraction method and**
- **Oxygen total measurement.**

The automated SEM/EDS will be mainly used to identify inclusions in the wire and the oxygen total measurement / the extraction method used to evaluate the shape of the inclusion or to improve the statistics. It will be employed when the diameter of the wire does not enable a measurement on the surface.

Chapter III: Influence of cleanliness on fine filaments drawing

The goal of this chapter is to study the influence of the cleanliness on the drawing of fine filaments. The selected methods and newly development described in chapter II will be employed for that purpose.

For that, the inclusions properties of different wire rods will be deeply studied. Then, the attention will be paid on their ability to be drawn.

From fracture obtained, the properties of critical inclusions for drawing will be pointed out.

By comparing these data with the inclusions present in the wire rod, previously identified, it will then be possible to understand the influence of the inclusion density, their types and their sizes on the wire drawing

10 Materials

The principal wire rods selected for the first study were provided by only one supplier. Three different wire rods (in chemical composition and quality) are submitted to wet wire drawing. They are labelled wire 1, wire 2 and wire 3. The grade of the steel wire is adapted to the final use of product. Their chemical compositions are given in Table 10. Wire 1 and wire 2 are from the same quality, while wire 3 is an improved quality for fine drawing, normally superior in term of drawability, compared to wire 1 and wire 2. Inclusions properties such as size, morphology or composition must satisfy the conditions imposed by the drawing of the thinner diameter wire.

The impact of carbon content of the wire can be evaluated since wire 1 and wire 2 are of the same quality, but differ in their carbon content. The chemical composition of the three wire rods have been measured by OES and reported on Table 10. Wire 1 contains 0.97wt% C while wire 2 and wire 3 contain 1.02wt% C.

Table 10 : Chemical composition of wire rods (wt%)

	C	**Mn**	**P**	**S**	**Si**	**Cr**	**Ni**	**Fe**
Wire 1	0.97	0.30	0.008	0.008	0.19	0.19	0.01	Bal.
Wire 2	1.02	0.29	0.011	0.008	0.20	0.19	0.01	Bal.
Wire 3	1.02	0.30	0.007	0.007	0.20	0.19	0.01	Bal.

For metallographic observations, the cross section and longitudinal sections of the wires were embedded. The samples were first polished with SiC paper from grade 80 to 2000, and then with diamond paste from 9µm to ¼µm. The samples were finally polished with OPS (Oxide Polishing Suspension). This step was not performed for inclusion analysis preparation in order to avoid contamination of the surface with oxide particles.

To reveal the microstructure, the samples were etched for 5 seconds using a 4% Nital solution.

Figure 55 shows optical and SEM micrographs of each wire rod studied. The microstructure of the wires is fully pearlitic with Fe_3C lamellae alternately with α ferrite bands.

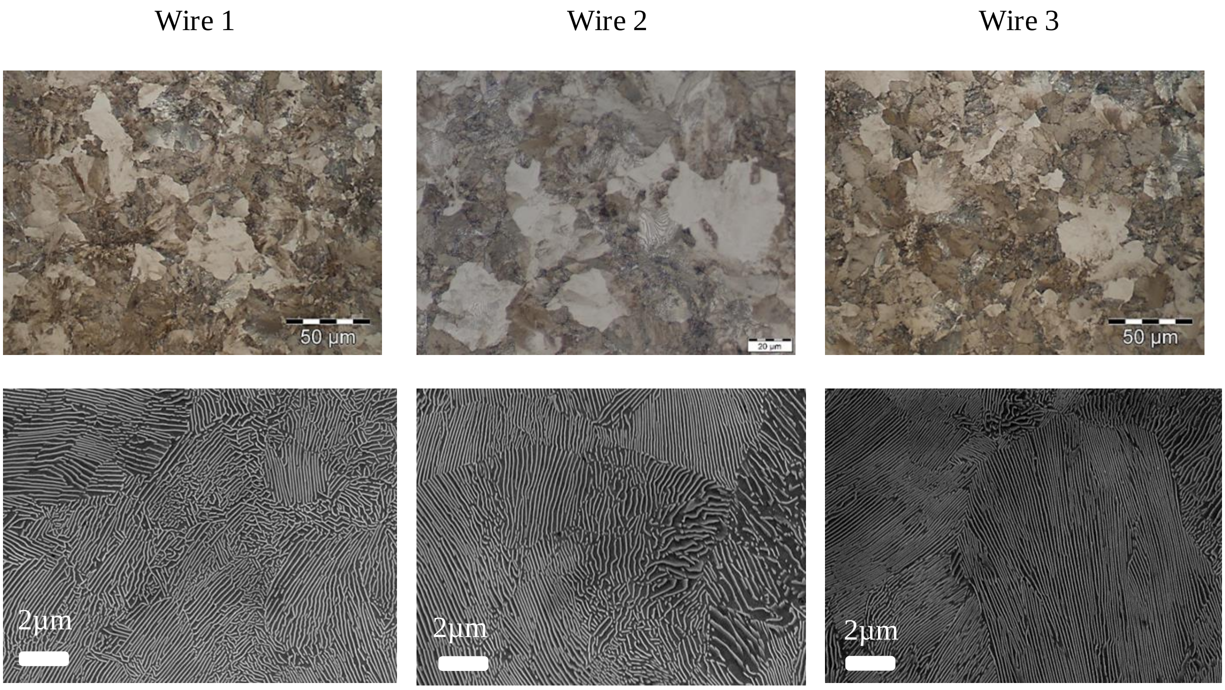
Wire 1

Wire 2

Wire 3

Figure 55 : Optical (top) SEM-SE (bottom) micrographs of the microstructure of the different wire rods

The interlamellar spacing (ILS) was measured from SEM images using the software ImageJ. The latter has been adapted to separate the cementite from the ferrite by grey levels. The dark part corresponds to ferrite and the light part corresponds to cementite lamellae. Then, ILS was measured by drawing a line of a given length and by counting the number of cementite lamellae crossing the line. A distance between two lamellae is then obtained. To have a representative measure, ILS was measured for ten lines per picture, for 10 pictures, so an average of 100 measurements.

Table 11 includes ILS, the ultimate tensile strength (UTS) and the hardness (Hv) of the materials.

Table 11 : Wire rod microstructural and mechanical properties

Rod	**ILS (µm)**	**Hv0.5**	**UTS (MPa)**
Wire 1	0.128 ± 0.010	371	1222
Wire 2	0.123 ± 0.011	410	1260
Wire 3	0.128 ± 0.010	415	1282

There is no difference even small between the interlamellar spacing of the three different wire rods. The carbon content has a slight influence on the hardness, and tensile strength changes from one wire to another. In addition, the wire will be drawn and heat-treated several times before WWD.

10.1 Inclusions present into steel wire

The three types of inclusions expected into high carbon steel, as mentioned in section 3.2 were indeed found: oxides, sulphides and oxy-sulphides. The distribution of each type is presented in Figure 56. The majority of inclusions in the wire rod are sulphide inclusions that represent more than 50% of the inclusions. The second major type is the oxide inclusions representing almost 40% of the inclusions of our high carbon steel. Oxy-sulphides represent ~7% of the inclusions. The distribution of the inclusion type is equivalent for the three wires.

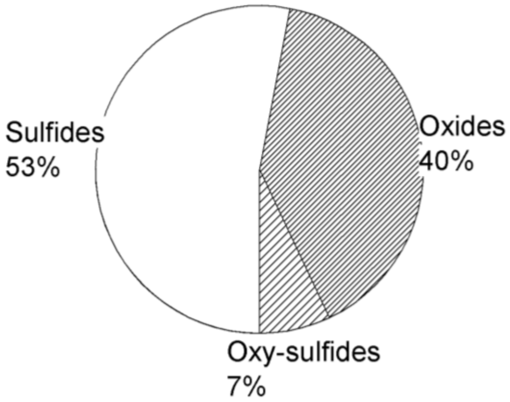

Figure 56 : Proportion of the different inclusion types present into the wire rods

An example of each inclusion type is presented in Figure 57 where a1) represents an oxide inclusion, a2) an oxy-sulphide inclusion and b) sulphide inclusions. For statistics, more than 500 inclusions were measured

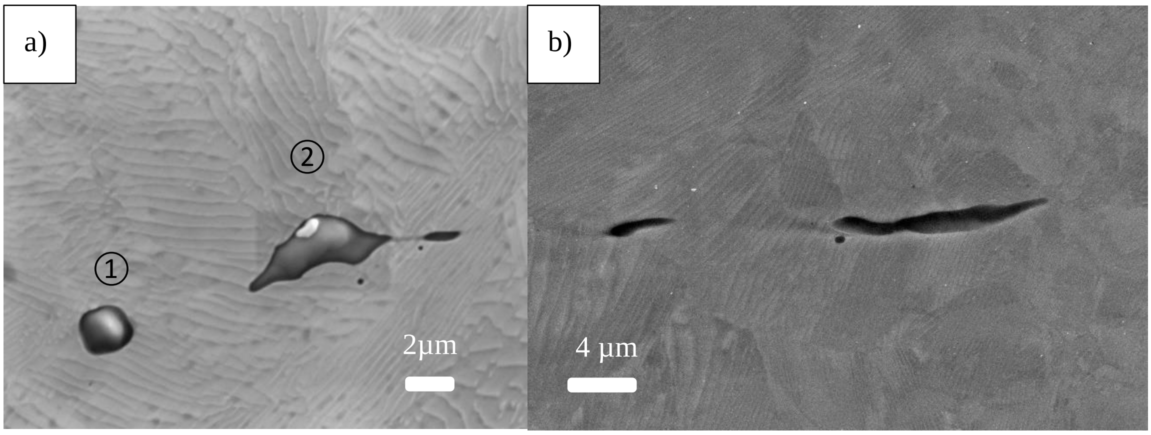

Figure 57 : SEM images of the different inclusion types a)1) oxide a)2) oxy-sulphide b) sulphides in wire rods

Figure 57 underlines the shape of the inclusions. Oxide inclusions have a rounded shape while the sulphide inclusions are elongated. The elongated shape of the later results from the previous step of hot rolling necessary to obtain the wire rod .The average aspect ratios defined as the ratio between the width and the length of the inclusions are reported in Table 12.

Table 12 : Average aspect ratio for different inclusion types

Inclusion types	**Average Aspect Ratio**
Oxides	1.83
Oxy Sulphides	2.53
Sulphides	5.26

Taking into account the volumetric fraction of inclusions, the partition of inclusions according to the aspect ratio, about 60% of the inclusions have an aspect ratio less than 3, see Figure 58. As mentioned in chapter I.4.1 an aspect ratio inferior to 3 after the rolling process expresses the non-deformability of the inclusion during the rolling process. We can conclude that half of the inclusions are considered as non-deformable in the wire rod.

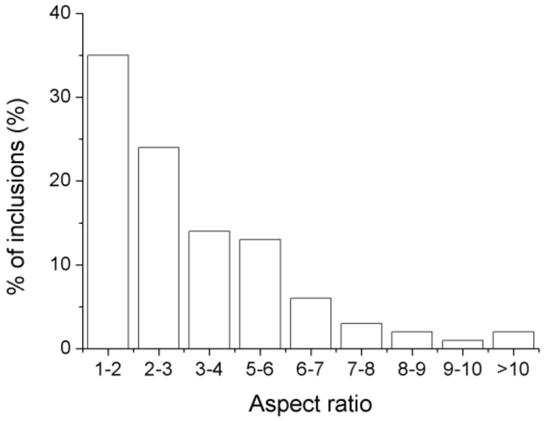

Figure 58 : Distribution of aspect ratio of inclusions measured in wire rods

10.2 Distribution of inclusions

It can be seen that the different types of inclusions are distributed homogeneously in the steel. The distribution of the inclusions on the longitudinal section, presented in Figure 59, has been assessed with SEM/EDS automatic data collecting, and demonstrates the homogeneity of the distribution of the inclusion along the surface.

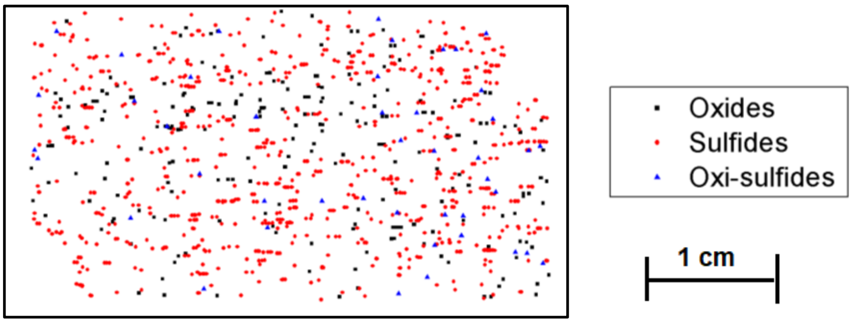

Figure 59 : Schematic representation of the distribution of inclusions over the longitudinal section

10.3 Inclusion density

To compare the cleanliness between the wire rods, inclusions automated analysis have been performed on the three wire rods. Several parameters were compared such as the inclusion density, the chemical composition of inclusions and their size. Those parameters could then be compared with the critical inclusions responsible of the fracture.

Since sulphides are considered as non-dangerous for the drawing thanks to their deformability, only oxides were studied.

The oxide density measured by SEM/EDS automated analysis for each wire is presented in Table 13. As explained in section 7.4, only the inclusions larger than 2µm are taken into account.

Table 13 : Oxide density for the different wires studied

	Density (inc/cm²)
Wire 1	725
Wire 2	491
Wire 3	469

The study of the oxide density reveals a large difference of oxides content between wire 1 and the two other wires. As explained before, the qualities of wire 1 and wire 2 are different than the quality of wire 3. It was expected that this difference of quality should be visible on the density level of oxide inclusions. However, there is only a significant difference depending on the carbon content of the wire (between wire 1 and wire 2). The difference of quality between wire 2 and wire 3 is not significant if the oxide density is considered.

10.4 Inclusion chemical composition

To study the difference between the wires, the chemical composition of the inclusions into the wires were measured by SEM/EDS. The ternary diagrams (SiO_2, MgO-CaO, Al_2O_3) are presented in Figure 60. Ternary diagrams enable a quick comparison of chemical composition of the inclusions into the wire.

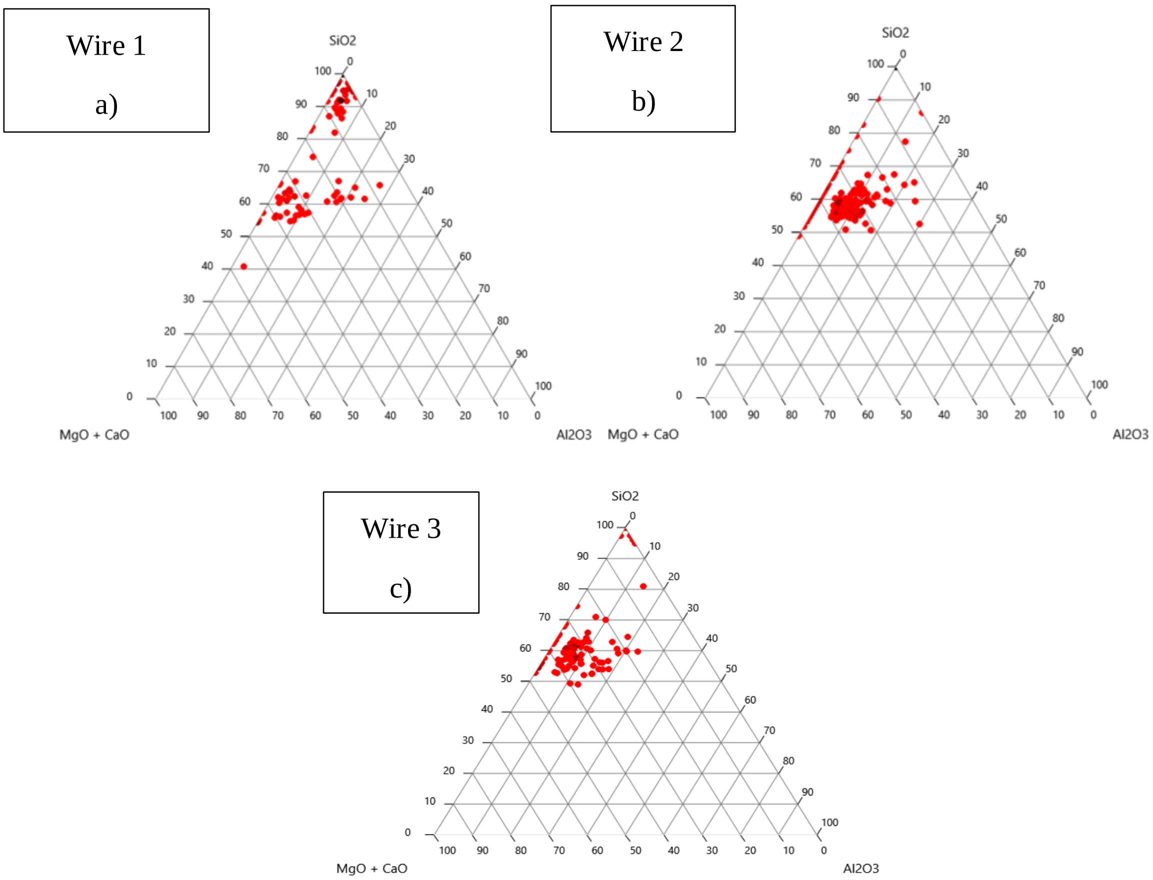

Figure 60 : Ternary diagrams of the wire rods used for the current study:

a) 0.97%C b)1.02%C c)1.02%C

The ternary diagrams for the three different wire rods underline the difference in the chemical composition of the inclusions present into the wire rods.

For wire 1, the inclusions are mostly pure SiO_2 inclusions, mostly located on the top corner of the ternary diagram. For wire 2 and wire 3, the compositions of inclusions differ and the SiO_2 inclusions are more complex, containing also CaO and/or MgO. Moreover, the amount of pure SiO_2 inclusions is reduced.

The partition of inclusions composition into the wire rod determined by automated SEM/EDS are reported in Table 14 and Figure 61

Table 14 : Distribution (%) of inclusion types into the different wire rods

	SiO_2	**SiO_2-MgO-**	**SiO_2-CaO-**	**SiO_2-CaO-MgO-**
Wire 1	67%	17%	7%	9%
Wire 2	29%	48%	12%	11%
Wire 3	25%	44%	13%	18%

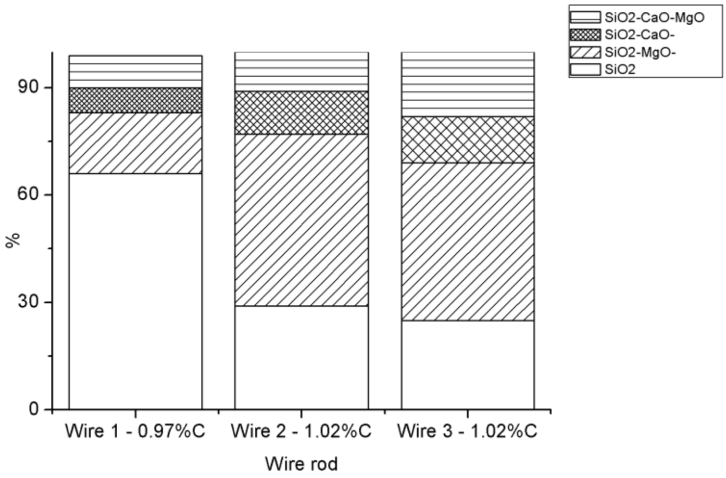

Figure 61 : Repartition of inclusion types into the different wire rods

Wire 2 and wire 3, with same carbon content, exhibit a nearly similar distribution of inclusions. However, the quality of these two wire rods are supposed to be different, anyhow, this difference is not reflected by a difference in the chemical composition of the inclusion. The difference of quality should be visible with another parameter than the chemical composition.

10.5 Inclusions size

The study of the inclusions size consists of the size distribution and the maximum size of the inclusions. The distribution of inclusion size is different for the three wires as shown in Figure 62. Wire 1 contains the biggest inclusions with a diameter superior to 9µm. Wire 2 presents inclusions with a diameter between 2µ and 9µm. Wire 3, which is from a higher quality, presents smaller inclusions with size between 2µm to 5µm. The difference between the two different qualities is not related with the chemical composition of inclusion or their density but with the size of the inclusion. (ECD was explained in section III.12.2.)

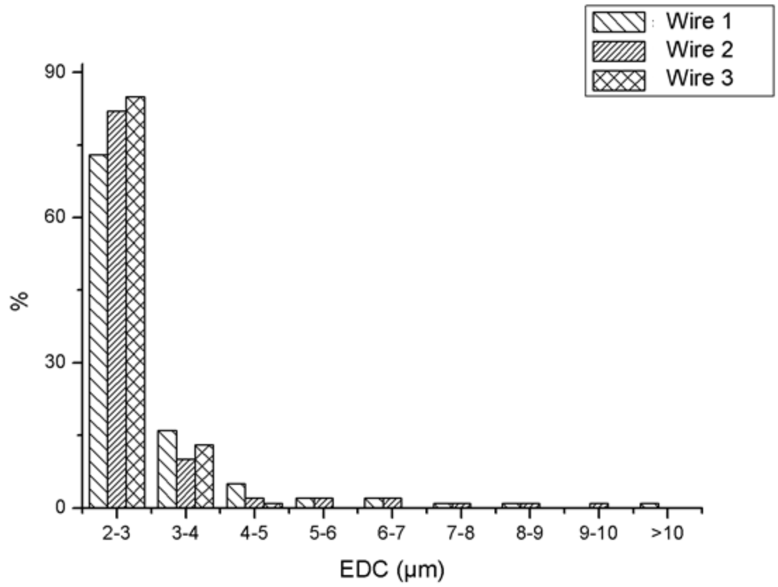

Figure 62 : Size distribution for the different wire rod qualities

In terms of average and maximum size of the different inclusion types, several trends can be extracted. There is a noticeable difference between the different types of inclusion. A clear difference is observed between wire 1, wire 2 and wire 3. For wire 3, the average size for each type is lower than for the two other wires. For wire 1 and wire 2, SiO_2 inclusions have a larger size, whether we consider the average or maximum size (Table 15). Both values decrease in wire 3. Same observations for SiO_2-MgO, which, by the way, are the largest inclusions if the maximum size is considered. For SiO_2-CaO, the opposite trend is observed.

Table 15 : Average and maximum ECD of the different inclusions for the studied wires

	Wire 1		**Wire 2**		**Wire 3**	
	Average ECD (µm)	Max ECD (µm)	Average ECD (µm)	Max ECD (µm)	Average ECD (µm)	Max ECD (µm)
SiO_2	2.89	6.59	2.89	6.25	2.48	4.14
SiO_2-MgO	2.82	9.19	2.47	8.84	2.47	5.21
SiO_2-CaO	2.25	4.27	2.36	4.39	2.27	3.92

10.5.1 Conclusions

The three wires used for the WWD trials were presented and analysed in this chapter.

The wires provided by the same supplier show some differences of quality and carbon content.

Wire 1 presents large differences of cleanliness in comparison with the two other wires in terms of density, chemical composition and size of inclusion.

There is no significant difference between their inclusion density and the type of inclusion present in the wire. The major noticeable difference is on the size of the inclusions.

These three different wires will be submitted to the same drawing tests to evaluate their performance.

11 Drawing test

With the same drawing parameters, the three different wire rods have been drawn into filaments with a final diameter of 60µm.

The list of the trials performed is presented in Table 16 which also includes the total length obtained and the number of fractures.

Table 16: Drawing trials to obtain a filament of 60µm diameter and fracture occurrence

	Die series	**Drawing speed (m/s)**	**Total length (km)**	**Nb of fractures**	**Drawability (fractures/100km)**
Wire 1	DS1	200	145	19	13
Wire 2	DS1	200	120	18	15
Wire 3	DS1	200	1100	54	5

From the total length drawn and the number of fractures obtained, a fracture ratio defined as number of fractures per 100km is calculated. This ratio is considered to be a good indicator of the drawability of the wire, meaning its ability to resist to the drawing process. These trials give a good idea of the drawability of the different wires. It is observed that the drawability is strongly impacted by the type of wire. Wire 1 and wire 2 show a lower drawability than wire 3. For wire 3, the fracture ratio is drastically reduced. For question of cost and relevance, the trials on wire 1 and wire 2 were stopped earlier than for wire 3.

It is attempted to link the drawability of the different wires with the fractures occurrence.

12 Results of fracture surface observation

Fractures that occurred during wet wire drawing were collected, observed and studied in order to determine their cause. SEM was employed for observation of the facture tips of the wire broken during WWD. Fractures during WWD happened into or at the exit of the drawing die. For the fracture due to inclusions, a central burst fracture type is always observed (Figure 63 a). This leads to a cup and cone fracture tip. Commonly, for fractures due to the presence of an inclusion, the inclusion is found on the top of the central burst fracture. However, sometime the inclusion can fall from the fracture tip. Then, only a hole containing previously an inclusion is found on the fracture tip (Figure 63 b). This hole gives an idea of the initial size of the inclusion

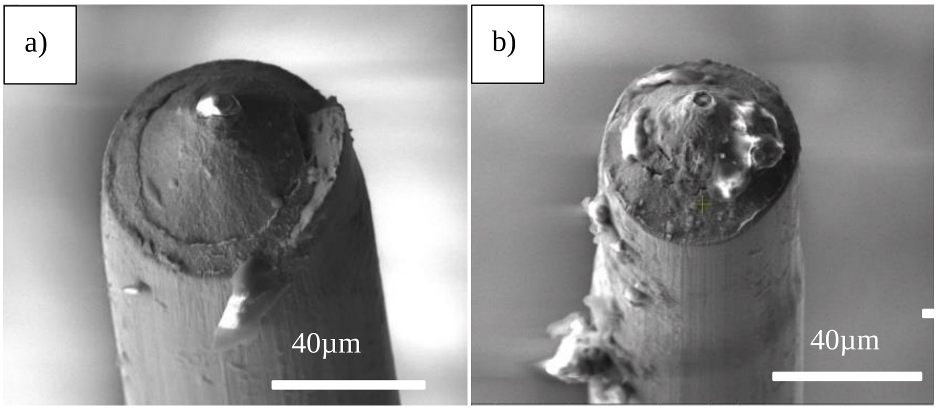

Figure 63 : Fracture presenting a necking a) with inclusion b) with a hole due to the presence of an inclusion

More than 200 fractures from the WWD collected from all the trials online have been studied.The fracture causes are summarized in Figure 64. 87% of the fractures are due to the presence of an inclusion. 10% of the fractures are due to overload, presenting a cup and cone fracture tip but without the presence of inclusions. These fracture are also sometimes be induced by a surface defect. 3% of the fractures could not be explained.

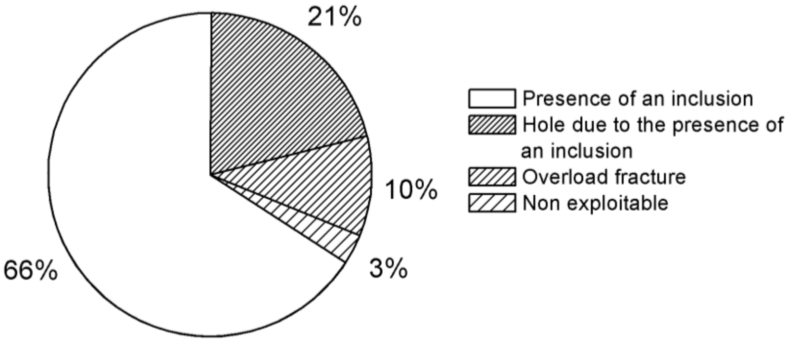

Figure 64 : Fractures causes determined by SEM analysis

12.1 Chemical composition of inclusions responsible of fracture

The chemical composition of inclusions responsible of fracture is also an important parameter. It is known that the mechanical properties and the impact of the inclusion on the surrounding matrix depend on the chemical compound present into the inclusions. EDS was employed to determine the chemical composition of the critical inclusions. **The first statement shows that meanly oxide inclusions appear to be the cause of fracture**. Inclusions exhibit two major different compositions: silicon-based inclusions (95% of the inclusions) and titanium-based (5% of the inclusions). As the silicates are the most involved into the fractures, they were analysed more into details.

Three typical inclusion chemical compositions are identified: pure SiO_2 but also SiO_2-MgO and SiO_2-CaO. MgO and CaO refer to the second major component present into the inclusion. Figure 65 represents the general EDS spectrum of the three types of inclusion.

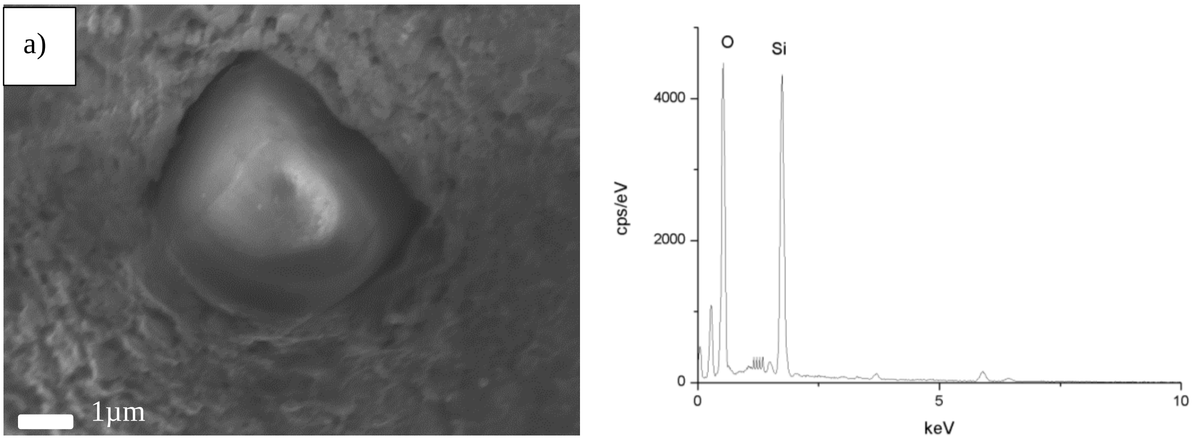

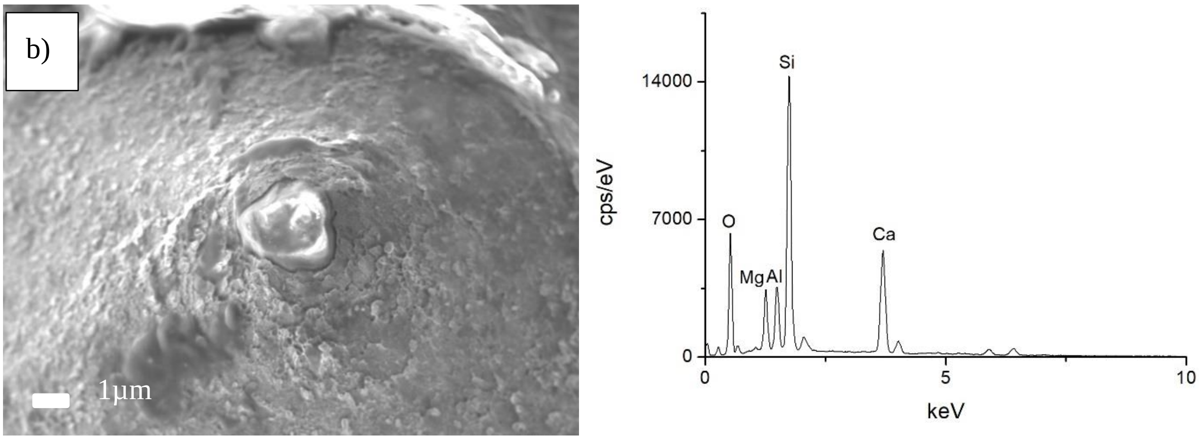

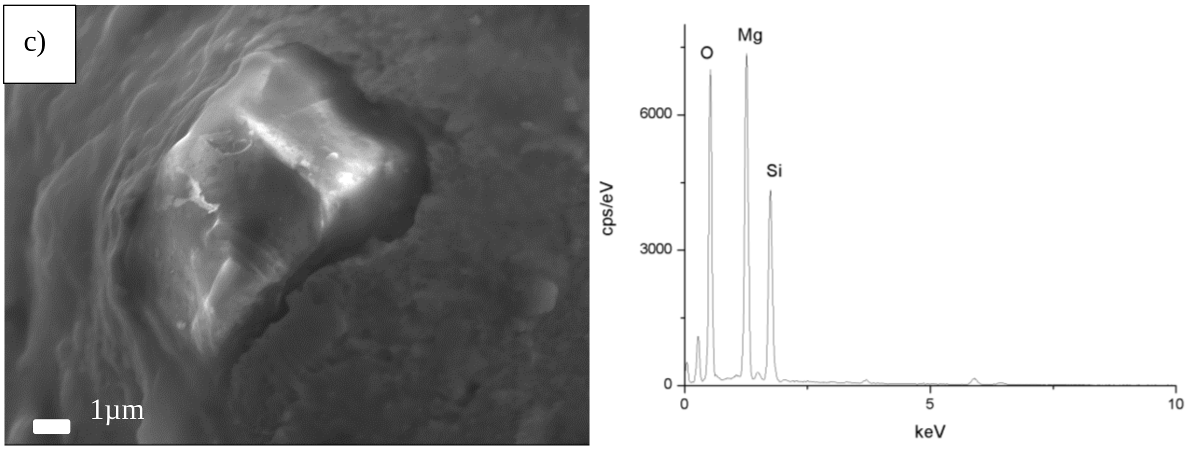

Figure 65 : Aspect of the principal inclusions responsible of fracture and the EDS spectrum associated:

a) SiO_2 b) SiO_2-CaO c) SiO_2-MgO

12.2 Size

For each fracture that still contained an embbeded inclusion, the inclusion size was measured. To have a repeatable measurement for each inclusion, the following procedure has been adopted. First, the two major axis of the inclusions were measured in order to to calculate the surface S_{inc} of the inclusion (equation 17)

$$S_{inc} = r_L * r_w * \pi \tag{17}$$

where, $r_L$is the radius of the length of the inclusion and r_w the radius of the width of the inclusion. From the area of the inclusions, the Equivalent Circular Diameter (ECD) is calculated. This function permits to classify the inclusions by their size whatever the morphology of the inclusions. It is defined as the diameter of a circle with the same area of the measured particle. It is calculated with the following equation (equation 18)

$$ECD = 2\sqrt{\frac{Sinc}{\pi}} \tag{18}$$

ECD is frequently used as a reference for the measurement of inclusions in order to compare the inclusions size independently of their morphology.

The drawback of this technique is that the size measurement depends on the apparent section of the inclusion. Meaning that if the inclusion is embedded in the steel matrix, only the visible section can be measured. It does not ensure that the measurement is done at the biggest section of the inclusion. However, the approximation is applied to both techniques: the measurement of the inclusion size on the surface by automated SEM/EDS and the measurement of the inclusion in the fracture.

The size distribution of those inclusions is presented in Figure 66.

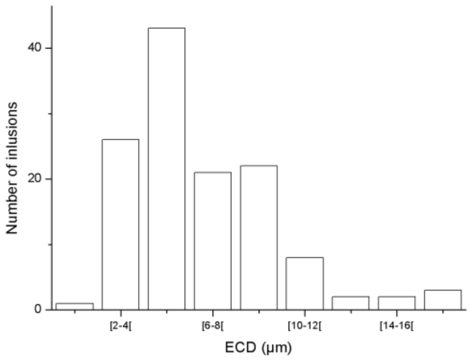

Figure 66 : Histogram of inclusion sizes estimated from measurements on the fracture surface

The range of inclusions size present into the fracture is quite spread, ranging from 2µm to 23µm in ECD size. The mean value of inclusions size is around 6µm in ECD.

12.1 3D investigation of inclusion causing fractures

The limitations of the 2D analysis on the size measurement previously reported needs to be overcome. For that, the broken wire was embedded in a Bakelite mount to observe the wire in the longitudinal direction.

The sample was then polished until the core of the fracture was reached. This method required meticulousness due to the very fine diameter of the fracture (Ø60µm). The first challenge was to be able to embed strongly the fractured wire to be resistant to the polishing step. The second challenge is to polish the broken wire until the core of the wire and the largest depth of inclusion. Figure 67 is an example of broken wire polished in the longitudinal way.

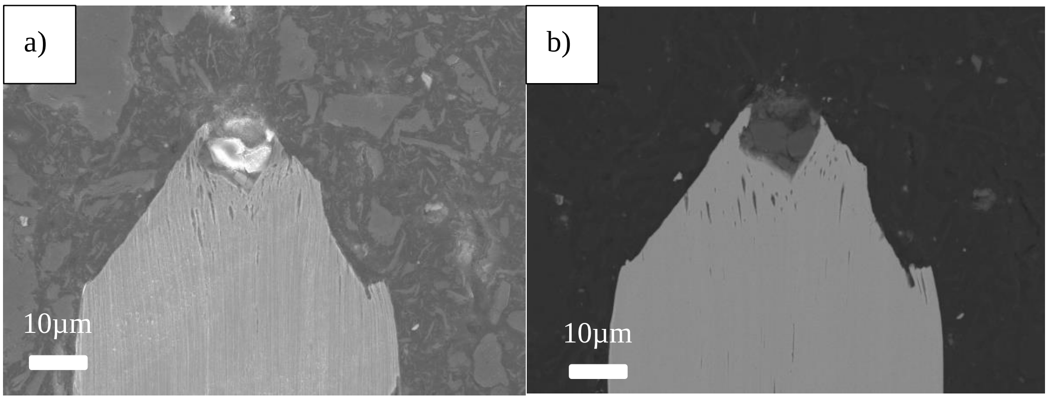

Figure 67 : SEM images of broken wire polished in the longitudinal side showing fracture due to an inclusion a) with secondary electrons, b) with backscattered electrons

Figure 67a) images the fractured wire etched with Nital solution to reveal the microstructure at the fracture point and around the inclusion. The microstructure is lightly impacted by the presence of the inclusion at the fracture point. The analysis of microstructure of drawn wire is difficult in the way that the grains are totally deformed during the drawing. The grains of pearlite are flattened in the transversal way and extended in the drawing axis.

12.2 Influence of drawing strain

Different drawing strains (ε) were applied to the filament by changing the diameter of the initial wire. As explained on section 2.4.2 the drawing strain depends on the initial and final diameter size. For these drawing trials, ε was ranging between 4 and 5.

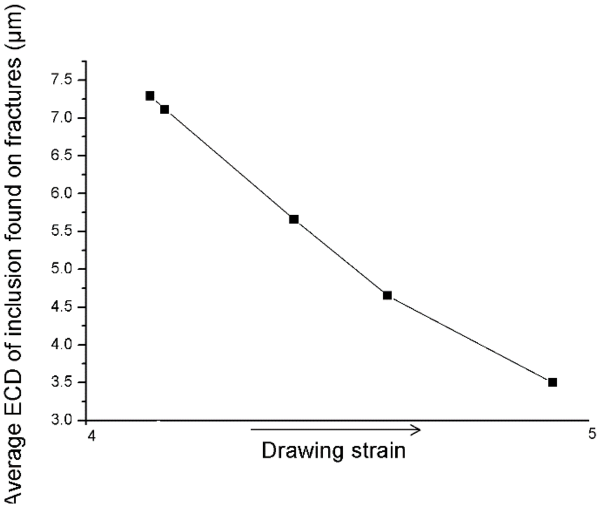

Figure 68 : Average ECD of inclusions found on fracture for different drawing strain

After these observations is could be concluded that a high drawing strain always leads to the fracture of the filaments during the wire drawing because of the presence of small inclusions (>3.5µm).

To verify this hypothesis, it was decided to draw a filament at the same drawing strain but starting from a larger diameter and ending to a final diameter of Ø0.20mm. Fractures were studied and compared to those observed in the Ø60µm filaments. A difference in morphology of fracture surface was observed for the filament with Ø0.2mm. In this wire, the fracture has not been induced by the presence of a single inclusion. This observation shows a correlation between the drawing strain and the final diameter of the wire. The cup and cone fractures are not observed anymore as it contains any visible inclusions (Figure 69).

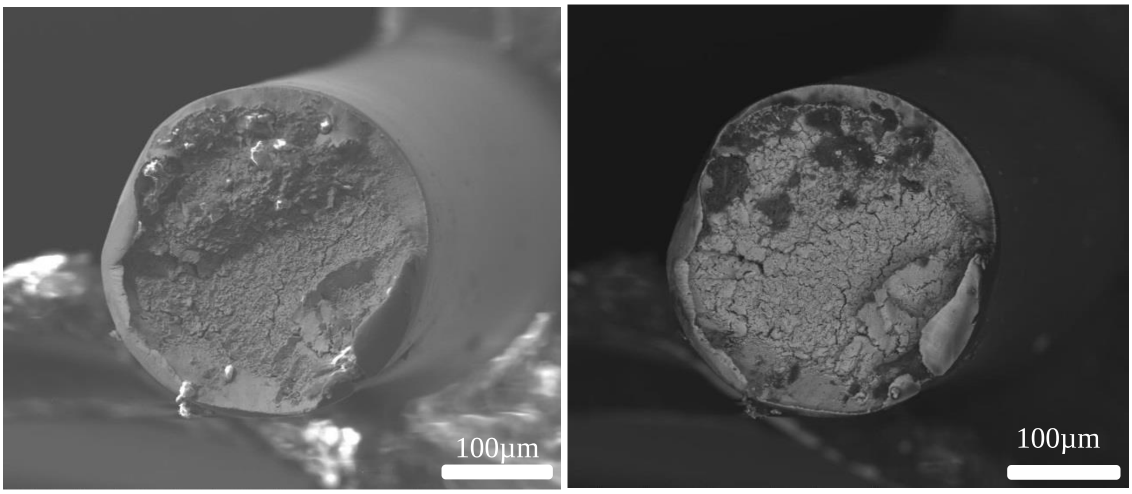

Figure 69 : SEM images of fracture obtained in an Ø0.20mm filament after wet wire drawing at high drawing strain (ε>4)

12.3 Influence of wire diameter

To study the impact of reducing the diameter of the filament, the size of the inclusions responsible of fracture was studied as a function of the diameter of the final wire after WWD (Figure 70) for the same drawing strain (ε>4). A linear trend is observed. The smallest is the final diameter of the wire, the most it is impacted by small inclusion size. From this statement, it can be concluded that the inclusion size is a decisive parameter concerning the wire drawing of fine filaments.

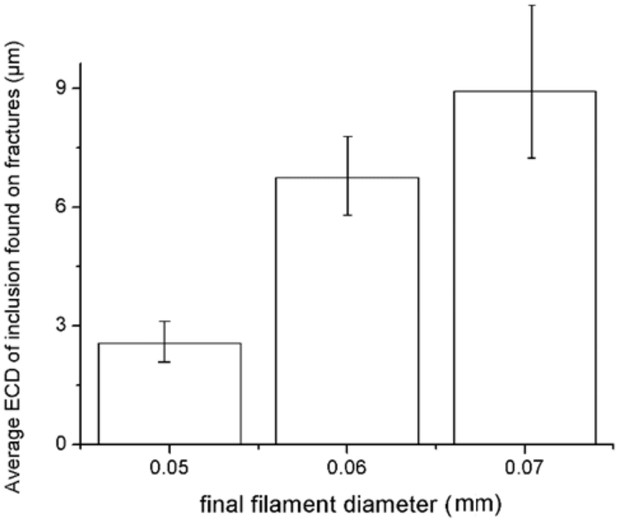

Figure 70 : Average ECD of inclusion found on fracture for different drawing final diameters

In conclusion, the size of the inclusions is an important parameter but this critical size of inclusion depends on the diameter of the final filament diameter and of the drawing strain. The ratio size vs the size of the final diameter is really important.

12.4 Influence of chemical composition on critical size of inclusions

It was observed that the final diameter of the filament and the drawing strain had an impact on the critical size of the inclusion responsible of fracture. The dependence of the critical size of inclusion and their chemical composition is questionable. As it can be noticed in Figure 71, there is a link between the chemical composition and their shape, but also on the critical size of the inclusion. The size of the inclusions found on fracture depends on their chemical composition.

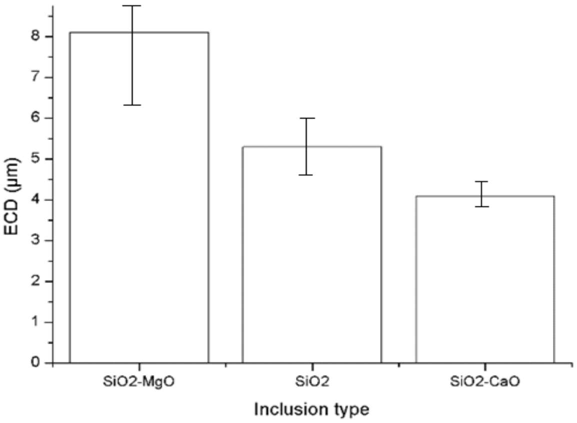

Figure 71 : Relation between the size and the chemical composition of the inclusion

For SiO_2-MgO inclusions, the average critical size is 8µm while for SiO_2-CaO the average critical size is 4µm. SiO_2 has an average critical size of 5µm. For a given drawing process, the size of inclusions responsible of fracture depends on their chemical composition. As the morphology of the inclusions is also linked to chemical composition, three parameters are involved in the fracture occurrence: the size of inclusion, the chemical composition and the morphology.

12.5 Shape of inclusions

As observed previously, the chemical composition of the inclusions has an influence on the critial size of different inclusions. The question therefore arises. Is this difference in size induced by a difference in the mechanical properties of the inclusion or its shape ?

The morphology of inclusions is expected to impact the stress distribution generated around inclusions. Some tendancies start to be observed between inclusion composition and the shape of the inclusions.

SEM images of Figure 72 show some examples of SiO_2 inclusions roughly round responsible for fractures. They are perfectly circular in each case.

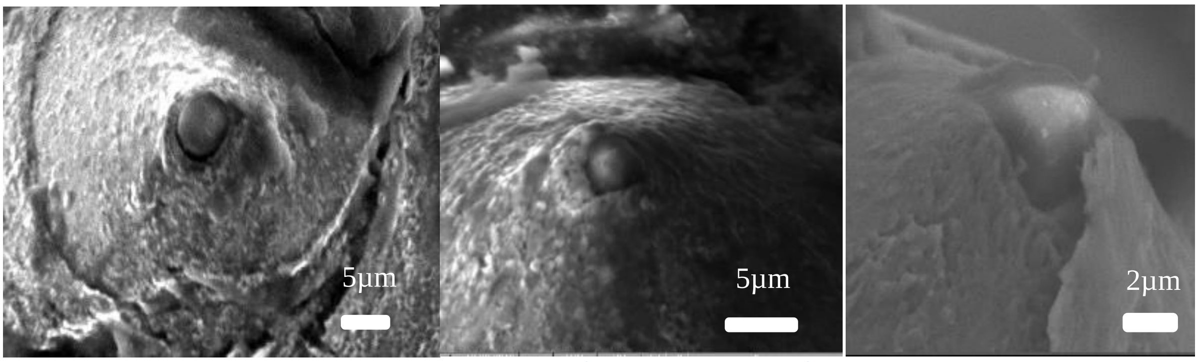

Figure 72: SEM images of SiO_2 inclusions on fractures

For SiO_2 inclusions containing Ca, they are ovoid (Figure 73), not perfectly round and not angular as observed.

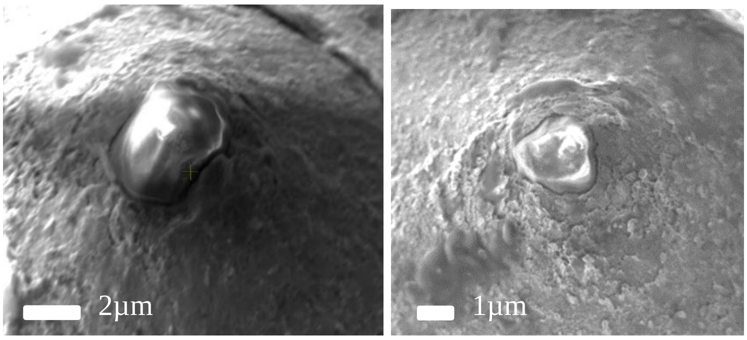

Figure 73 : SEM images of SiO_2-CaO on fractures

For SiO_2-MgO inclusions, SEM images presented in Figure 74 point out the ovoid shape. The inclusions are bigger than SiO_2-CaO and contain angles.

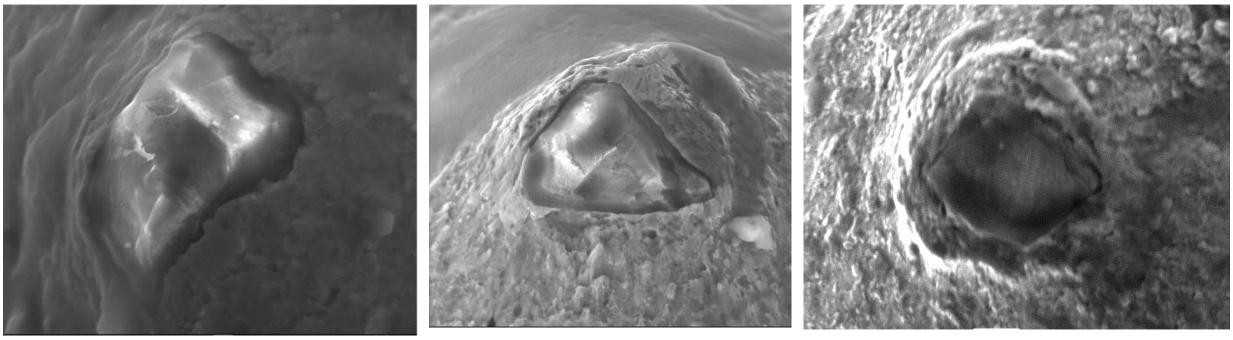

Figure 74: SEM images of SiO_2-MgO inclusions on fractures

The shape of the inclusions described from SEM observations of fractures were also identified by additionnal observations of inclusions collected with the extraction method. The morphology of the different inclusions observed after dissolution process are presented (Figure 75).

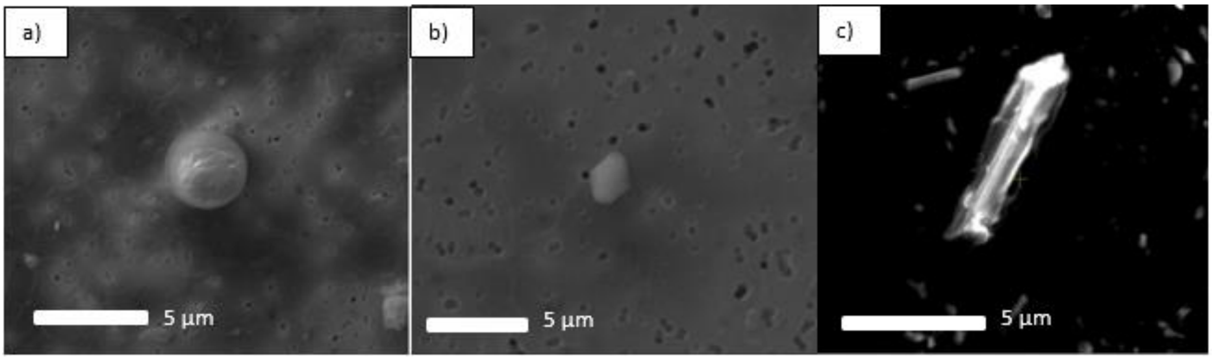

Figure 75 : SEM images of inclusions collected after filter analysis a) SiO_2 b) SiO2-CaO c) SiO_2-MgO

These observations confirm the previous observations. The SiO_2 inclusions present a spherical shape while the two other compositions present a more ovoid or elongated shape. They also differ in their aspect ratio (length/width) which values are reported in Table 17.

Table 17 : Aspect ratio of inclusions found on fractures

Inclusion type	**Average Aspect ratio**
SiO_2	1.05
SiO_2-CaO	1.26
SiO_2-MgO	1.66

The aspect ratio of SiO_2, close to 1, confirms the spherical shape of the inclusion. The aspect ratio allows the differentiation of the two others elongated inclusions and point out that SiO_2-MgO are the most elongated.

12.6 Conclusions

The inclusions responsible of fractures have been extensively studied on this part. More than 200 fractures were investigated for statistics matter.

The major conclusions are :

- 90% of the fractures occurring during WWD are related to the presence of inclusions
- Three different chemical compositions of inclusions were found on fracture : SiO_2, SiO_2-MgO, SiO_2-CaO

- The average size of inclusions responsible of fractures is 6µm which represent 10% of the final wire diameter
- The critical size of inclusions depends on the chemical composition of the inclusions
- The morphology of the inclusion also depends on the chemical composition of inclusions

Now that the inclusions responsible of fracture are fully identified, the next step is to correlate the fracture occurrence with the global cleanliness of the wire.

13 Impact of inclusions on WWD drawability

After an extensive study of the inclusions responsible of fractures, a comparison between inclusions present into the wire rod and the inclusions present onto the fractures is possible. The purpose is to make a link between the drawability of the wire and the cleanliness properties.

13.1 Influence of inclusion density

To study the influence of the oxide density on the fracture ratio obtained in WWD, the drawing of only three wires is not sufficient. To overcome this problem, the results from production were also used to evaluate the impact of inclusion density on drawability. As explained in section 11, the drawability of the wire is defined as the number of fractures per 1000km (kkm) obtained during the wet wire drawing. Below a certain threshold (Th_{inc}), the drawability is considered as good, above, the drawability is considered as non-sufficient. The experimental studies and the data from production are summed up in Figure 76.

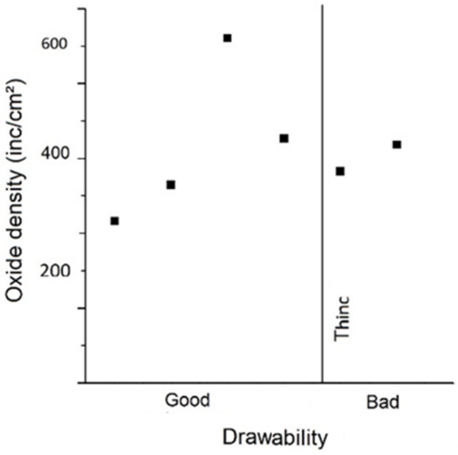

Figure 76 : Correlation between drawability vs. oxide density

Apparently, there is no obvious link between the drawability and the oxide density. A high density of inclusions does not lead to a bad drawability as one could imagine. However, the studied densities are in a too narrow range of values so it is difficult to extract some tendencies with such similar densities.

13.2 Influence of the inclusion type on drawability

With the results of cleanliness assessment of wire rod and the information on the critical inclusion on fracture during the WWD, the information can be crossed and the impact of cleanliness on drawability can be determined. For that, the usual cleanliness information (density, size and composition) are linked with the results of WWD.

Table 18 : Inclusions responsible of the fracture during WWD and critical size of inclusions

Wire rod	Inclusion types	Number of inclusions causing fracture	Average ECD (µm)	Std deviation ECD (µm)	% present in the wire rod
Wire 1	SiO_2	9	5.30	1.56	67
	SiO_2-MgO	10	6.30	1.25	17
Wire 2	SiO_2-MgO	10	8.64	3.95	48
	TiO_2	8	4.29	0.28	0
Wire 3	SiO_2-CaO	14	4.92	0.86	13
	SiO_2-CaO-MgO	9	4.99	2.18	44
	SiO_2-MgO	31	8.66	2.84	18

Wire 1 is the only wire that breaks at SiO_2 inclusions. It also breaks at SiO_2-MgO inclusions. In wire 1, it is observed that SiO_2 represents 67% of the inclusions and are responsible of 47% of the fractures while SiO_2-MgO inclusions initiate 53% of the fractures but represents 17% of the inclusions in the wire rod. For wire 1, it can be concluded that SiO_2-MgO inclusions are more critical than SiO_2 inclusions.

For wire 2, half of the fractures initiates at SiO_2-MgO inclusions and represent 48% of the inclusions present into the wire rod. The other fractures occur at TiO_2 inclusions. The amount if these inclusions were not measured on the wire rod.

For wire 3, three types of inclusions are found on fractures.

- SiO_2-CaO inclusions that represent 13% of the inclusions and are responsible of 25% of the fractures
- SiO_2-MgO inclusions that represent 44% of the inclusions and are responsible of 57% of the fractures
- SiO_2-MgO-CaO inclusions that represents 18% of the inclusions and are responsible of 16% of fractures.

From these observations, it is difficult to conclude on the impact of the chemical composition of the inclusion on the fracture occurrence. While for wire 1, it is really clear that SiO_2-MgO inclusions are more critical than the SiO_2 inclusions, for wire 2 and 3, the tendencies are less clear. It is difficult to conclude on the most critical inclusion from those experiments. Some deeper analyses have to be performed on the chemical composition of inclusion.

13.3 Influence of inclusion size

The sizes of inclusions reported in Table 13 are the average of the sizes measured for each inclusion. Inclusions containing SiO_2-CaO are in average smaller than the SiO_2-MgO as reported in section 11.4. It can be assumed that CaO present into the inclusion as an impact on the structure of the inclusions and their internal mechanical properties. SiO_2 are in average much bigger than the CaO inclusions. This tendency is observed for wire 2 and wire 3. For wire 1, the SiO_2-MgO inclusions responsible of fractures are smaller than the average SiO_2-MgO inclusions.

14 Introduction of ultra-clean wire

As the link between drawability and cleanliness is still hazardous, the idea of using a wire with completely different cleanliness properties was considered.

The remaining question is: what would happen if the wire does not contain inclusions?

Unfortunately, the design of a steel without inclusions is, with the current techniques, impossible. For our application, two high carbon steel wire rods with ultra-clean (UC) quality were developed and especially designed for this project by a steel supplier.

Table 19 shows the chemical composition of the two high carbon ultra-clean quality steels.

Table 19 : Chemical composition of ultra-clean quality wire rod

	C	**Mn**	**P**	**S**	**Si**	**Cr**	**Ni**	**Fe**
UC 94	0.95	0.31	0.007	< 0.004	0.201	0.21	0.013	Bal
UC 98	1.00	0.27	0.007	< 0.004	0.22	0.24	0.013	Bal

The comparison between ultra-clean quality and the normal qualities used for this project presents a large disparity on cleanliness assessment.

Table 20 presents the results of automated SEM/EDS analyses and combustion analyses performed on both ultra-clean and normal qualities. The ultra-clean quality wire rod reveals a considerable lower density of inclusions. The oxygen content and the inclusion density are lowered of 75% by the use of ultra-clean process. This high difference of cleanliness will allow a comparison with standard qualities and give more information about the influence of cleanliness on drawability.

Table 20 : Difference between standards and ultra-clean qualities

Supplier	**Quality**	**Carbon content (wt%)**	**Oxygen total (ppm)**	**Oxide density (inc/cm²)**
1	Wire 3	1.02	20.1 ± 2.3	474
2	UC	0.94	7.5 ± 0.5	71
2	UC	0.98	7.1 ± 0.8	64

Concerning the size of inclusions, the difference is not as clear. By comparing the size distributions, the inclusions size of the ultra-clean qualities is of the same order than the size of inclusions present on standard qualities (Figure 77). However, obviously, the probability that an inclusion with a critical size is passing through the die is lower than for the other qualities as the inclusions density is reduced by 75%.

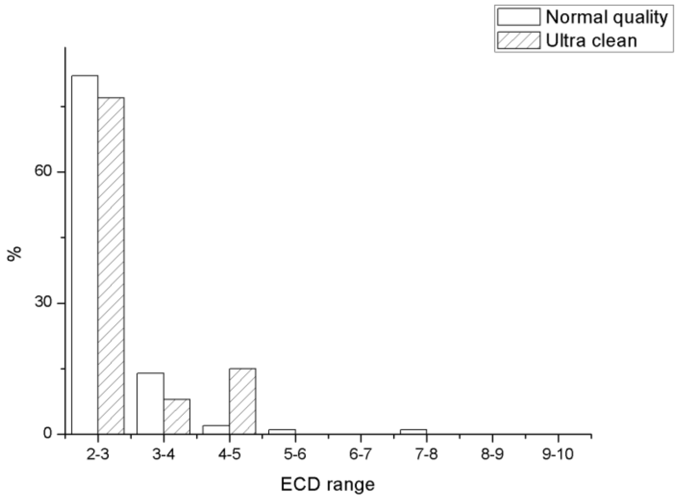

Figure 77 : Size distribution of inclusions for the normal and the ultra-clean qualities

Concerning the chemical composition of the inclusions, the difference is quite important. While the normal qualities are mainly containing pure SiO_2-based inclusions, others inclusions are found in UC quality.

The ternary diagrams of the two UC qualities (Figure 78) give a first insight of the decrease in inclusion density but show also the difference of chemical composition of the inclusions between normal qualities and UC qualities. Even a difference is observed between the two UC qualities.

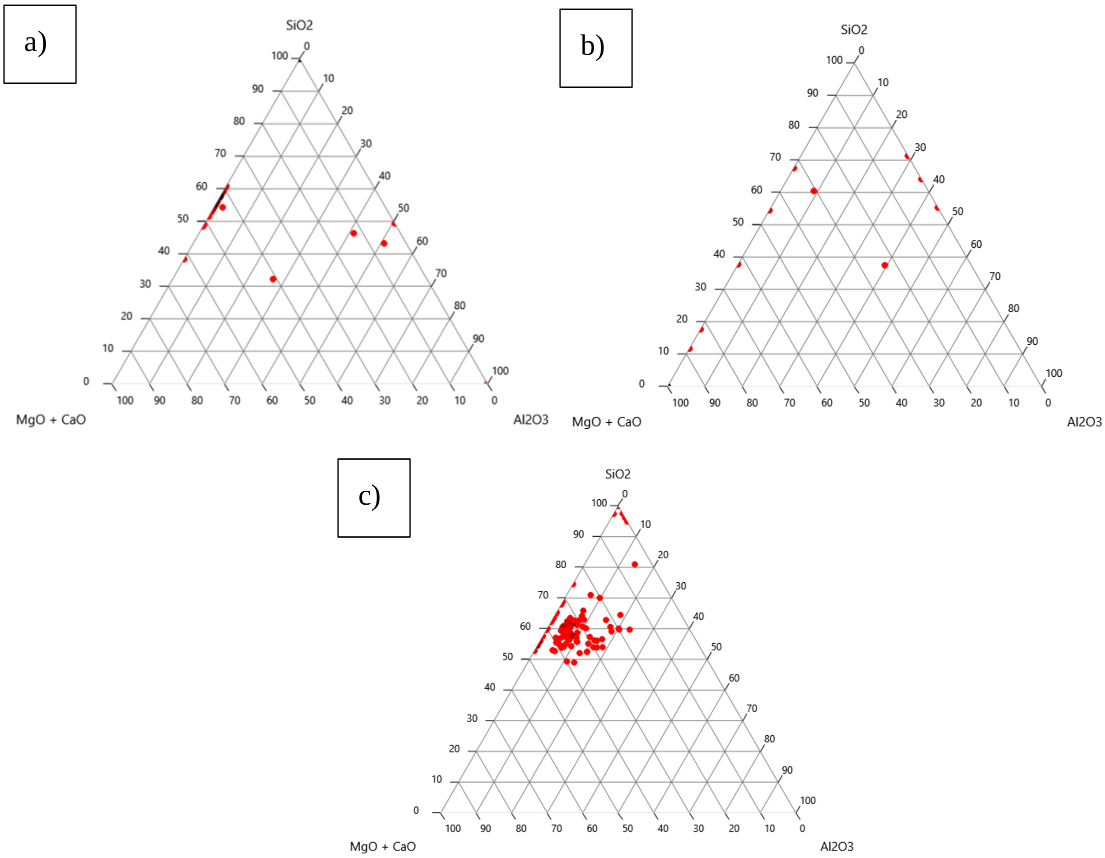

Figure 78: Ternary diagrams for a) ultra-clean 94 b) ultra-clean 98 c) standard qualities

The chemical composition of the inclusions present into the ultra-clean quality wire rods was investigated in more details (Figure 46). The first observation is the difference in chemical composition of the inclusions in the UC 94 steel and the UC 98 steel. UC 94 steel mainly contains SiO_2-MgO- and SiO_2-CaO-, while UC 98 steel mainly contains pure CaO inclusions (~50%). Another striking difference is that the ultra-clean quality contains a high amount of Al_2O_3 inclusions into the wire rod, contrary to the standard qualities. Al_2O_3 are one of the most studied inclusions in the literature.

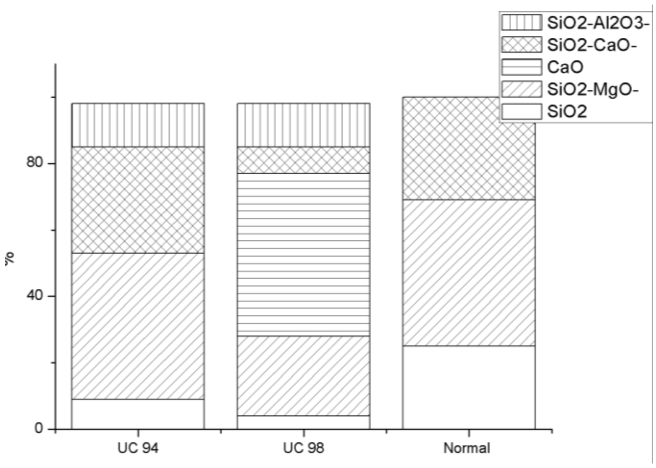

Figure 79 : Distribution of inclusions chemical composition into the ultra-clean quality wire rods

To conclude, two main differences exist between the ultra-clean quality steel and the reference steel: the inclusion density and the chemical composition of the inclusions. So the two parameters will be considered for the comparison between the standard qualities and the ultra-clean qualities.

14.1.1 Drawing trials with ultra-clean wires

To study the impact of the difference of cleanliness on the drawability of the wire, drawing trials were performed on the ultra-clean quality wires, UC 94 and UC 98. Same drawings conditions were set for both trials with ultra-clean quality and are summed up in Table 21. The purpose was to produce a spool of 240km of filaments without fractures. After three fractures, the test was stopped even if the 240km were not reached.

Table 21 : Die series and speed used for ultra-clean drawing

Parameters	**Settings**
Die series	DS1 – high angle
Speed	600 m/min

The total length and the number of fractures are presented in Table 22

Table 22 : Results of drawing trials with ultra-clean quality wires

Wire	**Total length drawn (km)**	**Nb of fractures**
UC 94	720	0
UC 98	480	0

Three spools of 240km were drawn for the UC 94 quality and two spools for the UC 98 without any fracture. These first results show that the cleanliness difference of the wire rod has a major influence on the fracture ratio. As the major difference between ultra-clean qualities and standard qualities is the inclusion density, it is concluded that the inclusion density of the initial wire rod plays an important role on the fracture occurrence. Figure 80 is an update of Figure 76 which includes the results of these experiments. The correlation between the drawability and the inclusions density appears now more clearly.

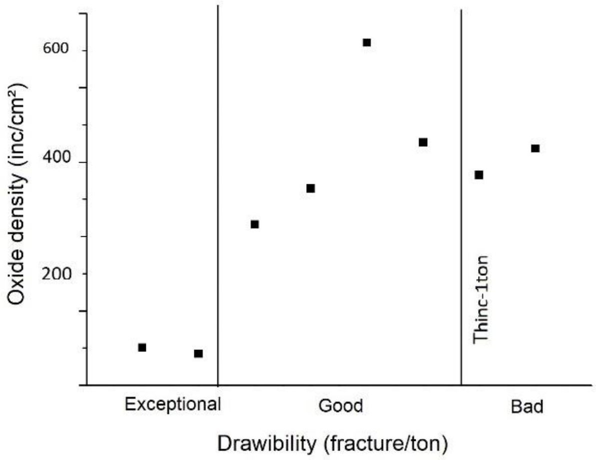

Figure 80 : Correlation between oxide density and drawability

The only clear and undiscussable point is that a very low oxide density sharply improves the drawability and a higher oxide density leads to degrade the drawability. However, there is no sharp limit under which the drawability switches from good to bad. However, the oxide density is not the only parameter governing the number of fractures obtained during WWD but also inclusions or drawing parameters.

- Influence of inclusions chemical composition

Concerning the influence of the chemical composition of the inclusion, the non-occurrence of fracture caused some trouble to evaluate this parameter. To be able to observe the inclusion responsible of fracture, the WWD drawing process was modified and the ultra-clean wires were drawn until a diameter of 50µm instead of 60µm. As the wire is subjected to a higher drawing strain, the probability to obtain fracture during the WWD is increased. This change of parameters leads to several fractures summed up on the Table 23.

Table 23 : Fractures with ultra-clean quality for drawing of Ø50µm filaments

Wire rod	Inclusion types	Number of inclusions	Average ECD (µm)	Std deviation ECD (µm)
UC 94	SiO_2-CaO	8	3.68	0.84
	At free inclusion matrix	7	/	/
UC 98	CaO	1	2.20	/
	SiO_2-CaO	15	3.47	1.00
	Hole	1	4.92	/
	At free inclusion matrix	1	/	/

For UC94 filaments, half of the fractures was initiated by an inclusion, mainly SiO_2-CaO inclusions, which are not the most numerous in the wire rod (Figure 79). Indeed, SiO_2-CaO inclusions are responsible of 53% of the fractures but only represents 32% of the inclusions. The most numerous inclusions, SiO_2-MgO that represents 45% of the inclusions, did not lead to fracture. In this case, the SiO_2-MgO inclusions are less critical for wire drawing than the SiO_2-CaO one. So it is clear that the volume fraction of inclusions does not govern by itself alone the drawability.

For UC 98 filaments, one fracture is caused by a pure CaO inclusion. Nonetheless, CaO inclusion represents 50% of the inclusions present into the wire. For SiO_2-CaO inclusions which leads to 90% of the fractures, they only represent 7% of the inclusions in the wire rod. It appears that CaO inclusions are less critical for the wire drawing than the SiO_2-CaO inclusions in this particular case.

From the literature, the melting temperatures of SiO_2-CaO or CaO are respectively 1544°C and 2570°C. This difference in melting temperature, as explained on section 4.1, expresses a difference in deformability. From the melting temperature of the inclusions, the conclusion would be that the CaO inclusions are less deformable than the SiO_2-CaO ones and thus, be more critical than the SiO_2-CaO during the WWD drawing. The results of the experimental trials related the opposite behaviour. The SiO_2-CaO inclusions seem more critical than the CaO inclusions. Again, one has to take into account the size of inclusions.

Table 18 contains the size of inclusions in the UC98 steel measured in the wire i.e. before drawing and measured on the fractured filament i.e. after drawing. It is observed that the CaO inclusions leading to the fracture is smaller than the SiO_2-CaO found on fractures. In comparison with the SEM/EDS measurements of the inclusion into UC 98 wire rod, the difference of criticity is also explained by the size of each inclusion type. In the wire rod and on fractures, in average, the size of the SiO_2-CaO inclusions is greater than the CaO inclusions as presented in Table 24.

Table 24 : Inclusions properties on ultra-clean 98 measured by SEM/EDS on wire rod and inclusion responsible of fracture during WWD

	ECD (µm)	
	Wire rod (before drawing)	Fractured filament
SiO_2-CaO	3.31 ± 0.10	3.47 ± 1.00
CaO	2.40 ± 0.35	2.20

The fracture at a certain inclusion is not only governed by the chemical composition of the inclusions but also by the size of the inclusion present into the wire rod. **It exists a critical size for each inclusion types.**

14.2 Conclusion

The drawing trials on the ultra-clean quality wire pointed out several tendencies.

- The density of oxide inclusions plays an important role. Very good drawability requires a very low density of oxide present in the wire.
- Concerning the influence of inclusion types on the fracture occurrence, it is difficult to conclude from these trials. The major statement would be that it exists a critical size of inclusion for each inclusion type.

15 Analysis of inclusions on non-fractured filaments

After studying the inclusions involved into the fractures and found that the type and the size of inclusions are linked, the question is the following:

What are the characteristics of inclusions that did not lead to fractures during the WWD?

To have a clearer view of the impact of wire drawing on inclusions and vice-versa, inclusions present on fine filaments were studied.

The observations were done on the longitudinal section of the wires. As for wire rod, longitudinal sections were analysed to study the elongation of inclusion along the drawing axis and to study the impact of the localization of the inclusion. The analysis of the chemical composition of the inclusions and their size in non-fractured filaments were performed with a SEM-EDS analysis to obtain information on inclusions size.

15.1 Influence of chemical composition of the inclusions

From SEM-EDS analysis, it appears that the inclusion chemical composition in the non-fractured filaments was comparable to the inclusion chemical composition in fractured filaments.

15.2 Influence of inclusion size

The measurements of the inclusions size in non-fractured filaments were performed manually applying the same technique than that employed for the fractured filaments. 100 inclusions have been studied. Figure 81 presents the difference in size of inclusions between fractured and non-fractured filaments.

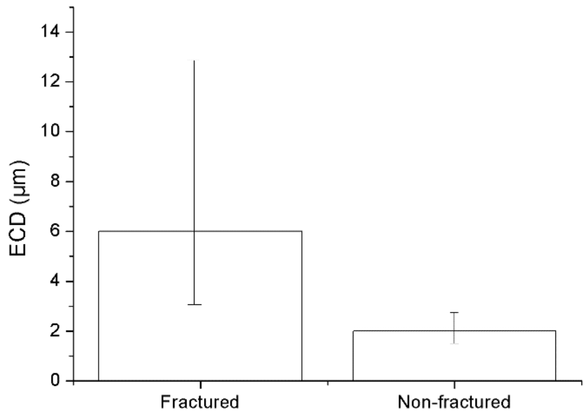

Figure 81 : Size of inclusions on fractured and non-fractured filaments

The size of inclusions observed in the filaments displays a significant difference according to the filament was broken or not. As explained on 12.2, the inclusion size present into the fracture is around 6µm, while the inclusions present into the non-fractured filaments are mainly small inclusions where the average size is around 2µm, maximum 3µm. The first statement is that it exists a critical size around 3µm above which the inclusion become dangerous for WWD.

However, the automated SEM/EDS measurement technique is not applicable on Ø60µm filaments as it is difficult to obtain a plain analysable surface from a filament of Ø60µm. The analysis of inclusion has to be done manually measuring each inclusion one by one. This technique is time consuming and in terms of statistics is difficult to obtain comparable results between Ø5.5mm and Ø60µm filaments. The length of the analysed sample has to be multiplied by 90 to obtain the same analysed area which is in practice not possible.

In view to improve the statistics concerning inclusion size, the dissolution technique has been used to observe the inclusions not responsible of fracture.

The filaments were dissolved with the acid dissolution technique. Approximately one gram (24 meters) of non-fractured filaments was dissolved. The brass coating was removed chemically before the dissolution. To have more information, the dissolution was performed also on the intermediate filament of Ø60µm. The size distribution of inclusions obtained after automated SEM/EDS analyses of the filter is shown on Figure 82.

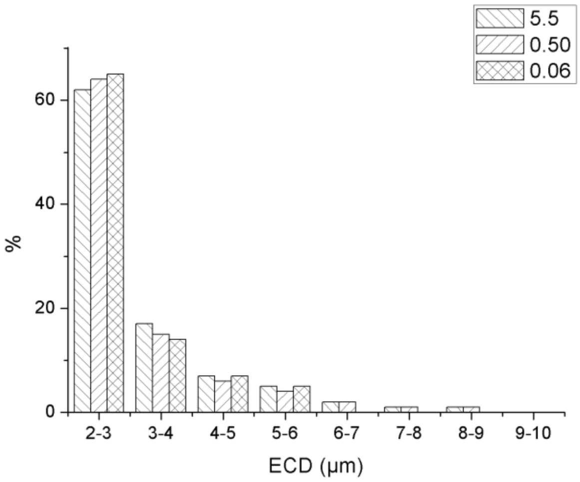

Figure 82 : Size distribution of inclusion at different steps of the process measured after dissolution of the wire

The size distribution measured after dissolution of the wire with different diameters shows slight difference. For the filament of Ø0.06mm, the inclusions measured are slightly smaller. While inclusions of 8µm in size are found on both Ø0.50mm and Ø5.5mm wires, only inclusions of 5µm in size are found on the filaments Ø0.06mm. From that statement, two conclusions can be drawn.

The first conclusion is that the size distributions are slightly different but comparable for all the diameters. From that, it can be concluded that the inclusions inside the wire rod do not fracture during the different drawing steps. If the inclusions had fractured during the drawing steps, the peak of the distribution would be different. Son secondly, one can conclude that the size of inclusions is not modified during the drawing.

In addition, the size of inclusions present in the filaments is bigger than the one observed by SEM/EDS. Therefore, the fact that only 2µm size inclusions are observed on longitudinal section of Ø60µm filaments is just a question of statistics.

15.3 Conclusions

With the analysis of the inclusions present into the non-fractured filaments, it can be concluded that:

1. The chemical composition of inclusions present into the wire rod and the final drawn filament is similar
2. The size of inclusions present into the wire is similar at the different steps of the process allowing us to conclude that the inclusions are not fractured during the drawing process.

16 Conclusions

Three wires provided by the same supplier used for the WWD trials were presented and analysed.

The wires exhibited some differences of quality and carbon content.

These three different wires were subjected to the same drawing tests, to evaluate their performance.

The fractures obtained during the drawing allow us concluding about the critical inclusions for wire drawing.

1. The inclusions present on fractures are oxides inclusions.
2. Three different types are predominant: SiO_2, SiO_2-MgO and SiO_2-CaO.
3. The size of the critical inclusions is in average around 6µm that represents 10% of final diameter.
4. The critical size of the inclusion depends on the chemical composition of the inclusions.
5. The fractures mainly happen in the last drawing pass when the diameter is the finest.

If we compare the critical inclusions with the analyses of the wire rods, the influence of the different cleanliness characteristic can be evaluated.

The oxide density, in a first place, does not seem to influence the drawability. However, after the development of an ultraclean quality wire, it was proved that the reduction of 75% of the oxide density leads to a drastic reduction of the fracture ratio.

However, it can be concluded that it exists a critical size for each type of inclusion.

For the size, it was measured that the size distribution of the inclusions stayed equivalent during at different steps of the drawing process, demonstrating that the inclusion did not fracture during the drawing process

Learning points:

1. **Inclusions present on fractures are oxides inclusions**
2. **Three different types are predominant: SiO_2, SiO_2-MgO and SiO_2-CaO**
3. **The size of the critical inclusions is in average around 6µm that represents 10% of final diameter.**
4. **The critical size of the inclusion depends on the chemical composition of the inclusions.**
5. **The fractures mainly happen in the last drawing pass when the diameter is the finest**
6. **A drastic reduction in oxide density allows a sharp reduction in drawability**
7. **It exists a critical size for every inclusion type**
8. **There is no difference of chemical composition between the inclusions present in the wire rod and the final filament**
9. **The inclusions do not fracture during the drawing process**

Chapter IV : Impact of drawing properties on fracture occurrence

The previous chapter clearly pointed out that the inclusions have a great influence on the fracture occurrence during the drawing process. It also showed that the chemical composition, the size and the density of inclusions notably influence the fracture ratio.

The question now is: for a given cleanliness, what is the influence of drawing parameters on the fracture occurrence?

As explained in section 2.2, the drawing parameters have a notable impact on the strain distribution along the cross section of the wire. It is therefore relevant to consider how these parameters affect the fracture occurrence.

17 Study of the influence of drawing parameters on fracture occurrence

17.1 Settings of the experiments

Experiments on a drawing machine have been performed to study the influence of drawing parameters on the drawability of the wire. Several parameters have been studied. To avoid the impact of cleanliness difference on the results, the same wire rod has been used for all the experiments. Wire 3 was selected for the tests. The chemical composition of the wire rod is described in Table 25.

Table 25 : Chemical composition of the wire rod used for online experiments (wt%)

C	Mn	P	S	Si	Cr	Ni	Fe
1.02	0.3	0.007	0.007	0.2	0.19	0.01	balance

Three parameters have been studied.

The first parameter is the microstructure of the intermediate wire. The intermediate wire refers to the wire deformed and patented, used for the wet wire drawing process. The wires have been patented at two different temperatures in view to modify their microstructure. To respect the confidentiality, the value of the temperatures will not be reported in the present document. These patenting temperatures aimed at providing a high tensile material (HT) and a low tensile material (HT) and will be referred in this way.

The mechanical and microstructural properties of the two wires have been studied and compared to understand the impact of each of them on the fracture occurrence. Three different tests have been performed on the two intermediate wires:

- Tension tests to evaluate the mechanical properties of the wires
- Torsion tests to evaluate the ductility and the resistance to shear stress
- Hardness tests

The interlamellar spacing was also measured since ILS is known to greatly affect the mechanical properties (Yield stress) of the pearlitic wire.

The results of the different tests are presented Table 26.

Table 26 : Mechanical properties and ILS of the LT and HT wires

Sample ID	UTS (MPa)	E (MPa)	YS (MPa)	Rp 0,2 (MPa)	Number of torsions	Hardness (Hv)	ILS (µm)
HT	1548 ±2	194314	1064	1127	31 ± 3	492 ± 8	0.075±0.012
LT	1479 ± 1	191004	970	1042	39 ± 3	471 ± 10	0.080±0.012

The strain-stress curves obtained from the tensile test are plotted in Figure 83.

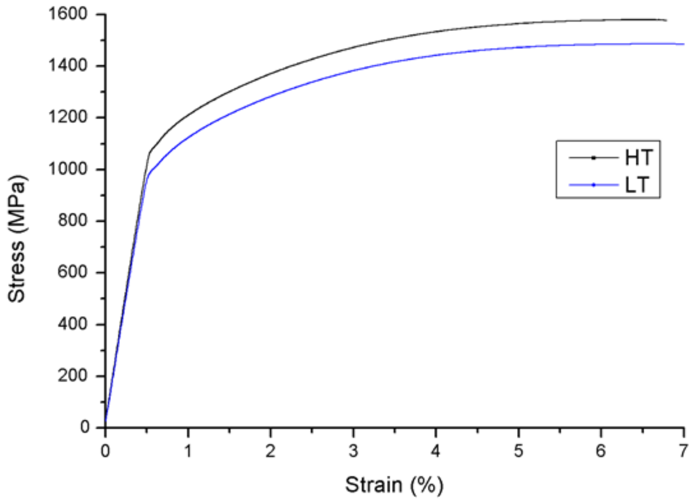

Figure 83 : Strain stress curves for HT and LT wires

Expected from the difference of thermal treatments, the mechanical properties of the two intermediate wires are different. The Young modulus is obviously not affected by the difference of heat treatment. An increase of 70MPa in UTS is measured in the HT material as compared to LT material.

As the consequence of high mechanical resistance of the HT wire, the ductility and the shearing aptitude (torsion test) is lower for the HT intermediate wire. As mentioned in chapter 5.4 the ductility of the material allows a better deformation during the drawing step. A higher ductility leads to a greater capacity of deformation of the wire. The higher hardness of HT wires agrees with the higher fracture ratio obtained for HT wires.

- Microstructure

For both intermediate wires, the microstructure was observed by SEM. The micrographs (Figure 84) shows a fully pearlitic structure obtained after the two heat treatments. By eye, no difference of microstructure is observed between the two intermediate wires.

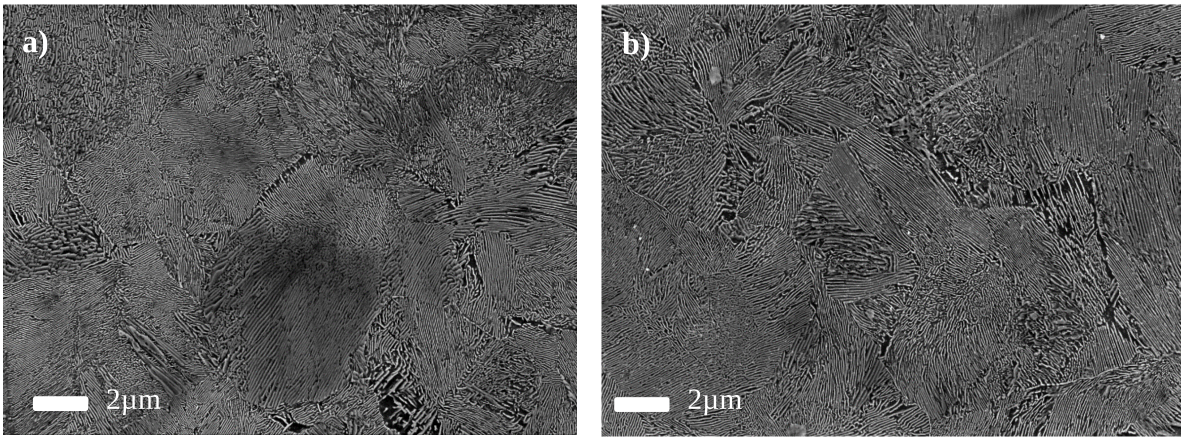

Figure 84 : Microstructure of intermediate wires a) HT wire b) LT wire

To have a representative measure, the ILS was measured for ten lines per picture, for 10 pictures, so an average of 100 measurements. Taking into account the standard deviation of the measurements, there is no difference in ILS between HT and LT materials.

The second studied parameter is the die series used for WWD process. Die angle is known to affect the fracture occurrence [74]. A lower die angle reduces the stress induced into the wire during the pass. This difference in stress plays a role on damage degree induced around the inclusion. The experiments have been performed with die series of different die angles. DS1 refers to a die series with high angle while DS2 refers to a die series with low angle.

The third parameter studied is the drawing speed. The speed of drawing is known to influence several parameters. A high drawing speed induces a lower friction coefficient. As the temperature increases, the lubrication is better and less stresses are engendered at the surface of the material. The higher temperature also influences the dynamic ageing. As the temperature increases during the process, the dynamic ageing is more important at higher speed. Ageing in wire promotes the dissolution of cementite into the ferrite phase which leads to a softening of the matrix. The mechanical properties of the final filament can be affected by this dynamic ageing.

Three different speeds have been tested for each wire and die series: 200,400 and 600m/min

For the online tests, the purpose was to draw a length of 100km. After three fractures, the test was stopped even if the desired length has not been reached. The total lengths of drawn filament were reported and the fractures collected for further investigation.

17.2 Results of the experiments

The test parameters and the results of the experiments are reported in Table 27.

Table 27 : Results of online experiments

Material	Die series	Speed (m/min)	Total length drawn (km)	Nb of fractures
HT	DS1	200	26.656	3
		400	5.201	3
		600	19.158	3
	DS2	200	31.707	3
		400	19.652	3
		600	27.944	3
LT	DS1	200	72.697	3
		400	100	2
		600	100	2
	DS2	200	100	0
		400	100	0
		600	100	1

It can be seen that the wire properties have an inconsiderable importance on the fracture ratio. With the HT wire, the length of filament never reached the 100km. The three fractures occurred at maximum before the 30km. For the LT wire, a large difference is observed on the results. For five of the six conditions, the required length of drawn wire was reached. The number of ruptures obtained with the LT wire is considerably reduced compared to the HT wire. The total lengths drawn for HT and LT materials add up and are respectively 130km and 573km. The fracture ratio for HT and LT materials are respectively 13.8 fractures/100km and 1.4 fractures/100km, so a reduction of 85% of the fracture ratio.

The results of drawing tests also show an influence of the die angle on fracture occurrence. With the high angle series, the total length of wire drawn was 324km, compared to a total of 380km for the low angle die series i.e. an increase of 17%. The fracture ratio per 100km is respectively 4.9 and 2.6 for high and low die angle, so a reduction of approximatively 50% of the fracture ratio

The influence of the speed is not obvious to comment with just a look on the drawing test results. A lower number of fractures is observed at high speed (600m/min) and the number of fractures decreases from low speed to high speed. On the contrary, for low die angle and LT, high speed is the only condition that leads to a fracture. To conclude from those results would be hazardous. The previous conclusions have been stated from the distance and the number of fractures obtained after the drawing. A deeper analysis is then performed on fracture analysis.

17.3 Fracture analysis

The 26 fractures occurred during the drawing experiments have been analysed is view to determine their cause. It was observed that inclusions were responsible of 92% of the fractures, which corresponds to the same ratio previously obtained for all the different wire rods and tests.
As for the pre-study, the fractures and the inclusions are analysed by SEM-EDS in terms of size and chemical composition.

17.3.1 Influence of die angle

The number of fractures and the average size of inclusions responsible of the fracture are presented in Table 28 according to the die series.

Table 28 : Influence of the die series on the number of fractures and the critical inclusion size

Die series	**Nb of fractures**	**Average of ECD (µm)**
DS1	16	6.43
DS2	10	6.29

The low angle dies series (DS2) leads to a low number of fractures, 10 compared to 16 for DS1. The average of critical sizes of inclusions is respectively 6.43 and 6.29 for DS1 and DS2. It cannot be concluded that the size of critical inclusions is impacted by the die series change.
In conclusion, a lower angle die reduces the fracture ratio but not the critical size of inclusions.

The chemical composition of the critical inclusion is reported in Table 29. It can be observed that both die series involve the same inclusions with the same amount in the fracture of the wire.

Table 29 : Influence of the die series on the critical inclusion chemical composition

	DS1	**DS2**
SiO_2-MgO	5	5
SiO_2-CaO	5	4
Hole due to the presence of an inclusion	4	1
At free of inclusion matrix	2	0

17.3.2 Influence of speed

The same study was conducted to understand the role of wire drawing speed on fractures. In Table 30, it is observed that the number of fractures is equivalent for the different speeds. However, the size of inclusions found on fractures of the filament depends on the drawing speed. A difference of 2 microns in average is observed between the highest and the lowest speed. Therefore, it is so difficult to conclude about the influence of drawing speed on the fracture occurrence. However, from a statistical point of view, these information should be confirmed.

Table 30: Number of fractures and inclusion sizes for different drawing speeds

Drawing speed (m/min)	**Number of fractures**	**Average of ECD (µm)**
200	9	7.88
400	8	5.01
600	9	5.84

The chemical composition of the critical inclusions is reported in Table 31. No obvious tendencies can be observed regarding the speed of drawing. For 200m/min, the fracture was sensitive to SiO_2-MgO inclusions and few sensitive to SiO_2-CaO inclusions. The opposite trend is observed for the speed of 400m/min. For 600m/min, the ratio between the two inclusions is equal. Again, it is also not possible to conclude on the influence of the drawing speed on the fracture occurrence.

Table 31 : Influence of the drawing speed on the critical inclusion chemical composition

	200 m/min	**400 m/min**	**600 m/min**
SiO_2-MgO	5	1	3
SiO_2-CaO	2	5	2
Hole due to the presence of an inclusion	2	2	2
At free of inclusion matrix	0	0	2

17.3.3 Influence of wire properties

It is visible than the number of fractures decreases abruptly for the different intermediate wires (Table 32). As the two intermediate wires came from the same wire rod, it can be assumed that the inclusions density is the same for LT and HT materials.

Nevertheless, the size of the inclusions leading to fractures during the WWD for both intermediate wires exhibits a large difference in the critical value (Table 32). The average sizes of inclusions leading to fracture for HT and LT materials are respectively 5.25µm and 8.92µm. Although the global cleanliness of the two intermediate wires is identical, a difference in the critical size is observed (Table 32). This suggests that the mechanical and microstructural properties of the intermediate wire influence greatly the critical size of inclusions. Therefore, by adapting the heat treatment of the wire, the fracture ratio can be reduced. As the probability to encounter a 5µm inclusion is higher than to encounter a 9µm inclusion, the fracture ratio is deeply impacted.

Table 32 : Number of fractures and critical inclusion size for HT and LT materials

Wire	**Nb of fractures**	**Average of ECD (µm)**
HT	18	5.25
LT	8	8.92

The chemical composition of the inclusions involved in the fractures is reported in Table 33. The fractures occur preferentially at SiO_2-CaO inclusion for HT material and at SiO_2-MgO for LT. This difference can explain the disparity of size between HT and LT.

Table 33 : Chemical composition of critical inclusions involved in fracture of LT and HT materials

	HT	**LT**
SiO_2-MgO	5	4
SiO_2-CaO	7	2
Hole due to the presence of an inclusion	5	1
At free of inclusion matrix	1	1

17.4 Deeper understanding of the influence of the drawing parameters on fracture and filament behaviour

The control of the drawing parameters as the die series enables the reduction of the fracture occurrence. Nonetheless, even if the objective is to reduce the fracture ratio during the WWD, an important goal is also to attain a high tensile strength in Ø60µm filaments. The drawing parameters can be adapted to meet the length expectation but the mechanical properties of the final filament have to be considered. Tensile tests have been performed on the drawn filaments of Ø60µm for each condition. The influence of the thermal treatment has also been considered. The results of the tensile strength performed on the different filaments are presented in Table 34. A difference of 124MPa in average is observed between the filaments obtained from the low temperature and high temperature heat treatments and drawn with the similar conditions.

The die angle is also having a strong impact on mechanical properties of filaments. In average, the disparity between DS1 and DS2 is 183 MPa. In this case, a lower die angle leads to a higher resistance of the filaments. It means that using a die with a small reduction angle decreases the fracture ratio during drawing and also improves the mechanical strength of the filaments. It has been reported that the mechanical properties are improved for certain die angle mainly due to ageing phenomena [74]. Regarding the impact of drawing speed, no obvious tendency can be observed concerning UTS.

Table 34 : Effect of process parameter on Ultimate Tensile Strength of the Ø60µm filaments

	Die series	**Speed (m/min)**	**UTS (MPa)**
HT	DS1	200	4716
		400	4739
		600	4751
	DS2	200	4934
		400	4951
		600	4934
LT	DS1	200	4610
		400	4680
		600	4633
	DS2	200	4783
		400	4792
		600	4828

To conclude, the use of a low angle die series allows a reduction of 50% of the fracture ratio and high mechanical properties of the filaments.

Another drawing parameters pair to consider is the mechanical properties of the entrance wire and the die angle. The internal forces applied during drawing are a factor of this difference. Indeed, there is a strain gradient through the filament. The edge of the wire is subjected to shear stress resulting from the contact of the die and to tension stress from the machine during wire drawing. However, the centre of the wire is more subjected to tension and less affected by shear. This generates a gradient of strain into the wire which can explain the difference in the behaviour of the wire during wire drawing and the occurrence of fracture at inclusion located in the centre. The nano-hardness test has been used to investigate the zone affected by shear strain. A local gradient of deformation can be pointed out by a local difference in mechanical properties such as hardness and Young modulus. Nano indentation tests have been performed on the cross section of filament to measure the gradient of mechanical properties. The speed, the die angle and the two intermediate wires were studied. The measurements were performed on a Nano-Indenter XP with a Berkovich tip indenter. The maximum load of 8mN was applied at a rate of 1.6mN/s. In each measurement, the maximum load was held for 2s before being released at the same rate. Indentation spots were separated by 6µm as represented in Figure .

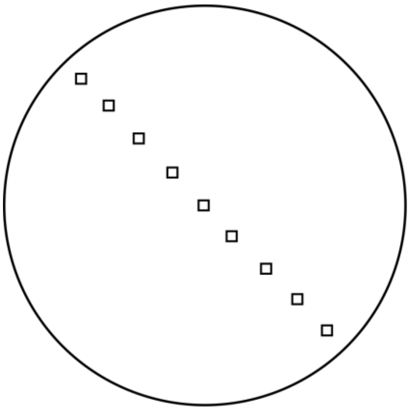

Figure 85: Schematic of the nano-hardness indentation along a diameter of a 60µm filament

First, the influence of the patenting temperature on the mechanical properties is studied. The difference between LT and HT materials is studied after drawing at a constant speed of 200m/s for both die series. The results are presented in Figure 6 with a) for the filaments drawn with DS1 and b) for the filaments drawn with DS2.

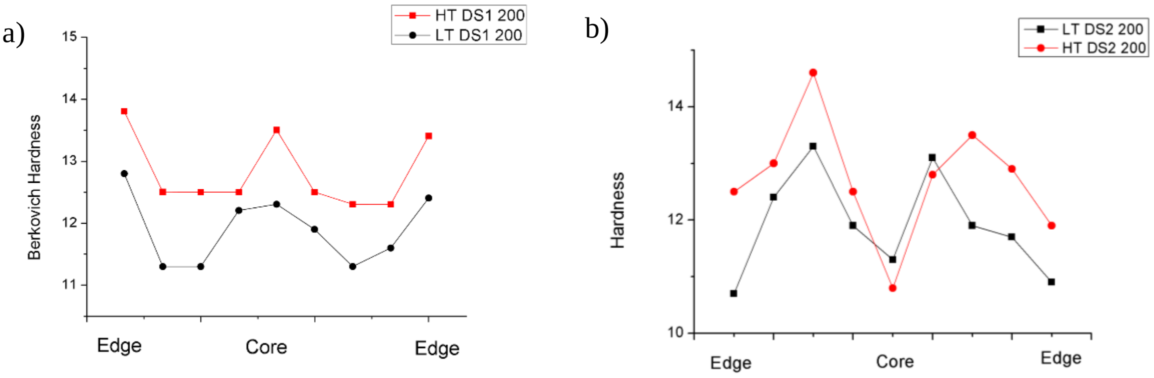

Figure 86: Influence of mechanical properties of the wires on the hardness profile of the filaments a) for DS1 b) for DS2

Figure 6 confirms the highest averaged values of hardness for material. The variation in hardness along cross section depends on the die series and not on the difference of wire mechanical properties. Using the DS1 die (high angle) results in a more marked difference in hardness between HT material and LT material than by using the DS2 die (low angle).

Additionally, as presented in Figure 7, the die series affect the location of the highest hardness value. Using the DS1 die series, the edge and the core of the wire present a higher hardness compared to the intermediate zone. For the wire drawn with DS2, the centre and the edge of the filaments present a lower hardness while the maximum value is between them. It underlines that with the use of DS2, the central part of the wire is less impacted on the core. This behaviour can explain the difference in mechanical properties between filaments drawn with DS1 and DS2 but also the reduction of fracture ratio with the use of a low angle die series.

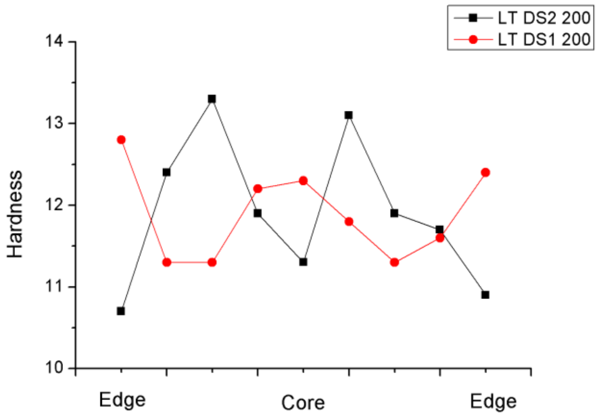

Figure 87: Influence of the die series on the hardness profile of the filaments

To study the influence of the drawing speed, three different LT filaments drawn at a speed of 200, 400 and 600m/s were studied. The other parameters were kept constant (treatment temperature and DS1). The results of nano indentation tests are presented in Figure 88

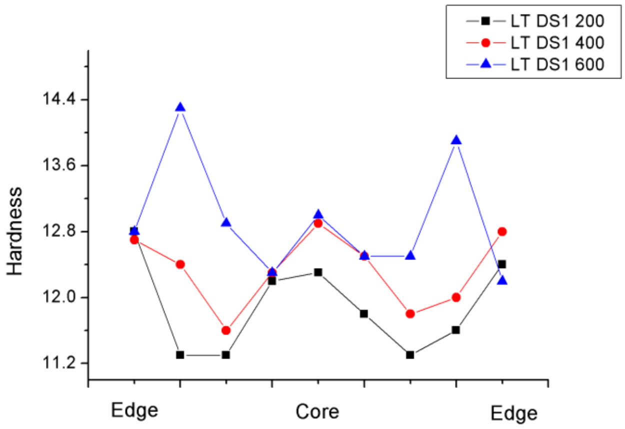

Figure 88 Influence of drawing speed on hardness profile of LT filament

Increasing the drawing speed results in an increase of average value of hardness. The location of hard zones is at the edge and at the centre of the filament drawn at a speed of 200 m/s and 400 m/s. The lowest hardness value is observed in the transition zone. For 600m/s, the tendency is different. The transition zones exhibit the highest value of hardness. This can be explained perhaps because of a promoted dynamic ageing due to higher temperature during the drawing.

However, even if tendencies can be observed, the results have to be considered with a critical analysis, as no repeatability of measurements has been performed. Because the equipment was not available at Bekaert, we had a limited access to external equipment.

18 Conclusions

The steel cleanliness has a major influence on the drawing capabilities. A single inclusion can lead to a fracture. Anyhow, for same cleanliness properties, the fracture ratio can be influenced by adapting the drawing parameters.

The mechanical properties of the wire and the heat treatment strongly affect the fracture occurrence and can lead to a reduction of fracture ratio around 85%. The critical size and chemical composition of inclusions leading to fractures change with the wire characteristics.

The die angle used for wire drawing impacts the fracture ratio. By decreasing the die angle of the die series about 2°, the fracture ratio decreases about 50%. In another hand, the critical size of the inclusions is not impacted by the die angle change.

Concerning the drawing speed, the conclusions are not so clear and do not seem to influence the fracture occurrence.

In terms of mechanical properties of the drawn filament, it is observed that the reduction of the die angle improves the tensile strength.

The die angle also results in a change of stress repartition along the filaments diameter which can explain the difference of fracture occurrence.

Learning points:

For same cleanliness properties, the drawing parameters have an influence on the fracture ratio. The mechanical properties of the intermediate wire and the die angle are proved to influence this fracture ratio

A lower die angle series is helping to reduce the fracture ratio but also to improve the mechanical properties of the resulting filament.

Chapter V : Impact of an inclusion during the wire drawing

After the previous observations on the link between the critical inclusions and the drawing process parameters on the fracture occurrence, the role played by the inclusion itself on the fracture of wire remains confused. The influence of the chemical composition and of the inclusion size has been proven. Nonetheless, the exact role played by the inclusion on the mechanical properties of the steel matrix during the wire drawing needs to be more investigated.

Hence, the current part focuses on the behaviour of the matrix surrounding the inclusion.

First, the micro-cracks, which may appear around the inclusions will be studied to understand more into details what are their occurrence modes and which parameters promote their occurrence.

The influence of interface properties between the inclusions and the surrounding matrix will be studied. Finally, the local deformation of the matrix around the inclusion will be investigated by means of both modelling and experimental observations.

19 Micro-cracks around inclusions

19.1 On final filaments

The non-fractured filaments were analysed in order to compare the difference between the critical inclusions and the inclusions that did not lead to fracture during the WWD.

In order to identify the impact of drawing on the non-fractured filaments, the samples were embedded and polished to be observed by SEM/EDS. Here, the main idea was to identify and measure the inclusions which are not critical during process and to compare them with the critical inclusions found on fractures.

The SEM observations allow identifying two different behaviours. While some inclusions are not deformed and totally embedded and surrounded by the matrix free of micro-crack Figure 89 a.), some inclusions are inducing cracks (Figure 89 b.).

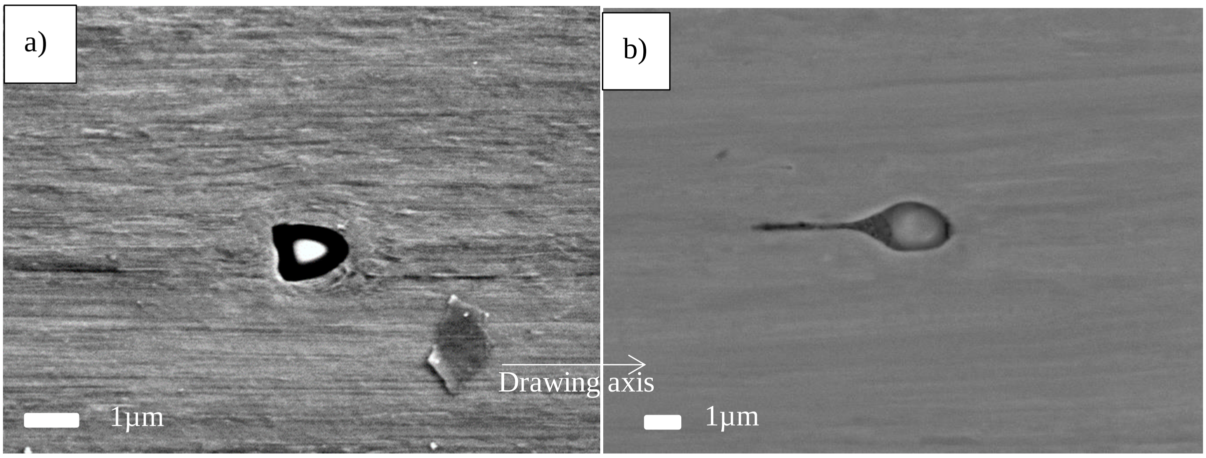

Figure 89: SEM picture of inclusions a) embedded in the matrix without cracking b) inducing a micro-crack

Those results are similar to observations reported by Yu et al. [75] on a rolling trip steel of 304 stainless steel. Indeed, the inclusions shape after WWD is comparable to the deformation of inclusions after hot rolling, as presented in Figure 850. In that latter case, elongated cracks are observed around the inclusion.

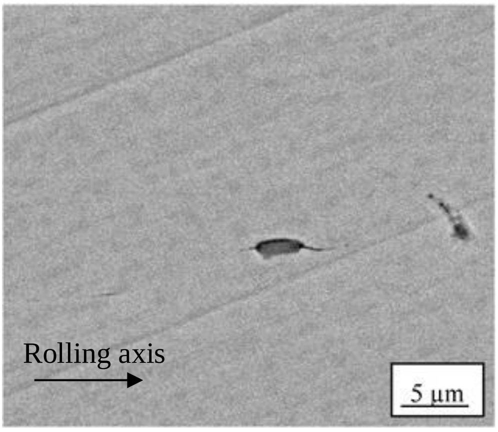

Figure 850 : SEM image of cracks around hard inclusions in strip steel [75]

In the case of a weak adhesion, cracks are initiated at the extremity of the inclusion along the deformation axis. Yu et al. [75] also studied by FEM the impact of inclusion shape and size on the ability to form cracks during rolling (Figure 91). Hard inclusions are always accompanied by cracks whatever the shape and the size of the initial inclusion. For spherical and square inclusions, the cracks opening occurs on both sides of the inclusion along the rolling axis. By contrast, triangular inclusions only induce crack at one of the angles.

In a same manner, the elongation of deformable inclusions follows the deformation of matrix independently of their initial size. By contrast, for hard inclusions, the size of the cracks is always relative to the size of the inclusions. This point is interesting as the encountered inclusions during the WWD process of the pearlitic steel are hard inclusions.

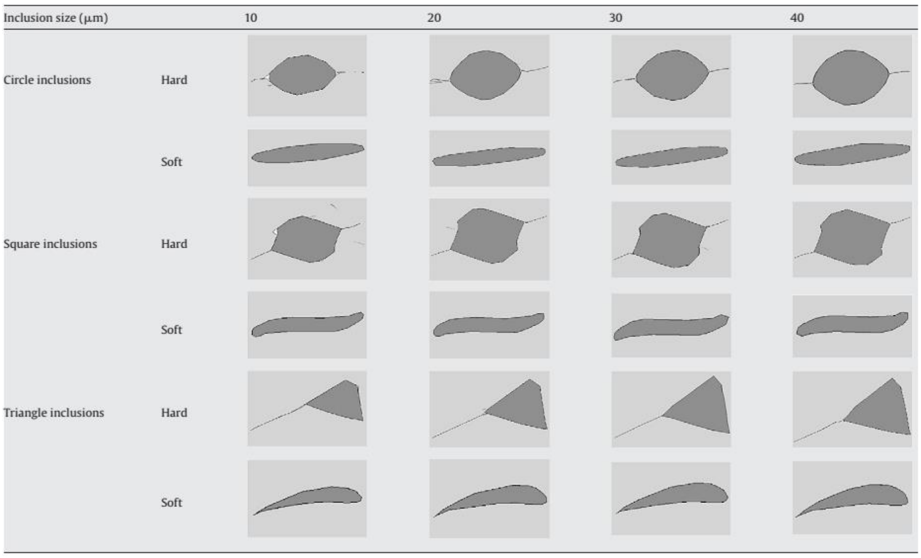

Figure 91 : Relationship between the inclusion and the matrix after rolling for various inclusion sizes [75]

When comparing both forming processes, the occurrence and the size of cracks around inclusions during fine filament drawing are much greater compared to the one occurring during rolling. This can be explained by the strain levels corresponding to the considered processing route (ε=0.3 for rolling and ε=4 for the fine filaments drawing). This can also explain why, in the case of the filaments, cracks are growing around much smaller inclusions (Ø=1µm) compared to hot rolling.

Based on the analysis of the micro-cracks surrounding the inclusions, some important deductions arise.

First, the cracks around inclusions are always parallel to the drawing axis. This gives additional indications about the fracture mode. If the WWD process would generate exclusively a normal stress, the cracks around the inclusion would grow perpendicularly to the drawing axis. The fact that the cracks around inclusions grow parallel to the drawing axis means that the stress is a combination of normal stress and shear stress. It can also be concluded that the fracture mode at inclusion point cannot be assimilated to the mode I fracture, but to the mode II. The crack extension does not result from opening but from sliding at the inclusion side.

In order to validate this hypothesis, the final Ø60 µm filaments were submitted to uniaxial tensile test. 15 tensile tests have been performed on the filaments and the corresponding fracture surfaces were investigated by SEM images. The typical encountered fracture surface is presented Figure 862.

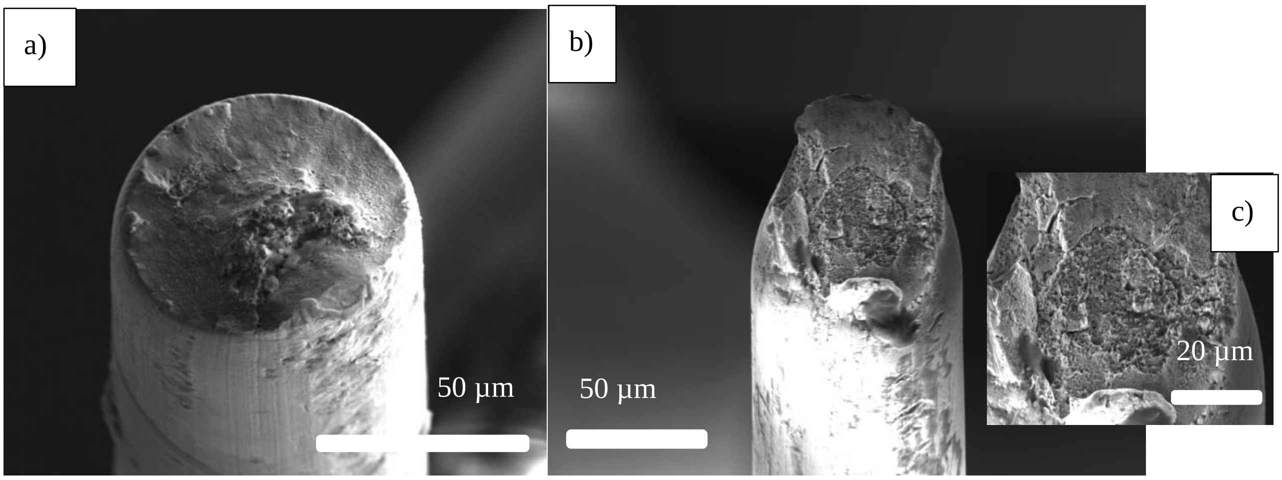

Figure 862: Fractures of Ø 60µm filaments under tensile test

The fracture is more likely ductile and no inclusion emerges or let a mark on the fracture surface. The inclusion is no more responsible of the fracture. In a Ø60µm filament under pure tensile stress, the inclusion is no longer the weak point as observed previously in the fractured wires obtained during WWD where the inclusion was on the centre of a cup and cone fracture.

For the present drawing process, it is found than 35% of the inclusions presented cracks at their surroundings. Not all the inclusions present into the filament lead to crack initiation.

To understand the parameters that promote the occurrence of these micro-cracks around inclusions, a statistics study has been performed on 100 inclusions surrounded by such cracks in 60µm filaments. The studied parameters were:

- The type of inclusions
- The size of the inclusion
- The size of the crack
- The localisation of the inclusions into the wire

To measure the size of cracks induced by the inclusion, the cracks from both sizes of the inclusions were measured as presented in Figure 873. The total length of cracks is the sum of the distance A and B.

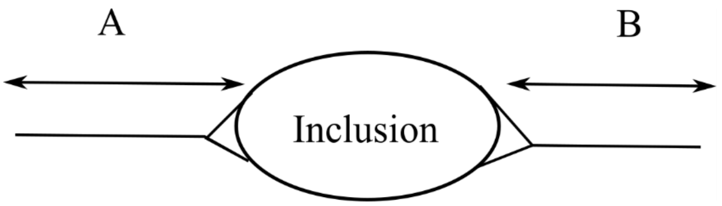

Figure 873: Measurement of the size of cracks induced around an inclusion

a) Influence of the inclusion type

It was proven in chapter III that the type of inclusions has a great impact on the fracture occurrence. As a complement, the present section focuses on its influence on the crack size. As the distribution of the different types of inclusions is equivalent, 25 inclusions of each type were considered for the statistical analysis. The corresponding occurrence of cracks and their size are reported in Table 35. No significant difference can be noticed between the different inclusion types on the crack occurrence. Same trends are observed for the size of the cracks induced around the inclusions. A difference of 1µm between SiO_2 and SiO_2-CaO inclusions is considered as not significant taking into account the standard deviation.

Table 35 : Influence of inclusion type on crack occurrence and crack size

	Occurrence of crack	**Size of the cracks (µm)**
SiO_2	40%	5.95 ± 4.52
SiO_2-MgO	42%	6.89 ± 5.21
SiO_2-CaO	38%	6.21 ± 4.96

b) Influence of the size of the inclusion

The size of the cracks is measured as a function of the size of the inclusion independently of the type of inclusion. The results are plotted in Figure 884.

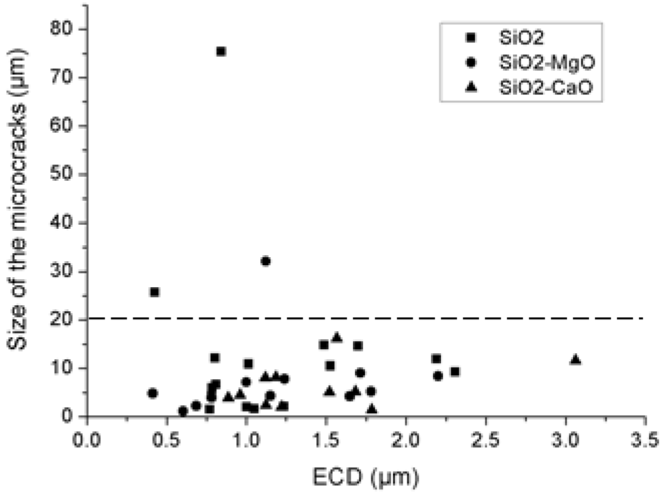

Figure 884: Influence of inclusion size on cracks size initiated around inclusions

The cracks induced around inclusions do not appear to be linked to the size of the inclusion. Some long cracks are introduced around small inclusions. However, the crack size is in general lower than 15 µm. An example of a crack size superior to 15µm is presented in Figure 895.

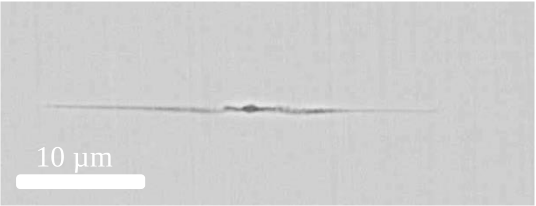

Figure 895: Example of a micro-crack longer than 15µm

The maximum size of crack observed is 75µm with an apparent crack of 38µm in front and 37µm behind the inclusion. These cracks were originated from a 1µm apparent diameter inclusion. Even if the inclusion mean size is different from the one of the critical inclusions responsible of fracture (6µm in average), the cracks introduced around the small inclusions exhibit a consistent size. Moreover, those cracks never propagate along the transversal axis.

c) Influence of the localisation

Because there is a stress variation through the cross section of the wire, it can be assumed that the cracks induced around the inclusions depend on the localisation into the wire. Therefore, the occurrence of cracks was studied along the wire diameter. .

It was first considered to study the distribution of inclusions and micro-cracks around inclusion in 3 dimensions. The use of X-ray tomography has been first considered. However, the spatial resolution of the apparatus made it impossible to distinguish the inclusions. To overcome this lack of 3D information, a statistical study of the localisation of the cracks along the diameter was performed. The wires were polished parallel to the wire length until a section of 60µm ± 3µm width. The section was divided in three zones (A, B, C) of same size (20µm), as presented in Figure 906.

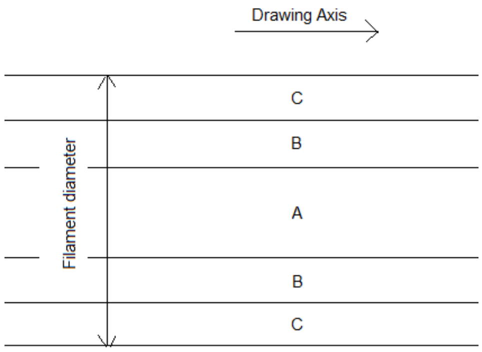

Figure 906: Schematic of separation of zones during filament study

The A, B and C zones correspond respectively to the centre, intermediate zone and outer ring of the wire. The number of inclusions has been counted on each zone and reported in Table 36.

Table 36: Repartition of the inclusions over the different zones

	A	**B**	**C**
Inclusions with cracks	11	13	11
Inclusions without cracks	24	27	14
Total	**35**	**40**	**25**

The quantity of micro-cracks differs from zones A, B and zone C. In zones A and B, about 32% of the inclusions were decorated by micro-cracks compared to 44% for the zone C. This shows that the zone under shear stress is more prone to initiate crack than zone under tensile stress.

A relevant parameter is also the size of the induced cracks. The micro-cracks around the inclusions are located in the front and backside of the inclusion. Table 37 summarizes the average length of the micro-cracks as well as their maximum and minimum lengths. While the amount of micro–cracks is greater in zone C than in zone A and B, their length, induced by drawing is higher in the zone A (Table 37). This is coherent with the higher tensile strain or shear level applied in the centre of the wire. This statement prove that the shear stress promotes the occurrence of this micro cracks while the tensile strain favour the increase of the crack size. Zone B appears to be optimum with a moderate shear and tensile stress level. This leads to a low amount of cracks with short lengths.

Table 37 : Size of crack in the different zones of the wire

	Average of total size of cracks (µm)	**Maximum length of cracks (µm)**	**Minimum of total size of cracks (µm)**
A	16.73 ± 21.64	75.36	3.93
B	6.54 ± 4.92	16.18	1.18
C	6.57 ± 4.95	14.75	1.41

From these complete data on the final filament, indicating that cracks evolution seems dependent for the stress repartition, one question still remains. When do these cracks start during the drawing process?

19.2 Occurrence of cracks during the WWD process

In order to have clear evidences of how cracks initiate around inclusions, at the end of the online trials performed in chapter IV, the machine was stopped. With this operation, a paternoster was obtained. This corresponds to an in-process wire passing through all of the different dies of the process. Then, samples of different diameters were collected between the different dies. With this process, the deformation of the wire can be studied after each pass of the WWD. For more sets of data, paternosters were obtained for two different die series i.e. two different die angles and for the high tensile (HT) filament.

From this paternoster, samples with different diameters and submitted to different drawing strains were collected. In addition, the reduction per pass was the same for the two considered die series, so the same filaments diameters are obtained and are comparable.

Five different steps of the paternoster were compared to study the influence of both die angle and drawing strain. The micro cracks at different drawing strains were studied. The characteristics in terms of drawing strain and percent of reduction for the selected wires are summarized in Table 38. To investigate the local distribution of the strain for the different process steps as well as the nucleation of micro cracks, the wires from paternosters were observed at different drawing strains ranging from ε=0 to ε=4. For statistics, 50 inclusions were observed and analysed by SEM.

Table 38 : Selected wires from the paternoster

Diameter (mm)	Drawing stain (ε)	% of reduction
0.60	0	0
0.30	1	40
0.20	2	60
0.10	3	80
0.07	4	90

Figure 917 represents the relative amounts of inclusions inducing cracks for the different drawing strains.

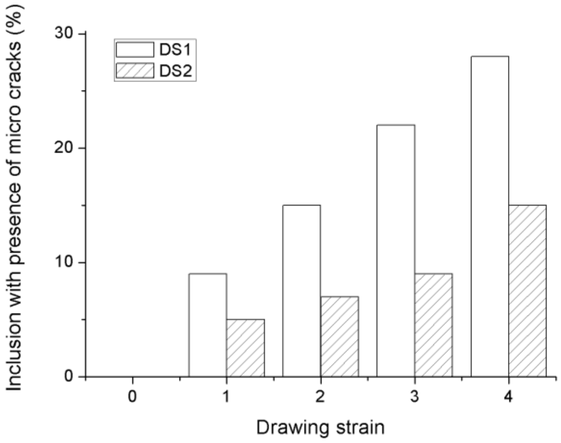

Figure 917: Percentage of inclusions inducing cracks for the different drawing strains

For the non-drawn wire, the inclusions do not present visible surrounding cracks. Nonetheless, the occurrence of cracks starts early in the drawing process. From ε=1, the decohesion between inclusions and the matrix occurs. For both die series, the multiplication of micro-cracks around inclusions is correlated with the increase in drawing strain. By contrast to the DS2 series (lower die angle), using the DS1 series results in a higher ratio of micro cracks surrounding inclusions.

The size of the cracks measured for both die series are reported in Table 39.

Table 39 : Average size (µm) of micro-cracks around inclusions for different drawing strains and different die series

Drawing strain	**DS1**	**DS2**
0	0	0
1	0.6	0.7
2	1.8	1.4
3	3.5	2.8
4	5.4	4.6

The measurement of the cracks length underlines the impact of the die series. The mean crack length tends to be lower for the DS2 series. However, the significance of such measurements is difficult to evaluate as the measure itself can be tedious. Indeed, two typical observations as presented in Figure 928. The measurement of the crack length as shown Figure 928 a) is easy since a line is following the inclusion. The defects shown Figure 928 b) are different as a part is closed and parallel to the wire matrix while another part is clearly open and a decohesion between the inclusion and the matrix is perceptible. In that latter case, the difficulty is to estimate if the decohesive zone and/or the total length of the cracks observed must be measured.

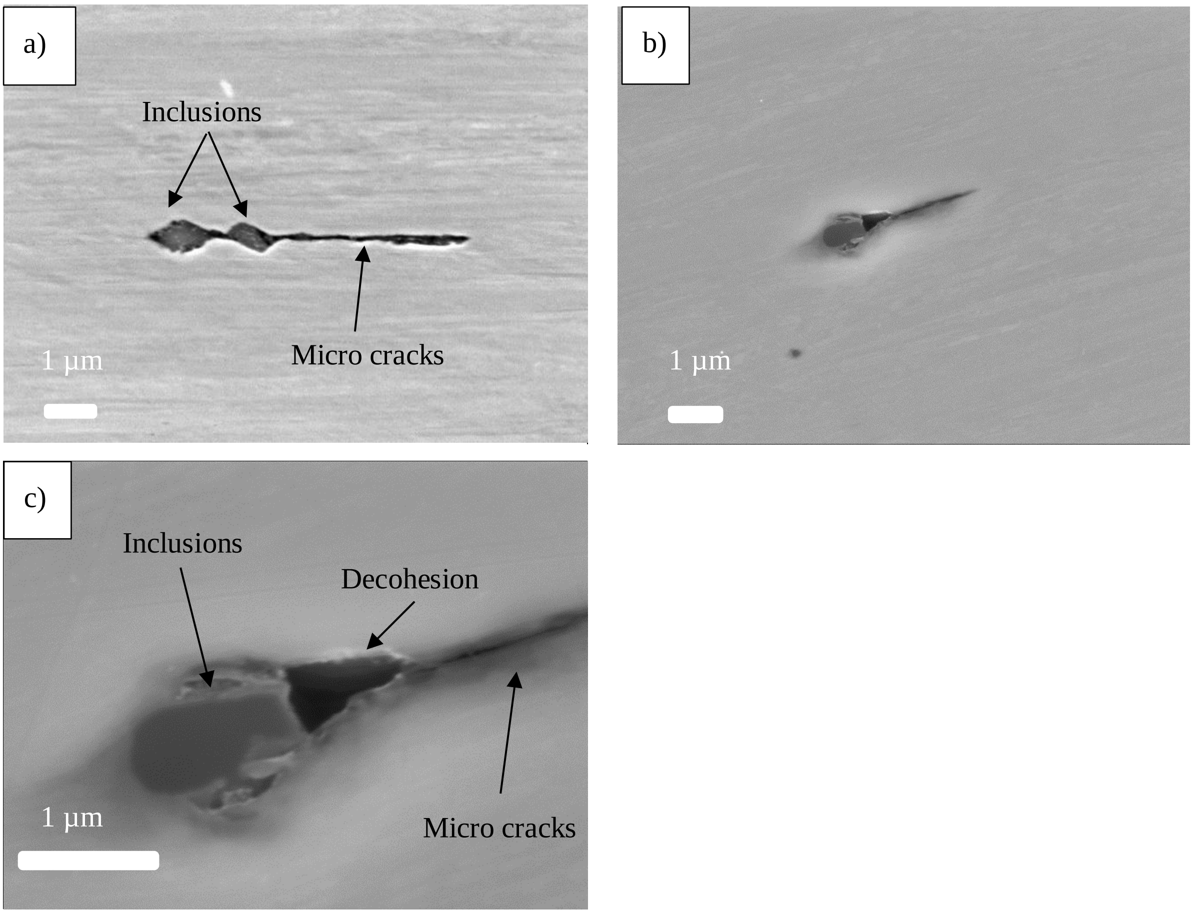

Figure 928: SEM images of example of occurrence of cracks a) without decohesion b) c) with decohesion

In order to solve this issue, a comparison with the state of art in case of rolling can be made. For rolling, this behaviour has also been noticed and explained by Figure 99. The decohesion starts at the edge of the inclusion along the rolling direction and grows. Then, with the compressive forces induced by the rolling, the opening is flattened and the crack takes the appearance of a line.

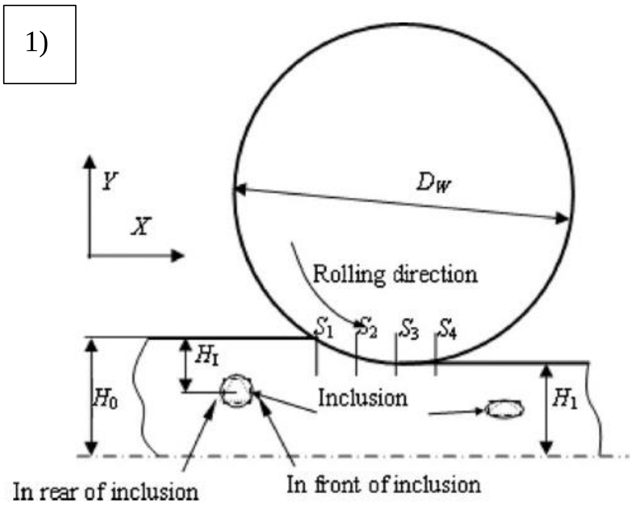

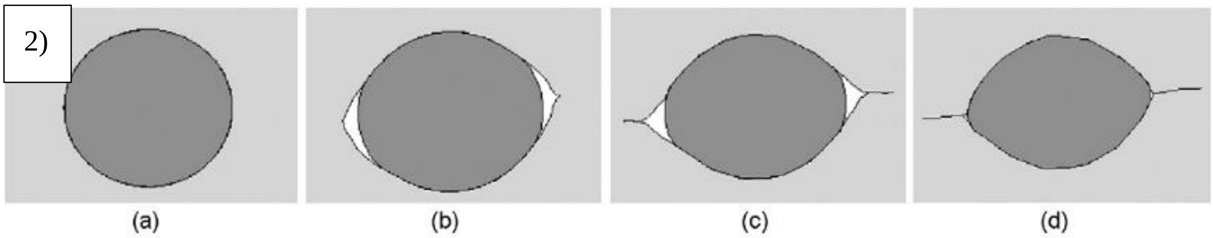

Figure 99 : 1) Schematic drawing of strip rolling with an inclusion 2) Relationship between the inclusion and the strip matrix in S1 (a), S2 (b), S3 (c), and S4 (d) position during rolling [75]

Regarding the present case, i.e. for WWD, the decohesion occurs whatever the shape of the inclusions (round, ovoid or straight) (see Figure 930). There is no preferred shape that promotes the decohesion between the inclusion and the matrix, which contradicts the results obtained in chapter III.

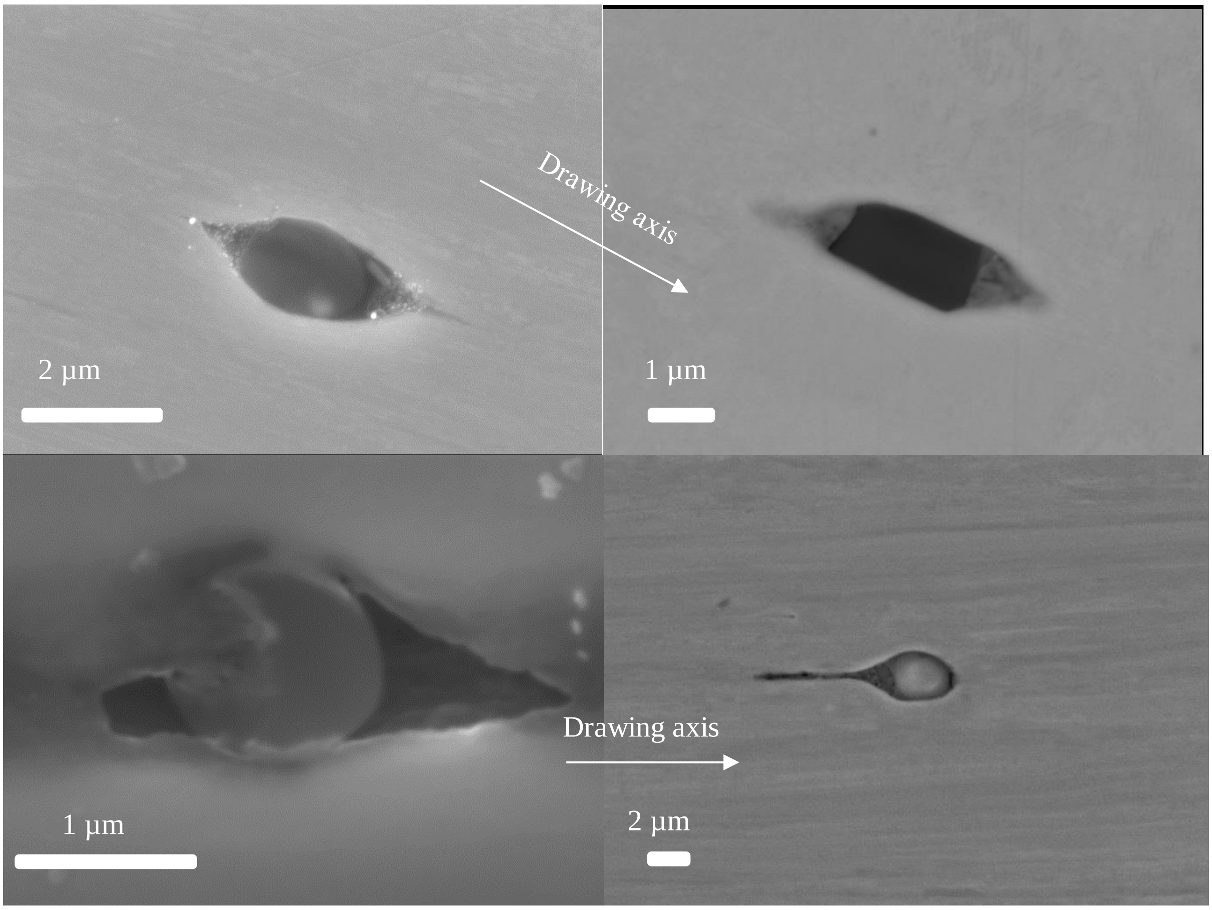

Figure 930: SEM images of decohesion around inclusions

By comparison with the fractured wires observed in the previous chapter, the shape of the cracks also differs. The SEM observations point out that the cracks propagated along the drawing axis. By contrast, during the step final of filament drawing, the opening of the cracks grows in the same proportion along the drawing axis and perpendicular to it.

The SEM observation of a 70µm diameter wire presents an initiation of a fracture around an inclusion in the centre of the wire. The initiation of the cup and cone fracture is visible and occurs more on one side of the fracture than the other side. Comparing the shape of the micro-crack in the present wire (Figure 951) with the shape of simulated cracks introduced around inclusion on copper wire (Figure 952), the similarity is high

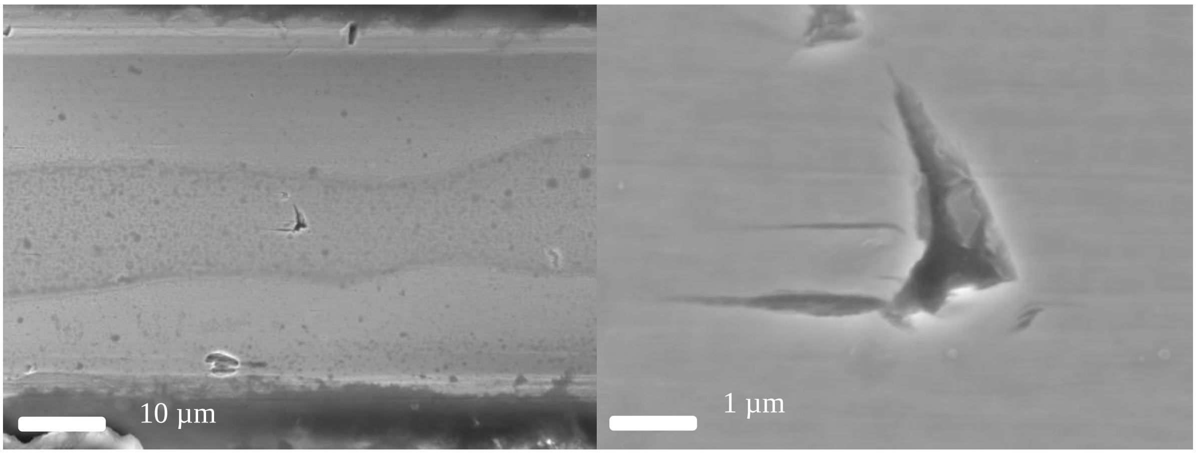

Figure 941: Example of fracture initiation in a Ø70µm filament

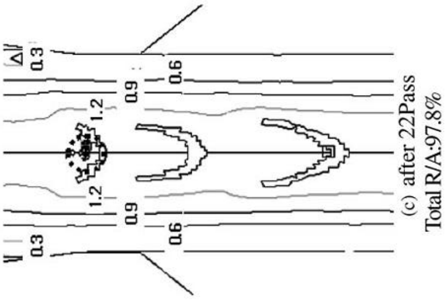

Figure 952 : Shape of micro-crack at 97.8% of deformation for copper wire (damage value) [60]

19.3 TEM analysis of the decohesion

With the use of SEM, the observation of the cracks is limited by the spatial resolution. To have a better understanding of the decohesion between the matrix and the inclusion, it was decided to observe the matrix/inclusion interface with TEM. For that, three FIB lamellae were extracted from an Ø0.3mm wire with a drawing strain ε=1. Two lamellae were realized and included two different inclusion types, a SiO_2-MgO inclusion and a SiO_2-CaO inclusion. The SEM images of the inclusions before the FIB sampling are presented in Figure 963. The inclusions do not present micro-cracks at their edge. The black line present at the edge of the inclusion in Figure 963 b) is a MnS inclusion. A third FIB lamella was extracted in the matrix free from inclusion. The TEM observations of the lamellae containing (SiO_2-MgO) and (SiO_2-CaO) are shown Figure 104(a) and Figure 104 (b) respectively.

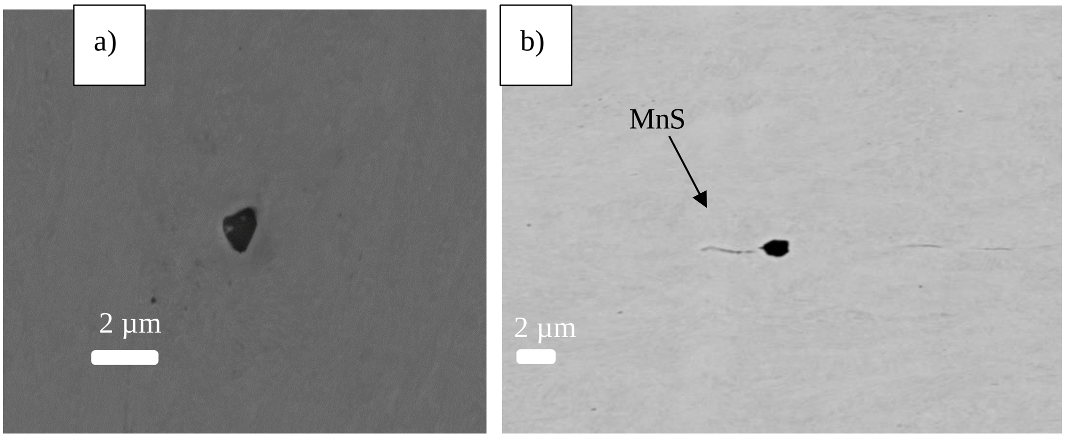

Figure 963 : SEM images of the overview of the inclusions cut by FIB a) SiO_2-MgO b) SiO_2-CaO

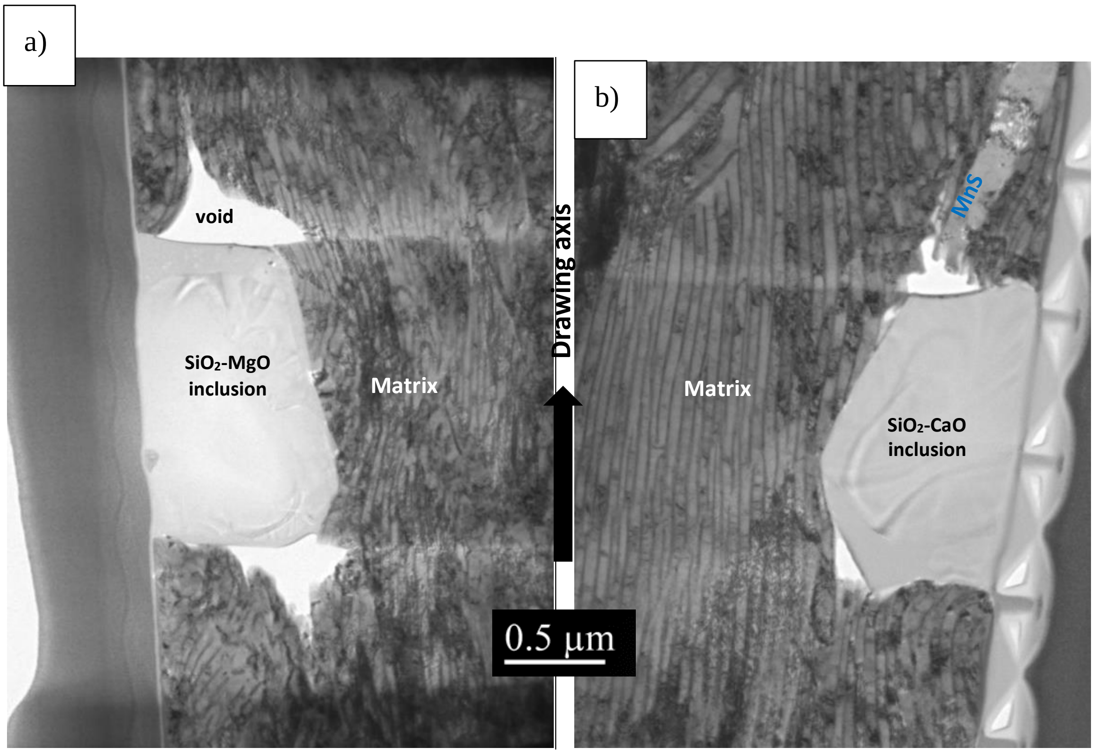

Figure 974: Overview of the inclusion into the deformed microstructure (ε≈1) observed with TEM a) SiO_2-MgO b) SiO_2-CaO

These TEM micrographs show similar size and shape of inclusions and voids, the conical white parts. The decohesion is more pronounced with SiO_2-MgO than with SiO_2-Cao suggesting that SiO_2-MgO appears to be more critical. This does not agree with the conclusions on the critical inclusion size from the fracture analysis. Indeed, in section 12.4, it has been shown that at equivalent size, SiO_2-CaO is more critical than SiO_2-MgO. It is therefore suspected that the chemical composition of the inclusions may play a role and has to be further studied.

Also, based on those TEM observations, it can be noticed that the decohesion does not occur at the edge of the inclusion and does not cover a full side of the inclusion. The decohesion is predominant under the surface visible with the SEM, in the deeper part of the matrix/inclusion interface. It could have been supposed from literature [66] and from the stress distribution [11] during the drawing that the decohesion would happen parallel to the drawing axis and start from the edge of the inclusions. In this case, the matrix is still cohesive with the inclusion on some part of the inclusion side. This part of the matrix still cohesive with the inclusion is highly deformed, as observed in Figure 985.

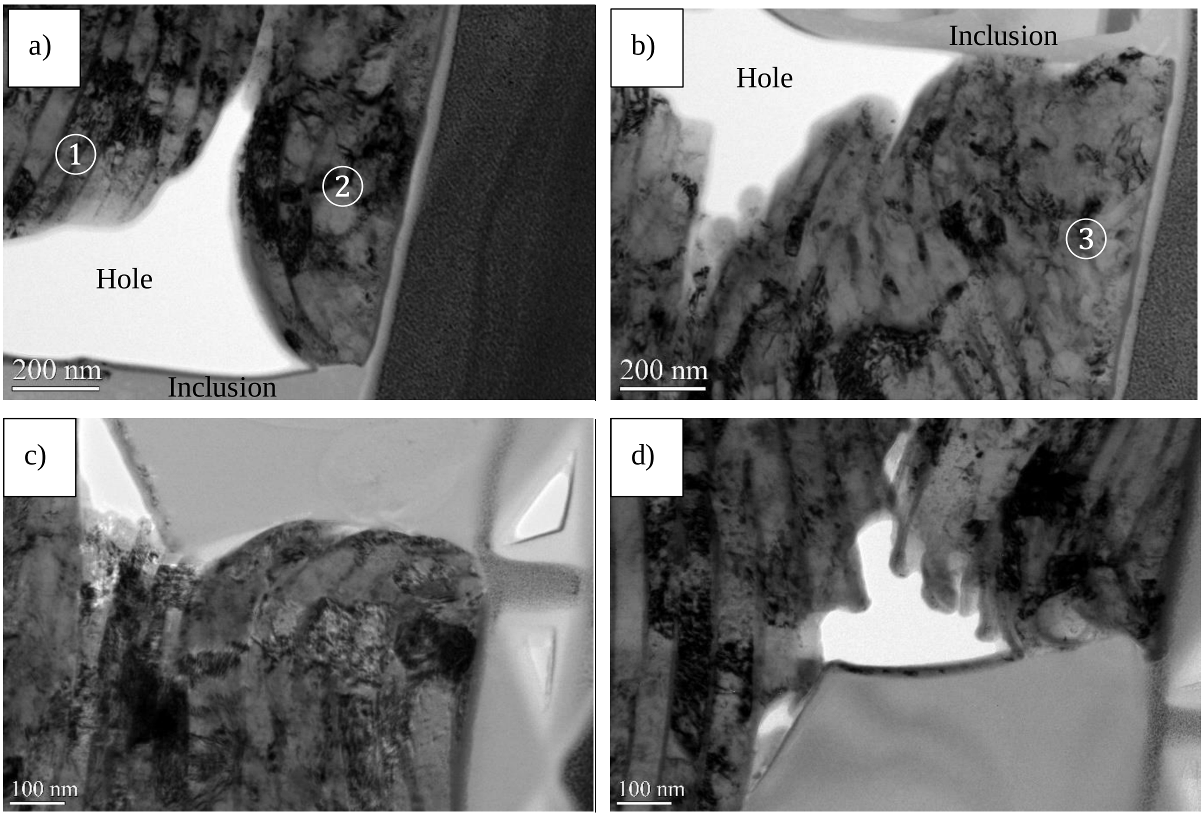

Figure 985: Cohesive zones between the matrix and the inclusion for a,b) SiO_2-MgO c,d) SiO_2-CaO

Figure 985 a) shows that the pearlitic structure is still identifiable in the disbonded zone (zone 1). The cementite lamellas are still aligned. This contrasts with the cohesive zone (zone 2) where the identification of pearlite is much more difficult. The lamellas of cementite are not easily identified. The phenomenon is even more marked in Figure 985 b) (zone 3). Cementite plates of the matrix seem to have disappeared in the cohesive zone suggesting a quasi-total dissolution of cementite in the pearlite bonded with the inclusion. The apparent cohesive strength between the inclusion and the matrix seems to promote a stress concentration in the cohesive matrix which leads to a large modification of the microstructure.

The same remarks hold for the matrix bonded with SiO_2-CaO inclusion but the phenomenon is less amplified, Figure 985 c) and Figure 985 d).

19.4 Conclusions

From the analysis of the micro cracks generated around the inclusions, several conclusions can be drawn:

- Not all the inclusions initiated cracks.
- The chemical composition of the inclusions does not bring an additional detrimental aspect.
- It has been highlighted that the localisation of the inclusions has a more pronounced impact in comparison with their size.
- Meanwhile, the amount of cracks is lower in the centre of the wire, their length is somehow more pronounced. By contrast, the outer ring presents a higher amount of cracks with shorter lengths. This behaviour is linked to the strain repartition.
- The influence of the inclusion chemical composition cannot be proved
- The size of the cracks is not linked to the size of the inclusions but more to their location in the wire.
- The decohesion between the matrix and the inclusion is not due to a uniaxial loading.
- The occurrence of the micro cracks is due to the combination of an intense tensile stress in the core of the wire and a shear stress due to die pressure
- The apparition of cracks around the inclusions is not present on the initial wire but are introduced early in the process (ε=1).
- A lower die angle enables a reduction of the crack initiation but does not influence the size of the crack induced.
- The decohesion occurs whatever the morphology of the inclusion.
- Inclusions that do not exhibit a decohesion during surface analyse can be the initiation site of decohesion in the third dimension.

20 Influence of chemical composition

The role played by of the chemical composition of the inclusion has been also studied. It can be assumed that during the formation of the inclusion and the solidification of the matrix around the inclusion, some chemical elements could have transferred from the inclusion into the matrix or in the other way, a depletion of a certain element is observed around the inclusion.

In order to investigate, with a high spectral resolution, the migration of such chemical elements, low acceleration voltage EDS measurements were performed on the inclusion and at its surrounding. The EDS measurements were performed on a JEOL 7200F FEG-SEM with an 80mm² Oxford EDS detector. A 5kV acceleration voltage is set to reduce as much as possible the interaction volume and obtain the best resolution.

20.1 Analysis of the diffusion of the chemical element with EDS

20.1.1 Line scan detection

Line scans have been performed on the inclusions to detect and study the distribution of the chemical elements in and around the inclusions. The measurement was performed on the longitudinal section of the wires. It is supposed that the temperature levels, which are reached during the heat treatment and for the different wire drawings, did not permit the diffusion of the chemical elements.

A line scan was performed on a SiO_2-MgO inclusion on a deformed wire (ε=4). The line scan starts from the matrix, crosses the inclusion and stops at the matrix in the other side of the inclusion as presented in Figure 996 a). The associated EDS results are presented in Figure 996 b).

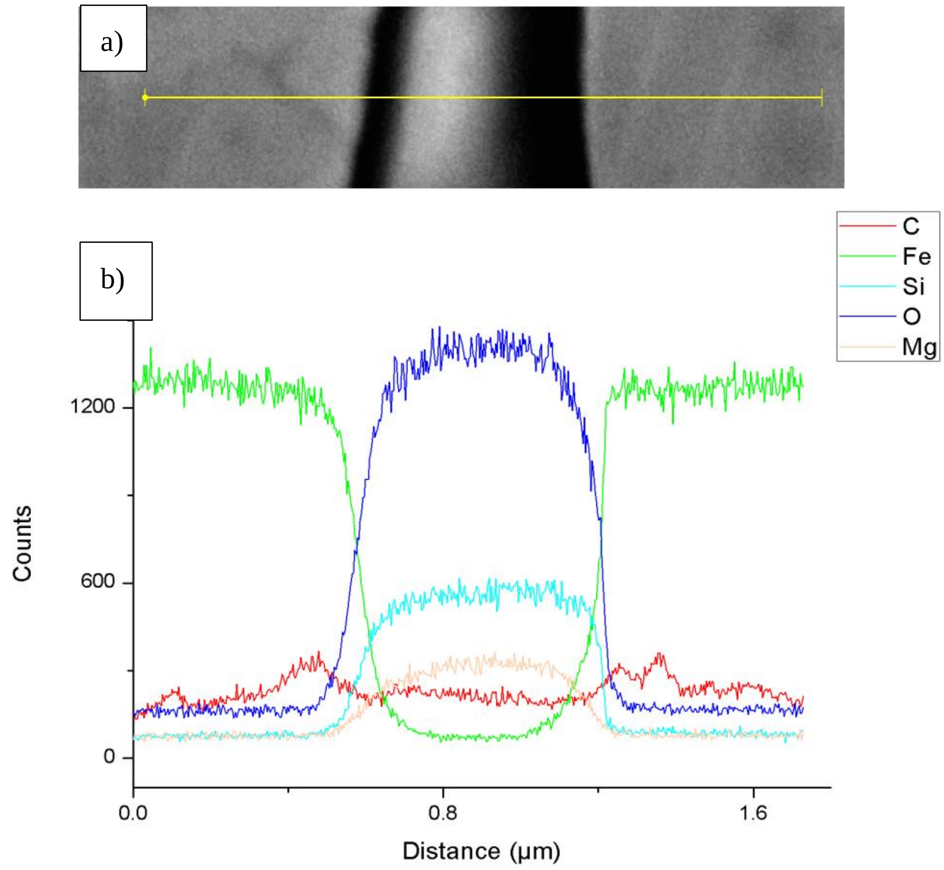

Figure 996: a) SEM image of the inclusion and schematic of the line scan b) corresponding EDS results

Such a line scan observation points out that there is a distinct boundary between the inclusion and the matrix. Elements like Si or Mg belonging to the inclusion do not appear to be present on the surrounding matrix. These observations are also valid for the other types of inclusions as SiO_2 and SiO_2-CaO.

20.1.2 Mapping detection

Spectral mapping of the inclusions in a deformed structure ($\varepsilon>4$) has been carried out in order to measure with more accuracy the distribution of the different chemical elements. Figure 1007 and Figure 1018 represent the chemical contrast image coming from BSE-SEM image of a SiO_2 inclusion and the corresponding EDS mapping. On the SEM image, three different grey levels are present in the inclusion. The grey level profile (red line) shows four different zones: zone 1 with a high grey value corresponding to the matrix; zone 2, darker, corresponding to the core of the inclusion; zone 3 corresponding to a lighter part than the inclusion but darker than the matrix. The crack opening (corresponding to zone 4) occurs at the interface between this second phase inclusion and the matrix.

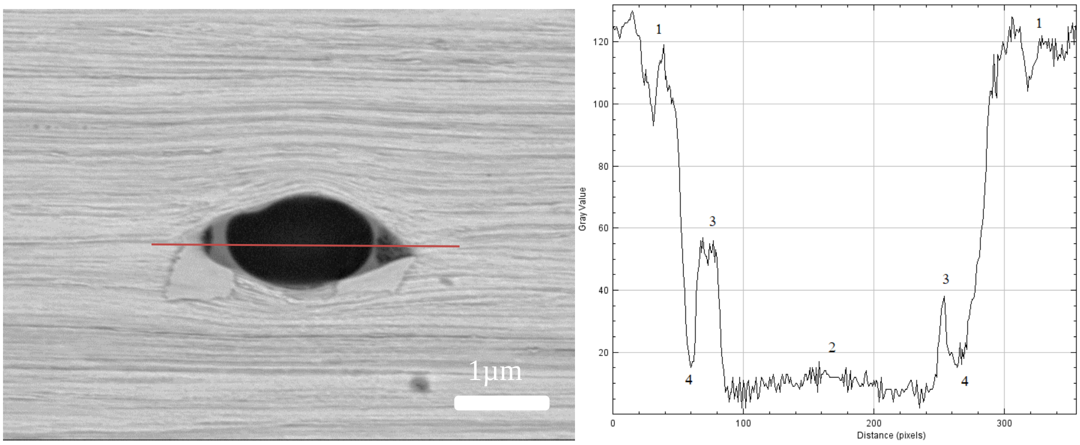

Figure 1007: a) BSE-SEM image of SiO_2 inclusion with rich Mg-Al parts on the extremities b) evolution of the grey level of the image along the red line

EDS mapping (Figure 101Figure 1018) shows an inhomogeneous partition of the chemical elements in the inclusion.

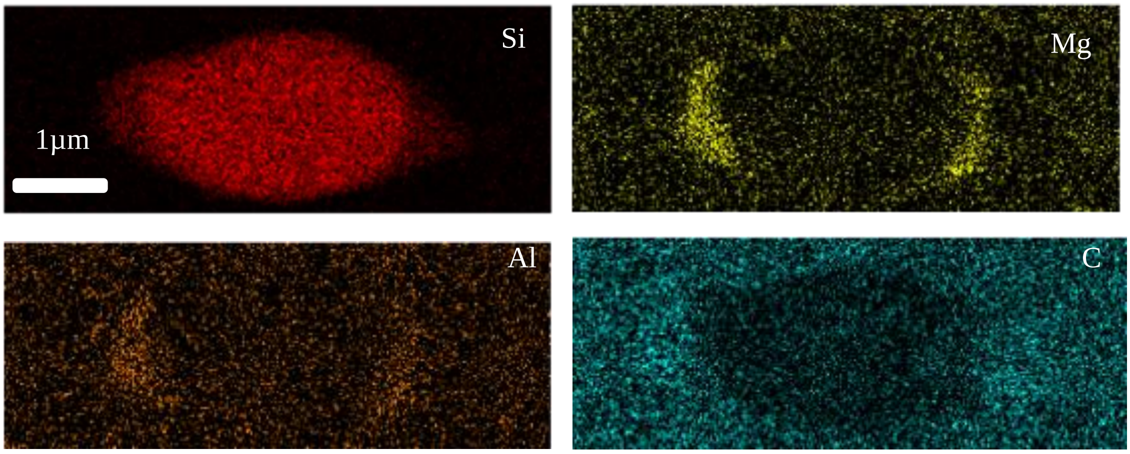

Figure 1018: EDS Mapping of Si, Mg, Al and C of a SiO2 inclusion in an Ø0.22mm wire

Although EDS gives some indications on the distribution of the chemical elements inside and outside the inclusion, the analysis of the inclusion/matrix interface remains difficult to perform due to the limitation in terms of spatial distribution related to the SEM micro-analysis technique. As the inclusions are small in size, the probe size has to be reduced to excite only the inclusion by decreasing the acceleration voltage. Nevertheless, as the probe size is reduced, the quality of the EDS spectrum is also reduced.

To improve the quality of the chemical mapping and overcome this issue, an inclusion was studied by Scanning Transmission Electron Microscopy (STEM). A FIB sampling was performed on a 50% deformed wire with an approximate diameter of 0.30mm. Two different types of inclusions (SiO_2-MgO and SiO_2-CaO) were chosen for analysis and are displayed Figure 10209 (TEM micrographs) and Figure 1030 (EDS elemental Mapping for both inclusions).

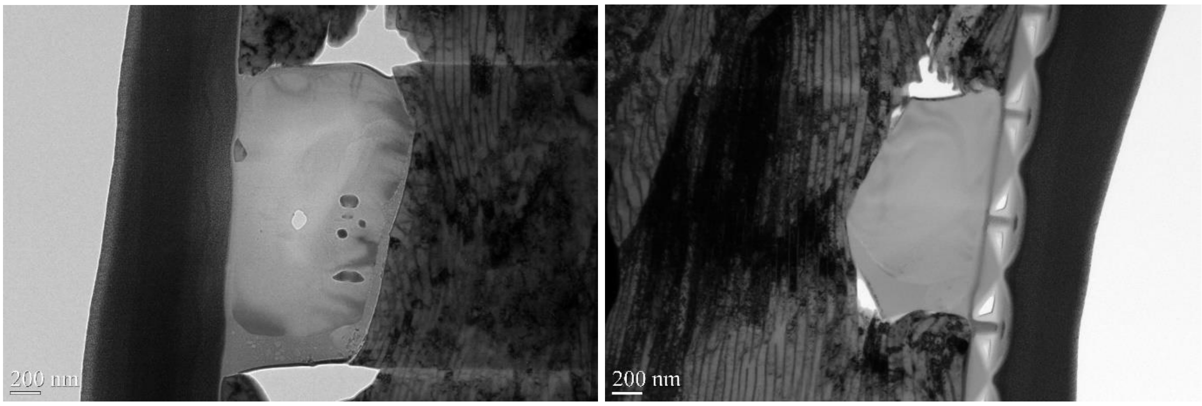

Figure 10209: TEM image of the section of an inclusion a) SiO_2-MgO b) SiO_2-CaO

Dark areas in the central parts of the inclusions of the EDS mapping images (Figure 1030) results from a too much thinning during the cutting step (FIB). This results in a lack of information from the centre of the inclusion.

The STEM chemical analyses support the two results of EDS analysis acquired with SEM. First, none of the chemical elements belonging to the matrix or to the inclusion is concentrated or depleted in the regions surrounding the inclusions. The idea of migration of chemical elements between the matrix and the inclusion can be forgotten.

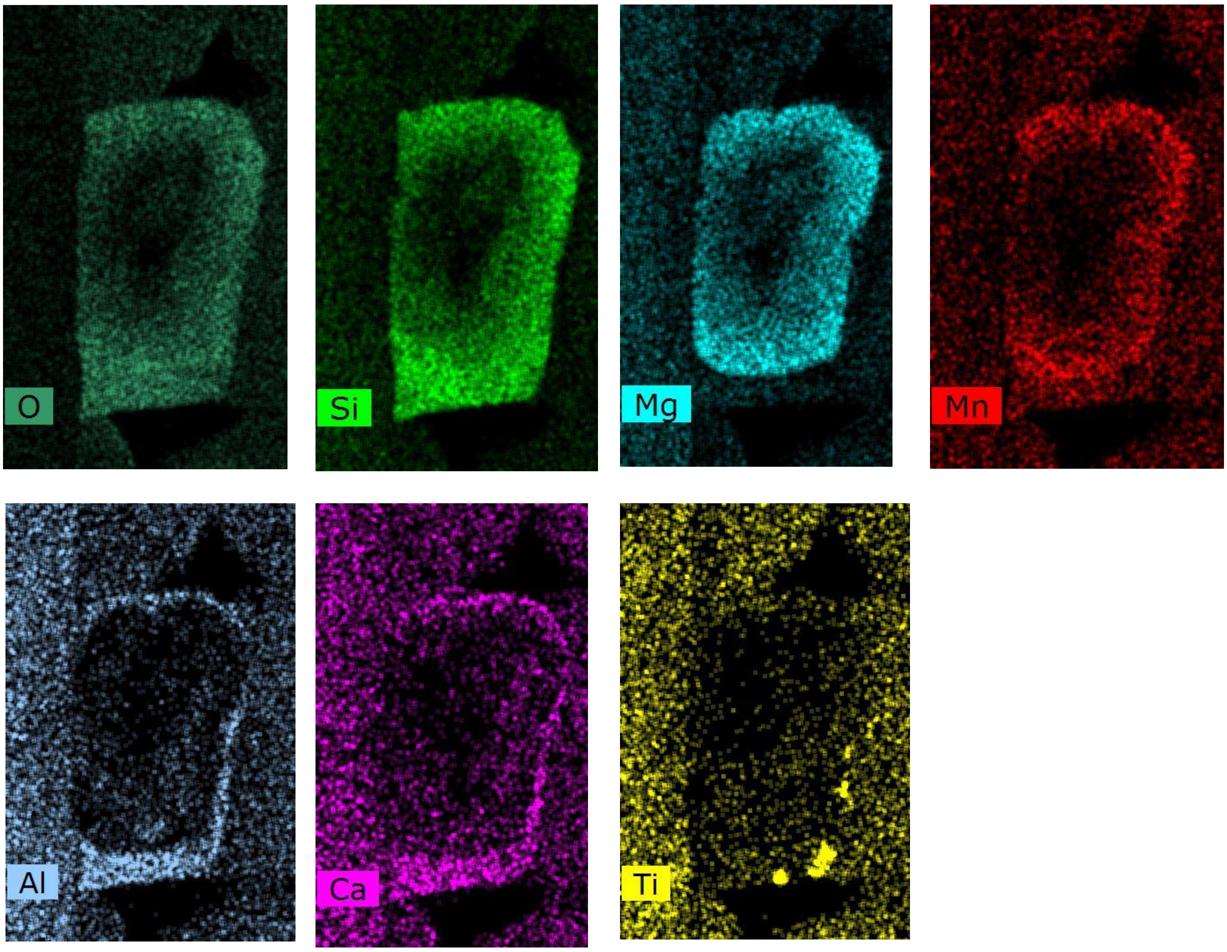

Figure 1030: EDS-STEM mapping of O, Si, Mg, Mn, Al, Ca and Ti elements in the SiO_2-MgO inclusion

However, all the chemical elements of inclusions are not homogenously distributed inside the inclusion. For SiO_2-MgO inclusion, oxygen and silicon are homogenously distributed. Then, two different behaviours are observed and the inclusion seems to be divided into two distinct zones. The core and the edge exhibit different chemical composition. Mg and Mn are exclusively in the core of the inclusion while the other elements as Al and Ca are entirely concentrated in an area surrounding the core of the inclusion. On the edge of the inclusion, the high concentration of Ti suggests the presence of Ti precipitates not homogenously distributed.

The core/edge interface has been analysed more in details with TEM (**Error! Reference source not ound.**1). It is observed that the core of the inclusions corresponds to a crystalline structure while the edge of the inclusion corresponds to an amorphous structure. Therefore, the decohesion occurs at the interface with the amorphous structure mainly composed of Al and Ca and not with the material of the core of inclusion composed of SiO_2-MgO.

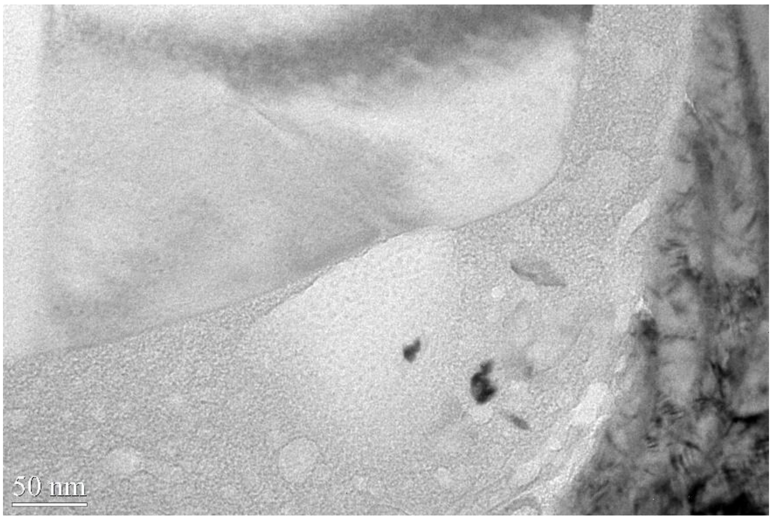

Figure 1041: TEM image showing the amorphous part of the inclusion between the core of the inclusion and the matrix

For the SiO_2-CaO inclusion, the mapping of chemical elements (O, Si, Mg, Al, Ca) looks different. Almost all the elements are homogeneously distributed inside the inclusion, except Mg which is absent in a part of the inclusion, see the red circle in (Figure 105). However, the structure is entirely crystalline and no amorphous phase has been observed for SiO_2-MgO.

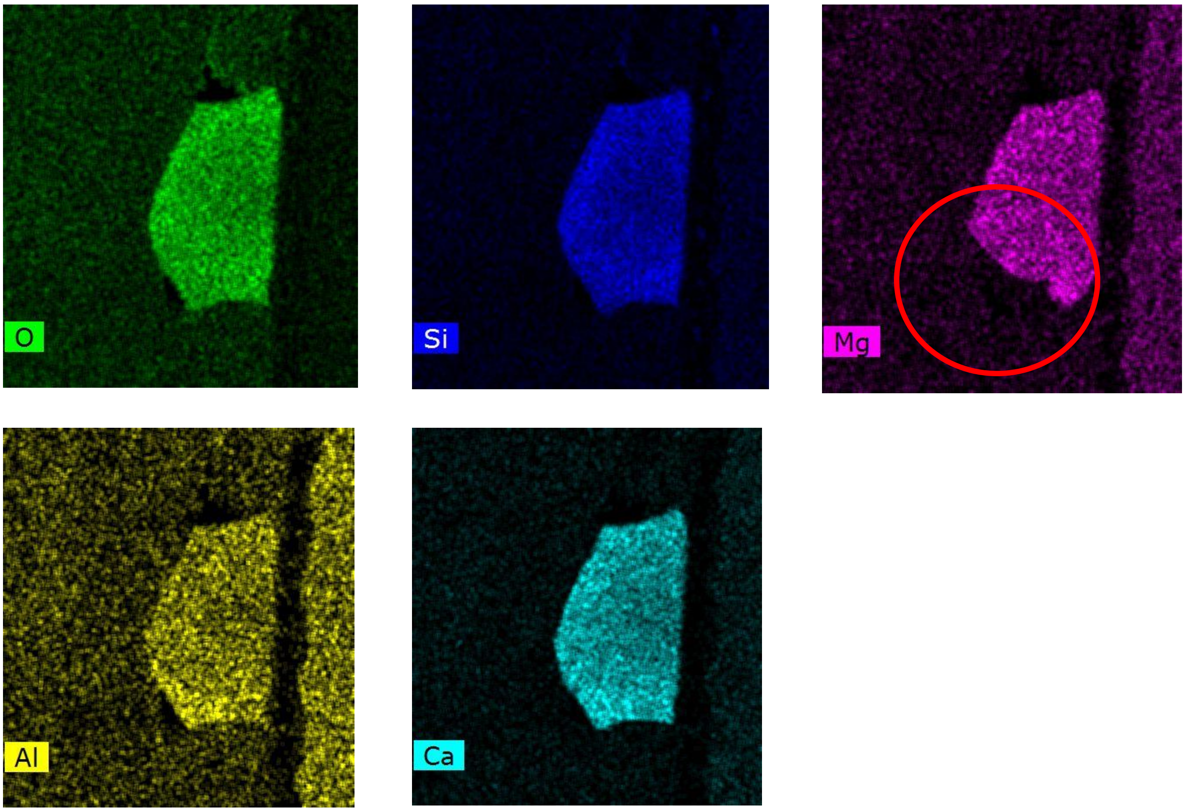

Figure 105 : EDS-STEM mapping of O, Si, Mg, Al, and Ca elements in the SiO_2-CaO inclusion

20.2 Conclusions

With the SEM and STEM analysis of the chemical composition of the inclusions and the surrounding matrix, several conclusions can be drawn.

First, the chemical composition of inclusions, especially near the matrix, is neither enriched nor depleted. As well, the surrounded matrix has not been subjected to a depletion of some elements present in the inclusion. So, there has been no interdiffusion between chemical elements of the inclusion and of the matrix. Nevertheless, the partition of the chemical elements in the inclusions is inhomogeneous.

Secondly, in some case, the inclusion structure such as SiO_2-MgO is hybrid comprising a crystalline core decorated by an amorphous phase at the border.

21 Estimation of the local deformation around the inclusion by numerical simulation

All the previous examinations underline the impact of the inclusion during the drawing. In order to have a better idea of the mechanical effect of the inclusion during the drawing, it was decided to use a mechanical model to assess stress and strain distribution around the inclusions during drawing. This will help to understand how it would affect the initiation of cracks as well as the final fracture. As the inclusion parameters cannot be experimentally modified in the wire, this strengthens using the simulation.

Several models developed on different software has been proposed in years to study the impact of the drawing process on wire [76–79] and also the impact of inclusions on wire drawing for different wire diameters and materials [60,61,66,67,75,80]. The main observation of is that the wire is not impacted uniformly during the drawing process.

The development of a numerical model and its implementation was not a part of this PhD study. It was then foreseen that the numerical approach will be performed by the Bekaert simulation team. The inputs of the numerical simulation were based on both literature results (for inclusions mechanical properties) and on the obtained experimental results presented previously.

Nevertheless, in order to understand how this numerical approach is applied to the case of an inclusion, the basics of the considered model are explained hereby.

21.1 Physical basic of the considered model

The model is based on the resolution of the second fundamental law of Newton. The second law states that the rate of change of momentum of a body is directly proportional to the force applied, and this change in momentum takes place in the direction of the applied force. The second law is defined by the following equation:

$$\vec{F} = m\,\frac{\overrightarrow{dv}}{dt} = m\vec{a} \tag{19}$$

where

- F is the applied net force
- m is the mass of the body
- a is the body's acceleration
- v is the velocity of the of the body

This equation alone doesn't allow the resolution of the equation for x, y and z directions. Other equations have to be implemented in the model for its resolution.
For that, Hooke's law is used and is defined by:

$$\bar{\bar{\sigma}} = \frac{\vec{F}}{S} = E.\bar{\bar{\varepsilon}} \tag{20}$$

However, this statement is only valid for pure elastic deformation. This is not representative of the case of the wire drawing as the reduction of the wire section involves large plastic deformation. The Hill Yield criterion is used to introduce a plastic deformation. Yield criteria are useful in a variety of structural engineering applications to accurately characterize the initiation of plastic deformation under various forms of loading. This knowledge can be critical for design and production of highly optimized structures. Theories to predict the macroscopic yielding of materials are crucial to model metallic materials to ensure adequate performance and failure prevention in a variety of applications. While many popular yield criteria adequately define a yield surface for isotropic materials (the most common model was defined by Von Mises [81]), in some applications a model of the material's state of anisotropy is required, which explain the use of the Hill criteria. Then the plastic deformation is defined as explained in Figure 1063.

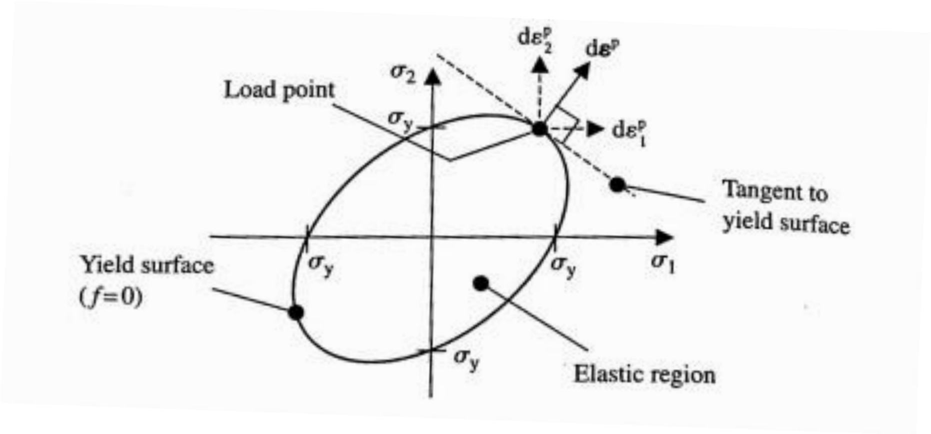

Figure 1063 : Von Mises Yield surface and load points [81]

If plastic deformation occurs, the loaded point is out of the elastic region. The plastic deformation of the material is then described as the displacement of the load point to fit to the yield surface.

The plastic potential described by the Von Mises yield criterion remains valid for many common metals that deform uniformly in all directions. However, in many circumstances anisotropy can cause significant deviations from the behaviour predicted by the Von Mises yield criterion, necessitating the use of an anisotropic yield criterion.[82]. The full details of the modelling loop are described in Figure 1064.

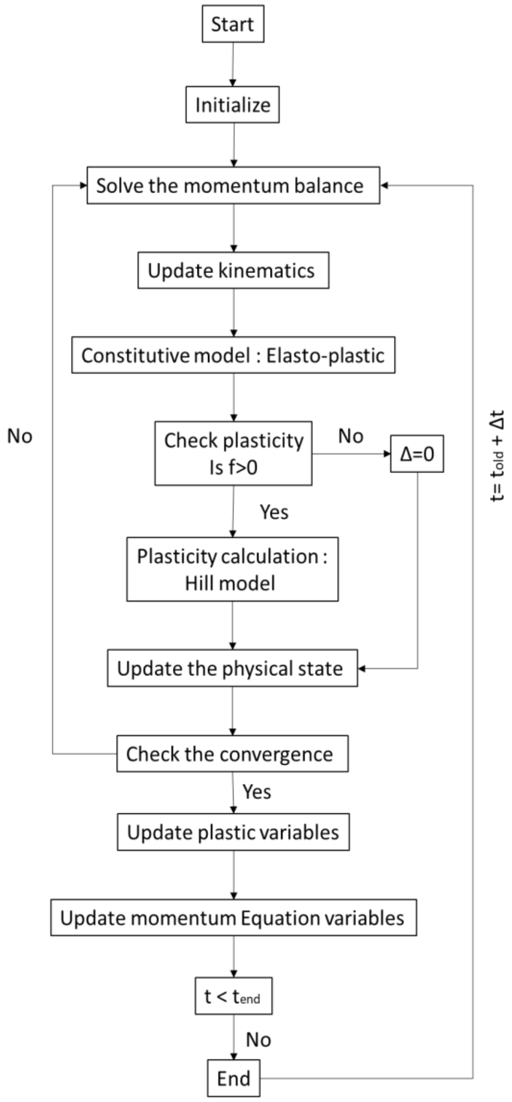

Figure 1074: Model of simulation

The materials characteristics are described in a different manner. For the die and the inclusions, the materials are considered as purely elastic following the Neo-Hookean elasticity, similar to the model proposed in Simo & Hughes [83]. The wire is submitted to high strain so the pure elastic model is not applicable. Hence, an elastoplastic model is applied to the material when describing the wire. For that, the Bathe model is used, its application is adapted to large strain orthotropic elastic-plasticity [84]. The Bathe model is a material model and an interface model for the formulation of large-strain elasto-plastic finite element analysis with frictional contact conditions. The above procedure allows the use of small-strain stress return maps in a large strain context; in the current implementation, the return map algorithm is given by some authors [85,86].

The applied modelling settings correspond to the last pass of the WWD i.e. to the wire reduction from a ~0.065mm diameter to 0.06mm diameter. As explained previously, the last pass of the drawing is the most critical for fracture occurrence. The die angle is set as a function of the experimental study. For the modelling, a 2D representation of the centre of the wire was considered. For symmetry reasons, only half a diameter was considered.

The model has been implemented in Open FOAM and the output results are read using Paraview data visualization application [87–90]. A first set of results shows how the components of the Cauchy stress tensor are distributed in the matrix that surrounds the inclusion. The Cauchy stress tensor is used for stress analysis of material bodies under deformation, here, when the inclusion passes through the die.

The simulation of the normal stress σ_{xx} (Figure 1085) where x is drawing axis, reveals that the stress into the wire is the same at each spot of the wire. By contrast, it is not the case for the inclusion itself. A higher stress develops at the extremities, in front and behind of the inclusions along the drawing axis. A positive stress on the back of the inclusion indicates that the inclusion is pushed into the wire. On the side of the inclusion, a negative stress is observed indicating that the material is pulled on the side of the inclusion because the inclusion is subjected to friction while passing through the die.

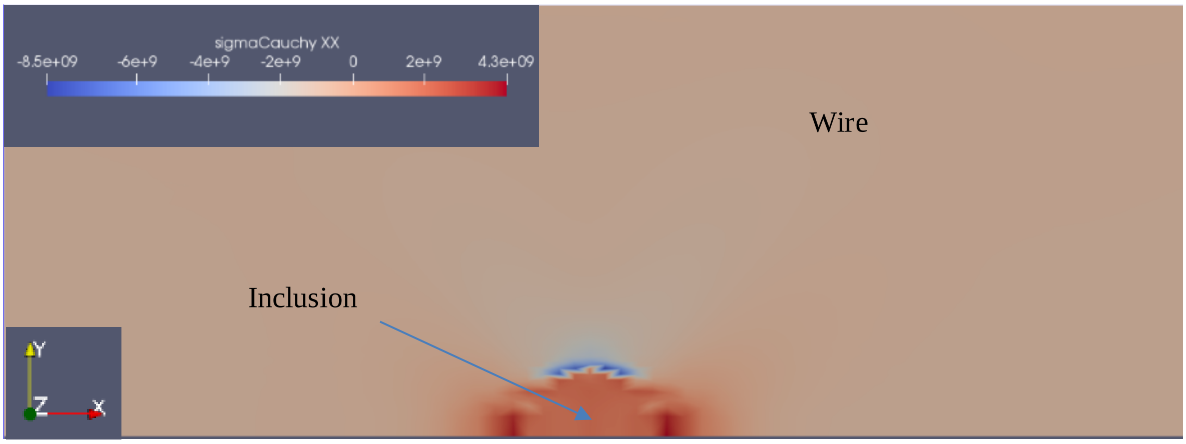

Figure 1085: Simulation of Cauchy stress σ_{XX}

The simulation of the normal stress σ_{yy} leads to the same conclusion for the value into the steel matrix of the wire i.e. a homogeneous partition of stress along the drawing axis and stress concentration close to the inclusion (Figure 1086).

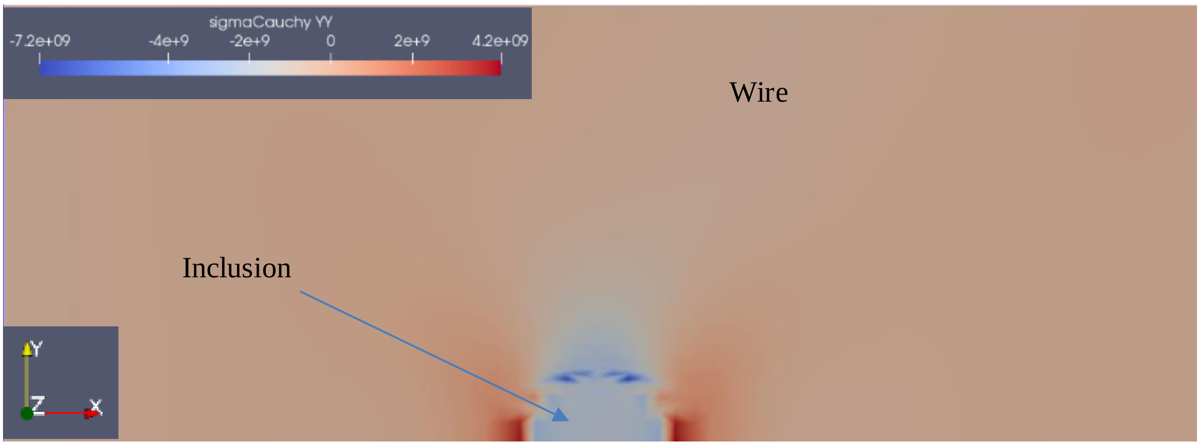

Figure 1096: Simulation of Cauchy stress σ_{YY}

The two red zones at the extremities of the inclusions suggest that the pulling stress is intensified in front and behind the inclusion. This explained partially the decohesion behaviour observed during the WWD. The rest of the inclusion is submitted to a negative stress i.e. a compression stress on the inclusion along the Y-axis. The material is pushed against the inclusion.

For the simulation of the shear stress σ_{xy}, the back of the inclusion 45° from the drawing axis is subjected to a negative stress and the front to a positive value (Figure 1087).

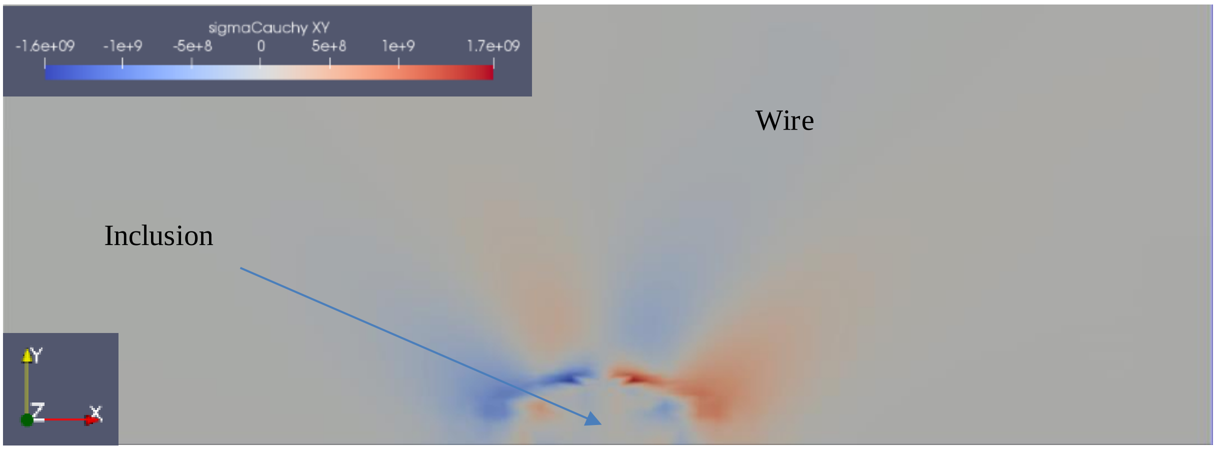

Figure 1107: Simulation of Cauchy stress σ_{XY}

In addition to the stress distribution, the aim of the simulation was also to estimate the influence of the chemical composition of the inclusions on the local deformation. As the fractures occur mainly on the last pass, the simulation was performed on the last pass of the drawing process. Two main sets of input parameters were considered, the mechanical properties of four types of inclusions as well as their size. In this part, the stress applied to the matrix at the inclusion interface were studied. In the next part the residual plastic strain after drawing is considered.

21.2 Measurement of mechanical properties of the inclusions

The determination of the mechanical and physical properties of the inclusion is primordial to evaluate their deformability and their impact on the mechanical properties. However, the measurement of these inclusions is not as easy as expected. The size of the inclusions does not enable their measurement by the common analysis techniques. A good method to determine partially the mechanical properties of the inclusion is the hardness measurement. Nano hardness tests are proved to be a satisfactory method to measure the mechanical properties of inclusions present on the wire. Wang et al [91] have determined the mechanical properties (hardness and Young modulus) of some inclusions like BN, MnS, Al_2O_3, and TiN. They found that for, BN and MnS inclusions, the hardness is lower than the surrounded matrix, while for TiN and Al_2O_3, the hardness is higher than the matrix. Therefore, they can act as sources of stress concentration in steel. However, a limited inclusion types are measured. Zhang et al. [39] calculated theoretically the Young modulus of complete system. Although, no experimental study has been performed to confirm the inclusion deformability, the measurement of the mechanical properties of the inclusions was attempted. However, despite several tests, the measurements could not lead to conclusive results. Thereby, the values of inclusion properties (density, Young modulus, Poisson coefficient) were selected from the literature from the literature [92–95] and listed in Table 40.

Table 40 : Properties of inclusions extracted from literature for simulation

	Density (kg/m^3)	**E (GPa)**	**ν**	**Ref.**
MgO	3470	249	0.18	[93]
CaO	3290	180	0.21	[92]
SiO_2	2490	73	0.17	[94]
Al_2O_3	3870	335	0.25	[95]

21.3 Influence of inclusion type

To have an idea of the local deformation of the matrix around the inclusion, the maximum residual strain was calculated for each inclusion type at different inclusion sizes (Figure 1118)

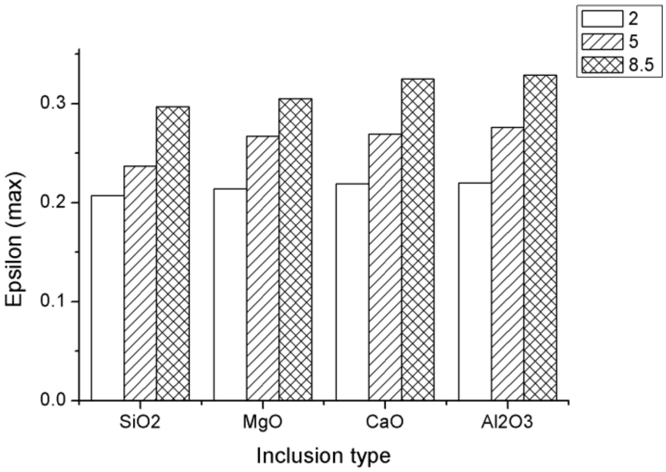

Figure 1118: Maximum residual plastic strain around inclusion calculated by numerical simulation for different inclusion types and sizes

The inclusion type does not seem to deeply influence the maximum residual strain around the inclusion. For an equivalent diameter of 8µm, the difference between the inclusion type is not significantly visible but tends to be more amplified with a size increase. Hence, when the inclusion size reaches 5µm, a SiO_2 inclusion has a lower impact on the matrix (ε=0.23 vs ε=0.27 for the other cases). For the biggest diameter (8.5µm equivalent diameter), the difference between the inclusion types are emphasized. While SiO_2 remains the less critical inclusion, MgO is also appearing to be less critical at higher size by comparison with CaO and Al_2O_3 inclusions.

This last observation is in agreement with the experimental analysis of the fracture tips obtained during WWD. It was concluded that the SiO_2-MgO inclusions are the most critical even at lower size, as they induce more strain in the surrounding matrix.

For a deeper analysis, the distribution of the residual plastic train around the inclusion is represented for the different inclusion types (for a fixed size, here 8.5µm) in Figure 11219. The impacted zone around the inclusion exhibits a butterfly wings shape on the side of the inclusion and a slight impacted zone on top of the inclusion, with a round shape. Along the longitudinal side, a gradient of deformation is created around the inclusion. From the simulation, it can be observed that the maximum deformation does not occur directly at the matrix/inclusion interface but a bit further in the matrix.

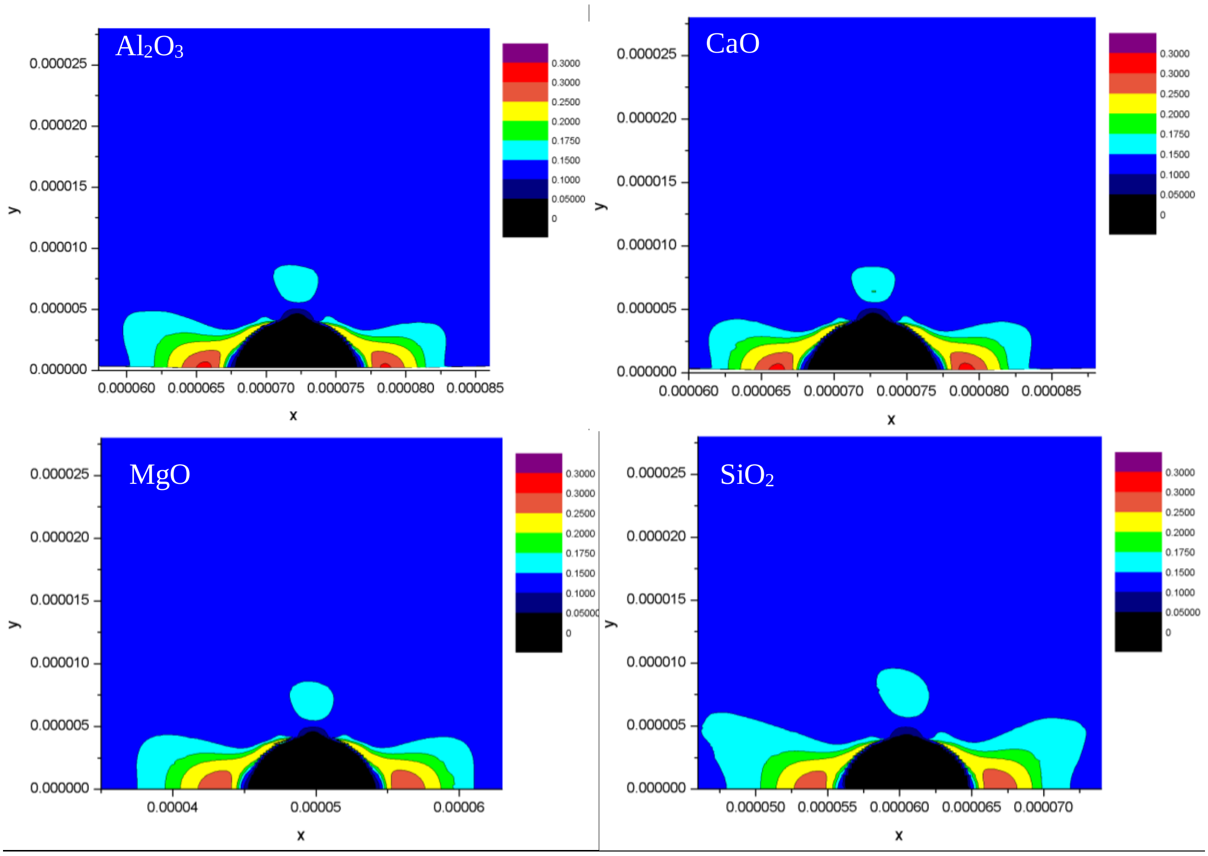

Figure 11219: Repartition of the plastic strain around the different inclusions

If now the different inclusion types are studied, differences are noticed. For Al_2O_3 and CaO inclusions, the altered zones present higher values of plastic strain, superior to 30% corresponding to the red zone. For SiO_2 and MgO inclusions, this red zone is not present, which means that the plastic strain around the inclusion is lower.

For SiO_2 also, the impacted zone seems larger than for the other inclusion types. To study the difference of the plastically deformed zone, two dimensions were measured: the length and the maximum width in the direction of the drawing axis and the opposite direction. The values are reported in Table 41.

Table 41 : Measurement of the impacted zone for the different types of inclusions

		MgO	**CaO**	**Al_2O_3**	**SiO_2**
Drawing direction	Length (µm)	6.03	5.69	5.51	6.17
	Width (µm)	3.33	2.84	3.01	4.71
Opposite direction	Length (µm)	7.14	7.41	5.49	9.57
	Width (µm)	3.43	3.61	3.22	4.47

The first statement concerning the size of the altered zones is that the zone is always larger behind the inclusion. This observation is common to every type of inclusion.

For Al_2O_3 and CaO inclusions, where the plastic strain value is higher, the altered zone is less spread, while for SiO_2, and MgO the altered zone is more spread but the value of plastic strain is lower. This tendency is even more pronounced for SiO_2. The length of the zone is becoming bigger than the diameter of the inclusion. These aspects proved that the mechanical properties of the inclusions have a pronounced effect regarding the deformation around the inclusion. In comparison with the information obtained in section 19.3, it can be observed that the impacted zone seems in a first place to be lower and approximately corresponds to 1µm. However, as the numerical simulation and the experimental studies have been performed on different step of the process and at different drawing strain, it is difficult to make a comparison.

As for the chemical composition, the repartion of the residual plastic strain is presented in Figure 1130 for the three different sizes for a fixed chemical composition (here SiO_2). The altered zones are greatly impacted by the size of inclusion. For an inclusion of 2µm, the butterfly wings shape is not yet visible, and the zone on top of the inclusion is also not visible for an inclusion of 2µm. The maximum value does not exceed $\varepsilon=0.2$. The only difference between a 5µm and 8.5µm inclusion only concerns the size of the altered zones. The maximum values of ε remains equivalent with a value between 0.25 and 0.30.

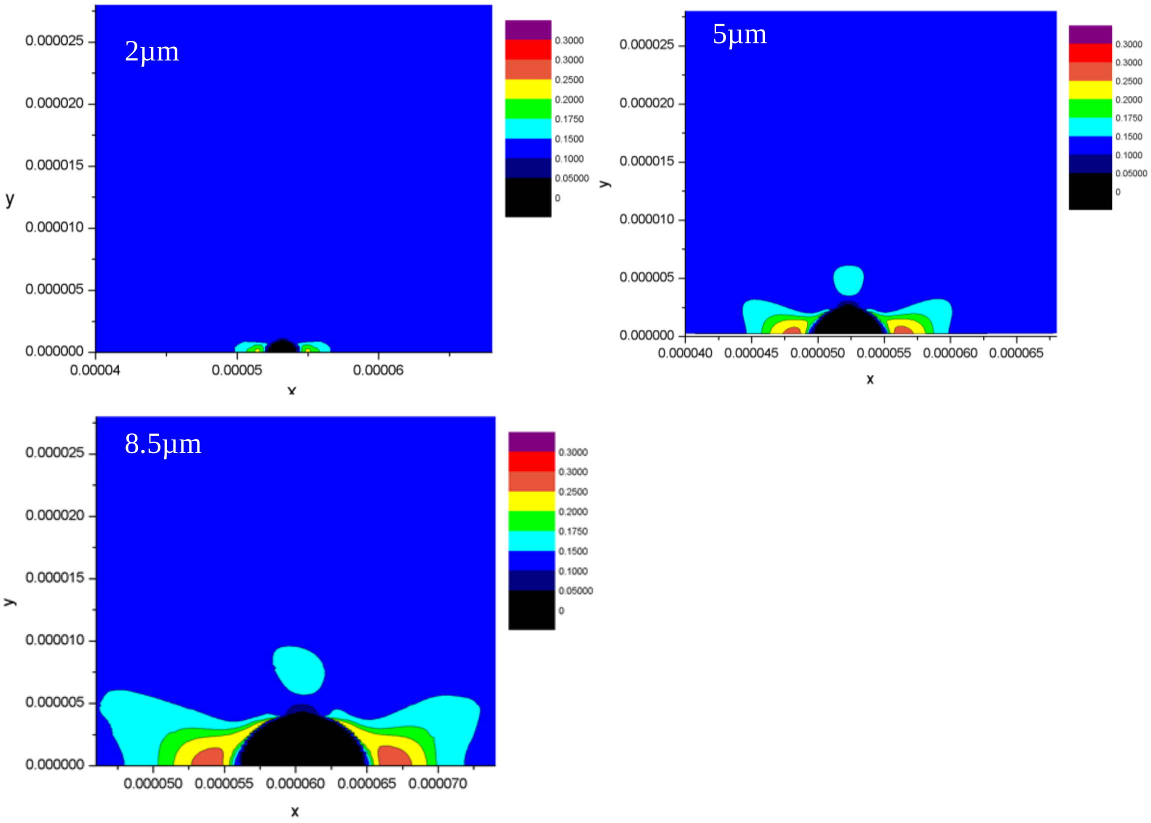

Figure 1130: Repartition of the plastic strain around SiO_2 inclusions with different sizes

However, the limitations of the simulation push us to be critical towards the results obtained. Indeed, several parameters are different from the experimental observations. First, for the modelling, the shape of the inclusion is set as spherical, so the influence of the inclusion shape observed during the experimental study is not implemented in the model. The second point concerns the interface between the inclusion and the matrix in the model, set as purely cohesive in the simulation , while in reality is not the case, because decohesion has been observed around the inclusions. The third parameter is the influence of multi pass. In the simulation, only the last pass of the drawing is considered while the drawing process is the succession of several reduction passes. So plastic strain is already cumulated around the inclusion.

In order to assess or validate the results obtained through the modelling, experimental characterization has been carried out via SEM/EBSD.

But from the tendencies observed with the modelling, a comparison with the experimental values can be done. To study locally the deformation around the inclusion, it was decided to focus on EBSD measurement to study the local deformation at the same scale and on the same plan than the modelling.

Then ASTAR measurement will provide very local information and information in 3D.

22 Study of local deformation with EBSD

In order to improve the understanding of the impact of the inclusion on the surrounding matrix, different samples were investigated by EBSD. For a long period, the use of EBSD was limited to the description of the crystallographic texture (e.g. grain orientation). With the recent evolution in terms of data processing, Wright et al makes this technique suitable for the estimation of local deformation levels [96,97]. The basic principal of EBSD mapping and the different components are explained below.

22.1 Principle

- Description of the technique

Electron backscatter diffraction (EBSD) is a scanning electron microscope–based microstructural-crystallographic characterization technique commonly used in the study of crystalline or polycrystalline materials. The technique can provide information about the structure, crystal orientation, phase, or strain in the material. Inside the SEM, the electron beam is focussed onto the surface of a crystalline sample. The electrons enter the sample and some may backscatter. Escaping electrons may exit near to the Bragg angle and diffract to form Kikuchi bands which correspond to each of the lattice diffracting crystal planes. These lines correspond to the so-called Kikuchi lines (Figure 1141). For each measured point, the backscattered electrons are detected and the corresponding diffraction pattern is obtained. With automation, the surface is scanned and it is possible to obtain a cartography of the crystallographic orientation of a sample [98].

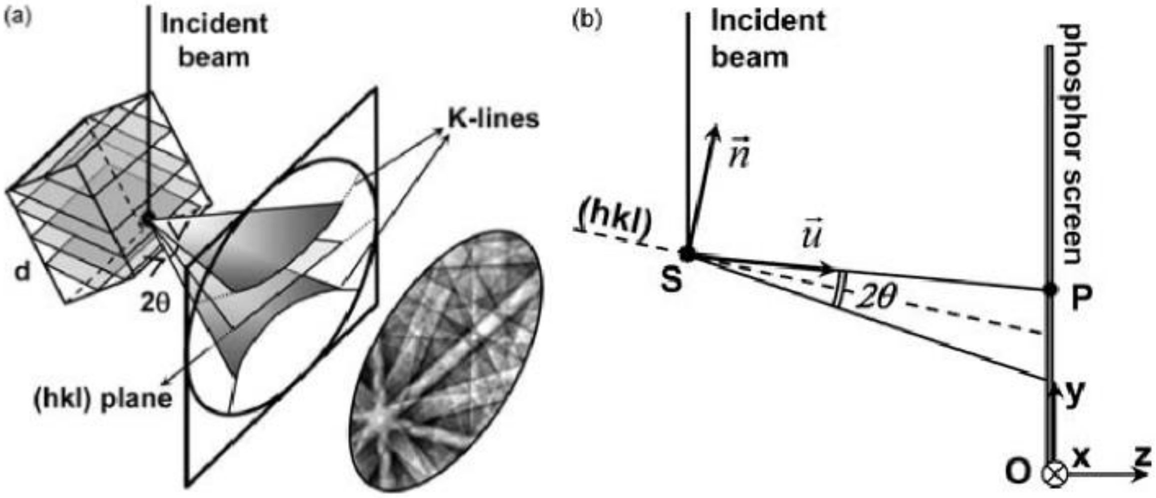

Figure 1141 : schematic of the formation of Kikuchi bands during the diffraction of backscatter electrons [99]

The second possible exploitation with EBSD is coming from the indexation of the diffraction pattern. This patterns permit to found back the crystalline orientation of the sample. It can be represented by the three Euler angles (also known as Bunge angle, Φ, φ_1, φ_2), as presented in Figure 1152. From this method comes out the cartography obtained by Orientation Imaging Microscopy (OIM) that enables the graphical representation of the crystallographic orientations.

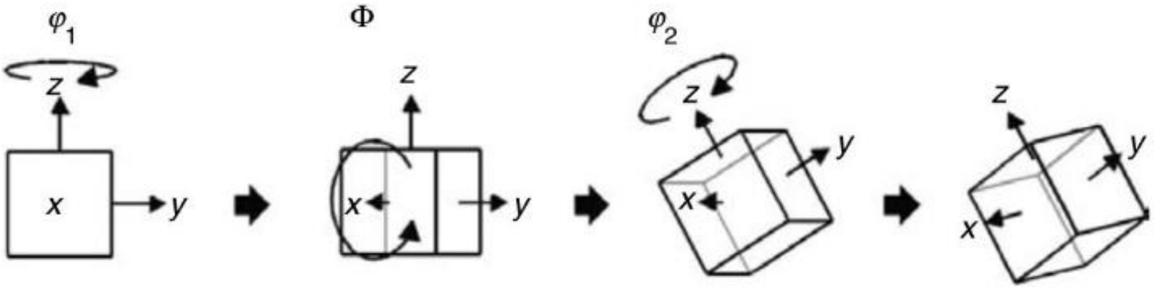

Figure 1152 : Representation of the different Euler angles [100]

First, EBSD enables the distinction of the different phases of a sample when the crystallographic lattice is different enough.

The basic approach enables also the characterization of the crystallographic plan. This is also called the Inverse Pole Figure (IPF). The cartography represents the normal to the hkl plans collinear to a chosen direction, with the help of colours. Figure 1163 shows an example of the aspect of an IPF cartography.

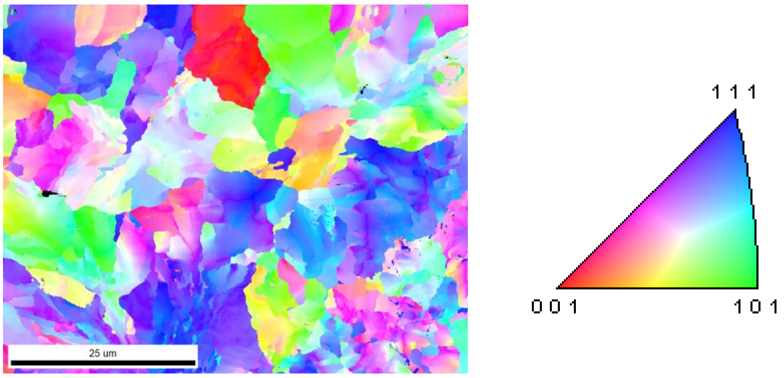

Figure 1163: Example of an IPF cartography of a pearlitic structure

Within the last decades, recent development in terms of post-processing of the EBSD data has led to an estimation of local strain levels, as well as an identification of the encountered dislocation structures [96,101,102].

The various approaches can be based on the impact of defects presence onto the pattern quality (Image Quality), but are more focused of the study of the misorientation that varies within the grains. Then, several parameters and/or criteria can be evaluated. This mainly depends if boundaries linked to

dislocation structures have to be highlighted (LSM approach) or if the studies focus on the dislocation's interactions by themselves (KAM, GOS, GROD approach).
The following paragraphs will give a short description of the parameters that have been selected in the present investigation.

- Image Quality (IQ) and Line Segment Method (LSM)

The first possible exploitation of EBSD is the image quality. In this case, each pixel from the cartographies enables the representation of the clearness of the diffraction pattern recorded, relating the thickness of Kikuchi lines. Consequently, the IQ criterion is strongly impacted by the non-indexed zones coming from SSD (Statistically Stored Dislocations) or from GND (Geometrically Necessary Dislocations), see Figure 124. The Image Quality (IQ) is calculated from the maximum intensity of the Hough peaks and is representative of the average intensity of the Hough peaks. Equation 18 defines the expression of this Hough peak intensity.

$$IQ = \frac{1}{N}\sum_{i=0}^{N-1} I_i \tag{8}$$

Where is N the number of identified peaks and I_i the intensity of peak
IQ maps based on a grey scale are affected by non-indexable patterns. Hence, lower IQ patterns correspond to a lattice distortion related to structures as grain boundaries and dislocations.

In complement, the presence of Geometrically Necessary Dislocations (GND) induces a change in the crystallographic orientation which can lead to the formation of sub-grain and grain boundaries with misorientation up to 15°.

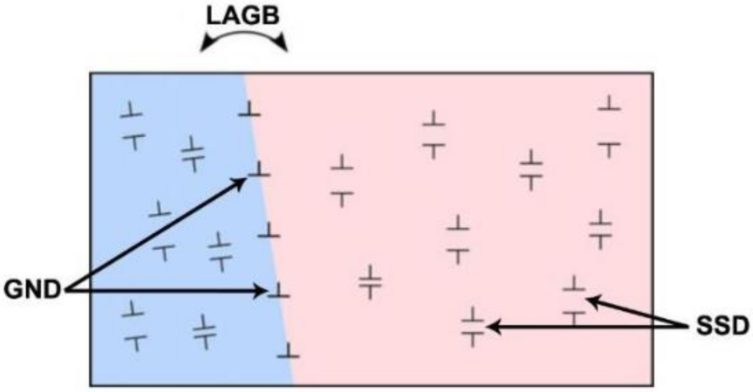

Figure 1174 : Diagram of SSD (Statistically stored dislocations) and GND (Geometrically Necessary dislocations) [96]

All these kind of boundaries can be evaluated through a Line Segment Method [103]. In this way, the grain boundaries are represented by calculation of the segment separating two neighbours with a disorientation above the selected criterion. This allows separating the Low Angle Grain Boundary (LAGB), as presented in Figure 1175, from the High Angle Grain Boundary such a grain boundary.

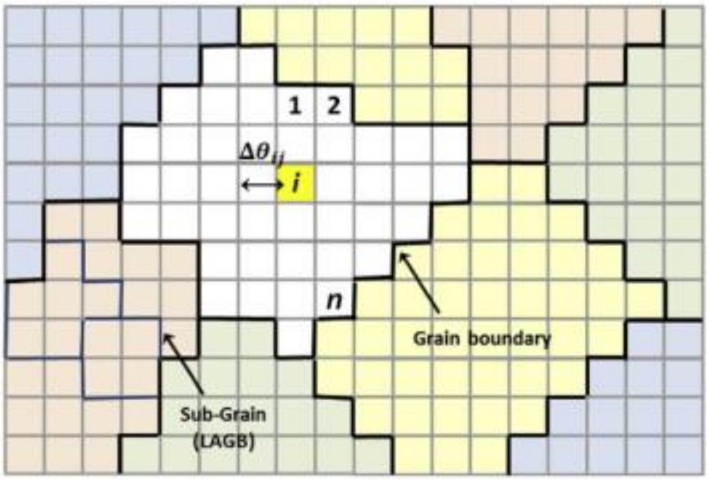

Figure 1185 : Diagram of the result from a EBSD scan with the LSM approach [103]

In the SSD regions, the global Burger's vector is close to zero on the contrary to the GND regions where there is a change in the crystallographic orientation. This can lead to the formation of subgrain boundaries. In that case, the diffraction pattern of volume is the superposition of the images of two subgrains resulting in a shift of the Kikuchi lines (Figure 1196). GND may also come from the distortion of network induced by a phase change

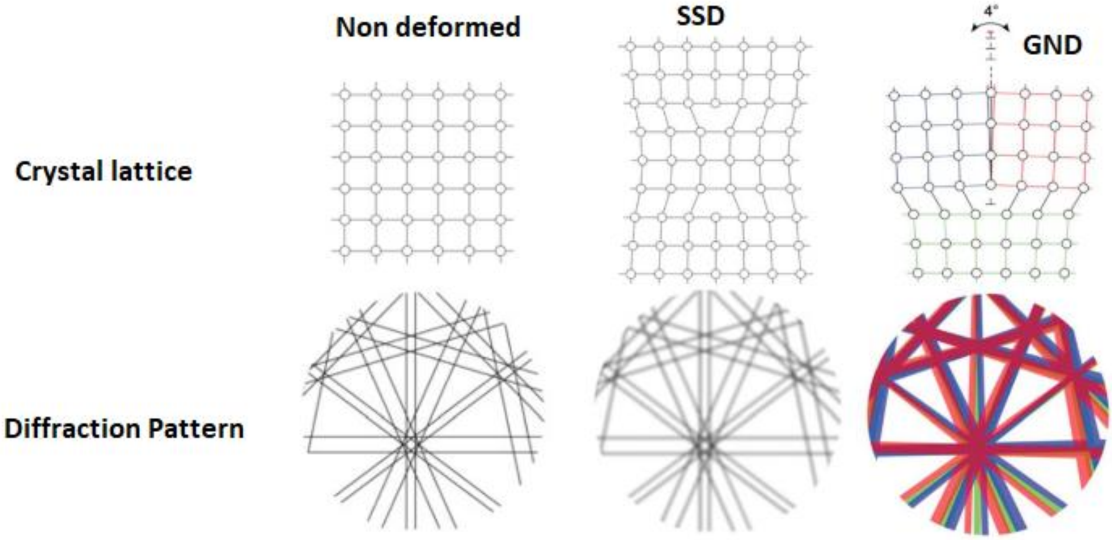

Figure 1196 : Impact of the crystal deformation on diffraction pattern [96]

The idea of using EBSD technique to evaluate strain within material was introduced by Buchanan et al [104]. They showed a link between image quality (IQ) and the plastic deformation. A calibration curve which linked the image quality to the strain variation was then established and enabled the evaluation of the plastic strain. However, IQ method depends on several factors such as: the energy of the electron beam, the emission current, the surface of the sample state and sometimes also the orientation crystal and results should be interpreted carefully.

Then, to complete the first approach of the estimation of local strain based on the dislocation effects with IQ/LMS, other misorientation-based criteria have been taken into consideration. Grain orientation spread (GOS), grain reference orientation deviation (GROD) and kernel average misorientation (KAM) maps are criteria mainly used when considering local deformation measurement by means of EBSD.

- Kernel based approach

Kernel Average Misorientation (KAM) calculates the average misorientation between a pixel I and its neighbours.

Hence, the local misorientation value assigned to the centre point (Pi) is the average of these misorientations as expressed by the following formula

$$KAM_{pi} = \frac{1}{N}\sum_{j=1}^{N} \Delta\theta_{i,j} \tag{19}$$

Two values of $\Delta\theta_{i,j}$ were used for this investigation, one $\Delta\theta_{i,j}$<3° and on with $\Delta\theta_{i,j}$<5°. With the KAM_{pi} value of the KAM at pixel I, $\Delta\theta_{i,j}$ the misorientation angle between pixels I and j , and N the number of surrounding pixels that exhibit a misorientation $\Delta\theta_{i,j}$ lower than 3° or 5°. If plastic deformation results from dislocation glide and crystal lattice rotation [105,106], this approach enables a quantitative evaluation of the local plastic strain gradients. In the present work, the KAM criterion is considered for accumulated plastic strain energy. The KAM depends on factors related to the measurement conditions and more specially the step size. To overcome this drawback, all the analyses were performed systematically with the same conditions.

- Grain based approach

Grain Reference Orientation Deviation (GROD) is based on the misorientation between a reference point of a grain and the other points. The reference point can be the mean misorientation of the grain or the point of the grain where the KAM is the lowest. It is defined by equation 20

$$GROD_i = \omega_{ik} \tag{20}$$

With ω_{ik} the deviation angle between orientation of pixel I and reference orientation of grain k.

GROD maps indicate the magnitude of the orientation changes to the initial crystal orientation (point with the lowest misorientation).

Grain Orientation Spread (GOS) is based on the misorientation averaged on the whole grain and is defined by equation 20. In this mode each point in the grain is shaded with the same colour in the maps.

$$GOS_k = \frac{1}{M}\sum_{i=1}^{M} GROD_i \tag{21}$$

With is M the number of pixels within the grain k.

22.2 Experimental study

Three samples collected at different steps of the process were analysed. The first sample is the wire rod of Ø5.5mm, the second one the intermediate wire of ~Ø0.60mm after patenting, the third one a 50% deformed wire with a diameter ~Ø0.30mm as summed up in **Error! Reference source not ound.**7.

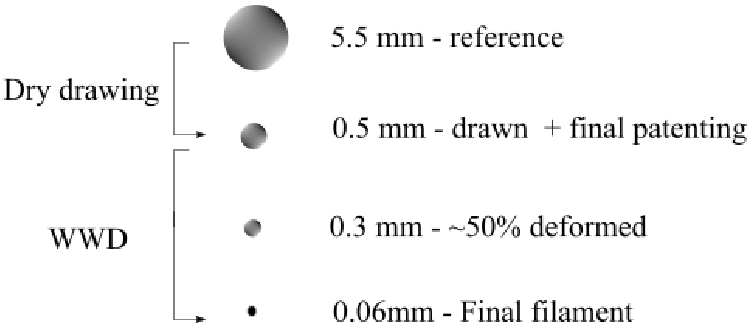

Figure 1207: Wires selected for EBSD measurements

The different samples were investigated on longitudinal sections embedded and polished with OPS. The longitudinal section was chosen to be in phase with the simulation presented previously. Two separate areas have been investigated: a local map around an inclusion and an overview map of the microstructure. EBSD scans were performed in a FEG SEM JEOL 7800F fitted with Oxford Instruments Nordlys Max 2 cameras. The software oxford instrument Aztec is used for EBSD acquisition. The EBSD results are then processed with the software TSL OIM.

The structure of the final filament (Ø60µm) would have been interesting to study by EBSD. However, the Kikuchi lines did not exhibit any contrast and therefore made SEM-EBSD analysis unfortunately not applicable. This is a big issue when the material to be investigated is highly as it is in the present case where the microstructure is twisted lines (Figure 1198).

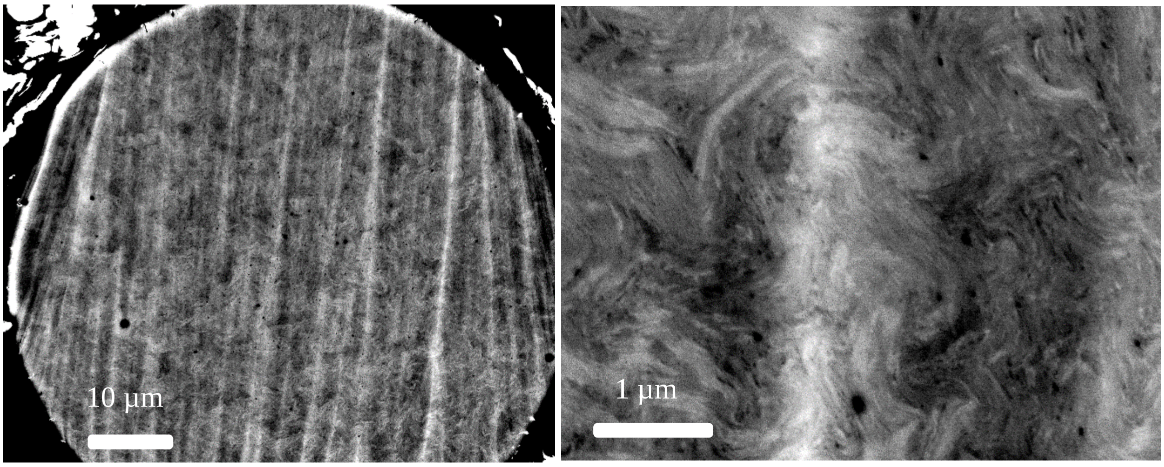

Figure 1218: BSE images of the cross section of a 60µm filament showing heavily deformed microstructure

In order to validate the misorientation criteria, a statistical study should be performed to verify the influence of the acquisition parameters. Here are considered the SEM parameters as the spot size and the beam current, and the EBSD setting such as the camera binning influencing the angular resolution and the step size influencing the spatial resolution. In order to have comparable and reliable results, the SEM and EBSD parameters were set in order to have the finest step size compared to the acquisition time. It was decided to set the SEM and EBSD parameters as described in Table 42.

Table 42 : SEM and EBSD parameters for EBSD acquisition

Parameters	**Value**
Acceleration voltage	15kV
Probe current	14
Binning	2x2
Step size	0.07µm

22.3 First difficulty: the particular case of the pearlite structure

The first difficulty is related to the studied microstructure. Pearlite, as described in section 0, is a bi-phased structure composed of alternate ferrite bands and cementite lamellae. This structure is at the origin of two limitations for EBSD measurement in a SEM.

First, the cementite (Fe_3C - orthorhombic structure) is lighter than the ferrite phase. Meanwhile, the interaction volume produced by the electron beam disperses more in the lighter phase, so the interaction volume will always diffuse into the ferrite bcc phase. Then ferrite will always be measured even if the beam is located on a cementite phase. Consequently, only the α ferrite (bcc iron) can be clearly identified with EBSD for a pearlitic structure. More recent investigations have shown that transmission based EBSD (such as ACOM or t-EBSD techniques) overcomes this difficulty and image the orthorhombic phase. Nevertheless, as those experiments are performed on thin foils, this type of analysis loses the statistical approach that is allowed by SEM based EBSD. In that case, the results have an interest if the interaction between ferrite and cementite is of first interest.

Also, the pearlitic structure is by default a strained structure. Indeed, Takahashi et al. [107] concluded that a certain density of Geometrically Necessary Dislocations (GND) is present inside the pearlite colonies. These GND are induced by cementite lamellae curvature as described in Figure 12229. They found a strong correlation between the crystallographic orientation gradients and the morphological orientation gradients and the morphological lamellar curvatures. This already pre-constrained structure is used as a reference point and is already non uniformed, depending from the interlamellar spacing.

In the present approach, the strain levels are estimated by comparing the KAM, GROD and GOS criteria with a reference material. Here, the reference should already exhibit slight levels of internal misorientations. This aspect must not be neglected when comparing to the other states which correspond to deformed structure issued from the successive drawing steps.

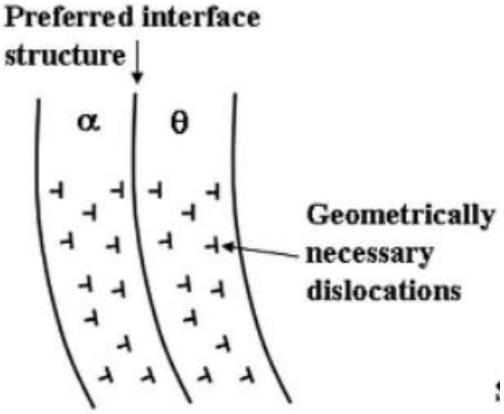

Figure 12229 : Mechanisms to accommodate the lamellar curvature [107]

The second difficulty of EBSD on pearlitic structure is the definition of “a reference structure unit”. Indeed, the GROD or GOS criteria, are defined by a grain identification However, in chapter 1, it is explained that pearlitic structure is divided into 3 major “units”, the prior austenitic grain, the nodule and the colony of pearlite. For EBSD, the determination of the studied unit is of most importance. Even if several studies were performed on pearlitic structures, the determination of a “grain” is experimentally difficult [107–109]. To be able to use the GROD and the GOS values, fixed parameters to define a unit had to be found. In the literature, several authors sort the different pearlitic nodules with EBSD. The misorientation between two pearlitic nodules is defined to be between 10 and 15° by the different authors.

To verify the interest of the use of the GOS and the GROD, the grain tolerance angle is modified and the grain size, the GOS and GROD are calculated by varying the grain tolerance angle in TSL OIM ® post-processing software. The maps obtained are presented in Figure 1230. Looking at the grain size maps, it is strongly influenced by the grain tolerance angle, especially between 5° and 10-15°. The angle of 10°-15° selected in the literature seems applicable to pearlite to determine a “grain” because a slight difference is observed on the grain size map. However, the difference between the calculation of the GOS and the GROD is too variable and depends greatly on the grain tolerance angle. For this reason, only the KAM and the IPF maps were analysed for the study of the local deformation.

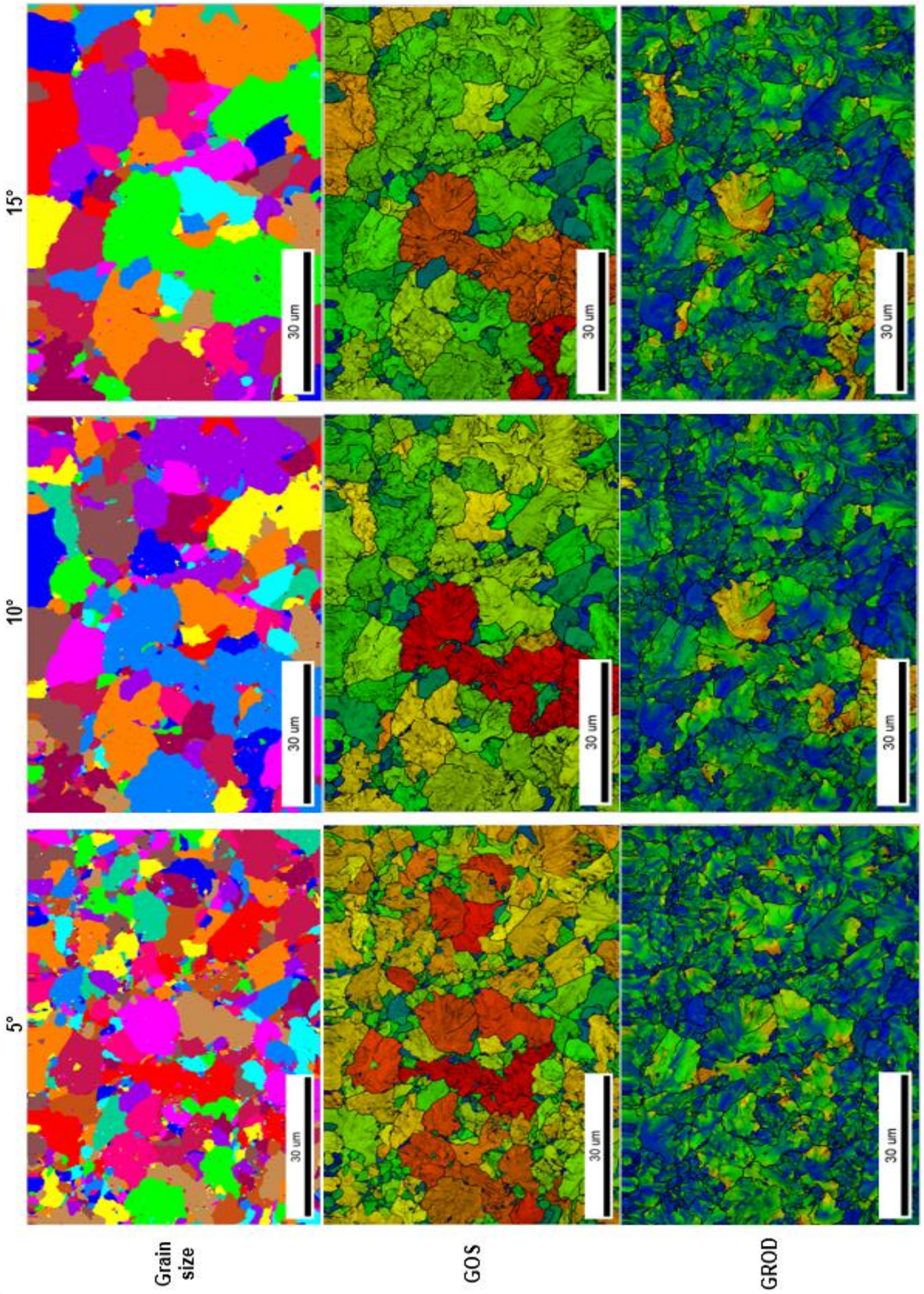

Figure 1230: Grain size, GOS and GROD maps for different grain tolerance angles

22.4 Interpretation of the EBSD results

For each considered case, EBSD analysis was carried out on both areas: in the matrix and around an inclusion. The purpose of such investigation is to estimate how the inclusion affects the local surrounding matrix. The global orientation of the microstructure can be deduced from IPF maps and an estimation of the misorientation gradient can be analysed with the KAM criterion. The IPF maps are presented in **Error! Reference source not found.**1 and the KAM maps are presented in Figure 1252.

The IPF maps show different aspects about the matrix. The matrix has colour variations by increasing the deformation. Moreover, this variation is also accompanied by a change in the morphology of the "grains" which are more elongated at high deformation level.

On both IPF maps and KAM maps, the inclusion appears black because of their non-indexation by EBSD. For IPF maps, as the deformation increases, a variation of places of disorientation around the inclusion (strongly visible on the image at 0.30 mm) is observed. The disorientation is lower for 5.5mm and 0.50mm diameter wires as the orientation colours around the inclusion are similar.

These first observations are confirmed on KAM distribution maps. If a 5.5 mm diameter wire would have been heat treated to have a non-deformed pearlitic structure, KAM variations can be converted to perlite colonies for disorientations induced by the curvature of cementite lamellae.

When the level of deformation applied has increased, the matrix in general and the area around the inclusion have higher KAM levels. In addition, the zones associated with these values of KAM are diffused in the matrix.

In order to further describe local deformation levels, a KAM level distribution study was completed.

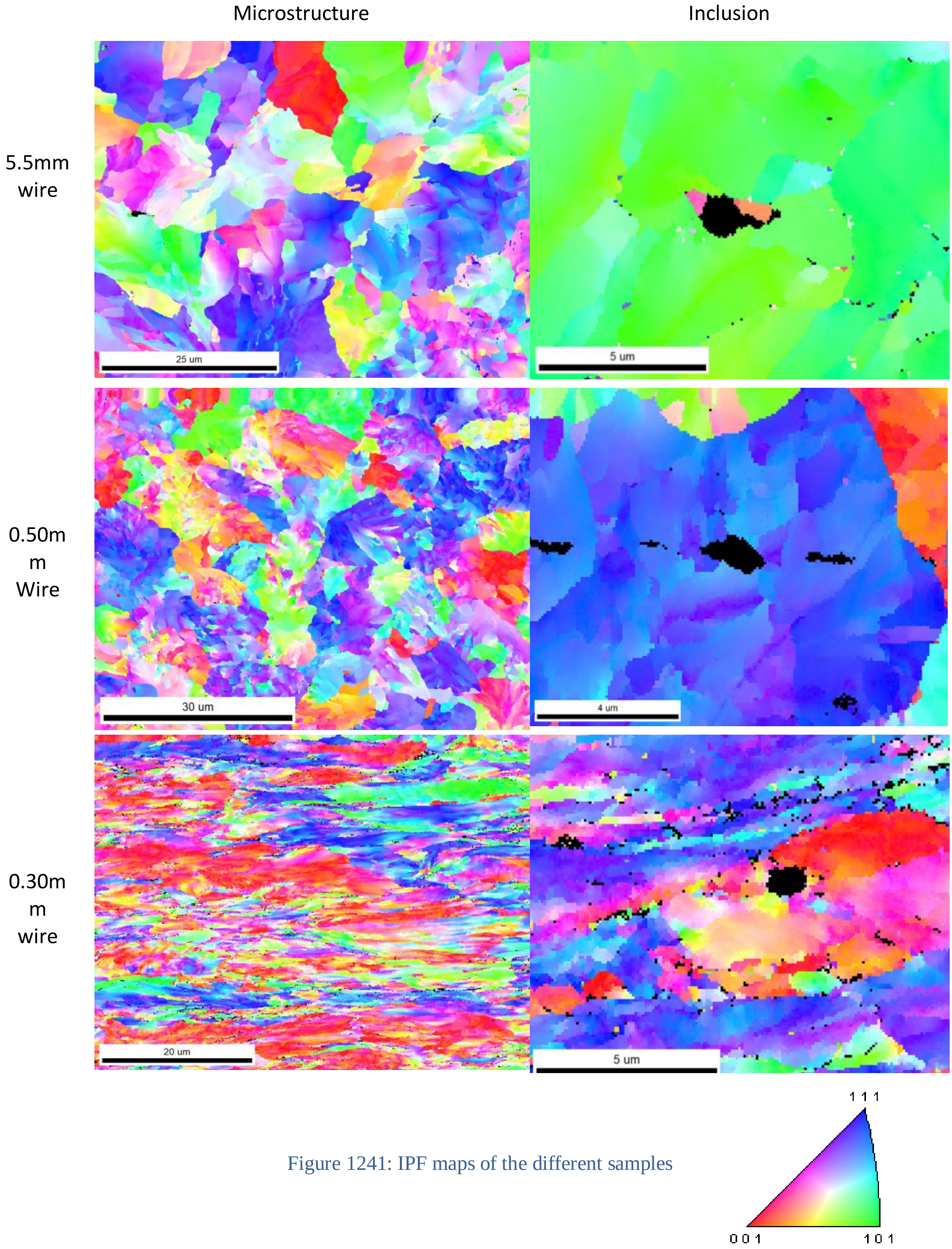

Figure 1241: IPF maps of the different samples

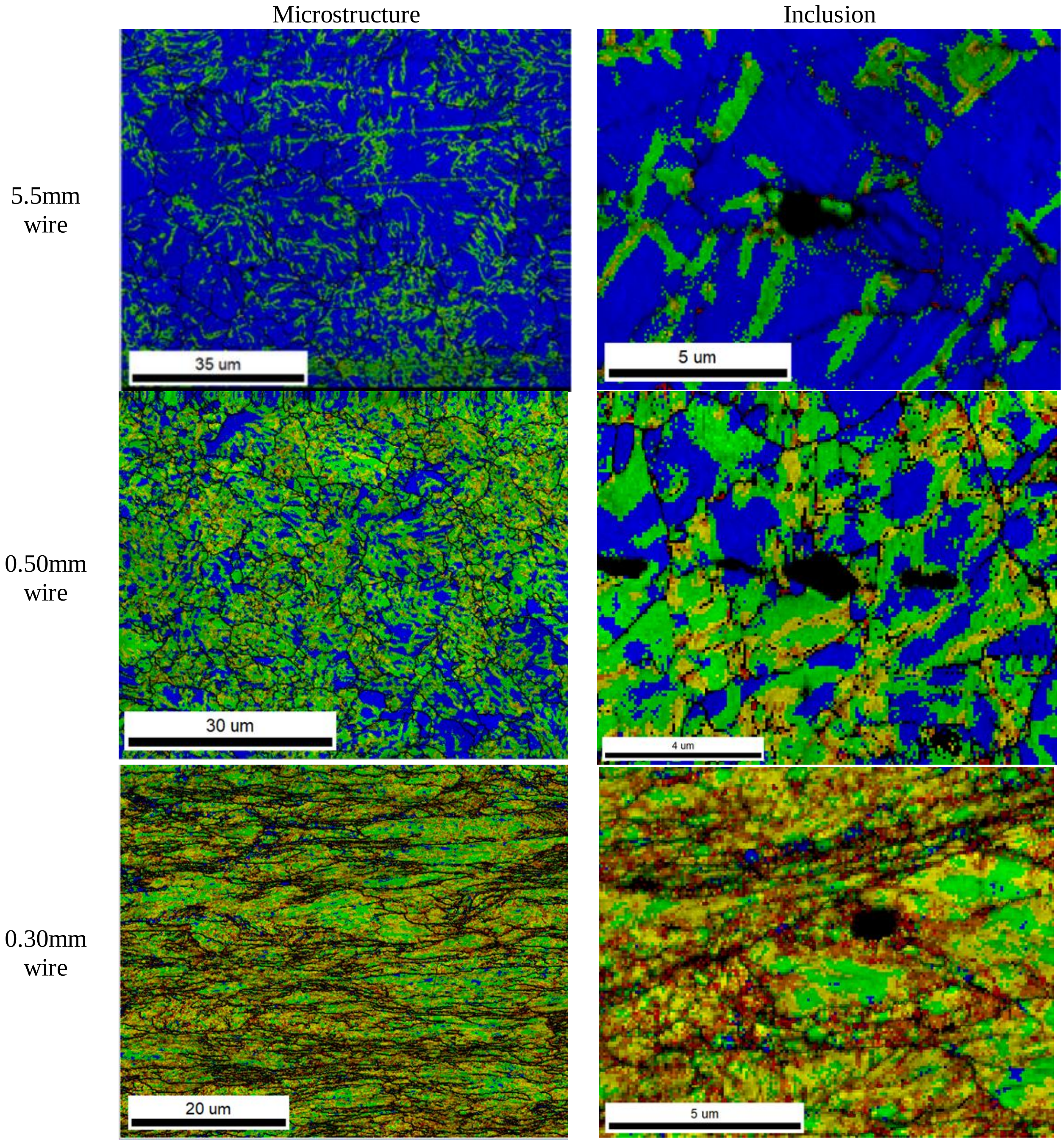

Figure 1252: KAM maps for the different samples

	Min	Max
🟦	0	1
🟩	1	2
🟨	2	3
🟧	3	4
🟥	4	5

The mean KAM values are reported for the different wires in **Error! Reference source not found.**

Table 43 : Average of KAM value for the different studied wires for the microstructure and around an inclusion

Wire diameter (mm)	Raw microstructure	Inclusion + microstructure
5.5	0.61	0.63
0.5	1.07	1.09
0.3	1.54	1.85

As the KAM is known to be related to the presence of GND, and that an increase of GND is related to local strain, then the results presented in Figure 1252 and **Error! Reference source not found.** confirm the observation of Takahashi. Some deformation levels are observed on the non-deformed pearlitic structure. When the wire is not submitted to loading, local misorientations are already observed.

Additionally, the KAM levels of the reference wire (Ø5.5mm) differs from the KAM level of the intermediate wire (Ø0.50mm). Note that the Ø0.50mm was patented in order to recover the microstructure of the wire and found back the initial microstructure. In theory the final patenting applied to the intermediate wire should recover completely the microstructure. Nevertheless, as the KAM is higher in the Ø0.5mm wire than in the Ø5.5mm wires, this points out that the effect of the patenting seems to be not sufficient to recover the microstructure. Although the shape of the grains looks somehow equiaxed, a residual strain is still present in the microstructure and mainly present at the so-identified “grain” boundaries.

Now, when considering the deformed structure, the KAM level is much more important than for the patented microstructure. Therefore, the strain of the wire during the wet wire drawing is visible by studying the average KAM values. Around the inclusion, logically, the tendency is similar. The average value of KAM increases when the diameter of the wire decreases.

Now, if the KAM average around inclusion is compared with KAM average on the microstructure, a difference exists. For the Ø5.5mm and Ø0.50mm wires, the difference between the mean KAM value in the microstructure and around the inclusion is similar. For the deformed wire (Ø0.3mm), the KAM average difference between the microstructure and at the inclusion surrounding is significant. A difference of 0.31 is present. This statement could suggest that the presence of the inclusion amplified the local misorientation compared to a free-of-inclusion microstructure.

Nevertheless, the approach based on the mean KAM value study is not optimal. Calculate the average KAM value around an inclusion gives a general idea of the misorientation level around the inclusion but in average over several microns. Consequently, the KAM values of the few microns at the edge of inclusions are averaged with the KAM value of the point far from the inclusions. Hence, the value is not representative of the very local misorientation around the inclusions.

To study into details the local misorientation, it was decided to study the KAM profiles over four sections around the inclusion. KAM values are reported along a two microns length over two preferential directions, horizontally and vertically as presented in Figure 1263. The results are presented in Figure 134. For each direction, the KAM values are reported for the intermediate wire (Ø0.5mm) and the deformed wire (Ø0.3mm).

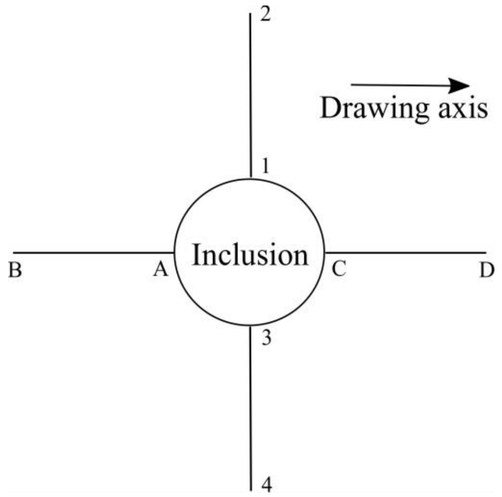

Figure 1263: Profile performed around the inclusion and identification of the sections

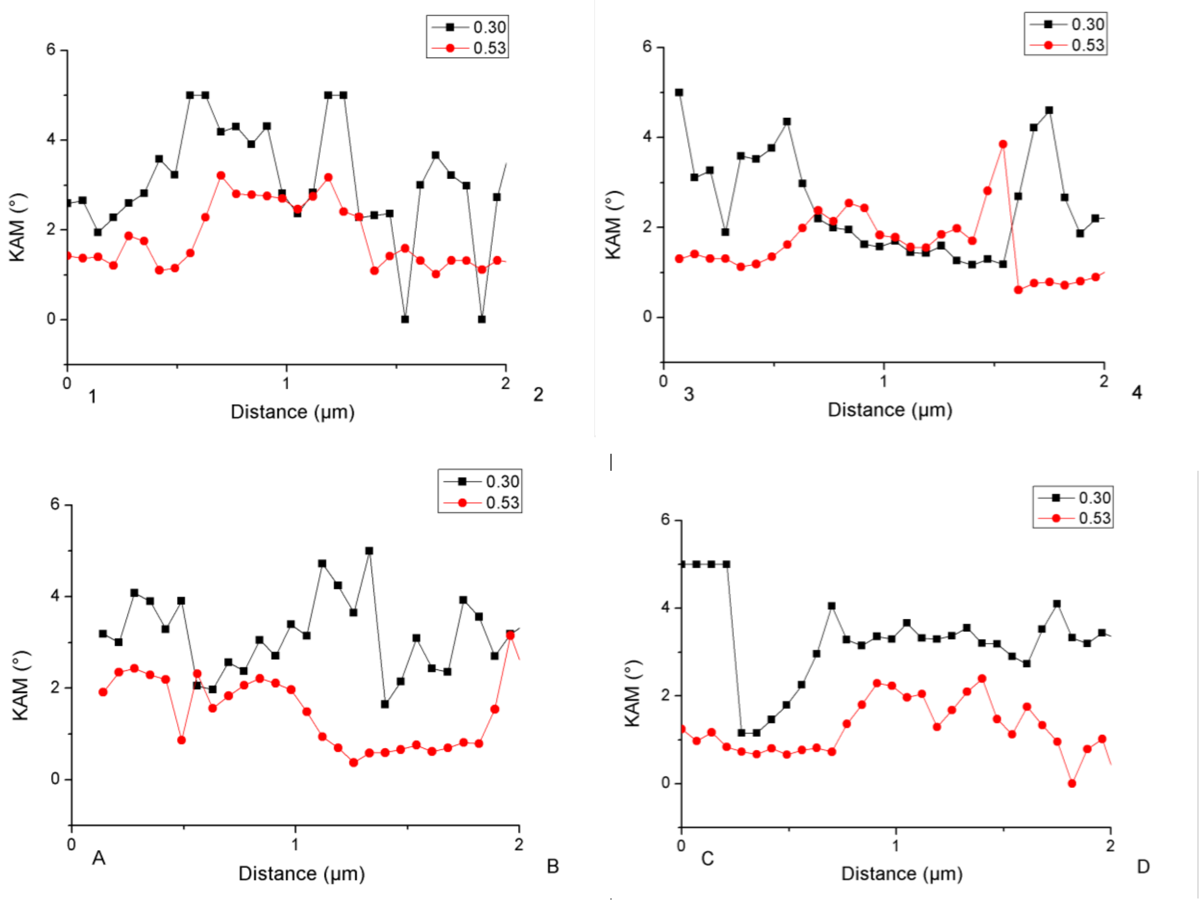

Figure 134: KAM value profile around the inclusions

From Figure 134, it can be concluded that the KAM values remain similar for all the considered directions. However, when comparing the deformed structure and the initial structure, KAM value does not increase suddenly at the inclusion interface when the sample is deformed. It is also noticed that the KAM values for the deformed wire are higher than for the intermediate wire. From this analysis, there are no significant differences between the perpendicular and the parallel direction with the drawing axis. The local misorientation seems not being influenced by the direction as the measured values are not significantly different if the measurement is performed parallel or perpendicular to the drawing axis. Referring to the simulation results, the horizontal side should be more impacted by the drawing than the vertical side of the drawing axis. Compression forces are more present perpendicularly to the drawing axis and tension forces are more present on the horizontal side of the inclusion.

This first set of measurements performed over 2 µm around the inclusions shows the impact of the strain in term of deformation levels but does not explain why cracks have initiated at the interface and in which direction. This measurement points out that the simulation might somehow be not relevant. In order to have a more local measurement and focus at the inclusion/matrix interface, the 50 nm step size used for SEM-EBSD is not sufficient.

22.5 Local misorientation

To overcome those problems, the idea came to perform the same measurements with the TEM and performing ACOM analysis with the ASTAR system developed by Rauch et al.[110] and provided by Nanomegas. The ACOM (Automated Crystal Orientation Microscopy) measurement is an automatic crystallographic indexing and orientation/phase mapping tool. The spatial resolution of an orientation or phase map is sensitive to most of the parameters related either to the microscope settings (responsible for the electron probe) or to the software built-in algorithm (responsible for the indexation). The typical angular resolution obtained with the ACOM-TEM system is up to 0.3 [111]. The difference between EBSD with SEM and ASTAR are compared in Table 44. It is observed that the spatial resolution is much improved by the use of ASTAR method. However, the angular resolution is lowered. This parameter has to be considered for the analysis of the results.

Table 44 : Comparison between EBSD and ASTAR technique

	EBSD (SEM)	**ASTAR (TEM)**
Radiation type	Electron	Electron
Geometry	Reflection	Transmission
Spatial resolution	30-90 nm	~10 nm
Angular resolution	0.08-1°	~1°
Depth of field	~10 nm	Lamella thickness

The quality of the diffracting signal is primordial for patterns indexation. The electron beam is scanned in combination with beam precession through the sample area [112]. A number of Electron Diffraction (ED) spot patterns from several sample locations are acquired at high speed using a CCD camera placed in front of the TEM screen. Local crystal orientations are obtained by comparing all individually obtained ED spot patterns via cross correlation matching techniques with pre-calculated ED templates. Phase and orientation identification is performed by patterns matching between experimental precession patterns with simulated templates (Figure 1285).

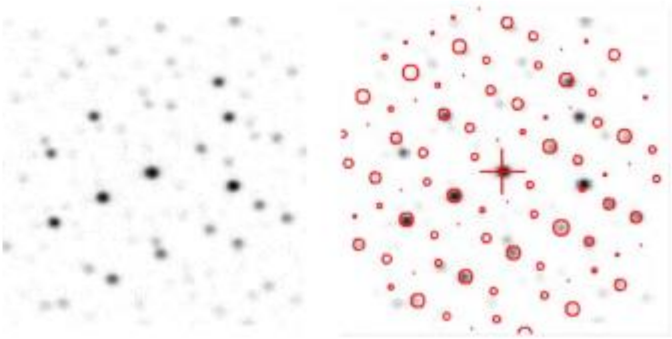

Figure 1275 : Example of ED spot pattern and correlation with pre-calculated ED template [113]

After the indexation of the patterns, the post treatment is performed with the TSL OIM software, as performed previously for the SEM-EBSD results, to obtain comparable results. The ASTAR scanning was performed on a FIB lamella containing the SiO_2-MgO inclusion. The TEM images, the IPF map and the KAM map are presented in Figure 1286.

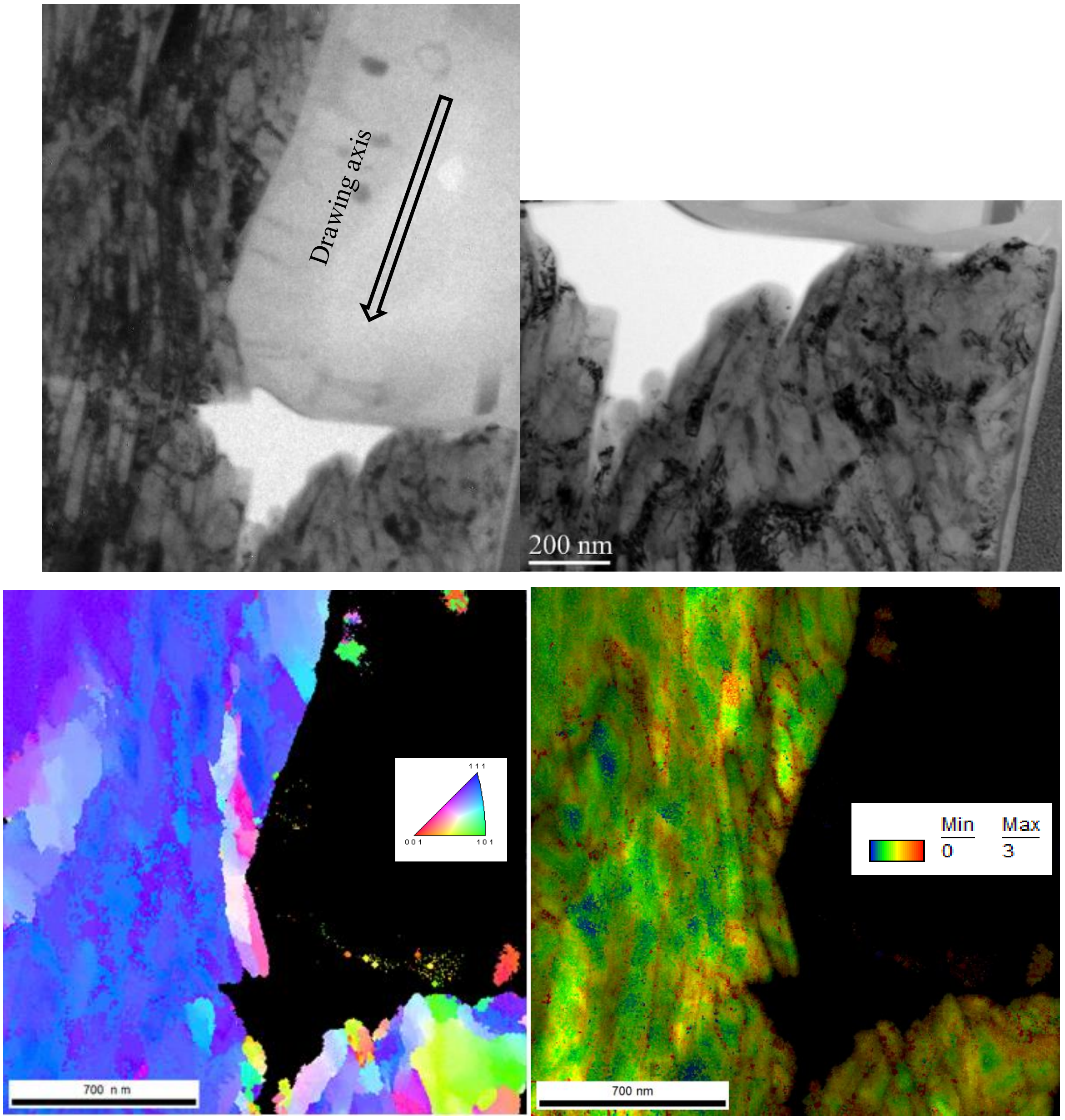

Figure 1286: TEM images and ASTAR IPF maps and KAM maps obtained with ASTAR measurement (SiO2-MgO)

By comparing the IPF map and the TEM image, the correlation is obvious. Far from the inclusion, a colour difference is less pronounced, meaning that the microstructure is slightly disoriented. However on the cohesive zone the disorientation is much more pronounced, this corresponds to a difference of colour more important in this zone. This observation can be linked with the observation with TEM images. In the cohesive zone, the microstructure is no more identifiable, the cementite lamellae are not observable, as if a new microstructure was created. This misorientation is, of course, introducing a difference of KAM level as observed on Figure 128.

A second FIB lamella containing the SiO_2-CaO inclusion has also been observed. Here the opening is less pronounced than for the first one. ASTAR measurement has also been performed on the edge of the inclusion and on the cohesive zone. The TEM images, The IPF map and the KAM maps are presented in Figure 129.

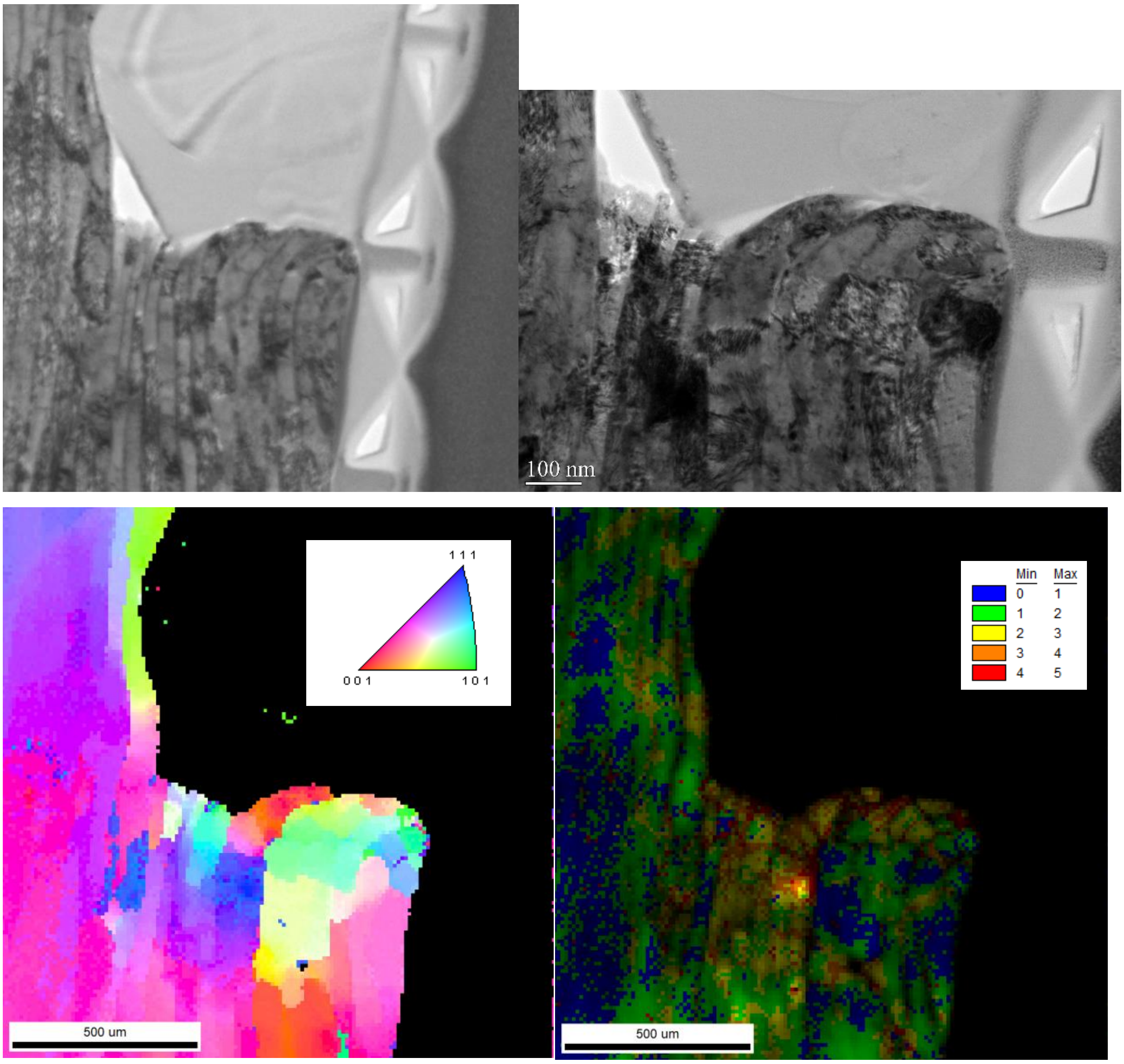

Figure 129: TEM images and ASTAR, IPF maps and KAM maps obtained with ASTAR measurement (SiO_2-CaO)

In this case, even if the decohesive zone is smaller than for the previous case, the same observation can be done. On the cohesive zone, the deformation is more pronounced along the drawing axis and on both cohesive zone and decohesive zone.

The inclusion type only influences the cracks opening, the deformation is equivalent.

These observations are in coherence with the observations from the modelling. Along the drawing axis, the microstructure is heavily deformed and is less impacted perpendicularly to the drawing axis.

22.6 Conclusions

The EBSD results confirm certain observation of the experimental study. The presence of the inclusion increases greatly the local misorientation of the matrix at its surrounding.

This increase of local misorientation due to the presence of an inclusion is already perceptible in non-deformed wires but is intensified on a deformed microstructure.

The ASTAR measurement locally confirmed the observation by TEM. The cohesive zone between the inclusion and the matrix is highly deformed while when the decohesion occurs the microstructure is less impacted by local deformation. In addition, the ASTAR measurement allows comparing the local deformation along the drawing axis and perpendicular to the drawing axis. It confirms that the local deformation is increased along the drawing axis but is minimum perpendicular to the drawing axis.

23 Conclusions

In this chapter, the rupture mechanism of the filament due to the presence of an inclusions during drawing and the impact on the stress and strain distribution have been studied into details.

From the study of the micro cracks around the inclusions, the different conclusions can be drawn:

- Not all the inclusions introduced cracks.
- It has been highlighted that the location of the inclusions has a more pronounced impact in comparison with their size.
- Meanwhile, the amount of cracks is lower in the centre of the wire, their length is somehow more pronounced. By contrast, the outer regions exhibit more cracks with shorter lengths.
- From this study, the influence of the inclusion chemical composition cannot be proved.
- The size of the cracks is not linked to the size of the inclusions but more to their localisation in the wire.
- The decohesion between the matrix and the inclusion is not only due to a uniaxial loading.
- The occurrence of the micro cracks is due to the combination of an intense tensile strength in the core of the wire and a shear stress due to die pressure.
- The apparition of cracks around the inclusions is not present on the initial wire but are introduced early in the process ($\varepsilon=1$).
- A lower die angle enables a reduction of the cracks initiation but does not influence on the size of the crack induced.
- The decohesion occurs whatever the morphology of the inclusion.
- Inclusions that do not exhibit a decohesion during surface analyse can be the initiation site of decohesion in the third dimension.

The EBSD results confirms some observations of the experimental study. The presence of the inclusion increases greatly the local misorientation of the matrix at its surrounding.

This increase of local misorientation due to the presence of an inclusion is already perceptible in non-deformed wires but is intensified on a deformed microstructure.

The ASTAR measurement locally confirmed the observation by TEM. The cohesive zone between the inclusion and the matrix is highly deformed while, when the decohesion occurs, the microstructure is less impacted by local deformation. In addition, the ASTAR measurement allows comparing the local deformation along the drawing axis and perpendicular to the drawing axis. It confirms that the local deformation is increased along the drawing axis but is minimum perpendicular to the drawing axis which was also observed thanks to the modelling.

The simulation also brings information on the stress distribution around the inclusion. The shear stress is more pronounced 45° from the drawing axis while passing through the die. This corresponds to the occurrence of a cup and cone fracture.

With all this information, the basic principal of the fracture mechanism can be summarized in an explanatory drawing

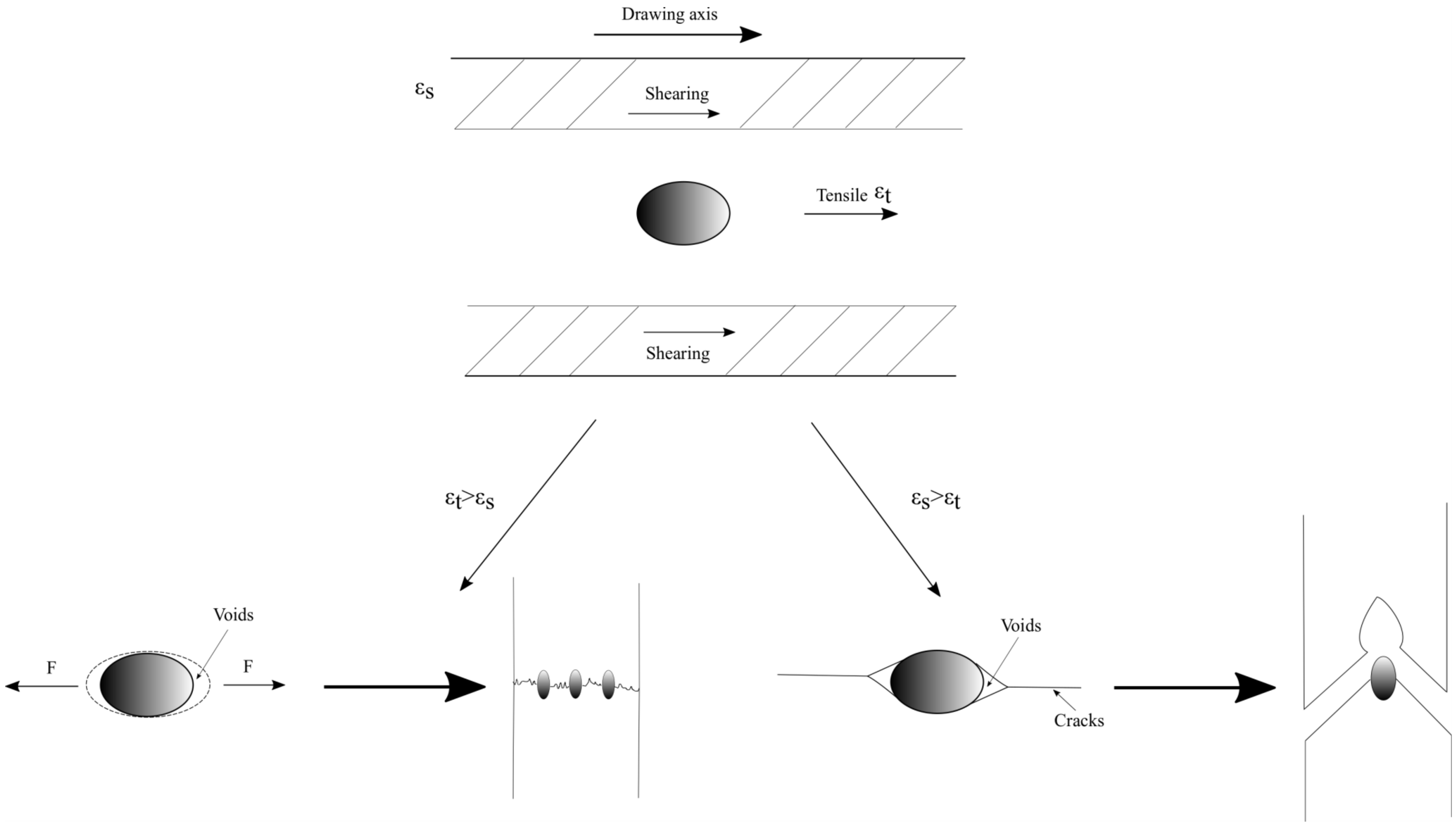
Drawing axis
ε_s
Shearing
Tensile ε_t
Shearing
$\varepsilon_t>\varepsilon_s$
$\varepsilon_s>\varepsilon_t$
Voids
F
F
Voids
Cracks

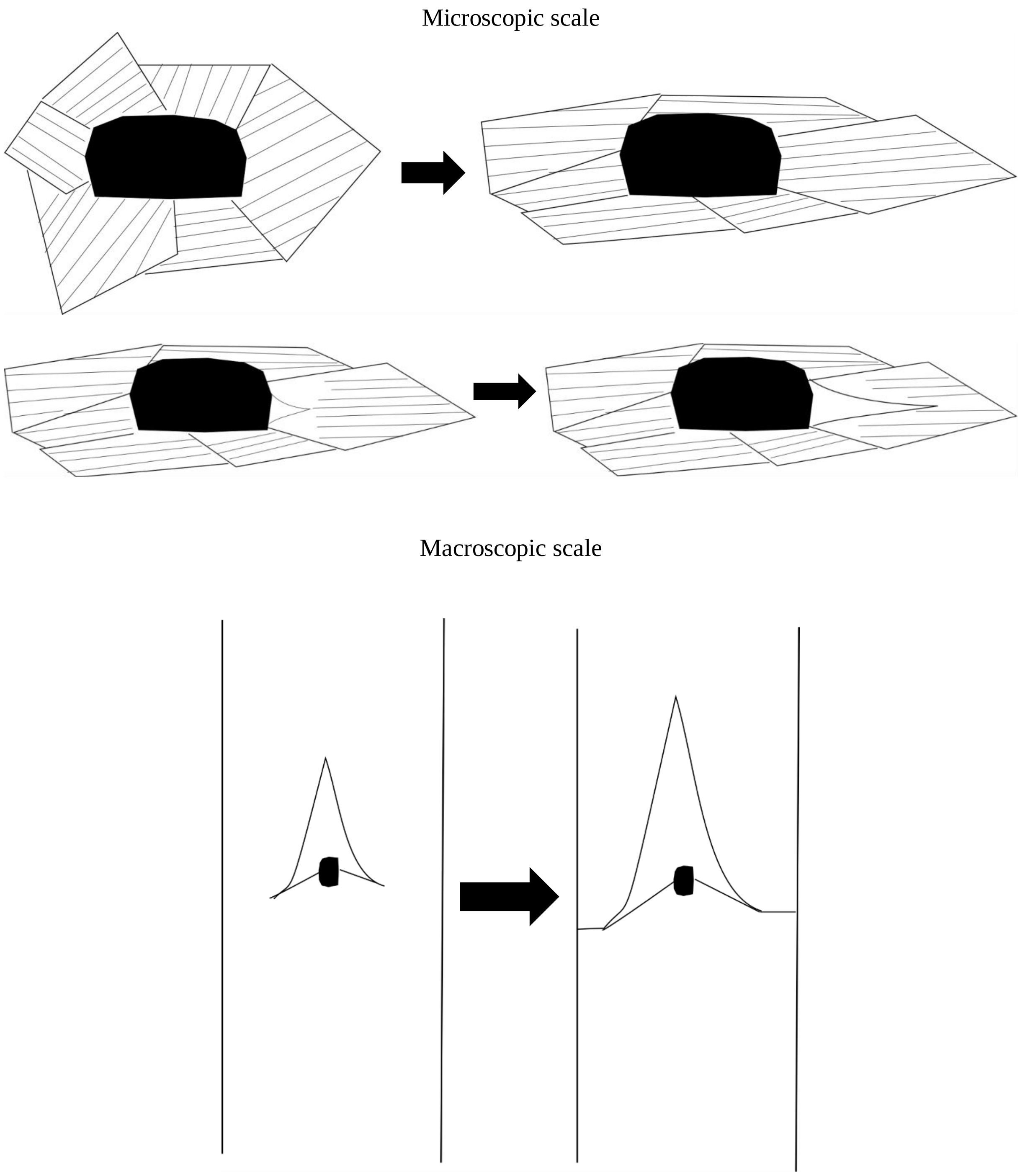
Microscopic scale
Macroscopic scale

Conclusions and perspectives

24 Conclusions and perspectives

24.1 General conclusions

A spool of 240 km is required by the customer. The major issue for the filaments drawing is the occurrence of fractures during the fine filament drawing. The occurrence of fractures during wet wire drawing (WWD) causes for the company a financial and a time loss. A pre study pointed out that 90% of the fractures were induced by the presence of a non-metallic inclusion in the fracture.

A literature study explains first the three specific aspects of the study: the wire drawing, the fine filaments and the presence of an inclusion.

Then, different cleanliness analysis methods have been evaluated. Four methods were selected: the automated SEM/EDS measurement, the OES/PDA, the extraction method and the Oxygen total measurement. The SEM/EDS method was found to be the most complete technique to measure the inclusion chemical composition, size and density. For the OES/PDA, the long development, now, allows a fast detection of the density and the chemical composition of the inclusions. For the results obtained with extraction method, the principal interest is to observe the morphology of the inclusion and enable the detection of bigger inclusions by increasing the statistics. These two objectives are respected by our extraction method. Concerning the oxygen total measurement, a perfect correlation was found between the oxide density measured with SEM/EDS and the total oxygen measured by combustion analysis.

The analysis of fractures obtained during the WWD has permitted to study the critical inclusions leading to fracture. The fractures mainly occur at oxides inclusions and more particular at silicates inclusions. Three major types of inclusions were identified as being critical: SiO_2, SiO_2-MgO, SiO_2-CaO with an average size around 6µm. These fractures mainly occur at the last pass of the drawing.
After drawing trials, it was concluded that the difference of cleanliness has a real impact on the occurrence of fractures, especially the inclusion density and size. Also it exists critical size for each type of inclusion.

Keeping constant cleanliness properties, the fracture ratio can be influenced by adapting the drawing parameters. The wire mechanical properties and heat treatment strongly affect the fracture occurrence and can lead to a reduction of fracture ratio around 85%. The critical size and chemical composition of inclusions leading to fractures change with the wire characteristics. The die angle used for wire drawing impacts the fracture ratio. By decreasing the die angle of the die series about 2°, the fracture ratio decreases about 50%. In another hand, the critical size of the inclusions is not impacted by the die angle change. Concerning the drawing speed, the conclusions are not so clear and do not seem to influence the fracture occurrence.

The last part of the PhD study allows us understanding in more detail the fracture mechanism involving an inclusion during the fine filament drawing. First, the study of the non-fractured filament shows the occurrence of micro-cracks at the edge of the inclusion, always parallel to the drawing axis. This cracks are not visible at the start of the wet wire drawing but form rapidly in the process already at $\varepsilon=1$. The study of the micro-cracks allows us to conclude that they are not always located in the centre of the filament. It was also concluded, viewing the shape of the micro cracks that they are induced by a combination of tensile and shear stress during the drawing
EBSD mapping proved that the presence of an inclusion increases greatly the local misorientation of the matrix at its surrounding. The ASTAR measurement locally confirmed the observation by TEM. The cohesive zone between the inclusion and the matrix is highly deformed while, when the decohesion occurs, the microstructure is less impacted by local deformation. It also confirms that the local deformation is increased along the drawing axis but is minimum perpendicular to the drawing axis. This confirms the information brought by the simulation. The simulation also brings information on the stress distribution around the inclusion. The shear stress is more pronounced 45° from the drawing axis while passing through the die. This corresponds to the occurrence of a cup and cone fracture. With all this information, the basic principal of the fracture mechanism has been drawn.

24.2 Perspectives

To go further in the understanding of the impact of inclusions on the drawing of fine steel filament of Ø60µm, the results of the study could be enhanced by improving the following points.
Some correlations between the drawability and the cleanliness of the wires were noticed. However, the real impact of the inclusion chemical composition on the drawability is not ideal. The different wires studied presented similarity in terms of inclusions chemical composition. The drawing of wires with different inclusions properties would bring additional information of the inclusion types.
Also, the measurement of the mechanical properties of the inclusions would strengthen the simulation and would bring interesting information on the behaviour of the inclusion and its interface with the matrix.
The last improvement of the results obtained with OES/PDA measurement enables a fast and reliable measurement of the inclusions. This advancement permits to increase the statistics by increasing the number of measurements and to detect rapidly various inclusions. By comparing the results from the

OES/PDA with the results of the drawability of the wires, an index could be defined to sort quickly the different qualities of wires and avoid the use of SEM.

Bibliography

25 Bibliography

[1] G.. Flauring, Iron Steelmak. (1999).
[2] N. Ridley, A Review of the Data on the Interlamellar Spacing of Pearlite, Metall. Mater. Trans. A. 15 (2007) 1019–1036. doi:10.1007/bf02644694.
[3] S.N. Doi, H.J. Kestenbach, Determination of the pearlite nodule size in eutectoid steels, Metallography. 23 (1989) 135–146. doi:10.1016/0026-0800(89)90015-3.
[4] P.R. Howell, The Pearlite Reaction in Steels Mechanisms and Crystallography, Mater. Charact. 40 (2002) 227–260. doi:10.1016/s1044-5803(98)00024-2.
[5] B. Garbarz, F.B. Pickering, Effect of pearlite morphology on impact toughness of eutectoid steel containing vanadium, Mater. Sci. Technol. 4 (2014) 328–334. doi:10.1179/mst.1988.4.4.328.
[6] T. Takahashi, M. Nagumo, Y. Asano, Microstructures dominating the ductility of eutectoid pearlitic steel, J. Japan Inst. Met. Mater. 42 (1978) 708–715. doi:https://doi.org/10.2320/jinstmet1952.42.7_708.
[7] I. Revolution, Theory of wiredrawing, (n.d.) 1–27.
[8] R. Wright, Wire technology - Process Engineering and Metallurgy, 2011. doi:10.1017/CBO9781107415324.004.
[9] M. Tintelecan, I.M. Sas-Boca, The Influence of the Dies Geometry on the Drawing Force for Steel Wires, Procedia Eng. 181 (2017) 193–199. doi:10.1016/j.proeng.2017.02.369.
[10] I.M. Sas-Boca, M. Tintelecan, M. Pop, D.A. Iluţiu-Varvara, A.M. Mihu, The Wire Drawing Process Simulation and the Optimization of Geometry Dies, Procedia Eng. 181 (2017) 187–192. doi:10.1016/j.proeng.2017.02.368.
[11] J.K. Hwang, I.C. Yi, I.H. Son, J.Y. Yoo, B. Kim, A. Zargaran, N.J. Kim, Microstructural evolution and deformation behavior of twinning-induced plasticity (TWIP) steel during wire drawing, Mater. Sci. Eng. A. 644 (2015) 41–52. doi:10.1016/j.msea.2015.07.034.
[12] K. Kirihara, Production Technology of Wire Rod for High Tensile Strength Steel Cord, Kobelco Technol. Rev. 30 (2011) 62–65.
[13] S. Lee, Process design of multi-stage wet wire drawing for improving the drawing speed for 0 . 72wt % C steel wire, J. Mater. Process. Technol. 210 (2010) 776–783. doi:10.1016/j.jmatprotec.2010.01.007.
[14] https://grabcad.com/questions/where-can-i-learn-to-create-wire-drawing-dies, (n.d.).
[15] X. Zhang, A. Godfrey, N. Hansen, X. Huang, W. Liu, Q. Liu, Evolution of cementite morphology in pearlitic steel wire during wet wire drawing, Mater. Charact. 61 (2009) 65–72. doi:10.1016/j.matchar.2009.10.007.
[16] X. Zhang, A. Godfrey, N. Hansen, X. Huang, W. Liu, Q. Liu, Evolution of cementite morphology in pearlitic steel wire during wet wire drawing, Mater. Charact. 61 (2009) 65–72. doi:10.1016/j.matchar.2009.10.007.
[17] L. Zhang, B.G. Thomas, X. Wang, K. Cai, Evaluation and Control of Steel Cleanliness: Review, 85th Steelmak. Conf. ISS-AIME, Warrendale,PA. (2002) 431–452.
[18] R. Kiessling, non-metallic inclusion in steel- Part V-, Institue of Metal, 1989.
[19] F. Ruby-Meyer, E. Hénault, M. Rocher-Bakour, F. Merchi, Improvement of inclusion cleanness in bearing steel and Catreated steel, Rev. Métallurgie. 104 (2007) 585–590. doi:10.1051/metal:2008002.
[20] E.T. Turkdogan, Fundamentals of steelmaking, The institute of Materials, n.d.
[21] A. Ghosh, Secondary Steel Making principles and Applications, CRC Press. (2000) 255–270, 274.
[22] L. Holappa, Secondary Steelmaking, 1st ed., Elsevier Ltd., 2014. doi:10.1016/B978-0-08-096988-6.00012-2.
[23] N. Dogan, R.J. Longbottom, M.H. Reid, M.W. Chapman, P. Wilson, L. Moore, B.J. Monaghan, Morphology and composition changes of spinel (MgAl 2 O 4) inclusions in steel,

Ironmak. Steelmak. 42 (2014) 185–193. doi:10.1179/1743281214Y.0000000219.
[24] S.K. Choudhary, Influence of Modified Casting Practice on Steel Cleanliness, ISIJ Int. 51 (2011) 557–565. doi:10.2355/isijinternational.51.557.
[25] K. Wang, M. Jiang, X. Wang, Y. Wang, H. Zhao, Z. Cao, Formation Mechanism of SiO2-Type Inclusions in Si-Mn-Killed Steel Wires Containing Limited Aluminum Content, Metall. Mater. Trans. B Process Metall. Mater. Process. Sci. 46 (2015) 2198–2207. doi:10.1007/s11663-015-0411-1.
[26] F.B. Pickering, S.W. Robinson, The plastic deformation and fractures of silicates inclusions in steel, Inst. Merallurgy, Incl. (1979) 246–255.
[27] L. Zhang, C. Guo, W. Yang, Y. Ren, H. Ling, Deformability of oxide inclusions in tire cord steels, Metall. Mater. Trans. B Process Metall. Mater. Process. Sci. 49 (2018) 803–811. doi:10.1007/s11663-017-1134-2.
[28] S. Kimura, I. Hoshikawa, N. Ibaraki, S. Hattori, T. Choda, Fracture Behavior of Oxide Inclusions during Rolling and Drawing, Testu-to-Hagane. 88 (2002) 53–60.
[29] C. Gatelier, H. Gaye, J. Lehmann, Control of complex inclusions during metallurgical treatments on liquid and solid steels, Steel Mak. Conf. Proc. (1991) 827–834.
[30] G. Bernard, P. V Riboud, G.U. Irsid, Étude de la plasticité d ’ inclusions d ’ oxydes *, (1981) 421–434.
[31] H. Iwai, B. Tsujino, S. Isa, T. Ao, On the behavior of the oxide inclusions of the system MnO-SiO2-Al2O3 in steels during hot-rolling, and their influence on tensile strength of steels, Testu-to-Hagane. 10 (1969) 23–36.
[32] T. Malkiewicz, S. Rudnik, Deformation of non-metallic inclusions during rolling of steel, J. Iron Steel Inst. 201 (1963) 33–38.
[33] K. Yamamoto, H. Yamamura, Y. Suwa, Behavior of Non-metallic Inclusions in Steel during Hot Deformation and the Effects of Deformed Inclusions on Local Ductility, ISIJ Int. 51 (2011) 1987–1994. doi:10.2355/isijinternational.51.1987.
[34] G. cheng Wang, S. li Li, X. gang Ai, C. min Zhang, C. bin Lai, Characterization and Thermodynamics of Al2O3-MnO-SiO2 (-MnS) Inclusion Formation in Carbon Steel Billet, J. Iron Steel Res. Int. 22 (2015) 566–572. doi:10.1016/S1006-706X(15)30041-8.
[35] J.S. Park, J.H. Park, Effect of slag composition on the concentration of Al2O3in the inclusions in Si-Mn-killed steel, Metall. Mater. Trans. B Process Metall. Mater. Process. Sci. 45 (2014) 953–960. doi:10.1007/s11663-013-9998-2.
[36] T.. Engh, Principle of Metal Refining, Oxford Univ. Press. (1992) 19–38.
[37] R. Maiti, E.B. Hawbolt, The effect of hot rolling on the inclusion morphology of a semi-killed and a calcium treated X-70 pipeline steel, J. Mater. Energy Syst. 6 (1985) 251–262. doi:10.1007/BF02833514.
[38] S.H. Chen, M. Jiang, X.F. He, X.H. Wang, Top slag refining for inclusion composition transform control in tire cord steel, Int. J. Miner. Metall. Mater. 19 (2012) 490–498. doi:10.1007/s12613-012-0585-3.
[39] L. Zhang, C. Guo, W. Yang, Y. Ren, H. Ling, Deformability of oxide inclusions in tire cord steels, Metall. Mater. Trans. B Process Metall. Mater. Process. Sci. 49 (2018) 803–811. doi:10.1007/s11663-017-1134-2.
[40] P.E. Waudby, Factors controlling the plasticity of silicates inclusions, Steel Times Annu. Rev. (1972) 147–152.
[41] T.J. Baker, K.B. Gove, A. Charles, Inclusion deformation and toughness anisotropy in hot rolled steel, Met. Technol. 3 (1976) 1183–1193.
[42] K.B. Gove, A. Charles, Further aspect on inclusion deformation, Met. Technol. (1974) 425–431.
[43] S.I. Gubenko, Effect of “nonmetallic inclusion–matrix” phase boundaries on the cohesive resistance of steel, Met. Sci. Heat Treat. 48 (2006) 13–18. doi:10.1007/s11041-006-0035-9.
[44] A. Nicholson, T. Galdman, Non-metallic inclusions and developments in secondary steelmaking, Ironmak. Steelmak. 13(2) (1986) 53–69.
[45] Y. Hu, W. Chen, C. Wan, F. Wang, H. Han, Effect of Deoxidation Process on Inclusion and

Fatigue Performance of Spring Steel for Automobile Suspension, Metall. Mater. Trans. B Process Metall. Mater. Process. Sci. (2018) 1–12. doi:10.1007/s11663-018-1187-x.

[46] J. Guan, L. Wang, C. Zhang, X. Ma, Effects of non-metallic inclusions on the crack propagation in bearing steel, Tribol. Int. 106 (2017) 123–131. doi:10.1016/j.triboint.2016.10.030.

[47] K. Lambrighs, I. Verpoest, B. Verlinden, M. Wevers, Influence of non-metallic inclusions on the fatigue properties of heavily cold drawn steel wires, Procedia Eng. 2 (2010) 173–181. doi:10.1016/j.proeng.2010.03.019.

[48] J. Petit, F. Lorenzi, Procedia Engineering Fatigue crack propagation in thin wires of ultra high strength steels, Procedia Eng. 2 (2010) 2317–2326. doi:10.1016/j.proeng.2010.03.248.

[49] Y. Akiniwa, Notch effect on fatigue strength reduction of bearing steel in the very high cycle regime, Int. J. Fatigue. 28 (2006) 1555–1565. doi:10.1016/j.ijfatigue.2005.04.017.

[50] K. Tanaka, Y. Akiniwa, Fatigue crack propagation behaviour derived from S-N data in very high cycle regime, Fatigue Fract Engng Mater Struct. 25 (2002) 775–784.

[51] K. Shiozawa, T. Hasegawa, Y. Kashiwagi, L. Lu, Very high cycle fatigue properties of bearing steel under axial loading condition, Int. J. Fatigue. 31 (2009) 880–888. doi:10.1016/j.ijfatigue.2008.11.001.

[52] K. Lambrighs, I. Verpoest, B. Verlinden, M. Wevers, Influence of non-metallic inclusions on the fatigue properties of heavily cold drawn steel wires, Procedia Eng. 2 (2010) 173–181. doi:10.1016/j.proeng.2010.03.019.

[53] Y. Tomita, Effect of desulphurization and calcium treatments on the inclusion morphology of O.4C-Cr-Mo-Ni steel, J. Mater. Sci. 29 (1994) 2873–2878. https://link.springer.com/content/pdf/10.1007%2FBF01117595.pdf (accessed July 27, 2017).

[54] T. Galdman, Developments in inclusions and their effects on steel properties, Iron Steel Mak. 19 (1992) 457–463.

[55] H.. Schwalbe, No Title, Enginnering Fract. Mech. (1977) 795–835.

[56] W.M. Garrison, A.L. Wojcieszynski, A discussion of the spacing of inclusions in the volume and of the spacing of inclusion nucleated voids on fracture surfaces of steels, Mater. Sci. Eng. A. 505 (2009) 52–61. doi:10.1016/j.msea.2008.11.065.

[57] W. Leslie, Inclusions and mechanical properties, Trans Iron Steel Soc. 2 (1983) 1–24.

[58] M. Yilmaz, Failures during the production and usage of steel wires, J. Mater. Process. Technol. 171 (2006) 232–239. doi:10.1016/j.jmatprotec.2005.07.007.

[59] S.-I. Ji, K.-H. Lee, Y.-S. Yang, The effetcs of Non-metallic Inclusions on Ductile Damage of High Carbon Steel Wire in Multi-pass Dry Drawing Process, Key Eng. Mater. 622–623 (2014) 155–161.

[60] H. Cho, H.H. Jo, S.G. Lee, B.M. Kim, Y.J. Kim, Effect of reduction ratio, inclusion size and distance between inclusions on wire breaks in Cu fine wiredrawing, J. Mater. Process. Technol. 130–131 (2002) 416–420. doi:10.1016/S0924-0136(02)00719-7.

[61] S. Norasethasopon, K. Yoshida, Influences of inclusion shape and size in drawing of copper shaped-wire, J. Mater. Process. Technol. 172 (2006) 400–406. doi:10.1016/j.jmatprotec.2005.09.020.

[62] W. Yan, H.C. Xu, W.Q. Chen, Study on inclusions in wire rod of tire cord steel by means of electrolysis of wire rod, Steel Res. Int. 85 (2014) 53–59. doi:10.1002/srin.201300045.

[63] C. Luo, Evolution of voids close to an inclusion in hot deformation of metals, 21 (2001) 360–374.

[64] Y.U. Hai-liang, B.I. Hong-yun, उढ L.I.U.X., T.U. Yan-feng, Strain distribution of strips with spherical inclusion during cold rolling, (2008) 2–7.

[65] G. Le Roy, J.D. Embury, G. Edwards, M.F. Ashby, A model of ductile fracture based on the nucleation and growth of voids, Acta Metall. 29 (1981) 1509–1522. doi:10.1016/0001-6160(81)90185-1.

[66] A. Melander, A. Gustavsson, An FEM study of driving forces of short cracks at inclusions in hard steels, Int. J. Fatigue. 18 (1996) 389–399. doi:10.1016/0142-1123(96)00069-2.

[67] K. Yoshida, I. Toshi, Analysis of wire break during drawing of fine wire with an inclusion by

FEM, Wire J. Int. (2000) 102–107.

[68] L.F. Zhang, B.G. Thomas, State of the Art in Evaluation and Control of Steel Cleanliness, ISIJ Int. 43 (2003) 271–291. doi:10.2355/isijinternational.43.271.

[69] L.E.K. Holappa, A.S. Helle, Inclusion Control in High-Performance Steels, J. Mater. Process. Tech. 53 (1995) 177–186. doi:10.1016/0924-0136(95)01974-J.

[70] T. Scientific, Internal brochure for OES PDA, (n.d.).

[71] Process-based steel cleanliness investigations and rapid metallurgical screening of inclusions by modern PDA techniques (Ramsci), n.d.

[72] D. Janis, A. Karasev, P.G. Jönsson, Evaluation of Inclusion Characteristics in Low-Alloyed Steels by Mainly Using PDA / OES Method, 55 (2015) 2173–2181. doi:10.2355/isijinternational.ISIJINT-2015-172.

[73] S.K. Michelic, G. Wieser, C. Bernhard, On the Representativeness of Automated SEM/EDS Analyses for Inclusion Characterisation with Special Regard to the Measured Sample Area, ISIJ Int. 51 (2011) 769–775. doi:10.2355/isijinternational.51.769.

[74] J. Pilarczyk, J. Markowski, FEM ANALYSIS OF EFFECT OF DIE ANGLE ON STRAIN AND STRESS, 44 (2005) 227–230.

[75] H. liang Yu, H. yun Bi, X. hua Liu, L. qing Chen, N. ni Dong, Behavior of inclusions with weak adhesion to strip matrix during rolling using FEM, J. Mater. Process. Technol. 209 (2009) 4274–4280. doi:10.1016/j.jmatprotec.2008.11.004.

[76] A. Kareem F. Hassan, A. S. Hashim, Three Dimensional Finite Element Analysis of Wire Drawing Process, Univers. J. Mech. Eng. 3 (2015) 71–82. doi:10.13189/ujme.2015.030302.

[77] a Milenin, Z. Muskalski, S. Wiewiórowska, P. Kustra, The multi-scale FEM simulation of the drawing processes of high carbon steel, J. Achiev. Mater. Manuf. Eng. 23 (2007) 71–74.

[78] G. Xu, F. Fang, Z. Li, Optimization of the Technology of Wire Drawing Based on Finite Element Modeling, Mod. Appl. Sci. 3 (2009) 193–198. doi:10.5539/mas.v3n5p193.

[79] Z. Muskalski, Selected problems from the high-carbon steel wire drawing theory and technology, Arch. Metall. Mater. 59 (2014) 527–535. doi:10.2478/amm-2014-0087.

[80] S.B. Son, Y.K. Lee, S.H. Kang, H.S. Chung, J.S. Cho, J.T. Moon, K.H. Oh, A numerical approach on the inclusion effects in ultrafine gold wire drawing process, Eng. Fail. Anal. 18 (2011) 1272–1278. doi:10.1016/j.engfailanal.2011.03.015.

[81] F. Dunne, N. Petrinic, Introduction to computational plasticity, Oxford Uni, Oxford University press, 2005.

[82] R.B. Colby, Ph.D.thesis. Equivalent plastic strain for the Hill's yield criterion under general three-dimensionalloading, (2013) 1–45. doi:http://hdl.handle.net/1721.1/83690.

[83] J.C. Simo, T.J. Hughes, Computational Inelasticity, 1998.

[84] M.Á. Caminero, F.J. Montáns, K.J. Bathe, Modeling large strain anisotropic elasto-plasticity with logarithmic strain and stress measures, Comput. Struct. 89 (2011) 826–843. doi:10.1016/j.compstruc.2011.02.011.

[85] P. Papadopoulos, J. Lu, On the formulation and numerical solution of problems in anisotropic finite plasticity, Comput. Methods Appl. Mech. Eng. 190 (2001) 4889–4910. doi:10.1016/S0045-7825(00)00355-8.

[86] L. Mettler, Numerical Implementation of an Anisotropic Finite-Deformation Plasticity Model, UC Berkeley, 2012.

[87] G. Chen, Q. Xiong, P.J. Morris, E.G. Paterson, A. Sergeev, Y.-C. Wang, OpenFOAM for Computational Fluid Dynamics, Not. Am. Math. Soc. 61 (2014) 354. doi:10.1090/noti1095.

[88] H. Jasak, OpenFOAM : Open source CFD in research and industry, Inter J Nav Arch. Oc Engng. 1 (2009) 89–94. doi:10.2478/IJNAOE-2013-0011.

[89] H. Jasak, A. Jemcov, Z. Tukovic, OpenFOAM : A C ++ Library for Complex Physics Simulations, Int. Work. Coupled Methods Numer. Dyn. m (2007) 1–20.

[90] J. Ahrens, B. Geveci, C. Law, ParaView: An end-user tool for large-data visualization, Vis. Handb. 836 (2005) 717–731. doi:10.1016/B978-012387582-2/50038-1.

[91] Y.N. Wang, J. Yang, Y.P. Bao, Effects of Non-metallic Inclusions on Machinability of Free-Cutting Steels Investigated by Nano-Indentation Measurements, Metall. Mater. Trans. A Phys.

Metall. Mater. Sci. 46 (2015) 281–292. doi:10.1007/s11661-014-2596-3.
[92] https://materialsproject.org/materials/mp-2605/, (n.d.).
[93] https://www.crystran.co.uk/optical-materials/magnesium-oxide-mgo, (n.d.).
[94] https://www.crystran.co.uk/optical-materials/silica-glass-sio2, (n.d.).
[95] https://www.crystran.co.uk/optical-materials/sapphire-al2o3, (n.d.).
[96] S.I. Wright, M.M. Nowell, D.P. Field, A review of strain analysis using electron backscatter diffraction, Microsc. Microanal. 17 (2011) 316–329. doi:10.1017/S1431927611000055.
[97] S.I. Wright, M.M. Nowell, S.P. Lindeman, P.P. Camus, M. De Graef, M.A. Jackson, Introduction and comparison of new EBSD post-processing methodologies, Ultramicroscopy. 159 (2015) 81–94. doi:10.1016/j.ultramic.2015.08.001.
[98] A.J. Wilkinson, T. Ben Britton, Strains, planes, and EBSD in materials science, Mater. Today. 15 (2012) 366–376. doi:10.1016/S1369-7021(12)70163-3.
[99] C. Maurice, R. Fortunier, A 3D Hough transform for indexing EBSD and Kossel patterns, J. Microsc. 230 (2008) 520–529. doi:10.1111/j.1365-2818.2008.02045.x.
[100] T. Maitland, S. Sitzman, Electron backscatter diffraction (EBSD) technique and materials characterization examples, Scanning Microscopy for Nanotechnology, Springer. (2006) 41–76.
[101] A.J. Wilkinson, G. Meaden, D.J. Dingley, High-resolution elastic strain measurement from electron backscatter diffraction patterns: New levels of sensitivity, Ultramicroscopy. 106 (2006) 307–313. doi:10.1016/j.ultramic.2005.10.001.
[102] T. Ben Britton, S. Birosca, M. Preuss, A.J. Wilkinson, Electron backscatter diffraction study of dislocation content of a macrozone in hot-rolled Ti-6Al-4V alloy, Scr. Mater. 62 (2010) 639–642. doi:10.1016/j.scriptamat.2010.01.010.
[103] J. Bouquerel, B. Diawara, A. Dubois, M. Dubar, J.B. Vogt, D. Najjar, Investigations of the microstructural response to a cold forging process of the 6082-T6 alloy, Mater. Des. 68 (2015) 245–258. doi:10.1016/j.matdes.2014.12.005.
[104] P.J. Buchanan, V. Randle, P.E.J. Flewitt, A simple procedure for the assessment of plastic strain in electron back-scatter diffraction patterns, Scr. Mater. 37 (1997) 1511–1518. doi:10.1016/S1359-6462(97)00245-5.
[105] A. Godfrey, W.Q. Cao, N. Hansen, Q. Liu, Stored energy, microstructure, and flow stress of deformed metals, Metall. Mater. Trans. A Phys. Metall. Mater. Sci. 36 (2005) 2371–2378. doi:10.1007/s11661-005-0109-0.
[106] J.B. Vogt, J. Bouquerel, F. Léaux, F. Palleschi, Fatigue damage assessment of alternator fans by EBSD, Procedia Eng. 66 (2013) 608–614. doi:10.1016/j.proeng.2013.12.112.
[107] T. Takahashi, D. Ponge, D. Raabe, Investigation of orientation gradients in pearlite in hypoeutectoid steel by use of orientation imaging microscopy, Steel Res. Int. 78 (2007) 38–44. doi:10.1002/srin.200705857.
[108] N. Guo, Q. Liu, Back-scattered electron imaging combined with EBSD technique for characterization of pearlitic steels, J. Microsc. 246 (2012) 221–228. doi:10.1111/j.1365-2818.2011.03601.x.
[109] A. Walentek, M. Seefeldt, B. Verlinden, E. Aernoudt, P. Van Houtte, Electron backscatter diffraction on pearlite structures in steel, J. Microsc. 224 (2006) 256–263. doi:10.1111/j.1365-2818.2006.01702.x.
[110] E.F. Rauch, M. Véron, J. Portillo, D. Bultreys, Y. Maniette, S. Nicolopoulos, Automatic Crystal Orientation and Phase Mapping in TEM by Precession Diffraction, Microsc. Anal. 22 (2008) S5–S8. http://www.microscopy-analysis.com/sites/default/files/magazine_pdfs/mag2008_November_Rauch.pdf.
[111] Nanomegas, ASTAR - Application notes nanoscale TEM orientation imaging analysis, (2016) 1–32. www.nanomegas.com.
[112] D. Viladot, M. Véron, M. Gemmi, F. Peiró, J. Portillo, S. Estradé, J. Mendoza, N. Llorca-Isern, S. Nicolopoulos, Orientation and phase mapping in the transmission electron microscope using precession-assisted diffraction spot recognition: State-of-the-art results, J. Microsc. 252 (2013) 23–34. doi:10.1111/jmi.12065.
[113] A. Valery, Microtexture characterization by Automated Crystal Orientation Mapping in TEM

for the development of advanced technologies in microelectronics To cite this version : HAL Id : tel-01688218 Caractérisation de microtextures par la technique ACOM-TEM dans le, (2017).

Abstract

The production of very fine filaments (60 µm in diameter) of high carbon and high strength steels remains a technological challenge. Indeed, during the drawing of these filaments, fractures have been observed limiting the obtaining of coils of great length. This study, in collaboration with company BEKAERT NV, is to understand the role of the microstructure of steel, and more specifically the steel cleanliness on the occurrence of fracture during wet drawing.

Methodologies for inclusion identification and for inclusion count were developed. 90 % of the fractured filaments were associated with an inclusion which was SiO_2, or SiO_2-CaO or SiO_2-MgO. The fracture of the wires resulted from debonding of the inclusion from the matrix. Inclusions exhibited a wide range of sizes but mostly around 6µm. The inclusion density did not appear as the only parameter that affects the fracture occurrence. An important effect of size and of chemical composition inclusion of the inclusions was found. A critical size of inclusions for fracture was observed but it depends on the chemical composition of inclusions. The drawing parameters also play an important role in the fracture occurrence. The wire mechanical properties and the die angle appear to be important parameters in view to reduce the fracture ratio.

A deeper analysis of the microstructural changes around the inclusion by EBSD combined to stress simulation underlines a real impact of the inclusion on the local deformation around the inclusion. The local analysis (TEM and ACOM - Automated Crystal Orientation Mapping) of inclusion/matrix interface shows a difference of microstructure at the inclusion edge along the drawing axis and a higher local deformation. The study of these different parameters makes possible to propose a fracture mechanism that takes into account the part of the material subjected to shear and the one subjected to tensile stress.

Keywords: **Pearlite, microstructure, forming process, fracture, severe deformation, spectroscopy**

Résumé

La fabrication de très fins filaments (60 µm de diamètre) d’aciers à haute teneur en carbone et à haute résistance mécanique reste un défi technologique. En effet, durant le tréfilage de ces filaments, des ruptures ont été observées limitant ainsi l’obtention de bobines de grande longueur. Le but de cette étude en partenariat avec la société BEKAERT NV est de comprendre le rôle de la microstructure de l’acier, et plus précisément la propreté inclusionnaire, sur l’occurrence des ruptures lors du tréfilage humide.

Il est clairement montré que la rupture lors du tréfilage est essentiellement associée à la présence d’inclusions. Ainsi, une première étape a consisté à développer une méthodologie pour identifier ces inclusions. 90% des filaments rompus impliquent les inclusions suivantes : SiO_2, ou SiO_2-CaO ou SiO_2-MgO. La rupture des fils résulte de la décohésion de l'inclusion de la matrice. Les inclusions présentent une large distribution de taille mais mesurent en moyenne 6 µm. Les paramètres critiques liés aux inclusions pour l’occurrence de la rupture sont multiples : densité d'inclusions, taille et composition chimique. La taille critique de l’inclusion dépend de la composition chimique. De plus, les paramètres du procédé de tréfilage jouent également un rôle important dans l’occurrence des ruptures. Les propriétés mécaniques du fil et l’angle de filière apparaissent comme des paramètres importants pour réduire le taux de rupture.

Une analyse plus approfondie des changements microstructuraux autour de l'inclusion par EBSD combinée à une simulation des contraintes soulignent un impact réel de l'inclusion sur la déformation locale autour de l'inclusion. L'analyse locale (MET et ACOM - Automated Crystal Orientation Mapping) de l'interface inclusion/matrice montre une différence de microstructure près du bord de l'inclusion le long de l'axe de tréfilage et une déformation locale plus élevée. L’étude de ces différents paramètres permet la proposition d’un mécanisme de rupture qui prend en compte dans le fil la part de matière cisaillée et la part de matière soumise à de la traction.

Mots clés : **Perlite, microstructure, mise en forme, rupture, déformation, sévère, spectroscopie**